Doctoral theses at NTNU, 2024:59

Thomas Treider

Earth fault location in non-radial resonant grounded networks

Theory, analysis and methods

Doctoral thesis

NTNU
Norwegian University of Science and Technology
Thesis for the Degree of Philosophiae Doctor
Faculty of Information Technology and Electrical Engineering
Departement of Electric Energy

NTNU
Norwegian University of Science and Technology

Thomas Treider

Earth fault location in non-radial resonant grounded networks

Theory, analysis and methods

Thesis for the Degree of Philosophiae Doctor

Trondheim, February 2024

Norwegian University of Science and Technology
Faculty of Information Technology and Electrical Engineering
Departement of Electric Energy

NTNU
Norwegian University of
Science and Technology

NTNU
Norwegian University of Science and Technology

Thesis for the Degree of Philosophiae Doctor

Faculty of Information Technology and Electrical Engineering
Departement of Electric Energy

ISBN 978-82-326-7718-4 (printed ver.)
ISBN 978-82-326-7717-7 (electronic ver.)
ISSN 1503-8181 (printed ver.)
ISSN 2703-8084 (online ver.)

Doctoral theses at NTNU, 2024:59

Printed by NTNU Grafisk senter

Preface

The research presented in this thesis was carried out between March 2020 and October 2023 at the Department of Electric Energy at the Norwegian University of Science and Technology. The main supervisor during this work was Professor Hans Kristian Høidalen, with co-supervision by Adjunct Professor Bjørn Gustavsen and Professor Irina Oleinikova.

Acknowledgements

This PhD project has been both an educational and at times challenging experience. Performing a literature review, preparing simulations and experiments, analysing the results and writing the thesis – in that order – was not as easy as first assumed. Starting out as a PhD student in a completely new field of research, it has been an iterative process of learning and research, successes and failures, before arriving at the current thesis.

I would like to thank my supervisor, Professor Hans Kristian Høidalen, for his supervision and guidance during this work. I would also like to thank my co-supervisors Adjunct Professor Bjørn Gustavsen and Professor Irina Oleinikova for their contributions. The ProDig project and the partners deserve thanks as well, in particular Anders Elvebakk at Statnett for his support in lending and setting up relays for me to test. I would also like to thank Svein Erling Norum and Bård Almås at the Department of Electric Energy at NTNU for their many hours spent facilitating my laboratory work. These contributions have all been much appreciated.

The work described in this thesis represents a major learning experience for me as a researcher, and it will hopefully also contribute with some new insights and knowledge for those who choose to read it.

Thomas Treider
Trondheim, October 2023

Abstract

A common grounding scheme for medium voltage distribution networks and high voltage sub-transmission networks is the resonance grounding scheme. Resonant grounded networks have few interruptions and a high quality of supply, but an important drawback is the particularly challenging conditions for protection systems and fault location methods during earth faults. Specialized methods are required to detect and locate earth faults, and although many fault location methods have been proposed and developed over several decades, reliable earth fault location remains a challenge. The fault location process can often become a manual process of trial and error, and it may take several hours to successfully locate faults. Earth faults are accompanied by overvoltages which are harmful to components in the network, and permanent faults can lead to insulation failure and additional faults. The classical distribution network is radial in structure, and the conventional fault location methods have also utilized this property. The high voltage sub-transmission network is however meshed, and increased meshing of the medium voltage networks as well alters the conditions for fault location methods. This can create both challenges and new opportunities.

This thesis studies earth fault location in non-radial networks. The research methods used include modelling and analysis of networks using electromagnetic transient software, theoretical analysis and development of novel fault location methods, and laboratory tests conducted using physical relays and network models.

First, the application of transient earth fault relays in non-radial networks is studied. Being the only real alternative in the meshed, sub-transmission network, these relays have been used extensively over many

years. However, transient earth fault relays have gained a reputation for being unreliable among several network operators, and operators are often reluctant to fully trust the relays' responses during faults. Understanding how well these relays really work in a non-radial network topology is therefore one important motivation behind the research presented in this thesis. Four different transient earth fault relays are analysed and tested in a laboratory setup with the goal of understanding their fault direction indication in non-radial networks. The results show that the lack of a clear forward/reverse direction combined with their inability to gauge fault distance can lead to inconclusive and contradictory responses in non-radial networks. Furthermore, as relays in different locations can have different operating conditions, it is concluded that each relay in the network should be analysed and set individually, contrary to what several relay manuals indicate. Changes made to the network topology in normal operation can also change the conditions for the relays in the network, so careful planning and analysis in advance is required to ensure selectivity and coverage for all faults. A lack of such planning is identified as the most likely cause of the problems experienced by network operators.

Second, the thesis presents novel fault location methods which contribute to more efficient fault location in non-radial networks. The research contributes to the development of methods aimed at precise distance to fault estimation in closed-ring networks, which are verified with promising results in simulations for both permanent and transient faults. The thesis also presents a method for detection, location and clearing of high impedance earth faults. This method consists of two independent earth fault indicators, one of which can be used to provide continuous fault indication throughout a sectionalizing process. As a result, the method can aid the network operator in narrowing down the estimate of the fault location. Laboratory tests demonstrate the feasibility of the proposed method, but the method's sensitivity is ultimately limited by the quality of the current measurements. The two earth fault indicators function up to 15–20 kΩ and 50 kΩ in the laboratory, respectively, but further study of real current sensors is required to predict the sensitivity in real networks.

Contents

Glossary

Abbreviations

ASC	Arc Suppression Coil
COMTRADE	Common format for transient data exchange [1]
DG	Distributed Generation
FPI	Fault Passage Indicator
HV	High Voltage
MV	Medium Voltage
OH	Overhead
RO	Research Objective
RQ	Research Question
TEFR	Transient Earth Fault Relay
TW	Travelling Wave

Symbols and notation

The notation is adjusted throughout the thesis to adapt to the corresponding research papers. As a result, the same parameters and variables may be notated differently in different sections of the thesis.

[1] Defined in IEEE Std C37.111

Section 2.2.1: Steady-state analysis

All phasors and impedances are fundamental frequency quantities.

C	Phase-ground capacitance of phase a. Subscript may specify feeder.
$C_{\Delta b}$, $C_{\Delta c}$	Deviation of capacitance to ground in phase b and c from the capacitance of phase a. Subscript may specify feeder.
C_{tot}	Sum of the capacitance to ground in phase a, b and c, i.e., $C_{tot} = 3C + C_{\Delta b} + C_{\Delta c}$. Subscript may specify feeder.
D	Asymmetry parameter: $D = h^2 Y_{\Delta b} + h Y_{\Delta c}$. Subscript may specify feeder.
$\vec{E}_a$, $\vec{E}_b$, $\vec{E}_c$	Phase-neutral voltage in phase a, b and c.
G	Phase-ground conductance of phase a. Subscript may specify feeder.
$G_{\Delta b}$, $G_{\Delta c}$	Deviation of conductance to ground in phase b and c from the conductance of phase a. Subscript may specify feeder.
G_{tot}	Sum of the conductance to ground in phase a, b and c, i.e., $G_{tot} = 3G + G_{\Delta b} + G_{\Delta c}$. Subscript may specify feeder.
h	Phase shift operator: $h = 1\angle 120°$.
$\vec{I}_a$, $\vec{I}_b$, $\vec{I}_c$	Phase current in phase a, b and c. Subscript may specify feeder.
I_{ASC}	Nominal ASC current, i.e., $I_{ASC} = \frac{V_{ph}}{\omega L_n}$.
$\vec{I}_n$	Current in the transformer neutral.
$\vec{I}_f$	Fault current.
$\vec{I}_0$	Zero-sequence current. Subscript may specify feeder.
k	Compensation degree.
L_n	ASC inductance.
L_{res}	ASC inductance corresponding to a network in resonance.
R_f	Fault resistance.
R_p	Resistance in parallel with the ASC inductance L_n.

$\vec{V_0}$	Zero-sequence voltage.
$\vec{V_n}$	Neutral-ground voltage.
V_{ph}	Nominal phase-ground voltage.
ω	Angular frequency: $\omega = 100\pi$ in a 50 Hz system.
Y	Phase-ground admittance of phase a, i.e., $Y = G + j\omega C$. Subscript may specify feeder.
$Y_{\Delta b}$, $Y_{\Delta c}$	Deviation of admittance in phase b and c from the admittance of phase a. Subscript may specify feeder.
Y_{tot}	Sum of the admittance to ground in phase a, b and c, i.e., $Y_{tot} = 3Y + Y_{\Delta b} + Y_{\Delta c}$. Subscript may specify feeder
Y_n	ASC admittance, i.e., $Y_n = \frac{1}{R_p} + \frac{1}{j\omega L_n}$.

Section 2.2.2: Transient analysis

C_g	Phase-ground capacitance, assumed identical in each phase. Subscript may specify feeder.
C_p	Phase-phase capacitance, assumed identical in each phase. Subscript may specify feeder.
f_{ch}	Charging transient frequency.
i_{ch}	Charging transient.
L_{ph}	Faulty phase inductance, measured between the fault and the main bus.
L_T	Transformer inductance.
R_f	Fault resistance.
R_{ph}	Faulty phase resistance, measured between the fault and the main bus.
R_T	Transformer resistance.

Section 4.2: Transient earth fault relays

C	Per phase capacitance, assumed identical in each phase. Subscript specifies feeder or group of feeders.
d	Per-unit distance to the fault, measured along the ring starting on feeder A.
f_{ch}	Charging transient frequency.

i_{ch}	Charging transient.
$3i_{0,k}$	Residual current on feeder k, measured at the transient frequency f_{ch}.
$3i_{0A}$	Residual current on ring-connected feeder A, measured at the transient frequency f_{ch}. Subscript may also specify feeder B or the remote-end bus RE.
I_0	Fundamental frequency zero-sequence current.
i_{hA}, i_{hB}	Part of i_{ch} returning in each of the two healthy phases of the two ring-connected feeders A and B, respectively.
i_{hR}	$i_{hR} = i_{hA} + i_{hB}$.
m	Factor describing the division of i_{hR} on the two ring-connected feeders, i.e., $m = \frac{i_{hA}}{i_{hR}}$.
M	Per-unit distance to the remote-end bus, measured along the ring starting on feeder A.
R	Factor describing the division of the charging transient in the faulty phase on two ring-connected feeders.
Relay A–D	Specific TEFR models defined in Paper II.
V_0	Fundamental frequency zero-sequence voltage.

Section 4.3: Precise fault location in closed-ring networks

All phasors and impedances are fundamental frequency quantities unless otherwise specified.

$\Delta\vec{I}$, $\Delta\vec{V}$	Change in current or voltage phasor, compared to a time t_0: $\Delta\vec{I}(t) = \vec{I}(t) - \vec{I}(t_0)$.
$\vec{I}_0$	Zero-sequence current. Subscript specifies feeder.
$\vec{I}_2$	Negative sequence current. Subscript specifies feeder.
$\tilde{I}_k$	Charging transient current. Subscript specifies feeder. This is not a fundamental frequency component.
$\vec{I}_F$	Fault current.
$\vec{I}_{F,A}$, $\vec{I}_{F,B}$	Fault current components on feeder A and B, respectively.
L_{AF}, L_{BF}	Inductance between the main bus and the fault, measured along feeder A and B, respectively.

L_{eq}	Equivalent inductance representing the parallel connection of L_{AF} and L_{BF}.
m_A, m_B	Factors describing the division of capacitive zero-sequence currents on two ring-connected feeders. See appendix B.
R_f	Fault resistance.
t_x	Time at which the fault distance estimate is extracted, measured from the time of fault inception.
$\vec{V}_n$	Neutral-ground voltage.
Y_0	Zero-sequence admittance.
$\bar{Y}$	Sum of admittance to ground in phase a, b and c.
Z_{AF}, Z_{BF}	Impedance between the main bus and the fault, measured along feeder A and B, respectively.
$Z_{0,AF}$, $Z_{0,BF}$	Zero-sequence impedance between the main bus and the fault, measured along feeder A and B, respectively.
$Z_{2,AF}$, $Z_{2,BF}$	Negative sequence impedance between the main bus and the fault, measured along feeder A and B, respectively.
$Z_{k,AF}$, $Z_{k,BF}$	Faulty phase self impedance between the main bus and the fault, measured along feeder A and B, respectively. Evaluated at the charging transient frequency.

Section 4.4: High impedance fault detection and location

All phasors and impedances are fundamental frequency quantities. Section 4.4 follows the notation used in section 2.2.1, with the following variables being unique to section 4.4:

$\Delta\vec{I}$, $\Delta\vec{V}$	Change in current or voltage phasor over an interval T, i.e., $\Delta\vec{I}(t) = \vec{I}(t) - \vec{I}(t-T)$.
ϵ_J	Magnitude threshold for triggering earth fault detection based on J_a, J_b or J_c.
$\hat{G}$	Identical to G_{tot} from section 2.2.1.
$\vec{I}_D$	Asymmetry current in the network: $\vec{I}_D = \vec{E}_a D$.
$\vec{I}_p$	Component of the neutral current $\vec{I}_n$.
$\Delta\vec{I}_p$	Change in current $\vec{I}_p$ over a time $T_{SW,p}$. Also referred to as the sectionalizing indicator.

J_a, J_b, J_c	Earth fault indicators based on phase currents.
K, K_p	Parameters for setting the sensitivity of the fault detection based on $\{J_a, J_b, J_c\}$ or $\Delta\vec{I}_p$, respectively.
$k_{\hat{G}}$	Parameter relating the shunt conductance to the shunt capacitance, so that $Y_{tot} = (k_{\hat{G}} + j)\omega C_{tot}$.
k_{R_p}	Parameter relating the parallel resistor R_p to the ASC inductance L_n, so that $R_p = k_{R_p}\omega L_n$.
L_p	Inductance representing the over-compensation of the ASC.
R_f^*	Fault resistance threshold for applying either a "low-R_f" or "high-R_f" approximation of the fault current.
t_f	Time of fault.
T_{SW}, $T_{SW,p}$	Length of the sliding window used to compute $\{\Delta\vec{I}_a, \Delta\vec{I}_b, \Delta\vec{I}_c\}$ and $\Delta\vec{I}_p$, respectively.
ϕ, ϕ_p	Parameters for setting the sensitivity of the fault detection based on $\{J_a, J_b, J_c\}$ or $\Delta\vec{I}_p$, respectively.

Chapter 1

Introduction

The resonance grounding scheme is widely used in electric power systems throughout Europe and China [1–4]. The fault current magnitude during single phase-to-ground faults, hereafter referred to as either earth faults or ground faults, is significantly reduced with this grounding scheme. The small fault current magnitude leads to the automatic extinction of many arcing faults, and permanent faults are less time-critical to disconnect from the network. The latter allows a controlled fault clearing process which affects as few customers as possible, and overall, the number of interruptions experienced by customers is reduced [5]. While this property is advantageous, the small fault current also introduces significant challenges for protection systems and fault location schemes.

With a fault current in the same order of magnitude as regular load currents, or even smaller, conventional protection systems such as distance protection and over-current protection are not sufficient. Furthermore, while earth faults have smaller fault currents than other fault types, they are associated with considerable permanent overvoltages which can be harmful to network components over time. Sustained overvoltages also have adverse effects on the system insulation and may result in cross-country faults, and a permanent earth fault represents danger to humans who may come in contact with live parts of the network. An earth fault can start out as a high impedance, low current fault which then evolves and becomes more critical, and earth faults are often identified as the source of wildfires [6, 7]. Therefore, network operators are required to detect

and disconnect earth faults from their networks within given time limits. Swedish and Norwegian regulations require that earth faults with fault resistances up to 5 kΩ and 3 kΩ must be detected within 5 s and 10 s, respectively [8, 9]. The Norwegian requirements do however allow earth faults to be present for 2 hours in higher network levels, which, given the aforementioned risks, reflects that earth faults are particularly challenging and time-consuming to locate. Moreover, earth faults are the most commonly occurring faults in Nordic distribution networks, constituting 50–80% of all faults [10]. For all of the above reasons, faster and more reliable earth fault detection and location is desirable. As a result, numerous research papers and PhD theses [5, 11–19] have been published over many decades, devising and testing new and creative solutions for fault location and protection of earth faults in resonant grounded networks. Commercially available relays have several protection functions dedicated to earth faults in resonant grounded networks, and new methods for fault location keep being proposed by researchers across the field.

Due to the fact that resonance grounding has been predominantly used in medium voltage (MV) distribution networks, the majority of the earth fault research has been oriented towards these networks. While distribution networks can be seemingly chaotic and complicated with their many feeders, lateral branches and distributed loads, they have traditionally been operated as radial networks [20–23]. As a result, most earth fault location methods found in the literature work on this assumption. This underlying assumption also means that very few, if any, of the fault location methods developed for radial networks can be applied in a non-radial network. To increase the reliability of the network, improve the quality of supply and facilitate the connection of distributed generation (DG) directly at the MV-level, some form of closed-ring operation of MV distribution networks could become more interesting for network operators [20, 21, 24–26]. Furthermore, with much of the meshed high voltage (HV) transmission and sub-transmission networks in Norway, Germany, Finland, Sweden and Denmark being resonant grounded [27], earth fault location in non-radial networks is a relevant and important issue to consider.

Most of the earth fault location research considers only the initial fault location task, which involves identifying the faulty feeder. In distribu-

tion networks, where the topology is generally more complicated and the number of circuit breakers and measurement points may be fewer than in the transmission and sub-transmission networks, the fault location process does not stop once the faulty feeder has been found. If the protection system finds the faulty feeder and trips it, the operator must re-connect sections of the network manually and monitor the presence of faults in the network. If the protection system is not able to locate and disconnect the fault, the network operator must manually locate the fault through sectionalizing. This involves isolating parts of the network systematically while monitoring the presence of the fault. For high impedance faults, the presence of the fault can be difficult to monitor reliably using the standard fault indicator V_0, and fault indicators based on a particular network topology fail to maintain a continuous fault indication once the network operators begins to re-configure the network. The lack of a continuous fault indication complicates and slows down the sectionalizing process.

For the meshed transmission and sub-transmission networks, the only viable option for directional earth fault indication available to network operators has been so-called transient earth fault relays (TEFRs)[1]. These relays have the benefit of being very fast as they rely on the fault-induced transients, and they should be able to provide directionality regardless of the network topology in question. While this makes them well suited for use in non-radial networks in theory, network operators have reported mixed experiences with them over the years [28]. While producing satisfactory results in some networks, the TEFRs have acquired an unfavorable reputation among other network operators. Though this issue has existed as an established truth among Norwegian network operators for many years, it is not well described or documented in the scientific literature. The network operators have few good options once these relays fail to give a clear indication as to which part of the network is faulty. The fault location process may then become both invasive and tedious, as reflected by the 2 hour time limit referenced earlier. Development of new methods and knowledge which can mitigate this and enable faster and more efficient fault location is therefore required.

[1] This category of relays is not strictly defined in the scientific literature, but it refers generally to earth fault relays relying on the fault-induced transients for their operation. These relays will be discussed in more detail throughout this thesis.

The above-mentioned challenges show the motivations behind this PhD thesis, which aims to develop faster and more accurate fault detection and location methods and schemes for application in non-radial resonant grounded networks.

1.1 Objectives

The overall purpose of this thesis is to contribute to the reduction of the time required to locate and clear earth faults in resonant grounded networks, with non-radial networks as a focal point. The term "non-radial" was introduced in the introduction and is used deliberately to encompass all networks which do not have a conventional radial structure, including both meshed networks at transmission and sub-transmission levels, as well as ring-operated distribution networks. Based on the aforementioned limitations of existing earth fault research, the following two research objectives (ROs) are set forth:

RO 1: Study the applicability of TEFRs in non-radial networks. It is of interest to investigate whether or not TEFRs are equally applicable in non-radial networks as in radial networks, and to understand how relays interpret fault direction in non-radial networks where forward and reverse directions are ambiguous.

RO 2: Develop new methods for more efficient fault location in non-radial networks. This research objective is focused towards two specific applications: 1) high impedance faults and 2) ring-operated distribution networks.

The first research objective is focused on the applicability of TEFRs in non-radial networks, and it is of special interest to be able to understand if and how their operation differs from that in radial networks. The main hypothesis at the beginning of this work is that the non-radial topology in itself creates problems for the relays as the idea of a forward or reverse fault no longer is clear. Two specific research questions (RQs) can be formulated in relation to RO 1: RQ 1) Do TEFRs have special limitations which could indicate that they are not applicable in non-radial networks,

and RQ 2) what determines their direction indication when they are part of a network loop?

The second research objective is more "open-ended" by design, and the research in this direction is necessarily more exploratory. However, two specific directions are identified: the first is the special challenge of very high impedance faults and their continuous indication during fault sectionalizing. The challenge of high impedance faults is well established in the literature, and the idea for a continuous fault indication came from input from network operators. Furthermore, the research topic in this thesis coincides with research efforts at CINELDI[2], in which a very specific closed-ring distribution network topology is being considered as means for developing better fault location methods. As a result of this cooperation, parts of this thesis are also focused specifically at developing and testing fault location methods for this closed-ring topology.

1.2 Scope and limitations

Distributed generation have been studied comprehensively in works such as [11] and will be outside the scope of this thesis. Its impact on some of the results is addressed briefly in the research papers, but it is not a key point of study. Furthermore, communications schemes are not considered in detail.

Although field tests are the ideal option for testing and validating any proposed fault location method, they do require the cooperation with and resources of a network operator, and such tests were unfortunately not possible to conduct as part of this PhD project. As a result, simulations are the main tool for analyses and validation throughout this thesis, although laboratory setups have been used both to study TEFRs and validate proposed fault location methods to the extent possible.

1.3 Thesis outline

When writing a thesis as a collection of research papers, the purpose of the thesis itself is to connect the individual research papers together and

[2]Centre for Intelligent Electricity Distribution. See website for information: https://www.sintef.no/projectweb/cineldi/

display them as a cohesive body of work. The six papers in this thesis are all related to earth faults in non-radial networks, but they cover different sub-topics and research objectives, and different research topics, theoretical concepts and contributions appear in several papers. As a result, there are probably several ways in which the papers could be grouped together, as well as different orders in which their contributions could have been presented. However, the thesis is organized according to the two distinct research objectives stated earlier, as the contributions related to each of them are almost independent. The five chapters of the thesis are organized as follows:

Chapter 1 - the current chapter - details the background and motivation for the thesis and sets the scope of the research. A summary of the main research contributions set forth by the thesis is also presented, along with an overview of relevant research papers written or co-written by the author.

Chapter 2 presents a literature review, detailing the state of the art for the relevant research areas. It also presents the important modelling approaches and equations used to describe and analyse earth faults, upon which the rest of the work in this thesis is built. This chapter is only used to describe the available scientific literature on the topic, and no new contributions are presented in this chapter.

Chapter 3 presents the main research methods and tools used throughout the thesis. This chapter presents the general approach used for modelling and simulating earth faults in resonant grounded networks, and two laboratory setups are also presented.

In chapter 4, the main results and contributions of the thesis are presented and summarized. It is in this chapter that all the author's contributions are presented, and the chapter is organized based on the research objectives. The papers are summarized, and some main results and ideas from the papers are discussed. Some additional results and analyses not included in the research papers are also presented in this chapter. Although the research and work presented is divided into several different areas, the reader can hopefully appreciate their common theme – earth fault location in non-radial resonant grounded networks.

In chapter 5, the overall contributions of the thesis as a whole are summarized, conclusions are provided, the limitations of the work are identified and discussed, and recommended future work is proposed.

Following chapter 5, the research papers which constitute the main work of this thesis are appended.

1.4 Scientific contributions

The scientific contributions made by the author are grouped according to the two main research objectives. The contributions are contained in six research papers I-VI, and the main contributions are as follows:

Analysis and testing of transient earth fault relays

- The research on TEFRs is contained in Papers I and II. The main focus is on conventional TEFRs based on the charging transient [29,30], and the behavior of the charging transient in a looped network is studied. Papers I and II show that due to the relays using the zero-sequence current to measure this transient, the polarity of the measured transient can be predicted to change for specific fault locations. The term crossover point is introduced to refer to these fault locations as the relays transition between seeing the fault in its forward and reverse direction. While Paper I presents a theoretical analysis of this, Paper II confirms this theory by performing tests of physical relays in a laboratory setup.

- In addition to the conventional TEFRs, two modern transient relay functions are also considered in Papers I and II. These functions represent the current state-of-the-art for TEFRs, and it is found that they behave very differently compared to the conventional relays. Most importantly they make use of several frequencies, including the fundamental frequency, which makes them more susceptible to other parameters, particularly the location of arc suppression coils (ASCs) in the network.

- Papers I and II illustrate that the behavior of the relays in more complex meshed networks can be difficult to predict, that changes made to the topology (e.g., connecting/disconnecting lines, moving ASCs) elsewhere in the network can affect the relays, and highlight that different TEFR models will behave differently overall. An important conclusion is that the relays should not be considered plug-and-play

with standard settings that are applicable everywhere in the network. The operating conditions for the relays can vary throughout the network, and changes made to the network topology in normal operation alter these conditions further. Therefore — to ensure sufficient sensitivity and selectivity — the placement and settings of the relays in the network should be coordinated, and each individual relay location should be analysed with respect to the possible configurations of the network.

New fault detection and location methods

- In Paper III, the author contributes with the development and testing of two methods for estimating the distance to earth faults in ring-operated networks. The two methods are based on the so-called "current ratio principle", in which the ratio of currents measured on each feeder in the ring is used to estimate the ratio of the impedances in the two paths to the fault location. It is highlighted at this point that this general current ratio principle is not invented by the author. Paper III shows that both the negative sequence current and zero-sequence can be used to implement this principle. The author contributes with the development of these methods, particularly with the derivation of the theoretical analysis and by adapting the established equations for zero-sequence currents in a radial network to a closed-ring topology. Please see page 145 for a detailed list of contributions made to Paper III.

- In Paper IV, the author studies the applicability of the two aforementioned methods for restriking and transient faults. Based on the analysis of the charging transient performed in Paper I, the author also proposes a third variant of the current ratio principle based on the charging transient. Together, Papers I and IV also demonstrate that the established charging transient model found in the literature, which is based on a radial network, can easily be adjusted to describe a closed-ring network.

- In Papers V and VI, the author proposes and validates two independent earth fault indicators for detection and location of high impedance faults. The first is based on combinations of phase cur-

rent increments, while the other is based on the increments of neutral point quantities. The latter indicator is suited for continuous fault indication during sectionalizing, provided that information about the network capacitances is available. The method is tested using a laboratory setup in Paper VI. The method is tested using a radial topology, and it is shown in chapter 4.4 of this thesis that the method can be implemented and made to function as a wide-area method in a meshed network as well. While the method is described in its entirety in Paper VI, paper V is included in the thesis for background and context.

1.5 List of publications

I: T. Treider, B. Gustavsen and H. K. Høidalen, "Analysis of transient earth fault relays in meshed resonant grounded networks," *16th International Conference on Developments in Power System Protection (DPSP 2022)*, Hybrid Conference, Newcastle, UK, 2022, pp. 350-355.

II: T. Treider and H. K. Høidalen, "Polarity crossover regions of transient earth fault relays in non-radial resonant grounded networks," *Electric Power Systems Research*, vol. 223, 2023, Art. no. 109598.

III: T. A. Zerihun, T. Treider, H. Taxt, L. B. Nordevall and T. S. Haugan, "Two novel current-based methods for locating earth faults in unearthed ring operating MV networks," *Electric Power Systems Research*, vol. 213, 2022, Art. no. 108774.

IV: T. Treider and H. K. Høidalen, "Estimating distance to transient and restriking earth faults in high-impedance grounded, ring-operated distribution networks using current ratios," *Electric Power Systems Research*, vol. 224, 2023, Art. no. 109765.

V: T. Treider, B. Gustavsen and H. K. Høidalen, "Steady-state, iterative method for locating and clearing permanent high impedance earth faults in compensated networks," *16th International Conference on Developments in Power System Protection (DPSP 2022)*, Hybrid Conference, Newcastle, UK, 2022, pp. 327-332.

VI: T. Treider and H. K. Høidalen, "Implementation and laboratory verification of method utilizing phase and neutral quantities for detection and location of low-current earth faults in resonant grounded networks," *IET Generation, Transmission & Distribution*, vol. 17, no. 24, pp. 5446-5457, 2023.

Chapter 2

Earth faults in the scientific literature

This chapter gives a summary of the most important scientific literature available on earth faults. This includes an extensive but not exhaustive overview of important fault protection and location methods that have been proposed, along with an overview of the common approaches for modelling and analysing earth faults.

When reviewing research on the topic of fault location in resonant grounded networks, terms such as "fault location", "faulty feeder selection", and "protection" are often used interchangeably. Although each can be defined to have specific meaning, they tend to be used differently by different authors, and the terms are often merged together in the literature. Resonant grounding have traditionally been synonymous with MV distribution networks, although some HV regional networks have used this grounding scheme as well. The typical distribution network is radial in structure, and due to distance protection not being applicable for earth faults, setting protection systems to detect and act on earth faults have been limited to and oriented towards determining the faulty feeder. Depending on how sparsely the system is equipped with measurements and protective gear, this faulty feeder determination may be enough for the protection systems to take action by disconnecting the entire feeder, or through sequential opening of breaker on the feeders. Considering that the requirements for earth fault protection is usually quite relaxed compared

to other protection systems, in the range of seconds as opposed to milliseconds for short circuits, the sharp distinction between protection and faulty feeder identification is often blurred. Furthermore, as obtaining the faulty feeder is often considered the end-goal for the protection systems, followed by a manual fault location process, the term "fault location" often implies simply obtaining the faulty feeder or section [4, 31, 32]. However, in the field of power system protection as a whole, "fault location" would typically imply a much more precise estimate of the faulted area, narrowed down to a few kilometers or meters as is the case for impedance based protection or travelling wave (TW)-based fault location.

Protection systems usually require some fault location capabilities, but faced with added requirements for safe and reliable operation within given time constraints. The distinction between earth fault protection systems and other fault location algorithms becomes increasingly vague as the fault conditions are moved outside the scope of regulations and safety requirements, such as during high impedance faults. For instance, Norwegian and Swedish network operators are required by law to have protection systems in place to detect and reliably disconnect earth faults up to 3 kΩ and 5 kΩ, respectively [8, 9], in their resonant grounded networks. Above this threshold, no requirements apply, and as such it becomes a matter of finding the faults as fast as possible, but now based mainly on the self-interest of the network operators to avoid unnecessary strain and damage to the system. A high impedance fault can be present in the system for hours before evolving into a more serious fault, either as damage to the tower construction due to heat or as a cross-country fault due to overvoltages and subsequent insulation failure. When standard earth fault protection fails to locate and isolate the fault, manual fault location takes on the task of the protection systems. With limited or no fault location indication available, this process must be based largely on systematic trial and error, which may be both slow and disruptive to end-users. In the worst case, the fault must evolve into a more serious fault before it can be found, in which case it may cause significant damage to the system in the process. New methods for locating high impedance faults can therefore be allowed to be slower than what would otherwise have been required for regular protection systems — locating a fault within a few seconds or a minute is a significant improvement on having to wait for the fault to evolve and

cause damage before being able to locate it.

The term "fault location" is used as a relatively loose term throughout this thesis; usually as the process intended to identify the faulty feeder or faulty section. When discussing precise distance-to-fault estimation, this will be emphasised whenever necessary to avoid any confusion. The term "protection" is taken to include systems designed to operate independently, that is without the need for a network operator, and which control circuit breakers in the system with the intention of clearing faults. While the development of protection algorithms and systems is outside the scope of this thesis, the term is relevant to include when reviewing relevant research literature on fault location.

2.1 Literature review

A common approach for sorting earth fault location methods and algorithms is to divide them into steady-state methods and transient-based methods. The former are based on measuring currents and voltages at the fundamental frequency, and as such the sample rate requirements are relatively low. The assumption of steady-state conditions does however limit the applicability to permanent faults, whereas faults with very short duration or evolving faults such as restriking faults are out of reach of such methods.

A steady-state analysis of the network is the basis for a lot of different methods found in the literature [2, 33–38]. In [2, 35–37, 39], variations of admittance-based earth fault protection are proposed. The basic idea is that the ratio of zero-sequence current and voltage on each feeder in the system, i.e., the apparent zero-sequence admittance, appears in distinct regions of the admittance-plane depending on whether the individual feeder is healthy or faulty [40]. This is similar to conventional distance protection, enabling the setting of distinct operating zones for the protection systems. Admittance-based protection does however not have any distance element, it is only able to distinguish between faulty and healthy states. If incremental values of current and voltages are used by subtracting their pre-fault values, the natural asymmetry of the system can largely be canceled out and sensitive operation can be achieved. Distributed compensation can however be an issue which requires less sensitive settings,

and networks with cables and feeders of very different sizes require special attention [41]. The admittance-based methods are also fundamentally dependent on a radial network to function properly, as several feeders can carry part of the fault current in the case of a non-radial network. References [33–35, 37, 38] utilize a steady-state analysis combined with incremental changes in currents and voltages to locate high impedance faults specifically. References [33, 34] propose a method in which the change in line and phase asymmetries are used to detect faults and determine the faulty feeder and phase. References [35, 38, 39] have similar approaches for detecting feeder admittances' deviations during high impedance faults, requiring some signal injection or other active measures to map the exact parameters of the system in its healthy state. The method presented in [37] monitors the change in each feeder's contribution to the zero-sequence voltage, essentially monitoring the admittance asymmetry.

In [31, 42] it is proposed to utilize the information from a large number of smart meters connected on the low voltage side of the load transformers in the network, and faults were located with a mean error of 1 km [42], proving the method's feasibility. The increased proliferation of smart meters makes such approaches a more viable option [43], although they are inherently dependent on accurate network data and robust and accurate measurements in the smart meters, which may not be available [44].

In addition to the previously mentioned methods, which are all passive methods based on the measurement of naturally occurring currents and voltages, several methods have been developed based on active injection of additional signals. These are also typically aimed at permanent faults. In [45], the authors propose using a mobile injection device to inject a signal with an off-nominal frequency, which could be traced through the network using dedicated sensors tuned to this particular frequency. In [46] it is proposed to use a thyristor-based injection device permanently installed in parallel with the ASC to inject a fast pulse in the network. In general, the common idea is to inject a superimposed signal which can be traced trough the network. Other methods have been proposed based on the active control of the ASC during fault, either by making the network temporarily under-compensated [47] or entirely isolated [48] so that the fault becomes easier to locate. A very common approach to ensure selectivity of conventional earth fault protection is the use of a

resistor connected in parallel with the ASC [16]. There are several schemes available as shown in [36, 40]: It can either be connected permanently, then with the purpose of limiting the healthy state neutral voltage; it can be connected in healthy state and disconnected shortly during faults in order to allow extinction of the fault; or it may be connected only during faults in order to provide a stronger wattmetric current for the earth fault relays to measure. The latter scheme is often encountered in the literature, although the dependency on a parallel resistor in this way is often considered undesirable, hence methods not requiring it citing this property as an advantage [41, 49–51]. In general, the downside of active methods is that they rely on external equipment which either add cost, complexity, or both, and which may malfunction or fail to operate correctly [50–53].

As mentioned previously, the steady-state methods are inherently limited to locating permanent and relatively stable faults. The second main category of methods, the transient-based methods, overcome this issue by utilizing the fault-induced transients to locate the faults. This way, the transient components of the currents and voltages are used as the useful part of the signals, making the fault location process more robust against transient and restriking faults, as well as becoming much faster than methods based on steady-state conditions. For instance, where steady-state methods usually require at least a few full cycles of the fundamental frequency to function, transient methods can operate within a few milliseconds or faster. The speed does in turn depend on the type of transients being used, and the transient-based methods can broadly be subdivided in two categories; low frequency transients – below a few kHz, including DC-components – and high frequency transients, which can be up to several MHz.

Many methods for earth fault location fall into the low frequency category. In reference [50], it is proposed to utilize the initial transient variation of the zero-sequence angle on each feeder to determine the direction to fault. By integrating the cosine of this angle over one period, misoperation due to angle oscillations and measurement accuracy can be avoided, and a fast decision can be made without the need for a parallel resistor. In [27], a similar principle is implemented and augmented using harmonics as well, where the contributions from all the frequencies present are used

for a better fault direction determination. While the cosine is used for the fundamental frequency angle, the authors argue that as the network appears as ungrounded at higher frequencies, the sine of the angle should be used for the harmonics. References [54] and [55] both present a transient directional relay principle based on a similar reasoning, and [55] argue that the apparent admittance of each feeder can be guaranteed to appear as either capacitive or inductive (depending on whether it is healthy or faulty) in one particular frequency range. The transient reactive power is therefore used as a criterion, predicting that the voltage should lead or lag the current by 90 degrees on a faulty and healthy feeder, respectively.

Whereas the methods proposed in [27, 50] work with phasors, the method in [17, 56] proposes implementing a transient principle with integration directly in the time domain. By computing and integrating the instantaneous zero-sequence power, the sign of the obtained zero-sequence energy is used to determine the direction to fault, and a long integration (up to 100 ms) ensures sensitivity in the case of high impedance faults with weak initial transients. The DC-component introduced by the ASC also contributes further to this energy calculation, a principle which is also proposed utilized by [57].

While [27, 56] represent relatively recent and sophisticated protection principles, and obtain high sensitivity due to the use of integration and multiple frequencies, many other methods utilize only one single transient frequency. The charging transient, a specific earth fault transient originating from the charging process taking place in the two healthy phases, is usually the dominant transient component seen during earth faults. It thus contains a lot of the useful information regarding fault direction, and the benefit of using this particular component is that it is both strong in magnitude, and that its frequency (which is usually in the range 0.1–4 kHz [58], where lower frequencies occur in larger networks) enables the use of a relatively low sampling frequency compared to the high frequency transients. Basic TEFRs have used this component for many years, and [29] and [30] both point to this particular transient when explaining their principle of operation. By comparing the polarity of the first transient peak observed in the zero-sequence current and voltage the direction to fault is determined. This is done directly in the time-domain, where forward and reverse faults are recognized by detecting transients with opposite or equal

polarity [59]. This principle has been prevalent for many years, but it is limited by fault resistance as the useful transients become too small for accurate measurement when the fault resistance increases. The detection principle is also vulnerable to missing the correct transient [41], hence the use of integration by many of the more recently proposed methods. In [23], the charging transient is proposed used (it is actually the dominant frequency component which is used, but this will typically be the charging transient). However, the phasors of this component are computed and the angle between the zero-sequence current and voltage is then used to determine directionality, similar to the use of general higher harmonics in [27]. The admittance-based methods have also been proposed improved by adding more of the harmonics observed during earth faults. In [60, 61], the admittance-based method from [36] is extended to include the apparent admittance both at the fundamental frequency and the harmonics. In this way, the method becomes applicable for transient and restriking faults as well as permanent faults. The method in [32] applies a combination of synchronized wide-area measurements and transient energy in a particular frequency band to select the faulty feeder and section. Similar to [55], the idea is to only consider a specific band of frequencies in which the zero-sequence impedance behaves in a particular way. In [62, 63] it is proposed to compute a transient impedance for each feeder. By considering both the sign and magnitude of the ratio of the average time-domain values of the zero-sequence voltage and current immediately after a fault occurs, the faulty feeder can be selected. This approach is yet another way of exploiting the polarity of transients on healthy and faulty feeders, combining the time-domain approach used by conventional TEFRs with the principles of the admittance-based methods. Several papers have also proposed using the estimated capacitance of each feeder to detect and locate faults. In [64], the same transient approach as in [62,63] is utilized to estimate the capacitance of the background network seen from each feeder. In [65, 66], the time-domain zero-sequence current and voltage are used to detect the deviation from a capacitive feeder.

As it can be seen from the above summary of TEFR principles, most of the available TEFRs are designed based on the assumption of a radial network. Several of the TEFRs are however supposed to be applicable in meshed networks as well (as can be verified by inspection of various relay

manuals), and the polarity-based TEFRs are well-established as directional earth fault protection in meshed networks. The use of resonant grounding at the sub-transmission and transmission level is found in both Norway, Germany, Sweden, Finland and Denmark [27], but research studying the application of TEFRs in such networks have not been found in the literature. A very limited number of cases are shown to verify their validity in non-radial networks, but it has however not been scrutinized and investigated in detail. With the mixed experiences with these relays mentioned in chapter 1 as a backdrop, the analysis of TEFRs in non-radial network is identified as an area of particular interest for this thesis.

Generally, the use of higher frequency fault transients is difficult and rarely done due to the high requirements for the sampling rate, the challenging signal processing required [11], and the very low magnitudes and fast decay time of the transients. One distinct category of methods based on high frequency transients is the TW-based methods [67–69], which use the arrival times of waves and their reflections to estimate the fault location very accurately. Reference [67] proposes utilizing the waves generated by the re-closing of circuit breakers. In [68], the travelling waves are generated by switching a thyristor in parallel with the ASC to produce a short burst of increased fault current, and the time between firing and reflection of the wave is used to determine the distance to fault. With a single measurement location the distance can be found with relatively high accuracy ($<5\%$ error), but it cannot distinguish between multiple possible fault locations. The improved version in [70] generates the travelling wave in a way which makes it applicable in any grounding scheme, and the accuracy reported is greater (error $\sim 0.1\%$). The benefit of the TW-methods is that very high accuracy can be achieved in any system grounding scheme, while the main drawback is that they require very high sampling rates, making them often a very expensive option [71]. Furthermore, the many loads and branches in distribution networks create a lot of reflection points which complicates the application of TW-methods [52]. The methods referenced above can estimate the distance to fault with reasonable accuracy, but determination of the faulty feeder and section must be accomplished with other methods.

Another category of fault location systems which appear to have some popularity is fault passage indicators (FPIs). Generally, these are de-

vices capable of determining whether a fault is in front of or behind the measurement point, based on for instance zero-sequence [49, 72] or negative sequence [73] quantities. With a number of FPIs spread out in the network, all reporting in to a centralized unit, the network operator can determine what the faulty section of the network is, thus improving on the accuracy of a simpler faulty feeder selection method. With a sufficiently fast communication system, an automated protection system can also be implemented based on FPIs. The accuracy of FPIs is however inherently limited by the number of devices used and the spacing between them, and to have fault location accuracy in the range of a few hundred meters, it is necessary to place FPIs every few hundred meters. For large rural overhead (OH)-networks this can be both costly to implement and maintain, and the communication requirements increase as the number of units increase. Nevertheless, as a tool for narrowing down the fault location process to a smaller section of the network, FPIs can be a good solution. Depending on the fault passage logic used by the FPIs, they will typically be subject to the same challenge as other directional methods when the topology is no longer radial. When the fault current can spread out and take several different paths in a meshed network, it is not obvious that FPIs will give the required coverage for all fault locations. Reference [74] proposes a system which locates faults in any system topology based on the input from FPIs, demonstrating that a system of FPIs can be effective. However, it appears as if the analysis assumes that each FPI always behaves correctly and outputs the correct direction indication, and it is not clear if the authors have considered that the directional indication from each FPI can become incorrect when the system topology changes.

Due to the lack of applicable distance protection for earth faults in resonant grounded networks, the faulty feeder or faulty section selection methods have been the traditional approach. However, several methods for precise distance estimation can be found in the literature. For instance, [75,76] propose methods for distance estimation which yielded promising results in field tests. The description of the methods' implementation is however not detailed, and it is not known to what extent these methods have been further developed. In [51], a few different impedance-based fault location methods are proposed, both for faulty feeder selection, as well as more precise location of faults. The most accurate fault location requires several

measurement points throughout the network and accurate zero-sequence network data, where the latter in particular is often difficult to obtain. In addition to these methods, which are conventional impedance-based distance estimation methods, the TW-based methods discussed earlier are capable of distance estimation. In [77], the author presented results from a method based on utilizing the charging transient for distance estimation. While faults could be located with approximately 1 km error, the method was limited to low-ohmic faults. Furthermore, as a single-ended method the distance estimate could result in several possible fault locations in the cases of branched feeders. Several transient-based methods were developed and evaluated in [14] with accuracy of a few hundred metres achieved, albeit for low-ohmic faults in radial networks. Additionally, the method proposed in [58, 78] is a recent attempt at utilizing the charging transient to implement a distance element. The benefit of this is that it avoids the impact of the load currents, and the method is relatively fast. However, this method appears to be in its early stages based on the reported results, and it is not known how robust this method will be in large, meshed networks where the charging transient frequency is close to the fundamental frequency and perhaps overlapping with regular harmonics present in the system. Generally, one important challenge with methods based on transient analysis is that they require a lot of parameters to establish an accurate model, and these parameters can be difficult to determine at the transient frequency. However, while being limited to low-ohmic faults, transient-based methods can clearly be efficient in many instances.

The previous review has cited references mostly aimed at or implicitly assuming a radial network topology. Some try to overcome this limitation and make the methods applicable in non-radial networks, for instance by adding a communication network scheme [23,79] or by utilizing a particular non-radial network topology to implement a distance element [26]. Most of the proposed methods are however aimed only at radial networks, and their application in non-radial networks is seldom discussed. This assumption of a radial system matters because the faulty feeder methods are often based on distinguishing between the faulty feeder and the background network, or between different feeders. This can be for instance by monitoring the asymmetry of each feeder (a fault appears as an asymmetry in the phase-ground admittance), monitoring the feeder capacitance (a healthy

feeder is almost behaving as a capacitance in the zero-sequence system, while a faulty is not), or by monitoring the direction of currents, power or energy, under the assumption that the faulty feeder feeds the rest of the network, or the other way around. Generally, these approaches cannot be assumed valid once feeders of the network become interconnected at both ends, or when they are parts of a large mesh. Faulty feeder methods basically reduce the fault location problem to a fault *direction* problem, and a forward or a reverse fault is ambiguous in a meshed system. For methods aiming at obtaining a precise distance to fault, the assumption also matters as they are derived from the assumed radial topology of the network.

Based on the limitation of directional methods in a meshed system, it is reasonable to assume that some form of line differential scheme could solve this problem. The authors of [63] proposed a transient differential scheme based on the zero-sequence currents measured on each feeder. The proposed transient differential scheme exploits the radial topology which enables all the measurements to be located in the same substation but limits the applicability to faulty feeder selection only. Overall, differential earth fault protection is rarely seen as a proposed solution in the literature, likely because it too is a relatively costly system to implement, with communication of accurately synchronized measurements over long distances. Similar to FPIs, it is also inherently limited to finding faults between the two measurement points, whereas more accurate fault location requires additional steps. Moreover, in a distribution system, the feeders have so many lateral branches and loads that a differential scheme for a faulty section selection scheme is not feasible. Distribution networks are usually also more sparsely equipped with measurements and breakers than transmission systems are, either due to them being less critical than the transmission systems, having fewer resources, or a combination of the two. The topology and criticality of transmission networks would suggest that differential protection is more likely to be employed there, although arguably still an expensive solution.

One subcategory of earth faults which is of special interest is what is commonly referred to as high impedance faults. Such faults can for instance be caused by trees leaning onto a power line, by a faulty insulator, or by a phase conductor coming into contact with an ungrounded wooden

tower [4, 80]. The term "high impedance" is also somewhat ambiguous as different authors attribute different meaning to it. For instance, 1 kΩ is considered high impedance in [42] while [6] cites regulations defining high impedances as being impedances twice the nominal phase voltage in volts, such as 25.4 kΩ in a 22 kV system and 76.2 kΩ in a 66 kV system. While the latter definition is very high, it is not uncommon for fault resistances to exceed 100 kΩ [4]. Earth faults with fault resistance up to a few kΩ's are generally within range of many existing methods and available earth fault relays, such as [6,56]. The challenge imposed by high impedance earth faults is that the high fault resistance effectively eliminates the high frequency earth fault transients, and the changes in the fundamental frequency quantities are very small. This means that even detecting the presence of high impedance faults in the network can be challenging, and highly specialized methods are required in order to detect and locate them. Moreover, when the fault resistance increases, the fault can become difficult to distinguish from the natural asymmetry of the network. A high impedance fault may even reduce the asymmetry of the network temporarily, depending on which phase it occurs in [4]. Therefore, it becomes important to account for the natural asymmetry of the network and other complicating factors such as measurement accuracy and noise. Neglecting this can lead to unrealistic performances in simulations, and experimental validation is therefore valuable. There are a few methods available in the literature reporting successful operation in the range of several tens of kΩ's, and who can refer to experimental validation of this. Reference [80] presents a probabilistic method which functioned up to 220 kΩ, [20] reports successful operation at 180 kΩ, the method in [4] can detect faults in the range 100–200 kΩ, and the methods in [39] up to 100 kΩ. A common approach utilized for very sensitive detection is the use of incremental changes in currents and voltages, thereby eliminating the impact of other parameters besides the fault itself. An accurate mapping of the network parameters in advance of the fault is also utilized to be able to better isolate the effect of the fault itself. Both of these approaches are effective, but they can be challenging to coordinate with changes in the network topology. Although some seemingly very sensitive detection methods exist, only the task of faulty feeder indication is considered. Narrowing down the fault location estimate is not considered, and none of the

reviewed research papers have presented an earth fault indicator capable of continued fault indication. Considering also that the conventional earth fault indication based on the zero-sequence voltage magnitude is not robust at higher fault resistances [4], this represents an interesting topic for further studies.

To summarize, TEFRs and their application in non-radial networks are identified as being of particular interest in this thesis. The combination of mixed reviews from network operators regarding their performance and the sparse literature available on the subject makes this interesting to pursue further. Improving the fault location process and developing new fault location methods for non-radial networks is also in scope, with particular emphasis on high impedance faults. Both of these research directions require an exploratory initial approach, starting with a theoretical analysis of earth faults. A more detailed description of the research methods is given in chapter 3.

2.2 Earth fault modelling

The most common approach for modelling and analysing earth faults utilized in the scientific literature is presented below, with emphasis on the steady-state fundamental frequency component and the charging transient component. The equations developed here can be found in many research papers and theses on earth faults, and they are introduced here as they are the starting point for further development in Papers I–VI, which are described in chapter 4.

2.2.1 Steady-state analysis

Healthy state

Fig. 2-1 shows the common network equivalent used for the purpose of steady-state fundamental frequency earth fault analysis, found for instance in [4, 34, 36]. The admittance to ground in each phase consists of conductance and capacitance, i.e., $Y = G + j\omega C$, while the neutral point admittance Y_n represents the ASC. The conductance is often omitted from the analysis as it is much smaller than the susceptance and can vary greatly with different insulators, pollution levels and weather [81]. It is however

important to include in the analysis of resonant grounded networks. Earth fault analyses are usually performed by evaluating the zero-sequence currents and voltage in the network, and phase-phase capacitances and the loads on the feeders are therefore neglected as they do not contribute to the zero-sequence currents [36]. The series impedance of the feeders is also neglected as it can be assumed that the voltage drop over the admittances is much greater than the voltage drop over the series impedances, and this greatly simplifies the analysis. With the network equivalent in Fig. 2-1, (2.1) can be derived to describe the phase currents on feeder A.

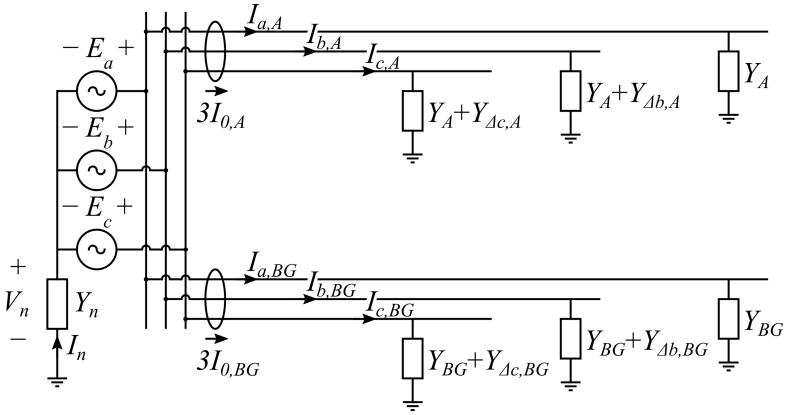

Fig. 2-1. Basic model for analysis of resonant grounded networks

$$\begin{aligned}\vec{I}_{a,A} &= (\vec{V}_n + \vec{E}_a)Y_A \\ \vec{I}_{b,A} &= (\vec{V}_n + h^2\vec{E}_a)(Y_A + Y_{\Delta b,A}) \\ \vec{I}_{c,A} &= (\vec{V}_n + h\vec{E}_a)(Y_A + Y_{\Delta c,A})\end{aligned} \tag{2.1}$$

In (2.1), $h = e^{j120^\circ}$. Let also the phase-ground admittance be defined as in (2.2).

$$\begin{aligned}Y_A &= G_A + j\omega C_A \\ Y_{\Delta b,A} &= G_{\Delta b,A} + j\omega C_{\Delta b,A} \\ Y_{\Delta c,A} &= G_{\Delta c,A} + j\omega C_{\Delta c,A}\end{aligned} \tag{2.2}$$

Equation (2.1) and (2.2) also apply to the feeder representing the background network, simply substituting the subscript "A" with "BG".

Next, two more parameters are introduced to enable more compact equations. Let $Y_{tot,A}$ denote the total phase-ground admittance on feeder A, and let the parameter D_A represent the asymmetry on feeder A, as given in (2.3).

$$\begin{aligned} Y_{tot,A} &= 3Y_A + Y_{\Delta b,A} + Y_{\Delta c,A} \\ D_A &= h^2 Y_{\Delta b,A} + h Y_{\Delta c,A} \end{aligned} \tag{2.3}$$

From (2.1) and (2.3), the zero-sequence currents on each feeder can be found by summing the three phase currents:

$$\begin{aligned} 3\vec{I}_{0,A} &= \vec{V}_n Y_{tot,A} + \vec{E}_a D_A \\ 3\vec{I}_{0,BG} &= \vec{V}_n Y_{tot,BG} + \vec{E}_a D_{BG} \end{aligned} \tag{2.4}$$

The total zero-sequence current on the feeders in the network must equal the current $\vec{I}_n$ returning in the neutral point:

$$\vec{I}_n = \vec{V}_n Y_{tot} + \vec{E}_a D \tag{2.5}$$

Here, $Y_{tot} = Y_{tot,A} + Y_{tot,BG}$ and $D = D_A + D_{BG}$ are introduced as system-wide parameters for compact notation. Depending on the application, the admittances are often assumed to be purely capacitive and identical in each phase. This simplifies the equations as $Y_{tot} \approx j\omega 3C$ and $D \approx 0$, but this generic notation is kept intentionally for now as both the network conductance and the admittance asymmetry are important parameters to consider when modelling the network in its healthy state.

The neutral voltage $\vec{V}_n$ can be shown to equal the zero-sequence voltage $\vec{V}_0$, so the two terms are used interchangeably. This voltage is the same everywhere in the network, and it is related to the neutral current by the neutral point admittance:

$$\vec{I}_n = -\vec{V}_n Y_n \tag{2.6}$$

The neutral point admittance consists of an inductance L_n, and a resistor R_p in parallel. This parallel resistor represents the active losses in

the inductor, although at may also include any external physical resistor added for protection purposes [36].

By combing (2.5) and (2.6), and by writing the admittances as sums of their real and imaginary parts, the neutral voltage in healthy state can be derived:

$$\vec{V}_n = -\vec{E}_a \left(\frac{D}{G_{tot} + \frac{1}{R_p} + j(\omega C_{tot} - \frac{1}{\omega L_n})} \right) \tag{2.7}$$

Equations (2.4) and (2.7) show that 1) the asymmetry of the network gives rise to the healthy state neutral voltage and thereby also zero-sequence currents on the feeders, and 2) the neutral inductance L_n can increase or decrease the voltage and currents. By expressing the neutral voltage magnitude as a function of the neutral point inductance, the resonance curve of the network can be derived. By convention, the rated current of the ASC is used as the variable, i.e., $I_{ASC} = \frac{V_{ph}}{\omega L_n}$, where V_{ph} is the rated phase voltage of the network. A resonance occurs when the inductive reactance of the ASC perfectly matches the capacitances of the network, i.e., when $L_n = L_{res} = \frac{1}{\omega^2 C_{tot}}$. The compensation degree of the system can be defined as $k = \frac{1}{\omega^2 C_{tot} L_n}$, with $k = 1$ corresponding to the resonance point. Compensation degrees $k < 1$ and $k > 1$ are referred to as under-compensation and over-compensation, respectively.

In Fig. 2-2, the magnitude of the neutral voltage in (2.7) is plotted in % of the nominal phase voltage V_{ph} for an arbitrary selected set of network parameters. It can be seen that the assumed value of the conductance in the system has a big impact on the magnitude of the resonance voltage level, and the contribution of R_p must be included to obtain reasonable values. In this example, the losses in the ASC have been modelled by using $R_p = 20\omega L_n$, as suggested in [17].

Faulty state

When a fault occurs in the network, for instance in phase a on feeder A, a fault resistance is added to the network equivalent in Fig. 2-3. All the equations previously derived are easily updated by the addition of either a fault current or a fault resistance:

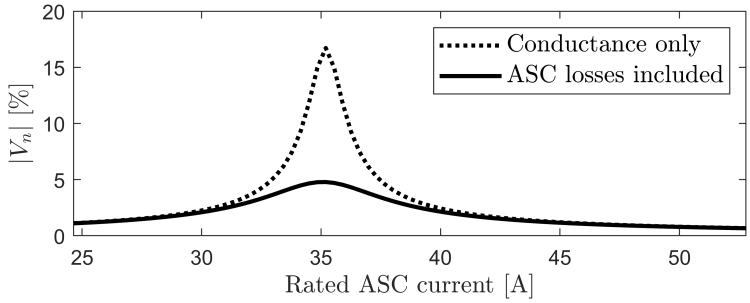

Fig. 2-2. Example of a resonance curve

$$\begin{aligned} 3\vec{I}_{0,A} &= \vec{V}_n Y_{tot,A} + \vec{E}_a D_A + \vec{I}_f \\ 3\vec{I}_{0,BG} &= \vec{V}_n Y_{tot,BG} + \vec{E}_a D \end{aligned} \tag{2.8}$$

$$\vec{I}_n = \vec{V}_n Y_{tot} + \vec{E}_a D + \vec{I}_f \tag{2.9}$$

$$\vec{V}_n = -\vec{E}_a \left(\frac{D + \frac{1}{R_f}}{G_{tot} + \frac{1}{R_p} + j(\omega C_{tot} - \frac{1}{\omega L_n}) + \frac{1}{R_f}} \right) \tag{2.10}$$

An expression for the fault current can be derived as well. The fault current for a fault in phase a on feeder A is simply

$$\vec{I}_f = \frac{\vec{V}_n + \vec{E}_a}{R_f} \tag{2.11}$$

Combining (2.10) and (2.11), the fault current can be written as a function of the phase-neutral voltage $\vec{E}_a$:

$$\vec{I}_f = \frac{\vec{E}_a}{R_f} \left(\frac{G_{tot} + \frac{1}{R_p} + j(\omega C_{tot} - \frac{1}{\omega L_n}) - D}{G_{tot} + \frac{1}{R_p} + j(\omega C_{tot} - \frac{1}{\omega L_n}) + \frac{1}{R_f}} \right) \tag{2.12}$$

This equation is general, but perhaps unnecessary detailed and cumbersome to apply in many situations. A common simplification is to neglect the admittance asymmetry, which implies that $D = 0$, and then express

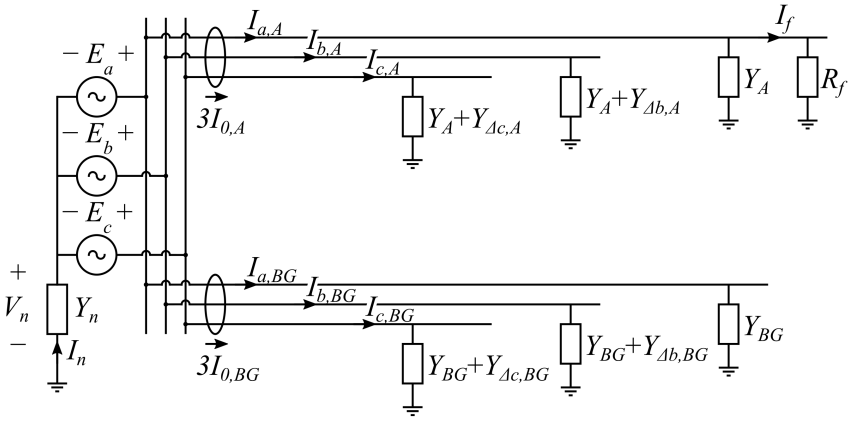

Fig. 2-3. Basic model for analysis of earth faults

$\vec{I}_f$ in terms of $\vec{V}_n$ instead. The fault current as function of the neutral voltage becomes:

$$\vec{I}_f = -\vec{V}_n \left(G_{tot} + \frac{1}{R_p} + j(\omega C_{tot} - \frac{1}{\omega L_n}) \right) \tag{2.13}$$

Combining (2.11) and (2.13), the simple during-fault equivalent in Fig. 2-4 can be derived.

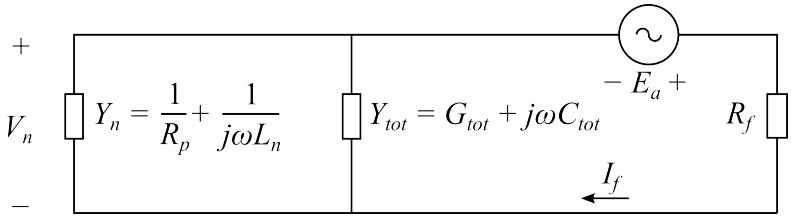

Fig. 2-4. Simple during-fault equivalent for earth faults [82]

2.2.2 Transient analysis

When an earth fault occurs in a network, a variety of transient components with different frequencies can be observed in the currents and voltages in the system. These transients stem from the transition from the

healthy state network to the faulty state network, during which the inductances, resistances and capacitances in the network oscillate. Although several different transient frequencies will be observed at different points in the network, the main earth fault transients are commonly considered to be the charging transient and the discharge transient. The discharge transient, discussed for instance in [17, 19], is typically described using a travelling wave-approach, and it is a single-phase phenomenon observed on the faulty feeder. This transient is usually very high in frequency and small in magnitude [14], making it ill-suited for use in fault location. It is not considered in any of the research papers in this thesis, so its detailed description is not included.

When the network is ungrounded or resonant grounded, the phase-to-ground voltage in the two healthy phases will rise during earth faults. This voltage rise represents a charging of the capacitances in these phases, and this charging process is associated with a particular transient usually referred to as the charging transient. This component has been described by many authors [17, 19, 78, 83], and in [83], this process is explained in its simplest form: A fault is assumed to take place close to the main bus bar in a radial system with a single power transformer, as illustrated in Fig. 2-5. The fault is bolted, leaving the capacitance to ground shorted in the faulty phase. A charging current then flows from the fault point to the neutral of the transformer where it is further divided into two equal parts, returning to ground via the capacitance of the two healthy phases. Note that no ASC is included in Fig. 2-5. As the frequency of the charging transient is higher than the fundamental frequency, the impedance of the ASC is significantly higher than that of the capacitances. As explained in [27], the inductance of the coil is tuned to the network capacitance at 50 Hz. At the n^{th} harmonic, the impedance of the ASC is n^2 higher than the capacitive reactance in the network. As a result, the ASC is assumed to only impact the steady-state components and thus omitted from the transient analysis [27, 84]. The charging transient analysis is therefore also valid in ungrounded networks. The leftmost circuit in Fig. 2-5 can be reduced to the equivalent LC-circuit shown to the right, and the natural frequency of this circuit can be used to estimate the frequency of the charging transient, given in (2.14).

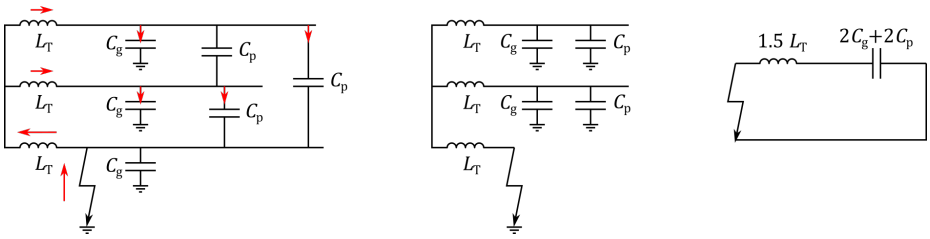

Fig. 2-5. The charging transient equivalent LC-circuit, derived from [83]

$$f_{ch} = \frac{1}{2\pi\sqrt{3L_T(C_g + C_p)}} \tag{2.14}$$

The analysis in [83] assumed that the fault occurred at the very beginning of one of the network feeders. If the fault occurs farther out on the feeder, the inductance of the faulty phase itself between the fault and the main bus can be included for a more accurate model. A more detailed RLC-circuit is presented in [19], where the impedance of the faulty phase is also included as shown in Fig. 2-6. Including the resistance of the circuit will give a better representation of the damping of the charging transient, but it is typically not required for estimating the resulting frequency. The natural frequency of an underdamped series RLC-circuit is given by (2.15).

$$f = \frac{1}{2\pi}\sqrt{\frac{1}{LC} - \left(\frac{R}{2L}\right)^2} \tag{2.15}$$

For small fault resistances the contribution from the last term is negligible and the frequency is therefore approximated with reasonable accuracy using the LC-circuit. Equation (2.14) is expanded by including the faulty phase inductance L_{ph} in Fig. 2-6 to produce (2.16).

$$f_{ch} = \frac{1}{2\pi\sqrt{(1.5L_T + L_{ph})(2C_g + 2C_p)}} \tag{2.16}$$

As mentioned previously, the charging transient is not the only transient component that occurs during earth faults. The discharge transient is a much faster transient associated with the rapid discharge of the faulty

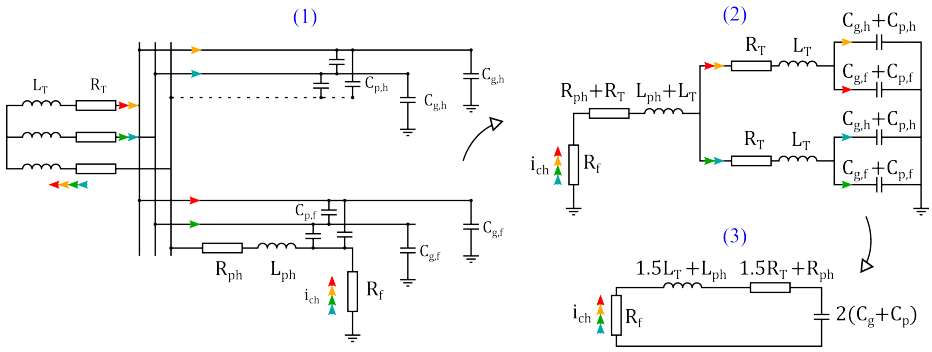

Fig. 2-6. A system represented by a faulty and a healthy feeder, and its equivalent charging current RLC-circuit [19]

phase itself, and in reference [12] it is proposed to analyse these two transients as coupled together and not as independent components. A fourth order model is provided in [12] to estimate the charging and discharge transient frequencies, the details of which are not repeated here. The frequencies are found as the solution to the characteristic equation in (2.17).

$$s^4 + s^2 \frac{L_1C_1 + L_2C_2 + L_1C_2}{L_1L_2C_1C_2} + \frac{1}{L_1L_2C_1C_2} = 0 \tag{2.17}$$

In (2.17), L_1, L_2, C_1 and C_2 are combinations of the line capacitances and line and transformer inductances. As the coefficients in front of s^3 and s are zero, the four solutions to (2.17) are two pairs of complex conjugates. The equation thus describes two distinct frequencies, the charging and the discharge transient. This equation also coincides with the first-order model in (2.14) when faults occur at the main bus ($L_2 = 0$ reduces the model order and results in the same coefficients). The approach used in [12] can be extended to produce a more accurate description of the network, but the frequency dependency of power system parameters will prohibit a higher order model from being accurate over a wide band of frequencies.

Chapter 3

Research methods, tools and laboratory setups

This chapter outlines the main research methods utilized throughout the six papers. Each individual paper contains the details regarding simulation models and input data, but the common approaches to modelling, simulation and analysis are presented in this chapter. The two laboratory setups used are also described in more detail than what could be fitted in the associated research papers.

The main research process (except for Paper VI), involves these basic steps:

- Create the required simulation model in ATPDraw [85]. ATPDraw is suited for transient studies and is used exclusively throughout this thesis.

- Define a parameter set for the simulations in ATPDraw, where the variable parameters in the simulations, such as the fault resistance, fault location, compensation degree and load level, can be studied in different combinations. Typically, a few hundred cases are defined and simulated in quick succession using ATPDraw's "multiple run" feature.

- The results from each simulation are outputted as separate files, stored either on COMTRADE format or as mat.-files.

- The simulation-generated currents and voltages are imported into Matlab [86] for further analysis. Implementation of phasor estimation and fault location algorithms is performed entirely in Matlab. Matlab is also used for preparation of COMTRADE-files before they are used to test relays in the laboratory.

3.1 Modelling of a resonant grounded network

ATPDraw is used exclusively for all the simulations. This subchapter describes the main approaches used when modelling a resonant grounded network, with specific model data found in each paper.

3.1.1 Modelling of lines and cables

The OH-lines and cables are modelled using either PI-equivalents based on 50 Hz data, or using frequency dependent models based on the line geometry.

PI-equivalents

Positive and zero-sequence parameters are used as input when modelling PI-equivalents, found in data sets [87] or standards [88]. The three-phase lumped RLC block in ATPDraw is used for the modelling of PI-equivalents, where 3x3-matrices for resistance, inductance and capacitance are required as input. These matrices are given in (3.1)–(3.3), and their elements are computed from the positive and zero-sequence parameters as described in (3.4) [89].

$$\mathbf{R} = \begin{bmatrix} R_{aa} & R_{ab} & R_{ab} \\ R_{ab} & R_{aa} & R_{ab} \\ R_{ab} & R_{ab} & R_{aa} \end{bmatrix} \tag{3.1}$$

$$\mathbf{X} = \begin{bmatrix} X_{aa} & X_{ab} & X_{ab} \\ X_{ab} & X_{aa} & X_{ab} \\ X_{ab} & X_{ab} & X_{aa} \end{bmatrix} \tag{3.2}$$

$$\mathbf{C} = \begin{bmatrix} C_{aa} & C_{ab} & C_{ab} \\ C_{ab} & C_{aa} & C_{ab} \\ C_{ab} & C_{ab} & C_{aa} \end{bmatrix} \tag{3.3}$$

$$\begin{aligned} R_{aa} &= (R_0 + 2R^+)/3 \\ R_{ab} &= (R_0 - R^+)/3 \\ X_{aa} &= (X_0 + 2X^+)/3 \\ X_{ab} &= (X_0 - X^+)/3 \\ C_{aa} &= (C_0 + 2C^+)/3 \\ C_{ab} &= (C_0 - C^+)/3 \end{aligned} \tag{3.4}$$

A conductance G is added to the PI-equivalent by placing $R = \frac{1}{0.5G}$ resistors between each phase and ground at both ends of the PI-segment. The value of G is not found in standard line data tables as it varies greatly with weather and pollution, as well as across different insulator types and voltage levels [81]. For OH-lines $G = 2\%$ of ωC_0 is used [90], while the conductance is assumed negligible for cables [91].

A key parameter in resonant grounded power systems is the capacitive asymmetry, which can be important to include in certain studies [41]. Asymmetry is required to produce healthy state zero-sequence currents and voltage in the model, as shown in (2.4) and (2.7). To obtain asymmetry in the model, the capacitance to ground in each phase is altered. According to [11], the asymmetry can be in the range 1–5% of $3C_0$. This can be implemented by adding shunt capacitors in individual phases as described in [11] or by manipulating the capacitance matrix in (3.3) directly. The exact value of this asymmetry is typically not available as it varies from network to network, but for modelling purposes it can be tuned to give the desired zero-sequence voltage and currents in healthy operation.

For implementation in a network model, the PI-equivalents are modelled to represent 1 km of line or cable. PI-segments are then connected in series to form longer lines, thus better representing the distributed nature of the line parameters.

Frequency dependent lines

To model frequency dependent lines and cables, different versions of the JMarti model in ATPDraw are used. With this model the line is modelled based on its geometry and material properties, available for standard line and cable geometries in for instance [87] and [88, 92], respectively. ATPDraw has a "Line Check" feature which is used to calculate the resulting positive and zero-sequence parameters of any line segment. The parameters of the line and cable models are then tuned to match the desired values for each type [87, 88, 92].

The frequency dependent OH-lines and cables are also modelled as 1 km segments and then connected in series to produce longer lines. The accuracy of the model fit and the resulting line parameters can be observed to vary with length, so using fixed length segments is done to ensure consistent line parameters everywhere in the network. It also enables distributing the line conductance, which is added as extra resistors to ground in the same way as for the PI-equivalents.

In the case of the geometry-based line models, if shunt admittance asymmetry is required, it can be included by considering an asymmetrical phase configuration and untransposed lines. This can however create problems when fitting the line model in the lower frequency range (below a few kHz). Alternatively, shunt capacitors can be added between phase and ground as described in [11].

3.1.2 Modelling and tuning of ASCs

The modelling of ASCs is done using the approach found in [17], where the ASC is represented by a constant inductor in parallel with a constant resistor. The use of a physical parallel resistor for protection purposes is not considered in this thesis. The resistor is instead meant to emulate the losses in the ASC and contributes to the damping of the network resonance curve, as was shown in section 2.2.1. The ASC is assumed to be connected to the system via the neutral point of one of the main power transformers in the system.

To find the correct setting of the ASC, ATPDraw's "multiple run" feature is used, which enables fast, sequential simulations with varying parameters. The nominal ASC current is varied over a wide range, and

the magnitude of the resulting healthy state neutral voltage is monitored to establish the resonance curve of the system. This enables a more accurate location of the resonance point of the system compared to one based on the nominal capacitances of the lines and cables. The latter option is especially challenging to use when the lines are modelled based on geometries. In the cases where a symmetrical line model is used, no resonance curve can be found with this approach. A small, single-phase capacitance (rated at 1 A, for instance) can then be added in the network to introduce the required asymmetry so that a resonance curve can be established. The resulting resonance point in the network can then be shifted 1 A when the capacitance is removed.

3.1.3 Modelling of earth faults

Earth faults are modelled as constant resistors connected between phase and ground, usually via a time controlled switch. In the case of the transient faults in Paper IV, a voltage dependent switch is used to emulate self-extinguishing and restriking faults.

3.1.4 Other components

The loads are modelled as constant impedance loads with a constant power factor and magnitude. Detailed modelling of loads, hereunder various load types and time varying loads, is not considered.

DG is not a focus of the work in this thesis, and modelling of DG is only performed for a few special cases in Papers III and IV. A simplified model consisting of a constant 50 Hz source and a reactance is implemented when needed, based on data from [11]. This is sufficient to study the qualitative impact of DG in Papers III and IV, but a more sophisticated model will be required for more accurate analyses of the influence of DG.

Reactive compensation devices and their potential impact are also not considered in any of the analyses.

3.2 Laboratory setups

3.2.1 Relay testing

The relay tests in Papers I and II are conducted using an Omicron relay tester and four physical relays. Fig. 3-1a and Fig. 3-1b display the setup, where several relays are tested at once. The voltage and current inputs are connected in parallel and series, respectively, ensuring that each relay sees exactly the same current and voltage. The voltage and current waveforms are outputted by the relay tester, and the binary output signals from the relays are recorded using the binary inputs on the relay tester.

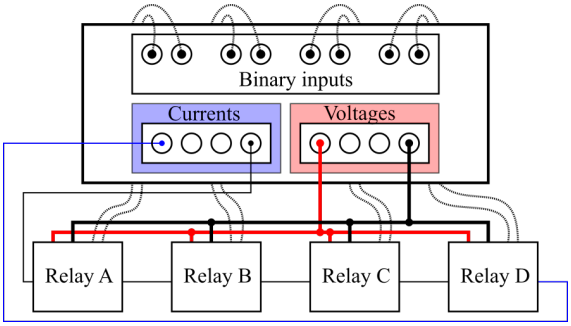

(a)

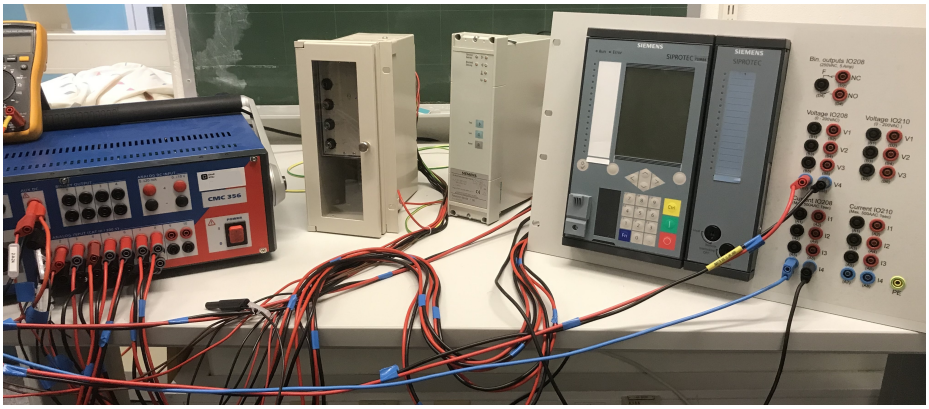

(b)

Fig. 3-1. (a) Setup for testing of multiple relays, and (b) a relay tester and three of the four relays tested in the lab

Splicing COMTRADE-files

The relay tester used is limited to playing back approximately 200k samples per test, or approximately 20 seconds when using the maximum available sample rate (10 kHz). Each fault record generated in ATPDraw is only a few hundred ms long, but multiple fault records are spliced together to mitigate the delays introduced by the software when changing from one record to the next. To enable all the relays to reset automatically between faults, a 3.1 second gap is left between the fault records (one of the relays needs 3 seconds to reset), resulting in five fault records being fitted into the 20 seconds of available playback. To avoid the relays accidentally tripping due to any discontinuities introduced by the splicing, a dummy signal representing healthy state conditions is inserted between the individual fault records. The magnitude of this signal is chosen based on the healthy pre-fault part of the next fault record in the sequence, and its phase angle is chosen so that no discontinuity occurs between the dummy signal and the next fault record. Fig. 3-2 illustrates such a COMTRADE-file produced by splicing five individual fault records.

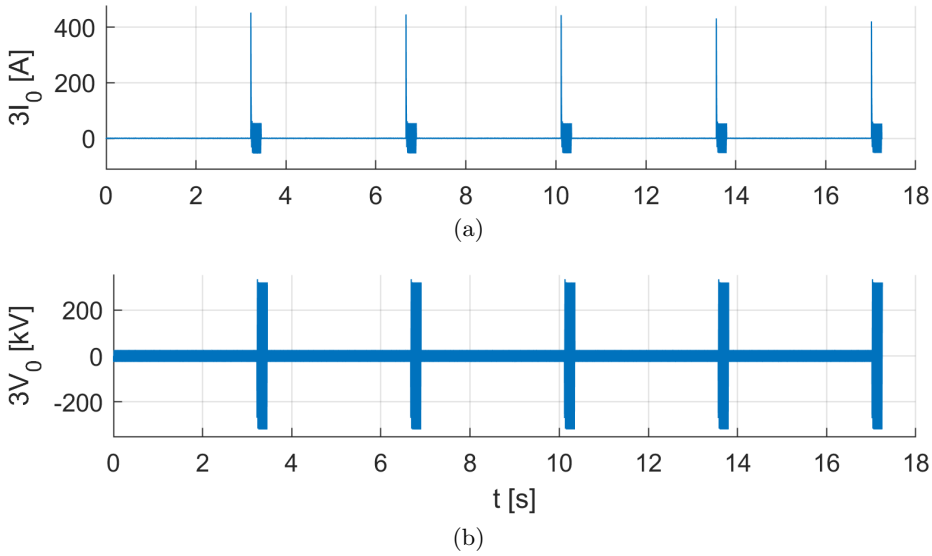

Fig. 3-2. Splicing of (a) $3I_0$ and (b) $3V_0$ from five separate fault records

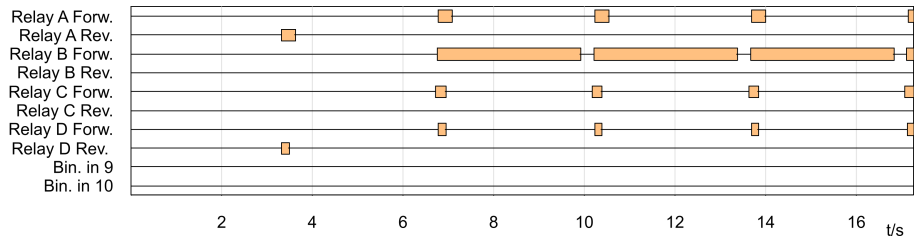

Fig. 3-3. Binary outputs from each of the four relays during five consecutive fault records

Logging the responses

Each of the relays tested are capable of signalling either "forward fault" or "reverse fault", and these binary outputs are logged using the binary input ports on the relay tester. An example of the binary responses of the relays during a set of five faults is shown in Fig. 3-3. All the relays are set up to signal a fault direction upon detection, so a lack of "forward" or "reverse" signal from a relay is interpreted as failure to detect the fault. The figure also demonstrates that relay B requires 3 seconds of healthy conditions to reset automatically, hence the 3.1 seconds of healthy signal inserted between the fault records.

The timestamped binary signals sent by the relays are also used to verify that the relays actually respond to the fault itself. Fig. 3-3 shows that the different relays do not signal a fault at exactly the same time - this is however consistent across all the tests and stems from the manufacturer-defined delay between fault detection and fault signalling within each relay.

3.2.2 High impedance earth fault testing

The high impedance earth fault tests in Paper VI are conducted in a scaled-down, physical distribution network model, implemented in the Smart Grid Lab [93]. This section describes the general laboratory setup, and provides some more details on the equipment and setup than what could be included in Paper VI.

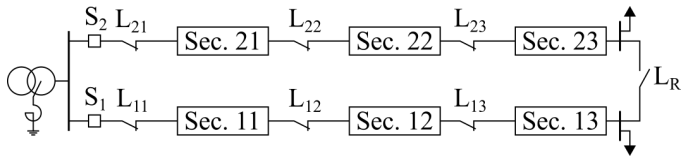

Fig. 3-4. Single line diagram depicting the two network feeders

Laboratory network layout

The laboratory network is a 400 V scaled-down equivalent of a generic distribution network. Fig. 3-4 shows the basic layout: Two feeders, each consisting of three segments, can be operated either in a radial or a ring configuration. Each segment is modelled using physical resistors, inductors and capacitors to create a physical PI-equivalent. The line parameters can be tuned to represent typical 22 kV OH-lines of various lengths and cross sections. Fig. 3-5 shows the physical switchboard used to set the line parameters for each segment, along with the various connection points DQAHAA-DQAHAD where loads or faults can be connected to the three phases in between each section. An identical set of connection points for the second feeder is located to the right, outside the frame of the picture.

Two loads are connected at the end of each feeder. One air-cooled resistor rated at maximum 5 A is used to load the healthy feeder, while a variable water-cooled resistive load is used to provide higher load currents on the faulty feeder. The loads in the network are varied between 3-9 A, which according to the laboratory documentation should represent approximately 50-150 A in a 22 kV network. The scaling of the laboratory model is discussed in more detail in Paper VI and in section 4.4.6.

For the high impedance fault tests in Paper VI, the network is operated as a resonant grounded network by placing a variable three-phase inductor in the transformer neutral. The value of this inductor can be changed in discrete steps by connecting the three phases in combinations of series and parallel. As the actual inductance of the various steps deviates somewhat from the nominal plate value, resonance tests are first conducted in order to identify the correct settings corresponding to the network resonance which is approximately 175 mA or 4.2 H.

The earth faults are modelled by using a manual switch to connect resistors up to 50 kΩ between phase and ground. Fig. 3-6 shows the ASC,

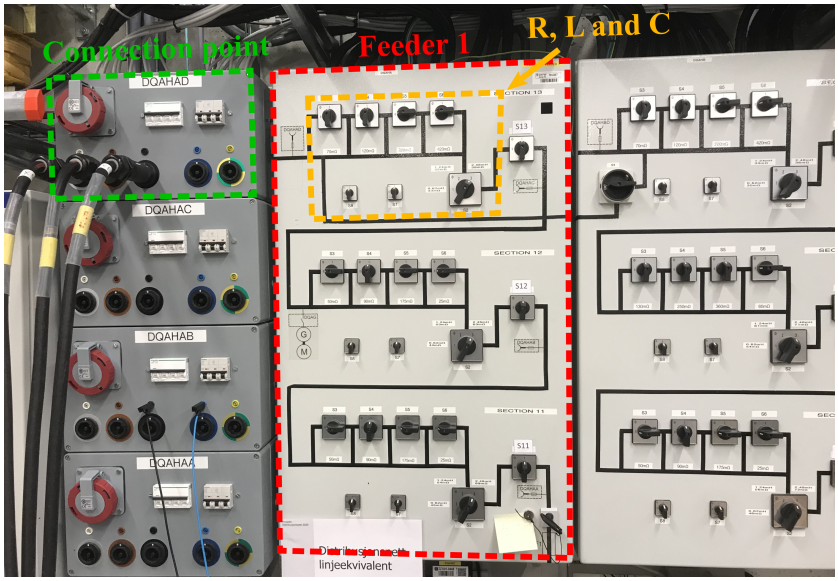

Fig. 3-5. Switchboard for the feeder equivalents

the fault resistances and the switch used to connect and disconnect the fault.

Recording equipment

An 11-channel recorder is used to log all the measurements, sampling at 4kHz. The recorder is set to include a 1 second pre-fault, triggering based on the measured fault current.

Current and voltage probes

Fig. 3-7 shows the locations of the current and voltage measurements that are used. In total, eight different currents are measured. The six phase currents are measured using Fluke i200s probes set to 0.1 V/A, as shown in Fig. 3-8, while the fault current and neutral current are measured using Gossen Metrawatt WZ 12-C probes set to 1 mV/mA. As these two currents are very small, 50-turn coils are used to better suit the available current rating of the probes. The laboratory tests also require two voltage

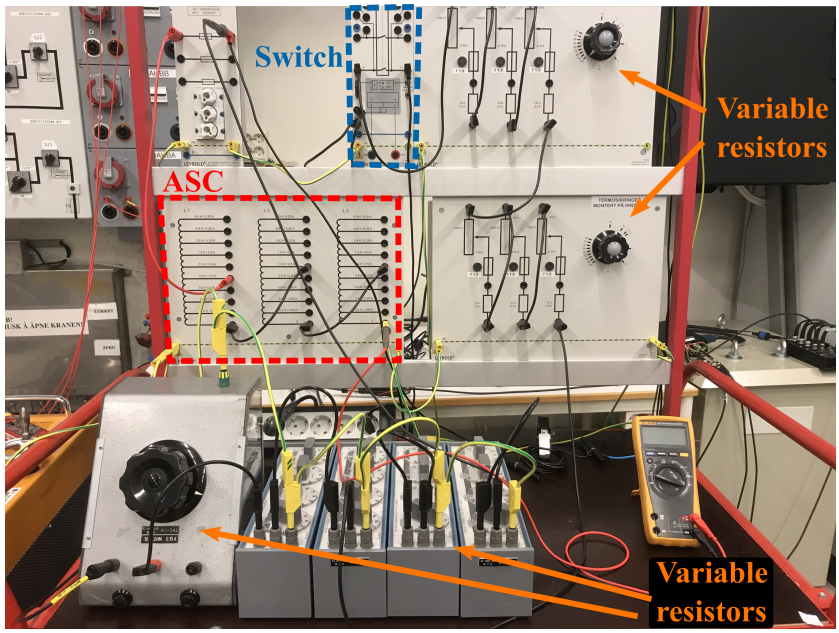

Fig. 3-6. Laboratory setup with ASC, switch and fault resistances

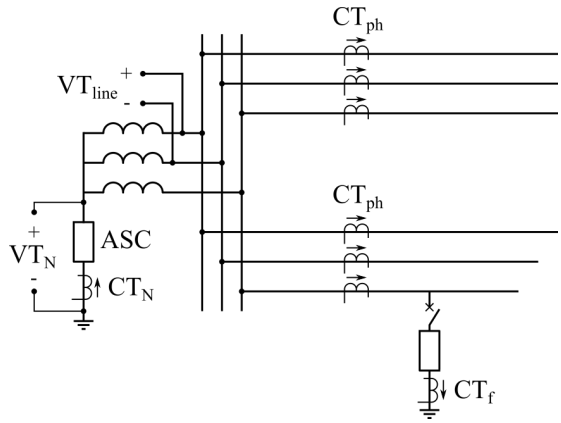

Fig. 3-7. Overview of voltage and current measurements in the laboratory setup

Fig. 3-8. Current probes used to to measure the six phase currents in the network

measurements. A Tektronix P5200 set to 1 V/500 V is used to measure the line voltage, while the neutral voltage is measured using a Tektronix P5200A set to 1 V/50 V.

Calibration

A voltage source is used along with variable resistors and an oscilloscope to calibrate the probes. The current probe calibration is illustrated in Fig. 3-9a: The voltage over the resistor is measured on channel 1 and scaled by the resistance to produce the current flowing in the circuit. The current measured by the probe is measured on a second channel, and amplitude and phase angle errors can be found by comparing the two waveforms. To account for the current dependency of this measurement error, the test is conducted with several different values of the primary side current. Matlab is then used to fit a curve to the data and produce phase and magnitude corrections as function of the primary current so that the measurements can be corrected. Fig. 3-9b shows the measurement errors for the six phase current probes. For the two current measurements utilizing the 50-turn coil, the coil is included in the circuit during calibration. A similar setup is used to calibrate the voltage probes, yielding voltage dependent correction factors for the magnitude and phase angle.

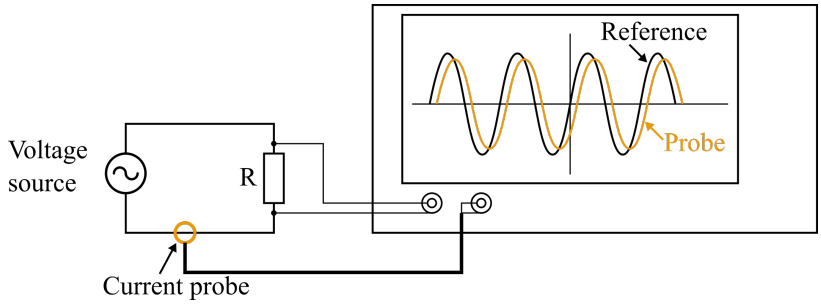

(a)

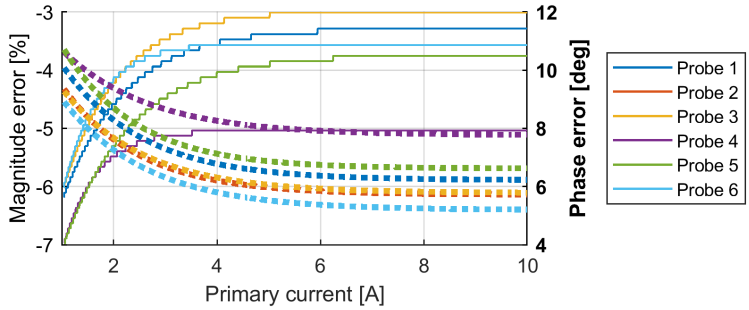

(b)

Fig. 3-9. (a) Setup for calibrating current probes, and (b) measurement errors (magnitude error on left axis (solid lines), angle error on right axis (dotted lines)) for the six phase current probes

Chapter 4

Research summary and contributions

This chapter summarizes the contributions of the work presented in the six papers in this thesis. The main work is contained in the six research papers, so the purpose of this chapter is to provide a summary of the work and connect the individual papers, as well as to provide some additional perspectives and lengthier discussions which could not be included in the papers.

4.1 Research objectives and overview of research papers

The two research objectives defined in chapter 1 are covered by the six papers in this thesis, as illustrated in Fig. 4-1. The first research objective is covered by Papers I and II, which present a theoretical analysis of TEFRs primarily oriented towards understanding the direction indication of the relays, and illustrate potential issues in a laboratory setup. The main focus of these two papers is the quantitative analysis of the charging transient and its appearance in the zero-sequence currents utilized by the TEFRs, and a qualitative comparison with the relays based on zero-sequence energy is made.

The second research objective is realized through Papers III-VI, in

which novel methods for earth fault location are presented and tested. Papers III and IV describe three of the methods, which are specifically aimed at distribution networks operated in closed-ring configuration, in which the ratio of currents measured at the two ring-connected feeders are used to provide a distance element similar to that which is used in conventional impedance-based distance protection. In Paper III the methods utilize fundamental frequency currents, and they are verified in simulations using permanent faults. In Paper IV, the two methods from Paper III are tested along with a novel transient method based on the same fault location principle. The focus of Paper IV is the performance of the three methods during transient and restriking faults. Finally, Papers V and VI present a novel method for detecting, locating and clearing high impedance earth faults. The majority of the contributions of these two papers are contained in Paper VI, where the ideas from Paper V are re-stated and developed further. Paper VI also presents a detailed fault detection logic along with results from the experimental verification performed on a physical laboratory setup.

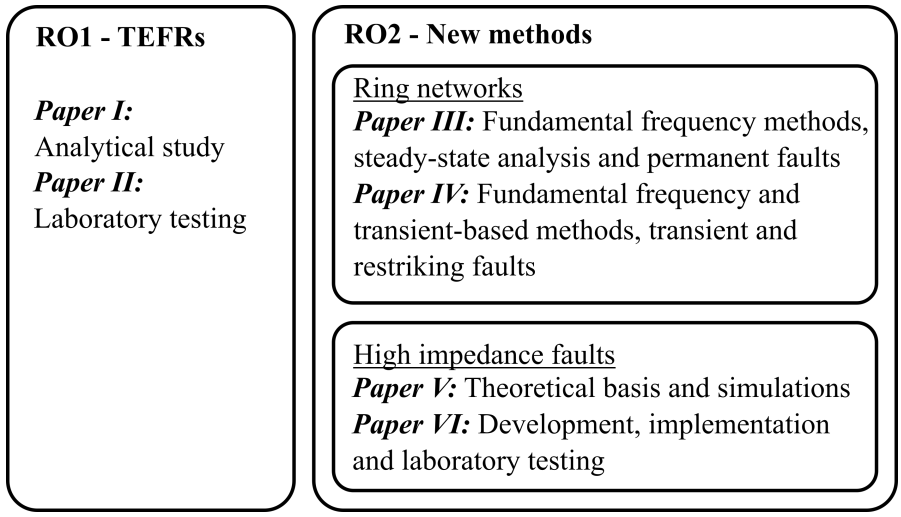

Fig. 4-1. Overview of papers and research objectives (ROs)

4.2 Contributions of Papers I and II: Transient earth fault relays

The motivation for studying TEFRs is primarily their reputation as unreliable among several Norwegian network operators. This unfavorable description of TEFRs is as mentioned earlier not founded in any scientific literature, and previous research done on the topic, although sparse, showed that other network operators had been satisfied with the functionality of the relays [28].

One possible cause of the network operators' mistrust in TEFRs is the way in which they are utilized. In the Norwegian resonant grounded transmission and regional sub-transmission networks, which are typically meshed and where earth faults need only be cleared within two hours [9], TEFRs are used as fault indicators. This means that the TEFRs are only used to signal faults, and the operator then conducts manual sectionalizing of the network based on evaluation of all the relay responses. Because the TEFRs do not trip any breakers automatically in such a scheme, their correct operation becomes less critical. However, being less critical, the motivation for network operators to test them as rigorously as other protection systems is lessened, which only increases the likelihood of misoperation due to erroneous settings and connections. Furthermore, TEFRs constitute a broad category of relays, and there may be significant differences in performance between legacy models and state-of-the-art TEFRs. A second explanation can therefore be that network operators associate the TEFR-term with their own poor experiences with a few particular legacy models, attributing that same poor performance to other and more reliable models. It is therefore plausible that the unfavorable view of TEFRs can be explained partly or entirely by mismanagement of the relays and unreliable performance of a few outdated relay models.

Nevertheless, it is of interest to study any possible technical explanations as well. Even if modern TEFRs would have improved sensitivity and reliability compared to previous models, it is still of interest to understand what governs their directional indication, and whether or not there are some inherent limitations to TEFRs' applicability in meshed networks. All TEFRs are in essence directional relays only, and directional relays without any distance element will by design face potential issues related

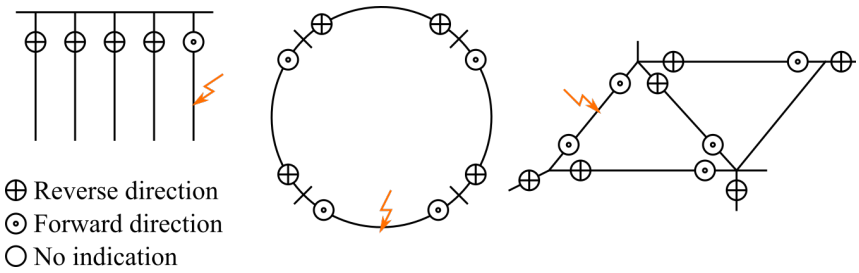

Fig. 4-2. Relay responses in radial and non-radial networks (re-created from illustrations in [30])

to distinguishing between forward and reverse faults when the network has loops and meshes. Consider the example in Fig. 4-2, which can be found in the manual of a commonly used TEFR [30]. In the radial network, the concept of a forward and a reverse fault is unambiguous, and the faulty feeder and section can be determined. In the case of the loop network and the meshed network, however, it is not as obvious how relays will respond. In the example in Fig. 4-2, the two relays on the faulted line are expected to see the fault as forward, but the correct responses of all the other relays in the network are not immediately apparent. The responses illustrated in the example appear somewhat intuitive, where it looks like the relays have been illustrated as seeing the fault as forward via the path with the shortest electrical or physical distance to the fault. This is not necessarily the case in practice, and if the number of relays in the network is reduced or the line lengths changed, it is not intuitive how the relays in the network will respond to faults.

4.2.1 Direction indication in non-radial networks

In Paper I, a theoretical analysis of TEFRs is conducted based on the assumed internal workings according to the literature. The *assumed* internal workings is emphasized as relay manuals generally give a superficial description of the underlying protection logic, and internal signal processing, filtering and proprietary settings are never disclosed. However, [29,30] give an idea of how the transient polarity principle has been implemented in two different relays, and [94] gives a description of the zero-sequence energy method used in that particular instance. In [95], the description

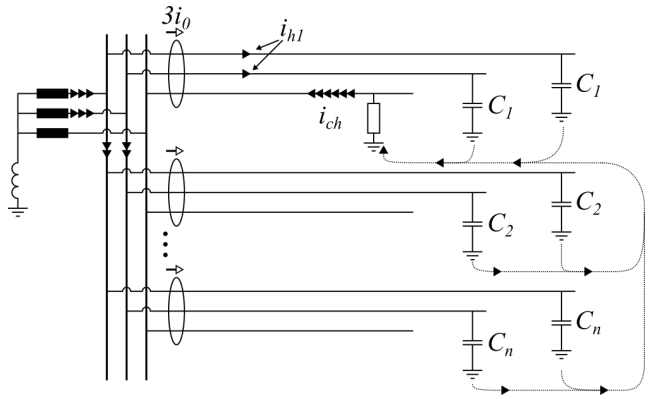

Fig. 4-3. Charging transient in a radial network

of the relay's algorithm is less detailed, although it is believed that [56] actually presents the basic algorithm used by that relay.

As the charging transient is the basis of the polarity principle used in conventional TEFRs, as well as being an important fault transient for the modern relays under consideration, the analysis in Papers I and II is focused on this. The charging transient model presented in section 2.2.2 is used as basis for describing its behavior in a radial and looped network. TEFRs measure the charging transient by measuring and filtering the residual current on the feeders, as illustrated in Fig. 4-3. Continuing with the assumption in [19, 83] that the charging transient component can be analysed independently of other frequencies, the circuit in Fig. 4-3 is used to derive the residual currents observed at each feeder in the network. Note that this analysis only pertains to the charging transient component, not the fundamental frequency.

From Fig. 4-3, the charging transient component of the residual current measured on the faulty feeder, in this case feeder 1, is given by (4.1).

$$3i_{0,1} = i_{ch}\left(\frac{C_1}{C_T} - 1\right) \tag{4.1}$$

On any of the healthy feeders, for instance feeder k, the measured residual current is given by (4.2).

$$3i_{0,k} = i_{ch}\left(\frac{C_k}{C_T}\right) \tag{4.2}$$

In (4.1) and (4.2), the capacitance C_k is the per phase capacitance for each of the healthy phases on feeder k, and $C_T = C_1 + C_2 + ... + C_n$ is the total per phase capacitance in each healthy phase of the n feeders in the network. The fraction C_k/C_T describes the portion of the charging transient returning on that particular feeder. Equation (4.1) shows that as the relative size of the faulty feeder compared to the background network increases – i.e., in terms of capacitance – the measured charging frequency component of the residual current is reduced. In the extreme case of a single feeder network, the charging frequency component of the residual current is zero. This will not be the case in a real network, and a residual current will therefore always be available for extracting the charging transient. On the healthy feeders the magnitude of the transient is much smaller, and in the case where certain feeders are very small compared to the rest of the network, the magnitude may be too small to measure reliably. However, as long as the faulty feeder can be identified, this is not a practical issue.

Fig. 4-4 shows the path through the network by which the charging transient travels in the case of an earth fault in a network with two ring-connected feeders. Based on this, the charging transient frequency component as it appears in the three measurement points $3i_{0A}$, $3i_{0B}$ and $3i_{0RE}$ is derived in Papers I and II and summarized in (4.3).

$$\begin{aligned} 3i_{0A} &= i_{ch}\left(m\frac{C_R}{C_T} - R\right) \\ 3i_{0B} &= i_{ch}\left((1-m)\frac{C_R}{C_T} - (1-R)\right) \\ 3i_{0RE} &= i_{ch}\left(\frac{C_R}{C_T}(m-M) + 1 - R\right) \end{aligned} \tag{4.3}$$

In (4.3), $C_R = C_A + C_B$ is the total per phase capacitance of the ring, $C_T = C_R + C_{BG}$ is the total per phase capacitance of the entire network, and M is the per unit distance around the ring to the remote bus measured along line A. The factor $m = \frac{i_{hA}}{i_{hA}+i_{hB}}$ describes how the charging transient divides itself among line A and B when returning to ground in the two healthy phases. It is not paid much attention to this in the papers as it can be known to be exactly 0.5 in the case of a homogeneous ring.

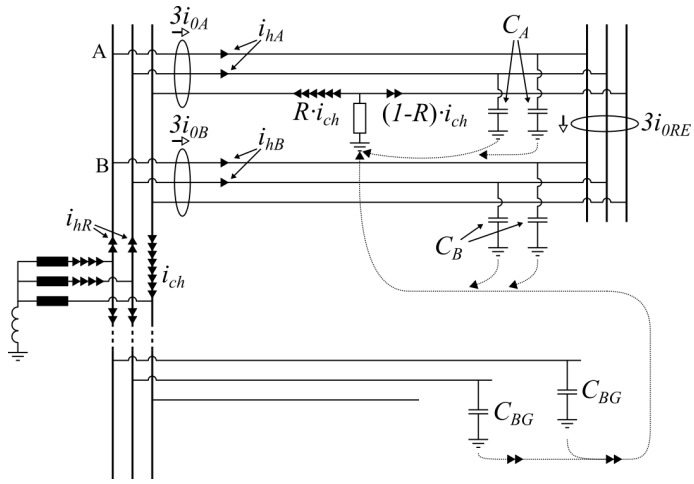

Fig. 4-4. Charging transient in a closed-ring network

The important property of m is that for a given network, it is fixed with respect to the fault location as a variable. With M and m known, the only unknown variable in (4.3) is R, which is the portion of i_{ch} which flows to the transformer via line A. When the ring is homogeneous, simple current division can be used to show that the per unit distance around the ring to fault d measured from terminal A is $d = 1 - R$.

The network in Fig. 4-5 is used extensively in the analyses in Papers I and II. This network has the same basic topology as in Fig. 4-4, and it is chosen deliberately as it enables a comparison between the simulation and laboratory results and the analytical formulae above. Papers I and II study the fault locations for which the currents in (4.3) become zero, using the

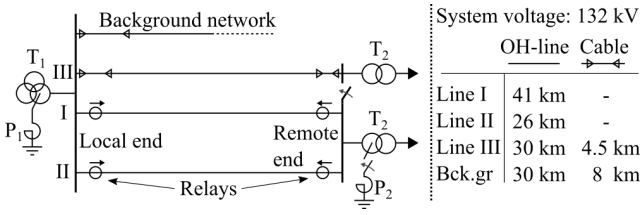

Fig. 4-5. Closed-ring operated network used in Papers I and II

network in Fig. 4-5. In these points the magnitude of the charging transient in the measured residual current is zero, and the polarity of the measured current changes as well. This can easily be observed from Fig. 4-4, for instance in the current measurement $3i_{0,A}$. The current $i_{h,A}$ always flows onto line A in the two healthy phases, and its magnitude relative to i_{ch} is independent of the fault location. In contrast, the current $R \cdot i_{ch}$ become smaller as the fault is moved closer to line B. Because the currents $i_{h,A}$ and $R \cdot i_{ch}$ are in phase with each other but passing through the current measurement $3i_{0,A}$ in opposite directions, the components cancel exactly at one particular fault location. As a result, no transient can be seen in $3i_{0,A}$ when the fault occurs in this point. This is illustrated in Fig. 4-6a, which can be found in Paper I. This figure confirms the analysis above, where the magnitude of the charging transient observed in the residual current measurements goes to zero when the fault occurs at approximately 0.08 p.u. and 0.92 p.u. (the p.u.-distance is measured around the ring starting on line A, so that both 0 p.u. and 1 p.u. correspond to the main bus). The charging transient magnitude in the faulty phase current is also included, where the charging transient is present with its correct magnitude. Fig. 4-6b displays time-domain plots of the zero-sequence current measured at terminal A, showing that the polarity changes as well at 0.92 p.u.. Given that the angle of the polarizing voltage V_0 changes only gradually as the fault moves around the ring, this means that the direction indication of the relays based on the polarity principle also changes in these points. Therefore, these points are labelled as crossover points.

By inspection of (4.3), the background network can be seen to impact the location of the crossover points on the ring. When the background network is much larger than the ring itself, i.e., $C_{BG} >> C_R$, the crossover points are located close to the main bus. As the background network shrinks, the crossover points move closer to the middle of the line. In the extreme case where $C_{BG} = 0$, the crossover points for $3i_{0A}$ and $3i_{0B}$ occur at the same point in the middle of the ring. A fault occurring in the middle of the ring would then not be visible for either relay at the main bus.

The significance of the equations in (4.3) is that they highlight an important difference between radial networks and closed-ring networks. As illustrated in Fig. 4-6a, the charging transient will not be measured with correct magnitude in the residual current. If the network is radially

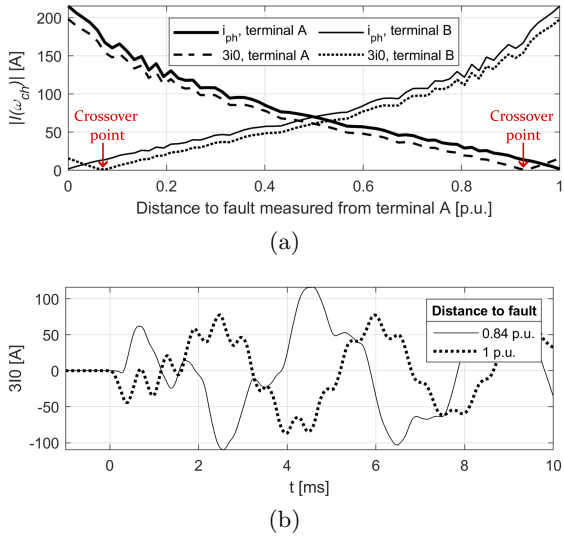

Fig. 4-6. From Paper I: (a) Magnitude of the charging transient component measured in the residual currents and faulty phase currents as function of fault location, and (b) time domain plots of $3i_{0,A}$ during faults located on either side of the crossover point at 0.92 p.u..

operated, a small part of the total charging transient also returns in the two healthy phases of the faulty feeder, and the contribution from the faulty feeder itself is therefore canceled out in the residual current. This is shown in (4.1). For most real applications the faulty feeder will be significantly smaller than the background network, i.e., $C_1 << C_T$ in (4.1), so the magnitude error is not significant. Thus, this does not become an issue with respect to either the sensitivity or the directionality of the protection. The polarity principle only needs a measurable magnitude to operate, along with a correct polarity relationship between the transient current and voltage, both of which can be expected to be present in the radial network. In the closed-ring network, however, it is seen from (4.3) and Fig. 4-6 that this effect of the charging transient component being cancelled out in the residual current is more extreme. This ultimately leads to the charging transient being invisible in the residual current for certain fault locations, and relays based on its measurement will fail to operate. The laboratory tests in paper II also show that the TEFRs based

on the polarity principle change their direction indication close to these theoretically predicted locations, although some difference between the two relays is observed. This is likely due to small differences in the internal signal processing and implementation of the polarity principle.

As opposed to the polarity principle relays, the modern relays based on the zero-sequence energy [94,95] utilize more of the signal than just the charging transient. For simplicity, if the zero-sequence energy relays are thought of as using two different frequencies, for instance the charging transient and the fundamental frequency, the relays can then have crossover points at different locations for each frequency. The charging transient behaves as illustrated previously, and due to its high frequency, it is not affected by ASCs. The fundamental frequency, however, is very much affected by the system grounding and the placement of the ASCs, and the crossover point for this frequency will in most cases be different than for the charging transient. Considering also that each frequency contained in the zero-sequence energy signal has different magnitude and damping determined by the fault location, fault resistance and inception angle, and that the weighting of each frequency used by the relay is unknown, the quantitative analysis becomes very challenging. A qualitative analysis can however be made, and Paper II illustrates how the two modern relays are the only ones affected by the ASC placement. Consider Fig. 4-7, taken from Paper II. Fig. 4-7a and Fig. 4-7b show that the crossover point for the charging transient is unaffected by the addition of a second ASC in the network (note the change in the location of the crossover point compared to Fig. 4-6 from Paper I, in which the network is modelled using PI-equivalents instead of a frequency-dependent model which results in slightly different network parameters). The 50 Hz-magnitude is however significantly changed as a result of the new ASC. Fig. 4-7c and Fig. 4-7d also show the sign of the fundamental frequency zero-sequence power in these two configurations. In the network with only one ASC (Fig. 4-7c), the fault direction indication according to the fundamental frequency is the same for all fault locations ($cos(\angle I_0 - \angle V_0)$ is always negative). With two ASCs, a change in direction occurs close to 60 km.

Despite being affected by the ASCs in the network, Paper II also illustrates that the two zero-sequence energy relays do not give the same direction indication in all cases. The two relays are actually more different

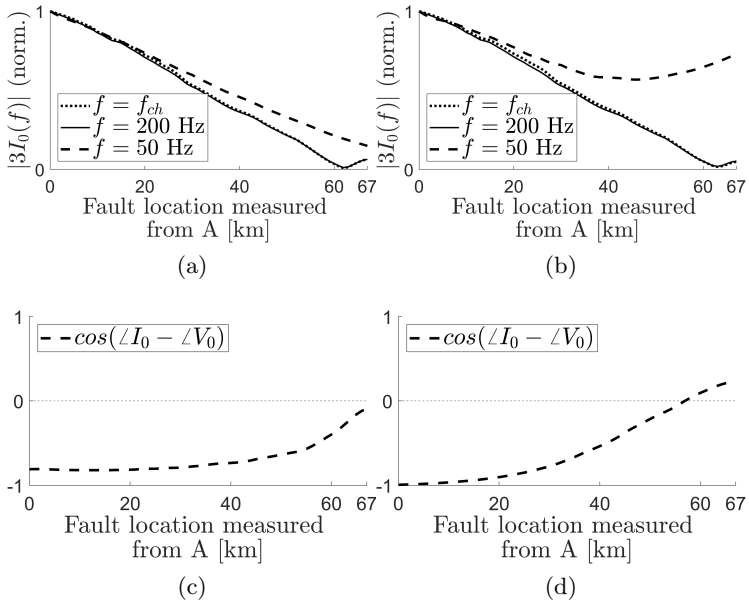

Fig. 4-7. 50 Hz zero-sequence power factor during the first 20 ms of the fault, measured at local end Fd. I, in the case of one (a) or two (b) ASCs in the network

in their responses than the two polarity principle relays, and the second ASC in the network impacts them very differently (adding the ASC shifts their crossover points in different directions). Although the frequency dependent model used in Paper II is not accurate at 50 Hz, it would still be expected that two relays based on the same operating principle would exhibit a similar response when being fed the same current and voltage. This just highlights that although both relays refer to zero-sequence energy as the basis for their operation, their operating principles are actually quite different. While relay D is believed to run the algorithm in [56] where the zero-sequence voltage and current are multiplied directly in the time-domain, relay C actually only uses the zero-sequence voltage as a polarizing quantity. The magnitude of the zero-sequence voltage is not actually used in the calculation done by relay C, and it is therefore not entirely accurate to refer to it as an energy-based relay in the same way as relay D. While relay D integrates the instantaneous zero-sequence power to obtain the

zero-sequence energy, relay C actually integrates the active and reactive zero-sequence currents at different frequencies and sums them together. Furthermore, relay C is based on phasors, while relay D works directly in the time-domain. This explains why relay C and D behave differently despite both operating principles being derived from the expected flow of zero-sequence energy. Relay C and D will also both make use of more than just two frequencies, and they have different internal processing of each frequency which results in different responses. Therefore – with unknowns regarding both the actual algorithms and internal settings – an analytical, quantitative analysis of crossover points becomes very uncertain and is hardly fruitful for anything beyond an approximate analysis of a single frequency.

4.2.2 Sensitivity issues

Another point raised by Papers I and II is that due to the lack of a distance element, TEFRs are perceived as binary devices - forward or reverse, on or off. With manuals advising specific system-wide settings [29, 30], the network operators can be given the impression that no individual analysis is required when setting a TEFR. In addition to the crossover point analysis, Paper I also highlights the insufficiency of universal settings for TEFRs in a network.

A second example network has been analysed during the relay testing, but the results are only briefly addressed in Paper I. The network, shown in Fig. 4-8a, is a generic meshed network more representative of a resonant grounded sub-transmission system. Fig. 4-8b shows an example of how the background network can influence the operating conditions of relays in the network: The current measured by the relay in A facing B is plotted for three fault locations on the protected line AB. Two different network configurations are also shown, where the difference between the two configurations is the connection or disconnection of line BE in the background network. It can be seen that for faults close to A, the current magnitude is comparable in both network configurations, while the measured transients change significantly when the fault is close to B.

Fig. 4-9 shows two examples of how the relays in the lab respond to this change in network configuration. Relay B and Relay D are given the measurements from all the six relay locations on the mesh ABC, and

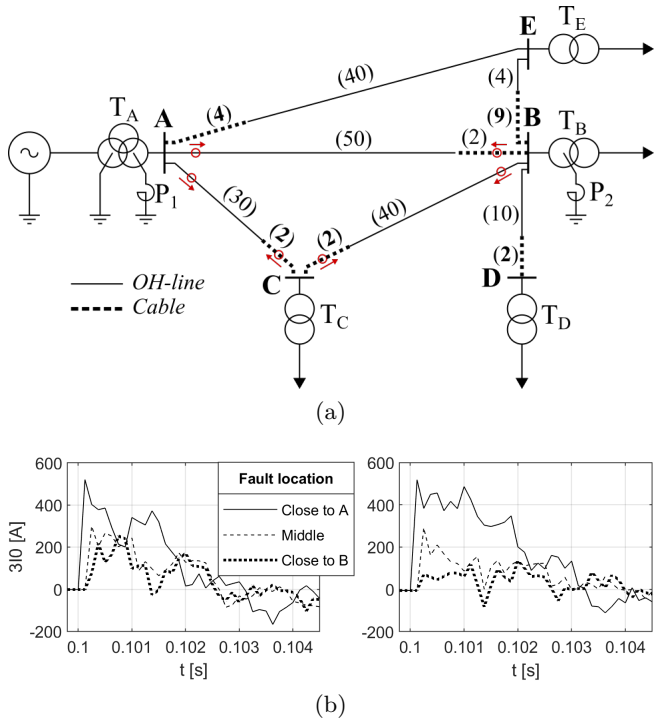

Fig. 4-8. (a) A meshed network and (b) resulting fault transients measured by relay in A facing B when line BE is disconnected (left) and connected (right).

their responses are recorded. This test is performed for both network configurations, i.e., with line BE either connected or disconnected. Fig. 4-9a shows that relay D is affected by the changed network configuration, but the relays on the protected line always see the fault between them. The responses of the relays on lines AC and BC can be observed to change with both the fault location and network configuration. Fig. 4-9b shows that Relay B fails to protect the line in either case: when line BE is connected the faults close to B are not seen by both relays, and when line BE is disconnected the faults close to A are not seen by both relays.

Without actually analysing the above cases in advance through simulations, it would likely be difficult to predict these issues. Relays could be set to have sufficient sensitivity and coverage on the protected line in one

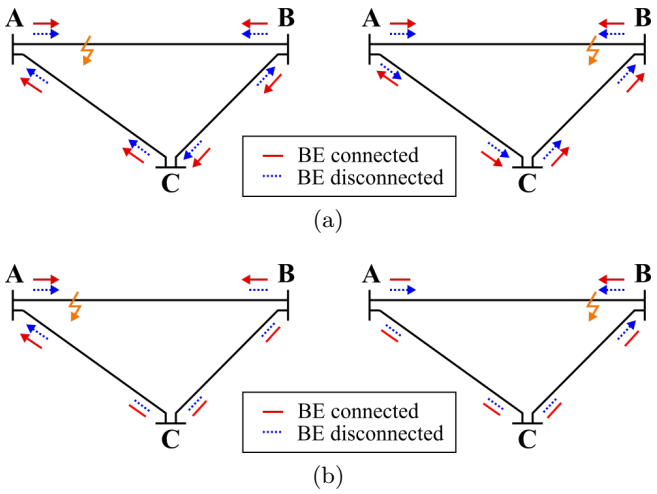

Fig. 4-9. Relay responses in the network in Fig. 4-8a when equipped with either (a) Relay D or (b) Relay B. Line BE is either connected or disconnected from the network, and the fault occurs on line AB close to A (left) or close to B (right). Arrows show indicated fault direction, no arrowhead corresponds to lack of fault detection.

particular default network configuration, but the same settings may not be sufficient in another configuration. The surrounding network contributes with producing the fault transients, so all likely network configurations must be considered when setting the TEFR pickup level.

Reduced sensitivity may also occur at and around the crossover points themselves. By definition, the transients cannot be measured when the fault is at the crossover point, but the magnitude of the charging transient in the residual current measurements decrease gradually around the crossover point. In Paper II it is emphasized that unless the relays are set extremely sensitively, the crossover point will actually appear as a crossover region in reality. Fig. 4-10 illustrates this for one TEFR, now considering the network in Fig. 4-5, where a decreased sensitivity (i.e., a higher pickup threshold on the relay) increases the size of the region around the crossover point for which the relay fails to see the fault. There is also significant difference between the sensitivity of different relays: When using the laboratory tests to locate the crossover points for each relay in the network in Fig. 4-5, relay A sees all the faults with the settings rec-

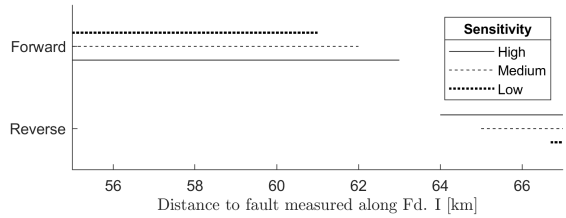

Fig. 4-10. From Paper II: Crossover region of relay A

ommended in the manual, whereas the sensitivity of relay B has to be increased several times compared to its recommended settings to be able to detect all faults.

The above examples illustrate that the network operator can face issues related to insufficient sensitivity, either due to crossover points or due to changing network configurations. Relying on recommended settings found in relay manuals may also lead to very different coverage depending on the type of relay used, something which operators would likely not be aware of without conducting detailed analyses of the relays. New network topologies might have adverse, or at least unexpected impacts on the relays in the network, which further illustrates the need for planning the protection system holistically and with different operating points and network configurations in mind to ensure sufficient coverage. However, increasing the sensitivity may not be a viable solution. For instance, other network events such as switching operations can cause relays to indicate a fault if set too sensitively [30]. Measurements from real CTs are also imperfect and noisy, so a lower allowable pickup value is even imposed by some relays [94], and setting the correct pickup level must be done individually in each network [95]. Therefore, although it may appear to be beneficial to use the lowest possible pickup level, too sensitive settings can also be problematic in non-radial networks, as will be shown next.

4.2.3 Selectivity issues

Using the network in Fig. 4-5, the crossover points of the four relays A-D are determined using the laboratory setup and reported in Paper II. Based on the locations of these crossover points, possible issues related to selectivity can be found. Although the network in Fig. 4-5 is designed

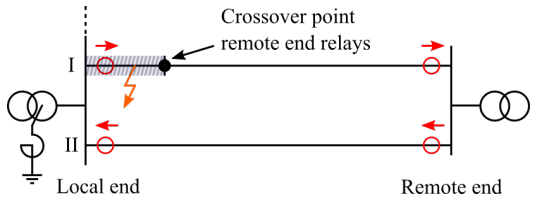

Fig. 4-11. From Paper II. Inconclusive relay responses.

primarily to investigate the location of the crossover points, possible issues observed in this network are still of interest to discuss.

The first example of this is shown in Fig. 4-11, in which it is imagined that the four relays protecting the ring-connected feeders are identical. Based on the observed crossover point for each of the four relays, it is found that faults in the shaded region (approximately the first 0.5-1.5 km of line I) cannot be reliably determined as a forward fault by the relays on line I or on line II. Instead, a circular indication as shown in the figure will occur, with all four relays indicating a fault in the clock-wise direction. Given the unusual topology, this example is perhaps more of a theoretical exercise than a representation of a realistic problem, since line I is almost twice as long as line II. Therefore, the situation could be resolved by adding an observation point somewhere on line I with two new relays.

The second example studied in Paper II shows that not only can inconclusive responses occur, but also contradicting responses. In the example in Fig. 4-12a, in which it is imagined that the relays at the local and remote end are of different types, it can happen that both pairs of relays see the fault between them, indicating a fault both on line I and line II. This can occur because with the second ASC connected at the remote bus transformer, the fundamental frequency zero-sequence currents measured by the two remote end relays no longer need to be identical. Therefore, it is possible for both the remote end relays to signal a fault forward, giving rise to the situation shown in the figure. As opposed to the previous example, the difference in line lengths is not the issue, and it cannot be resolved by splitting line I in two shorter segments. This will still not eliminate the problem with the relays on line II seeing the fault between them, and the fault can therefore still not be located correctly. However, it is proposed in Paper II to consider the magnitude of the current measurements to rem-

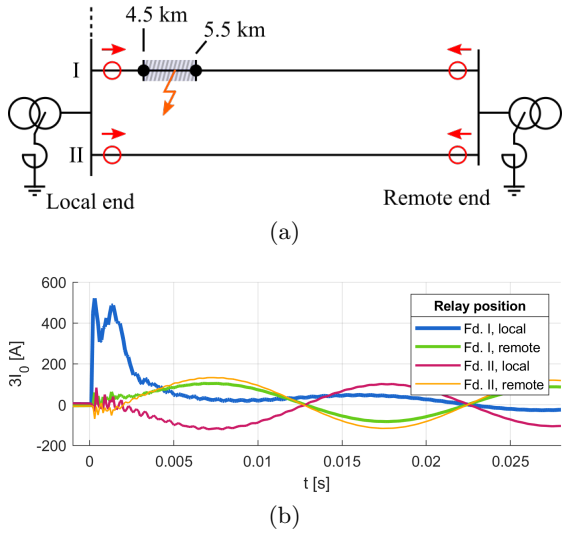

Fig. 4-12. From Paper II. The current waveforms help determine the fault on line I.

edy the situation. The magnitude of the residual currents is usually not suited for fault location as there are many parameters impacting this, but a comparison of the relative magnitudes at different points in the network could be useful. In the example in Fig. 4-12b, the currents can obviously be used to reject the responses of the relays on line II.

Both of these examples illustrate that increasing the sensitivity of the relays as much as possible, assuming it could be done without creating problems with false detection during switching operations or other network events, is not always possible. Even such a simple network as the one considered here illustrates how the responses of the relays may not be intuitive, and that analyses of such scenarios must be considered to avoid selectivity issues. If the example responses from the relay manual shown in Fig. 4-2 are perceived to be typical, i.e., with relays seeing faults as forward in the direction with the shortest physical or electrical distance to fault, then the response of the local end relay on line II in Fig. 4-12a would for example be very little intuitive as it sees a majority of faults on the ring as forward faults.

4.2.4 Summary and answer to research questions

At the beginning of this work, a key research objective was to understand more of the directionality of TEFRs in a non-radial network. Specifically, RQ 2 asked what determines the direction indication of a relay when a forward/reverse direction to a fault is ambiguous. As many TEFRs point to the charging transient as basis for their operation, Paper I and II have presented a detailed comparison of the charging transient's path in a radial network and a closed-ring network to illustrate their fundamental differences. Based on analysing the charging transient in the phase domain for a simple network with two of the feeders operated in a closed-ring configuration, fault locations have been identified in which the magnitude of the charging transient frequency component measured in the residual current become zero. The charging transient does not actually have zero magnitude in these locations, it is rather a consequence of using the residual current as a means for measuring it. This phase-domain approach to analysing the charging transient, as found for instance in [30], clearly demonstrates that the charging transient can be measured like this with negligible errors in a radial network, but not in a closed-ring network. Based on the charging transient model and the circuit in which it flows, it is also argued that the polarity of the measured residual current changes in these locations. These points have therefore been labeled as crossover points, and the basic TEFRs which base their operation on the charging transient will change their direction indication in these points as well.

Using a laboratory setup and four different TEFRs, the theoretical analysis is largely confirmed in Paper II, albeit with some reservations. First of all, the two relays that are believed to operate based on the charging transient alone switch their direction indication in the crossover points as expected, and the predicted issues related to sensitivity are also observed in the region around the crossover points. The two relays do however not respond in exactly the same way to the same fault, illustrating that the specific implementation chosen by each relay manufacturer also impacts the results. Furthermore, two modern relays with different operating principles are compared to the charging transient relays, and it is found that the analytical crossover point location do not match these relays. This is as expected based on what is known (and assumed) about their operating principles, which predicts that these two relays will be affected by other

factors such as the number and positions of ASCs in the system. The laboratory tests show that the two modern relays also have crossover points somewhere on the ring, and that sensitivity issues can occur in the region around these points. However, without clear knowledge of their internal workings, analytical expressions for these two relays cannot be derived. Although a qualitative analysis of these relays is attempted, further studies are required to be able to say something more accurate about their behavior. Even for the two most basic relays, the location of the crossover points will in practice be approximate, and the relays cannot be accurately modelled based solely on the charging transient analysis presented in these papers. A general understanding can be gained from such an analysis, but it is preferable to perform simulations and conduct tests with physical relays to determine their exact responses.

The lack of a clear forward/reverse direction in a non-radial network is not unique for TEFRs, given that any directional relay must change its direction indication between forward and reverse at some point as the fault is moved along the loop. One important reason for this becoming a potential issue for TEFRs is that they have no way of gauging the fault distance. Compared to distance protection, which necessarily also must deal with an ambiguous forward/reverse direction in meshed networks, it is not possible to set TEFRs to have a certain distance reach. Distance protection can have different zones set relatively accurately to ensure selective operation, whereas TEFRs cannot. In TEFRs, only the pickup threshold for the current or the transient energy can be used to indirectly alter the reach of the relays. However, the magnitude of the fault transient is determined by more parameters than the fault distance, such as for instance the fault resistance and the inception angle, so the exact distance covered by the relay cannot be linked to the pickup threshold of the relays. It is worth mentioning that one relay actually allows separate thresholds in the forward and reverse direction [94], and while this enables better selectivity, it is still limited and reliant on an analysis of the network in question to take advantage of this feature.

RQ 1 addressed a broader issue, asking whether or not TEFRs are equally applicable in radial and non-radial networks, or if they have some special properties or limitations which suggest that they are not applicable in non-radial networks. To answer this question, the results and discussions

from Papers I and II must be summarized.

Firstly, in the case of a closed-ring network the crossover points are likely to create issues, as illustrated by the various challenges seen in the papers. This occurs due the fact that one or more relays on the ring can have their crossover point on the line which they are supposed to protect, and this can lead to inconclusive or contradicting relay responses. In large, meshed networks, however, this does not have to be the case. The crossover points, which necessarily must exist, can be located somewhere in the background network, far away from the protected line in question. With normal sensitivity settings, they would then not become an issue. This does however require further study on other network topologies to determine, and the identified protection challenges created by the crossover points can at this point only be predicted in closed-ring networks. There are however other potential issues to consider for meshed networks. First, the modern zero-sequence energy relays [94, 95] are used throughout Papers I and II as alternatives to the conventional polarity principle relays [29, 30]. The papers demonstrate that the modern relays are susceptible to other factors such as ASC placement, and this becomes particularly relevant in transmission or sub-transmission networks, where the compensation is typically divided among several ASC distributed in the network. It is also demonstrated in the papers that having a mix of different TEFR models in the network can add to the complexity of the situation as different relays will be impacted differently by changes in various network parameters.

Secondly, an important factor impacting the sensitivity and selectivity of the relays is their settings. In the instances where the manuals actually recommend any specific pickup-level, these recommendations are given based on system-wide parameters [29, 30]. This would then imply that all the relays in the network should have the same settings. This is perhaps reasonable when the network in question is a single-bus radial network, in which the relays on the beginning of each feeder will have relatively similar operating conditions during faults. In a meshed network, however, the operating conditions may be very different in different parts of the network, meaning that a standard setting could be very sensitive in one location while being very little sensitive in another.

An important conclusion based on the work presented in these two

papers is that TEFRs should be planned and coordinated properly in advance, and sufficient coverage and selectivity cannot be expected with a plug-and-play approach. TEFRs can generally function well in non-radial networks, but a network operator cannot expect to achieve the desired protection as easily as in a radial network. Even in simple network topologies, the responses of the relays and their varying operating conditions are not always intuitive. The point of conducting an analysis of a network with respect to the potential issue of crossover points is not to be able to determine exactly where each relay has its crossover points, but rather make sure that it is not located on the protected line itself. This is the most critical case which must be avoided because it would lead to an erroneous fault indication for faults on the protected line itself, meaning that other measures such as communication between relays could not resolve the issue. In addition to this, an analysis of the network in advance is required to ensure that the relays do not have any unwanted blind spots. In the cases where the relays have a recommended setting this may not be sufficient to cover the line in question as expected, and as it has been shown it is not necessarily straightforward to increase the sensitivity of the relays without encountering other misoperation. Furthermore, many TEFRs only permit one set of settings, and these must be valid in any system configuration that may occur. Changing the topology of parts of the network may affect relays elsewhere in the system in unexpected ways, making it important to study this in advance. Relays at different locations in the network may also face very varying operating conditions, making standard global settings a poor choice.

Based on these observations, the answer to RQ 1 is that the TEFRs are applicable in non-radial networks, but they are at the same time less straightforward to apply there compared to radial networks as they require more planning and analysis in order to function properly. The main hypothesis presented in chapter 1 was that the non-radial topology itself creates problems for the relays as the idea of a forward or reverse fault is no longer clear. This is partly correct in that it is more complicated to make TEFRs work and provide selective and secure coverage. The placement and setting of each relay should be considered individually, thereby abandoning the idea of system-wide settings. Network operators must also consider that different network configurations can create very different op-

erating conditions for the relays, and understanding how each relay will be impacted by such changes is more complex to understand in meshed networks. At this point the non-radial networks likely differ significantly from radial networks, as radial distribution networks with a single main bus bar typically result in very similar operating conditions for all the relays. Using simulations to analyse and test the relays is suggested as the best way to uncover and fix issues with coverage and selectivity. Treating the relays as plug-and-play devices without considering these issues appears as the most likely single reason for why certain network operators will have mixed experiences with these relays.

4.2.5 Limitations and proposed future work

Limitations

The following limitations should be considered when interpreting the results and discussions presented in this subchapter:

- The results from Papers I and II are based on two simple topologies, and the identified issues may be less severe in other networks.
- The analysis has not considered anything besides the directionality of the relays. In practice, other factors such as measurement errors and noise, switching transients, and transient and restriking faults would likely affect the four relays very differently. The results in this thesis are valid for comparing directionality, sensitivity and selectivity during permanent faults, but not for saying that some of the relays perform better or worse than others.

Future work

With more time available, the following tasks would have been prioritized:

- Although papers I and II display potential issues, it can be argued that some of these issues will be less likely to occur in real networks with larger meshes and several buses and relay pairs distributed around one loop. Based on this, the most interesting continuation of this work would be to apply the ideas discussed regarding the need for holistic planning and coordination of the relays in an actual network. A benchmark network, for instance by CIGRE or IEEE, can

be used to investigate to what extent the identified issues are likely to become problems in reality, and which are the most pressing.

- Develop a methodology for gauging the relay responses, thus being able to make better decisions in the cases with contradicting or inconclusive relay responses. It is for instance shown that the magnitude of the currents in the network can provide useful information in these cases, and it should be investigated which signals can be used to aid in this process. Furthermore, the theoretical understanding of the modern TEFRs requires further study.

4.3 Contributions of Papers III and IV: Precise fault location in closed-ring networks

Papers III and IV present three novel fault location methods for use in closed-ring distribution networks, based on the ratio of different current components measured at the beginning of each feeder. Depending on which current components are used, the ratio of these currents corresponds to the ratio of specific impedances between the measurement location and the fault location. If the impedances of the ring-connected feeders are known in advance, the distance to fault can be estimated from the current ratio. This fundamental fault location principle has not been created by this author, and the same basic idea has been presented elsewhere in the scientific literature [20, 26]. The other authors of paper III formulated this idea and worked out preliminary versions the two methods which are proposed in that paper. The detailed contributions made by this author to Paper III are listed along with the paper on page 145 in appendix A.

The main contributions of papers III and IV are the development and testing of three novel methods applicable in ring-operated networks. Because the testing of each method is described extensively in the papers, and as each paper is self-contained with detailed results, this subchapter is limited to providing a summary and discussion of the overall results and applicability of the proposed methods.

4.3.1 Precise fault location based on current ratios

The two papers present three variations of the same fault location principle for use in a closed-ring network, which can be explained by the generic circuit in Fig. 4-13. The fault current is assumed to consist of two components, each flowing along feeder A and B, so the ratio of them corresponds to the ratio of the impedances along the two paths:

$$|\frac{\vec{I}_{F,A}}{\vec{I}_{F,B}}| = |\frac{Z_{BF}}{Z_{AF}}| \tag{4.4}$$

If the two fault current components $\vec{I}_{F,A}$ and $\vec{I}_{F,B}$ can be measured at the beginning of each feeder, the impedance ratio can be estimated. If the impedances of the two feeders are known, then this impedance ratio can be translated to a fault location on the ring. Fig. 4-14 illustrates this process. This general principle can be implemented in a few different ways, and it is hereafter referred to as the current ratio principle.

In order to apply the current ratio principle, it is necessary to find ways to measure or estimate the two parts of the fault current – $\vec{I}_{F,A}$ and $\vec{I}_{F,B}$ – so that they can be used to estimate the distance to fault. In the case of a short circuit fault, the fault current is so large that the measured currents consist mainly of the fault current. Whether the phase currents or one of the sequence components are used, reasonable accuracy can be achieved with a very simple logic. However, during earth faults the fault current is generally much smaller than for short circuit faults, and other disturbing elements in the current measurements corrupt the results. Therefore, papers III and IV present three versions of this principle tailored

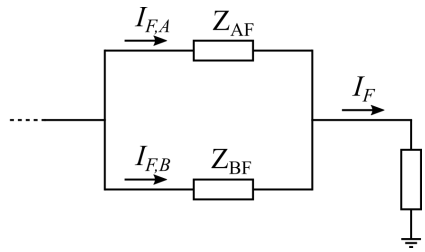

Fig. 4-13. Basic circuit for fault location in closed-ring network based on current ratios

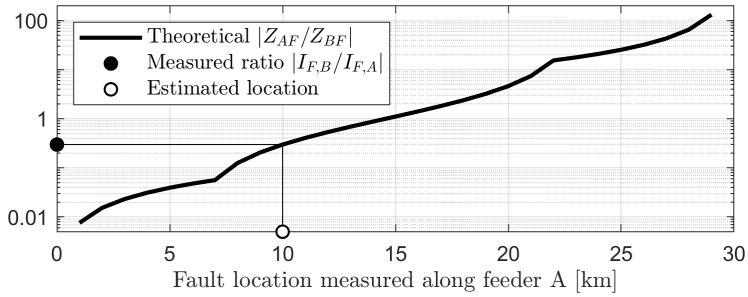

Fig. 4-14. Converting an observed current ratio to a distance estimate on a 30 km long ring

specifically to earth faults, where the zero-sequence currents, the negative sequence currents and the charging transient are identified as options for implementing the current ratio principle. All the three methods are derived in detail in Papers III and IV, so a brief summary of them are given below.

Negative sequence currents

The negative sequence currents measured on each of the two feeders are used. By subtracting the pre-fault values of these currents, the influence of load asymmetry can be removed. The resulting increments, $\Delta\vec{I}_{2,A}$ and $\Delta\vec{I}_{2,B}$, are used to estimate the negative sequence impedance ratio, as described in (4.5).

$$|\frac{Z_{2,AF}}{Z_{2,BF}}| = |\frac{\Delta\vec{I}_{2,B}}{\Delta\vec{I}_{2,A}}| \tag{4.5}$$

Zero-sequence currents

The zero-sequence method can also be used, and the incremental changes are used to remove the influence of healthy state currents flowing due to network asymmetry. However, the faulty state zero-sequence currents consist of the fault current as well as a significant capacitive component which increases during fault. This component must be removed, shown in (4.6).

$$|\frac{Z_{0,AF}}{Z_{0,BF}}| = |\frac{\Delta 3\vec{I}_{0,B} - \Delta\vec{V}_n m_B \bar{Y}}{\Delta 3\vec{I}_{0,A} - \Delta\vec{V}_n m_A \bar{Y}}| \tag{4.6}$$

For this method, the neutral voltage is required, along with data on the zero-sequence admittance of the feeders and their branches. The admittance $\bar{Y}$ is the sum of the phase-ground admittance in each phase, or simply $3Y_0$ if phase asymmetry is neglected. The factors m_A and m_B are used to account for the fact that the current $\Delta\vec{V}_n\bar{Y}$ will be distributed unevenly among the two feeders in the case of feeders with a mix of different line types. These factors can be found experimentally, either by performing simulations or measurements in the network, as described in Paper III. They can also be calculated analytically, and the procedure for doing this is shown in detail in appendix B.

Charging transient

In addition to the two fundamental frequency methods, the charging transient is also considered in Paper IV. The charging transient model presented in section 2.2.2 is modified to describe a ring-network. The only change required is to replace the inductance L_{ph} of the faulty phase in (2.16) with an equivalent inductance between the faulted point and the main bus. This equivalent inductance, L_{eq}, is simply the parallel connection of the inductance along each of the two paths.

$$L_{eq} = \frac{L_{AF}L_{BF}}{L_{AF} + L_{BF}} \tag{4.7}$$

With this modification, the frequency of the charging transient can still be calculated using (2.16). With this model as a starting point, the current ratio principle can be implemented by measuring the charging transient in the faulty phase on each of the two feeders. Let $\tilde{I}_{k,A}$ and $\tilde{I}_{k,B}$ be the charging transient components measured in the faulty phase k on feeder A and B, respectively. The ratio of these two components then corresponds to the ratio of the self-impedances in the two paths:

$$|\frac{Z_{k,AF}}{Z_{k,BF}}| = |\frac{\tilde{I}_{k,B}}{\tilde{I}_{k,A}}| \tag{4.8}$$

When using the charging transient, the impedances in (4.8) must be calculated at the observed charging transient frequency.

Selecting the correct impedance

The current ratio principle has been presented as being based on extracting the fault current from the measured currents. If this is achieved using either the negative sequence current or the zero-sequence current, it would be expected that the same impedance ratio should be used for comparison with the current ratio in either case. The fact that the negative sequence method must use the negative sequence impedance, and the zero-sequence method the zero-sequence impedance, shows that each method does not actually estimate the ratio of the fault current components. Rather, the current ratios in (4.5) and (4.6) each calculate the ratio of the *change* in currents that stem from the fault. The theoretical derivation of the methods in Paper III does not capture this properly as neither the phase-phase nor phase-ground coupling is included in the equations. However, by using the correct sequence impedance with each sequence current, each method works as intended. The charging transient method works by using the self-impedance of the faulty phase.

4.3.2 Results

All three methods are tested using the network in Fig. 4-15, which is based on a real Norwegian distribution network where the closed-ring operation is currently being considered. Except for minor changes to the lengths of two feeders in the background network, the important difference between the results in Paper III and Paper IV is that the latter are obtained using a frequency dependent line model better suited for studying the transient period of the faults.

Permanent faults

The two fundamental frequency methods are tested in Paper III, with an isolated transformer neutral. The results, shown in Fig. 4-16, demonstrate that both (4.5) and (4.6) are correct, and that the use of their corresponding sequence impedances yields very accurate results. The four scenarios

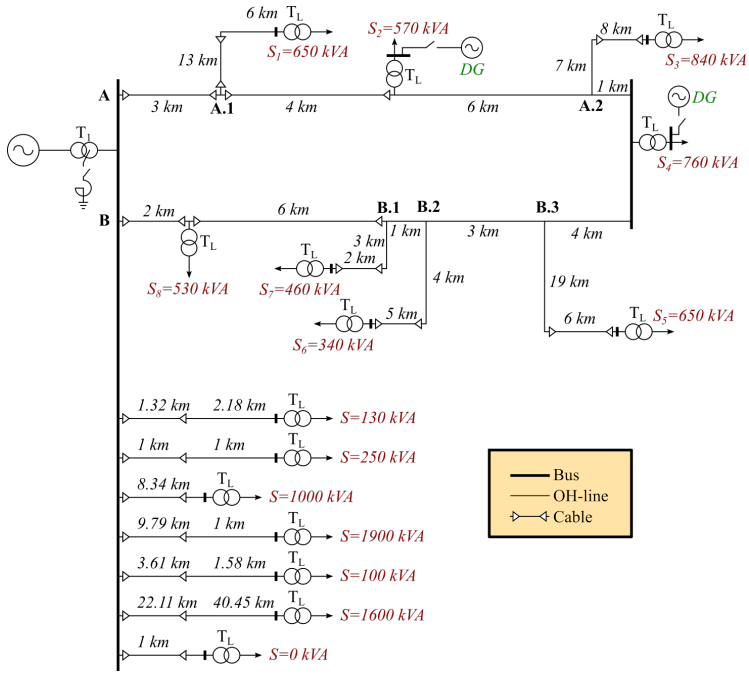

Fig. 4-15. Network used in Paper IV, based on a Norwegian distribution network. Paper III also uses the same topology with only minor changes to the size of the background network.

are different combinations of fault resistance and load asymmetry, demonstrating that the use of incremental values makes both methods robust against load asymmetry and high fault resistances.

The transient method is tested with permanent faults in Paper IV. The impact of removing the loads and the lateral branches on the ring is investigated as shown in Fig. 4-17, demonstrating that these two factors contribute to the reduced accuracy of this method. The impact of loads is that the charging transient is given alternative paths, and the branches contribute with currents which disrupt the accuracy of the current ratio. Although these contributions are relatively small, the error of the impedance estimate becomes very significant when the fault is located close the main bus.

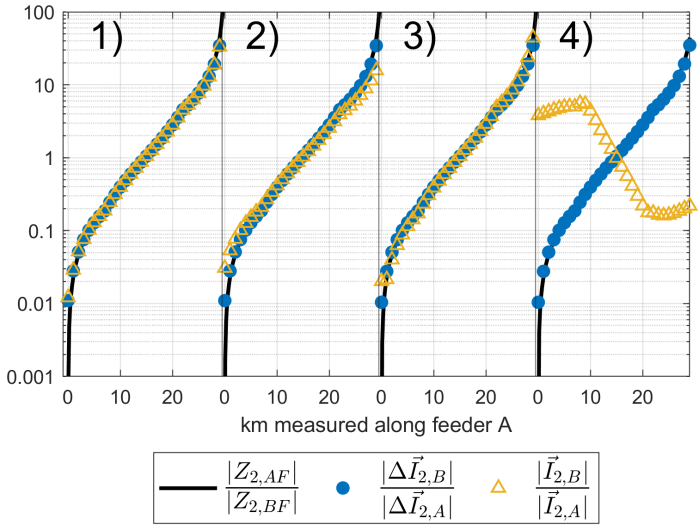

(a)

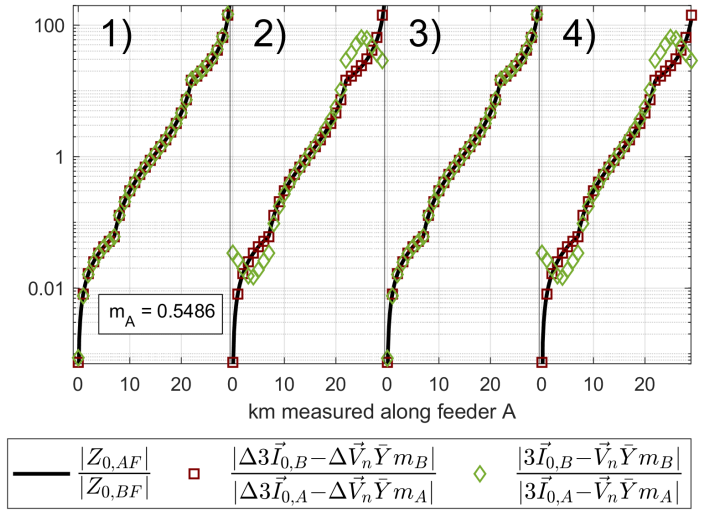

(b)

Fig. 4-16. (a) Negative sequence and (b) zero-sequence method results for four different scenarios: 1) $R_f = 1\Omega$, symmetrical loads, 2) $R_f = 1k\Omega$, symmetrical loads, 3) $R_f = 1\Omega$, unsymmetrical loads, 4) $R_f = 1k\Omega$, unsymmetrical loads.

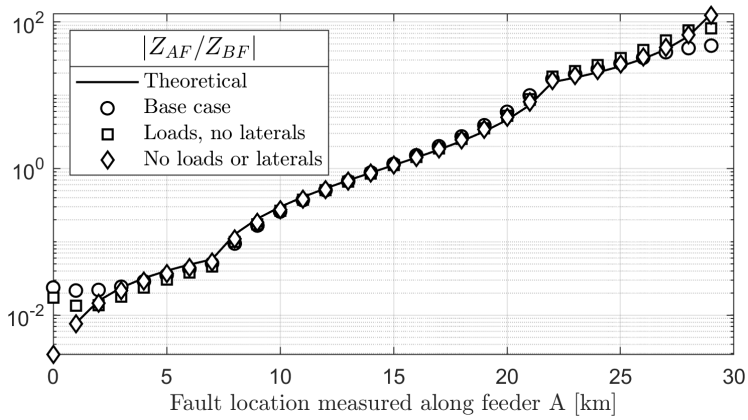

Fig. 4-17. Theoretical impedance ratio and estimated impedance ratio based on simulated transients

Transient and restriking faults

Paper IV further studies the performance of the three methods during transient and restriking faults. Both the fundamental frequency methods are derived from a steady-state analysis, but if they are to be applicable for transient faults as well, a fault location estimate must be produced before steady-state conditions can be reached. One important parameter which must then be considered, and which is overlooked during the permanent fault simulations in Paper III, is the time t_x at which the distance estimate is extracted, measured from the time of fault inception.

Fig. 4-18 illustrates how the negative sequence method and zero-sequence method estimates vary throughout a permanent fault. The negative sequence estimate reaches its final value much faster than the zero-sequence method, enabling a lower value of t_x without a significant loss in accuracy.

The results in Paper IV show that $t_x = 5$ ms is a good compromise between the need for speed during transient faults and the increased accuracy obtained by reaching steady-state conditions during permanent faults. However, the mechanism involved in determining the transient dynamics of the system has not been investigated in detail, and other values of t_x may perhaps give better results in other networks. With a logic to determine whether or not a fault is permanent, the value of t_x can then perhaps

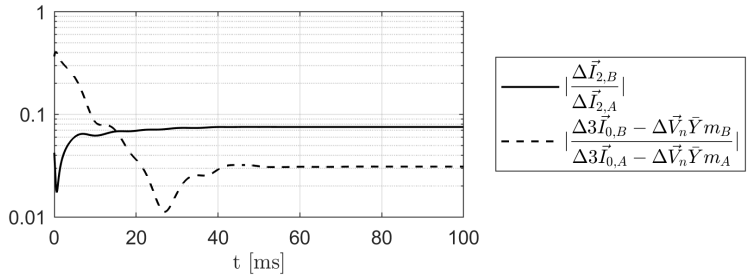

Fig. 4-18. Magnitude of the two ratios during a 1 Ω fault occurring at $t = 0$ at point A.1 in the network. The network is operating with an isolated neutral point.

be optimized in each case. However, transient faults without restrikes can be present for only a few milliseconds, and it is preferable for the methods to be able to handle these faults as well.

Fig. 4-19 illustrates how the system grounding and fault resistance impacts the accuracy of the three methods in the case of restriking faults. The negative sequence method is only marginally affected by the change in system grounding and fault resistance, whereas the zero-sequence method generally performs worse in the case of a resonant grounded system. The transient method is the least accurate method in any of the scenarios considered.

4.3.3 Summary and future work

The results in Paper III and IV demonstrate that the current ratio principle can be implemented in several ways and applied to locate earth faults in a closed-ring network. From the results in the two papers, the negative sequence method stands out as the most promising of the three methods. This is due to the method's overall high accuracy in all the considered tests, and it has been proved sufficiently fast to handle transient and restriking faults as well. The negative sequence method is also easier to implement than the other two as it has a simple logic and requires little input data to function. The zero-sequence method requires both zero-sequence impedance and admittance, and zero-sequence system data are generally considered to be less accurate due to their dependency on the ground properties. The charging transient method requires the self impedance at the

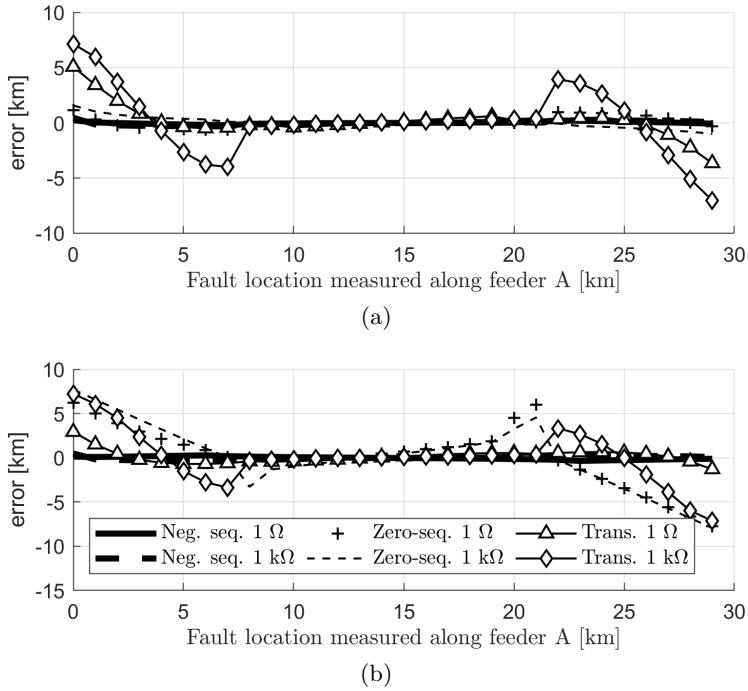

Fig. 4-19. Accuracy of the three methods in the case of faults with 1 Ω and 1 kΩ in (a) isolated and (b) resonant grounded network. The fault is modelled with a voltage dependent switch, creating restrikes if the phase voltage exceeds 4.5 kV.

charging transient frequency, and the signal processing is more challenging than for the other two methods. Furthermore, it is not accurate enough to be used in a network with laterals and branches, making it ill-suited for a distribution network. The main challenge for the negative sequence method is that it is adversely affected by the DG-units in the network, and accurate measurement of all three phase currents may not be readily available in distribution networks.

The methods are currently limited to providing fault location only, and they all assume a separate fault detection stage which determines that the fault is in fact on the ring itself and not in the background network. Furthermore, the methods require the network to be operated with this very specific closed-ring topology, which as of yet seems to be unusual in

distribution networks. The benefits of closed-ring operation is however well known and reported in the literature, and the results from Papers III and IV demonstrate that it can enable new approaches for precise earth fault location.

4.4 Contributions of Papers V and VI: High impedance fault detection and location

Papers V and IV present a novel method for detection, location and clearing of very high impedance earth faults in resonant grounded networks. Paper V describes this method at an early stage, which is then refined an expanded upon in Paper VI. Paper VI thus contains the main results, but Paper V has been included as part of the thesis for background and context.

In short, the proposed method relies on two separate fault indicators, which when used together provide sensitive and selective fault indication. The first indicator is based on the measurement of phase currents on the beginning of each feeder, and both Papers V and VI consider a radial network topology when deriving these indicators. However, with two-ended measurements these phase current indicators are applicable in non-radial networks as well, as is shown later in this subchapter. The second fault indicator is based on the neutral current, and this indicator is intended for use both during the fault detection stage and a subsequent sectionalizing process. By accounting for the change in compensation degree during a sectionalizing process, this indicator continuously monitors the presence of a fault in the network. It is therefore suited for aiding in location of the fault through manual sectionalizing, and it is not limited to any network topology. If more than one ASC is used in the network, a wide-area approach must be used to consider the total neutral current in the network. This is also illustrated later in this subchapter.

As Paper VI contains all the main elements of the method along with laboratory testing, this subchapter focuses on presenting a summary of the proposed method, along with some analyses and results that have been omitted from the papers.

4.4.1 $\vec{V}_n$ during high impedance earth faults

While $|\vec{V}_n|$ is a good earth fault indicator for faults with a low fault resistance, its application is limited at higher fault resistances. The threshold used for triggering earth fault detection based on $|\vec{V}_n|$ in earth fault protection is commonly set to be higher than the resonance point voltage in the network to avoid false alarms during normal operation of the network, typically 0.1 p.u. or higher [95–97]. Moreover, even if a lower threshold is selected for more sensitive detection, the increase in fault resistance eventually limits the detection capabilities.

Fig. 4-20 illustrates the magnitude of $\vec{V}_n$ before and during an earth fault, computed using (2.7) and (2.10) and assuming a small asymmetry in phase b (note that $\hat{G}$ has replaced G_{tot} to follow the notation used in Paper VI). For low fault resistances, $|\vec{V}_n|$ is close to 100% regardless of which phase the fault occurs in. As the fault resistance increases, the difference between the three phases becomes more apparent. For faults in phase a, the fault can even reduce the value of $|\vec{V}_n|$ below its pre-fault value, if the resistance is high enough (in this case for $R_f > 20$ kΩ).

The point at which $|\vec{V}_n|$ cannot be used for fault detection depends on several system parameters such as the voltage level, network size and asymmetry. Fig. 4-21 illustrates how faults with a particular fault resistance impact the magnitude of $\vec{V}_n$ in three different networks (see the caption of Fig. 4-21 and the figure itself for network data). Together, Fig. 4-20 and Fig. 4-21 demonstrate that there is no clear fixed relationship between $|\vec{V}_n|$ and the fault resistance, but it is apparent that the applicability of $|\vec{V}_n|$ as a fault detection criterion can become limited to a few kΩ's in practice. As a result, conventional earth fault protection based on a $|\vec{V}_n|$-criterion will not be able to operate for higher fault resistances.

$|\vec{V}_n|$ is also of limited value for monitoring the presence of a fault during a sectionalizing process. Consider the example in Fig. 4-22, where (2.7) and (2.10) have been used to calculate the neutral voltage in a network with the same parameters as in Fig. 4-20. The figure shows the neutral voltage magnitude as a function of the nominal ASC current in four different states: healthy pre-fault operation (solid blue) and during initial fault (solid red), as well as healthy and faulty state (dashed curves) in the same network when 15% of the network has been temporarily disconnected in an attempt to clear the fault. If the fault is low-ohmic, it is easy to use $|\vec{V}_n|$

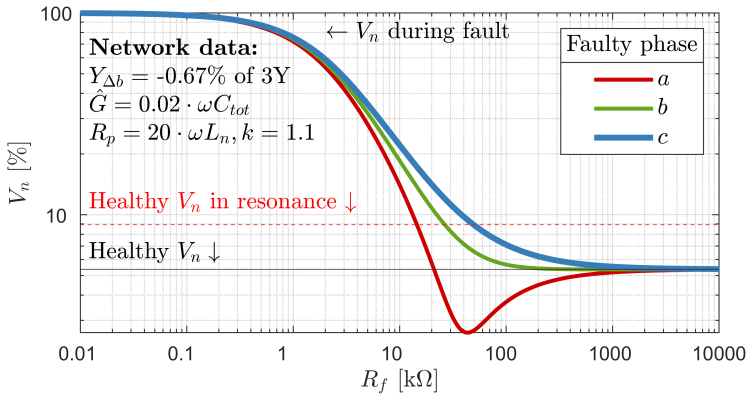

Fig. 4-20. $|\vec{V}_n|$ computed using (2.7) and (2.10) in a 22 kV network with a 50 A charging current and 5 A over-compensation

to determine whether or not it remains present in the network after the attempted fault clearing, as shown in Fig. 4-22a: The voltage's increase is significant when the fault first occurs, and its decrease is equally significant if the fault is cleared successfully. However, if the fault is high-ohmic as in Fig. 4-22b, the situation is more challenging. The initial fault detection would be challenging due to the relatively small increase in $|\vec{V}_n|$, and the voltage would drop below its pre-fault value after sectionalizing, regardless of whether the fault is cleared successfully or not. Determining if the fault is still present in the system is thus not possible without knowledge of the new resonance curve of the system. Had the network been operated in an under-compensated state before the fault, $|\vec{V}_n|$ would increase after the sectionalizing regardless of the fault being cleared successfully or not. As a result, it is not possible to monitor $|\vec{V}_n|$ to determine whether or not a high impedance fault is cleared successfully.

The above examples illustrate that as the fault resistance increases, the use of $|\vec{V}_n|$ as a fault indicator becomes very inaccurate. Moreover, the actual value of R_f where this occurs will vary from network to network, depending on parameters such as voltage level, size and asymmetry.

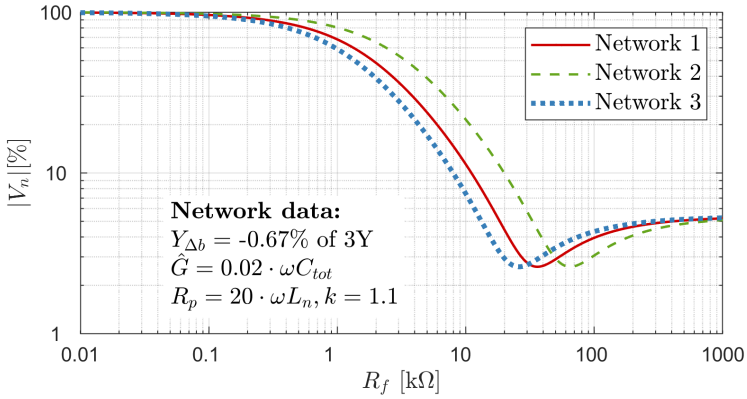

(a)

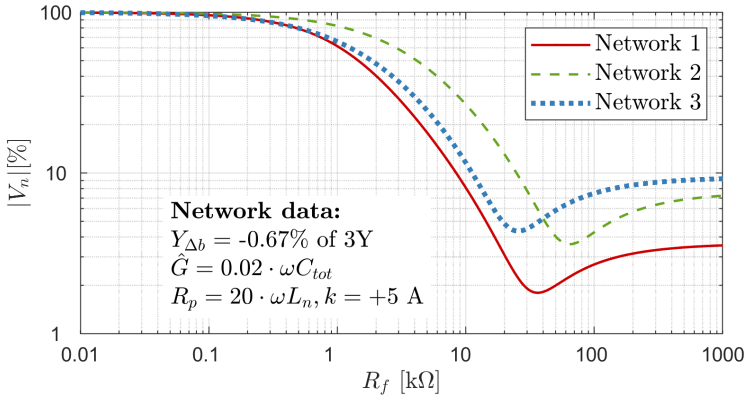

(b)

Fig. 4-21. Magnitude of $\vec{V}_n$ during fault in phase a in three networks with different line voltage and total capacitive charging current, assuming either (a) 10% or (b) 5 A over-compensation. Network 1 (11 kV, 30 A); Network 2 (66 kV, 100 A); Network 3 (132 kV, 500 A)

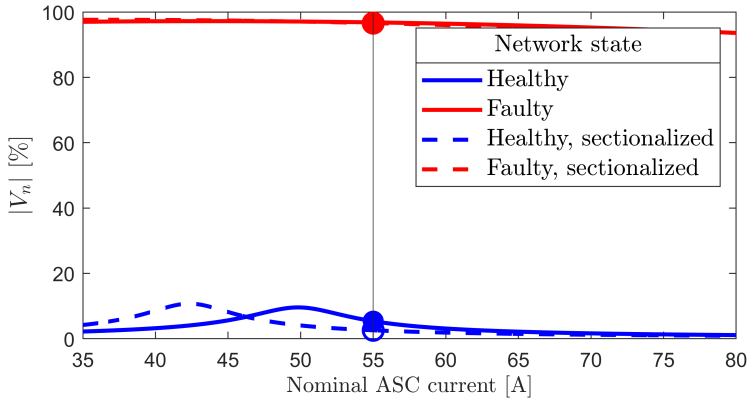

(a)

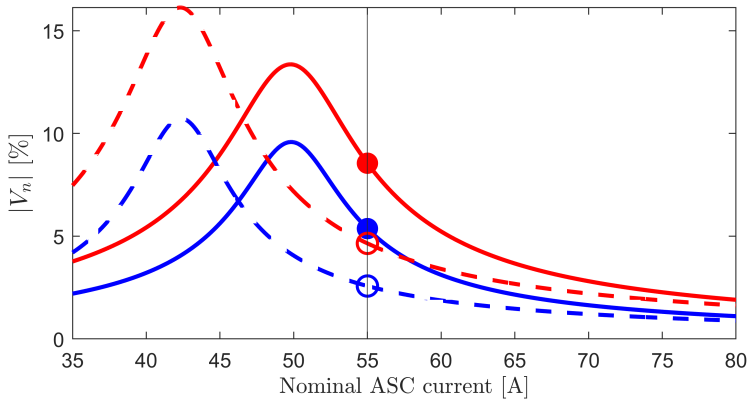

(b)

Fig. 4-22. Example of neutral voltage (% of nominal phase voltage) in various network states in the case of (a) a 100 Ω and (b) a 15 kΩ fault. Vertical line shows 10% over-compensation in the pre-fault network. The fault occurs in phase a, and the network has the same parameters as in Fig. 4-20.

4.4.2 $\vec{I}_f$ during high impedance earth faults

Equation (4.9) describes the fault current as a function of the voltage $\vec{E}_a$ and various system parameters. It corresponds to (2.12) with two changes: G_{tot} is replaced by $\hat{G}$ according to the notation used in Paper VI, and $L_n = (k\omega^2 C_{tot})^{-1}$ is used to express the ASC inductance L_n as a function of the system capacitance and compensation degree.

$$\vec{I}_f = \frac{\vec{E}_a}{R_f}\left(\frac{\hat{G} + \frac{1}{R_p} + j\omega C_{tot}(1-k) - D}{\hat{G} + \frac{1}{R_p} + j\omega C_{tot}(1-k) + \frac{1}{R_f}}\right) \tag{4.9}$$

This equation may be unnecessarily detailed for certain analyses, but it can be replaced by approximations valid at either low or high values of R_f. Consider first the case where R_f is low. Equation (4.10) shows that the magnitude of $\vec{I}_f$ is determined by the conductive elements, asymmetry, the compensation degree and the amount of capacitance in the network.

$$\lim_{R_f \to 0} \vec{I}_f = \vec{E}_a\left(\hat{G} + \frac{1}{R_p} + j\omega C_{tot}(1-k) - D\right) \tag{4.10}$$

Next, assume that $\hat{G} = \frac{1}{R_p} = D = 0$. Equation (4.9) is reduced to (4.11):

$$\vec{I}_f = \frac{\vec{E}_a}{R_f}\left(\frac{j\omega C_{tot}(1-k)}{j\omega C_{tot}(1-k) + \frac{1}{R_f}}\right) \tag{4.11}$$

As R_f increases, the fraction in (4.11) approaches 1. Therefore, at high values of R_f, the fault current can be approximated as being a function of $\vec{E}_a$ and R_f only, as shown in (4.12).

$$\vec{I}_f \approx \frac{\vec{E}_a}{R_f} \tag{4.12}$$

Note that the assumption of $\hat{G} = \frac{1}{R_p} = 0$ is not actually required to arrive at this result. However, it simplifies the next step, which is to determine an approximate value of R_f for which the transition between the "low-R_f" approximation and "high-R_f" approximation occurs. Let this value be denoted R_f^*. From asymptotic analysis of functions like the

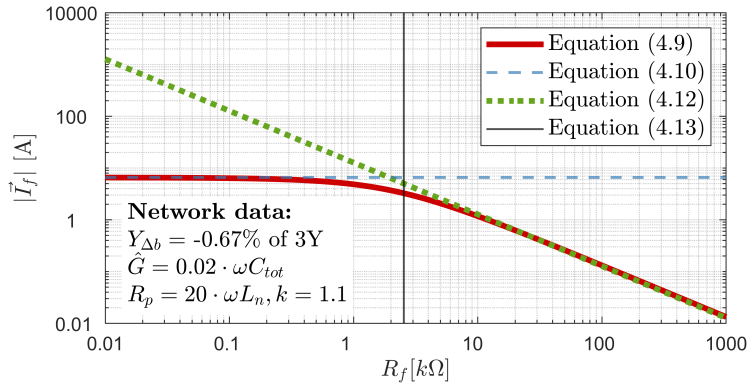

Fig. 4-23. Calculated magnitude of the fault current as function of the fault resistance in a 22 kV network with 50 A charging current.

one in (4.11), R_f^* corresponds to the "breaking point" of the curve and is given by (4.13) [98].

$$R_f^* = \frac{1}{|\omega C_{tot}(1-k)|} \tag{4.13}$$

Fig. 4-23 shows how well the above approximations are able to estimate the fault current. The estimated value of R_f^* is also included. Note that R_f^* does not match the breaking point between the two approximations perfectly because (4.10) and (4.12) have different assumptions regarding $\hat{G}$, R_p and D. However, it gives a decent approximation of the breaking point of the curve. For $R_f << R_f^*$, (4.10) is a valid approximation of (4.9), while (4.12) is valid for $R_f >> R_f^*$. For $R_f \approx R_f^*$, neither approximation is accurate and (4.9) must be used.

4.4.3 Proposed method

Phase current indicators

Both the proposed earth fault indicators attempt to estimate the fault current in real time, and the phase current indicators do this by monitoring the three fundamental frequency phase current phasors on each feeder. The change in current over a short time interval T_{SW} of a time-varying current

phasor $\vec{I}(t)$, $\Delta\vec{I}(t)$, is computed as

$$\Delta\vec{I}(t) = \vec{I}(t) - \vec{I}(t - T_{SW}) \tag{4.14}$$

As shown in both papers V and VI, the current increments in each phase on a single feeder can be combined to produce the following earth fault indicators:

$$\begin{aligned} J_a &= \Delta\vec{I}_a - \frac{1}{2}\Delta\vec{I}_b - \frac{1}{2}\Delta\vec{I}_c \\ J_b &= \Delta\vec{I}_b - \frac{1}{2}\Delta\vec{I}_a - \frac{1}{2}\Delta\vec{I}_c \\ J_c &= \Delta\vec{I}_c - \frac{1}{2}\Delta\vec{I}_a - \frac{1}{2}\Delta\vec{I}_b \end{aligned} \tag{4.15}$$

As long as the time-interval T_{SW} is short enough, the load variation is assumed to be so small that the three indicators J_{a-c} are zero in a healthy network. It is further shown in the papers that once a fault occurs, they remain zero on all the healthy feeders, while they exhibit the following relationship on the faulty feeder (assuming a fault in phase a):

$$\begin{aligned} J_a &= \vec{I}_f \\ J_b &= -\frac{1}{2}\vec{I}_f \\ J_c &= -\frac{1}{2}\vec{I}_f \end{aligned} \tag{4.16}$$

In (4.16), $\vec{I}_f$ is the fault current. By monitoring the three indicators on each feeder and looking for the above relationship between them, the indicators provide both fault detection and faulty feeder selection in one operation. Fig. 4-24 illustrates the detection logic for phase a, where a fault is signaled when both J_b/J_a and J_c/J_a come into the red zone. The parameters K and ϕ can be varied, where large values give increased sensitivity while smaller values give increased security. The ideal settings for these parameters have not been investigated in detail, but $K = 0.1$ and $\phi = 15°$ are found to be a good balance in Paper VI. In addition, a magnitude threshold for J_{a-c} must be considered as well to avoid false detection due to naturally occurring noise. The detection logic shown in Fig. 4-24 must be implemented for each phase and monitored simultaneously.

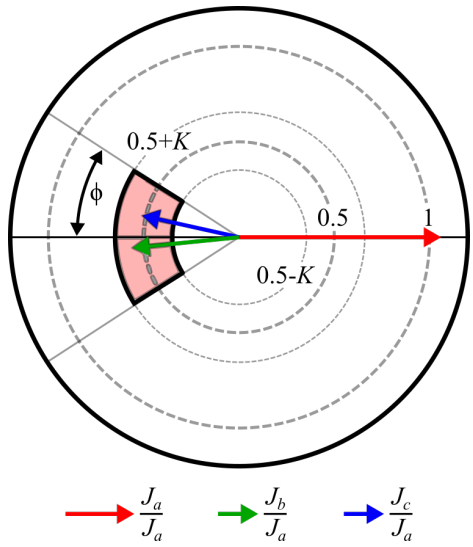

Fig. 4-24. Relationship between phase current indicators on a faulty feeder with earth fault in phase a

Sectionalizing indicator

The second earth fault indicator is based on measurement of the ASC current and voltage. In addition to this, knowledge of the system's compensation degree or total capacitance is required as input. Consider the network in Fig. 4-25. With knowledge of the system capacitance, the coil split-notation is introduced, as shown in Fig. 4-25a. This notation divides the ASC inductor in two parallel components, each conducting a portion of the inductive ASC-current. L_{res} perfectly matches the system capacitance, thereby providing the exact inductance required to operate the network in its resonance condition. The second inductor, L_p, therefore contains the remainder of the ASC-current which is not used to compensate the capacitive current in the network. This current, the inductive part of the current labeled $\vec{I}_p$, can then be thought of as the over-compensation current of the network. With a compensation degree k in the network, this inductor is related to the physical inductance L_n as described by (4.17)

$$L_p = L_n \frac{k}{k-1} \tag{4.17}$$

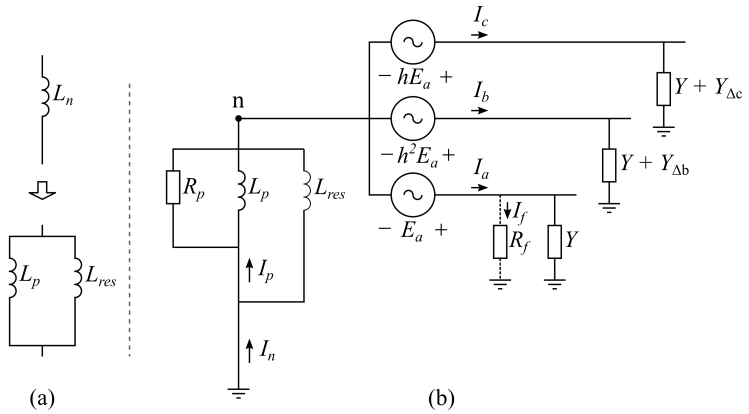

Fig. 4-25. (a) Coil split and (b) definition of the current $\vec{I}_p$

The over-compensation inductor L_p is a theoretical construct, and it is valid for $k > 0, k \neq 1$. The value $k = 1$ corresponds to a network in resonance, for which L_p becomes an infinitely large inductance, as can be seen by evaluating either $\lim_{k\to 1^-} L_p$ or $\lim_{k\to 1^+} L_p$. For $k > 1$, L_p acts as an inductor and gives an over-compensated network. For $k < 1$, L_p becomes negative and acts as a capacitance which makes the network under-compensated. The resulting current $\vec{I}_p$ is shown in Fig. 4-26.

The significance of $\vec{I}_p$ is best illustrated through the equivalent circuit in Fig. 4-27. Here, it is apparent that the current $\vec{I}_p$ corresponds to the asymmetry-current $\vec{I}_D$ in the healthy network, assuming that the conductance in the network is negligible. When the fault occurs, $\vec{I}_p = \vec{I}_D + \vec{I}_f$, and therefore the fault current can be estimated as $\Delta\vec{I}_p \approx \vec{I}_f$. The current increment $\Delta\vec{I}_p$ is therefore used as the second earth fault indicator in the proposed method, and it can be implemented with the same type of logic as the phase-current indicators. See Fig. 4-28. This indicator can also be used to provide continuous fault indication throughout a sectionalizing process, hence being labeled the sectionalizing indicator.

Fault detection and location based on the indicators

Once an earth fault occurs in the network, both the phase current indicators J_{a-c} and the sectionalizing indicator $\Delta\vec{I}_p$ will indicate a fault. Their

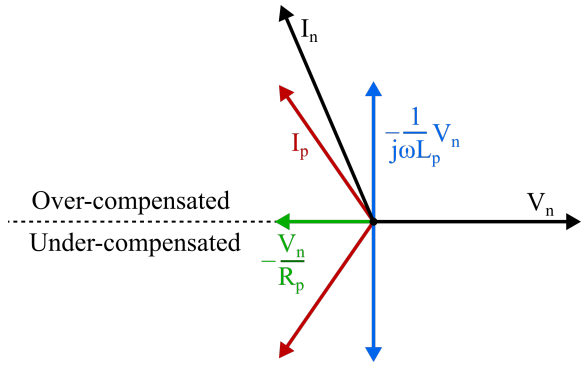

Fig. 4-26. Phasor diagram showing $\vec{I}_p$ in an over-compensated and an under-compensated network ($\vec{V}_n$ and $\vec{I}_n$ not drawn to scale)

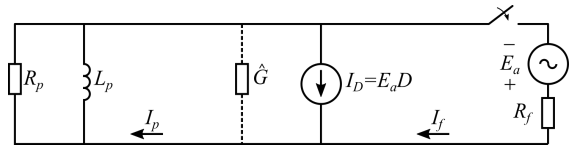

Fig. 4-27. Equivalent circuit for evaluation of $\vec{I}_p$ in a healthy and a faulty network

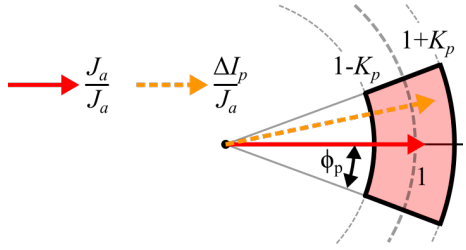

Fig. 4-28. Relationship between the sectionalizing indicator $\Delta\vec{I}_p$ and the faulty phase current indicator J_a

simultaneous operation is beneficial as it ensures selectivity: Single-phase events could in theory trigger J_{a-c}, but not $\Delta\vec{I}_p$, and changes in the operating point of the ASC could trigger $\Delta\vec{I}_p$, but not the indicators J_{a-c}.

When both indicators signal a fault, both fault detection and faulty feeder selection is achieved simultaneously. When deriving the phase current indicators J_{a-c}, it was emphasized that the length of the sliding window T_{SW} must be so short that the load can be assumed constant. As a result, the fault indication from these indicators disappear after a time T_{SW}, after which they return to zero. Should the fault disappear on its own after this time, the phase current indicators would again signal a fault in the same phase. Limiting the length of the sliding window is not a concern for $\Delta\vec{I}_p$ as $\vec{I}_p$ remains constant during fault as long as the network topology is kept constant (the fault itself can develop, but $\Delta\vec{I}_p$ still estimates $\vec{I}_f$). Therefore, once a fault occurs, the computation of $\Delta\vec{I}_p$ can be done using the last known pre-fault value of $\vec{I}_p$. For instance, say that a fault is detected at time t_f, and that $\Delta\vec{I}_p$ has been computed using a sliding window with length T_{SWp}. The computation of $\Delta\vec{I}_p$ after t_f then becomes $\Delta\vec{I}_p(t) = \vec{I}_p(t) - \vec{I}_p(t_f - T_{SWp})$. This ensures that $\Delta\vec{I}_p$ keeps indicating a fault and estimating the fault current until the fault is cleared.

When switching operations are performed during the sectionalizing of the network, $\vec{I}_p$ is simply computed using an updated value of k which is estimated based on knowledge of the distribution of the capacitance in the network. The pre-fault value $\vec{I}_p(t_f - T_{SWp})$ is kept unchanged, although this is a simplification which may reduce the accuracy of the fault current estimate in the subsequent sectionalizing process. From Fig. 4-27 it is apparent that as long as the current source $\vec{I}_D$ remains unchanged, this approach is valid. If the sectionalizing in the network severely alters this current, however, the accuracy of $\Delta\vec{I}_p \approx \vec{I}_f$ is reduced.

4.4.4 Wide-area adaptation of the method

When applying the proposed method in a non-radial network, the phase current indicators can only be implemented on meshed parts of the network if two-ended synchronized measurements of the phase currents are available. While the sectionalizing indicator presented thus far is valid in any network topology, it does assume a network with only one ASC. In

non-radial networks, however, it it not unlikely to have two or more ASCs sharing the compensation of the system. If this is the case, the sectionalizing indicator requires the synchronized measurements of the currents in all the ASCs in order to operate. If these measurements are available, the indicator is computed in exactly the same way, with $\vec{I}_n$ being the sum of all the currents in the ASCs, and k being the total compensation degree of the network.

Simulations of the network in Fig. 4-29a are used to demonstrate the validity of the method using wide-area measurements. A 20 kΩ fault occurs on the line between station A and B, as shown in the figure. The phase currents at both ends of the line are measured, and their sum is used to calculate the phase current increments as shown in (4.18), before (4.15) is applied as before. Similarly, the neutral current of the network is calculated as the sum of the neutral currents measured in each of the two ASCs, i.e., $\vec{I}_n = \vec{I}_{n,P1} + \vec{I}_{n,P2}$. As $\vec{V}_n$ is the same everywhere, it can be measured over any of the ASCs. The resulting phase current indicators and the sectionalizing indicator are plotted in Fig. 4-29b, showing that the method is valid in this wide-area format as well.

$$\begin{aligned} \Delta\vec{I}_a &= \Delta\vec{I}_{a,A} + \Delta\vec{I}_{a,B} \\ \Delta\vec{I}_b &= \Delta\vec{I}_{b,A} + \Delta\vec{I}_{b,B} \\ \Delta\vec{I}_c &= \Delta\vec{I}_{c,A} + \Delta\vec{I}_{c,B} \end{aligned} \tag{4.18}$$

4.4.5 Laboratory testing

Due to the unavailability of field tests in a real distribution network, a laboratory setup is used instead to provide some practical testing of the proposed method. The Norwegian Smart Grid Laboratory [93, 99] is used for this purpose, and the results from these tests are reported in paper VI. Both the phase current indicators and the sectionalizing indicator function as intended, but the observed sensitivity is however lower than what is observed in simulations. The laboratory tests thus highlight some key differences between simulation results and physical tests.

The first issue that is observed is that the phasor estimation needs to account for the off-nominal frequency encountered in the network. Whenever the system frequency deviates from its nominal 50 Hz value, which is

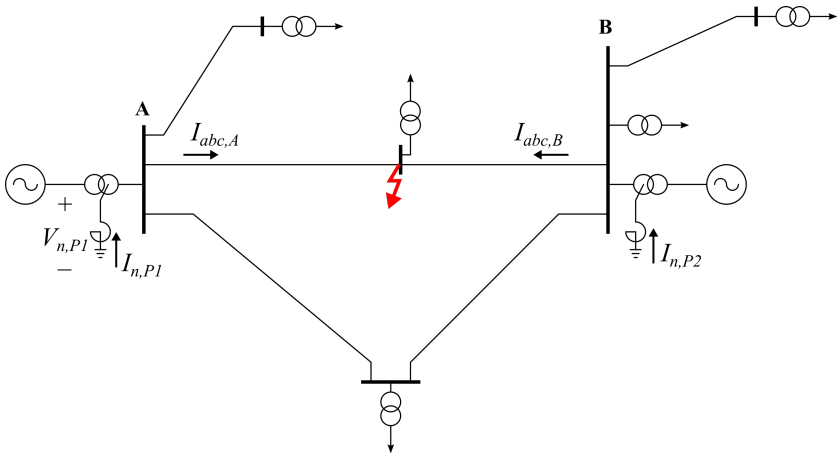

(a)

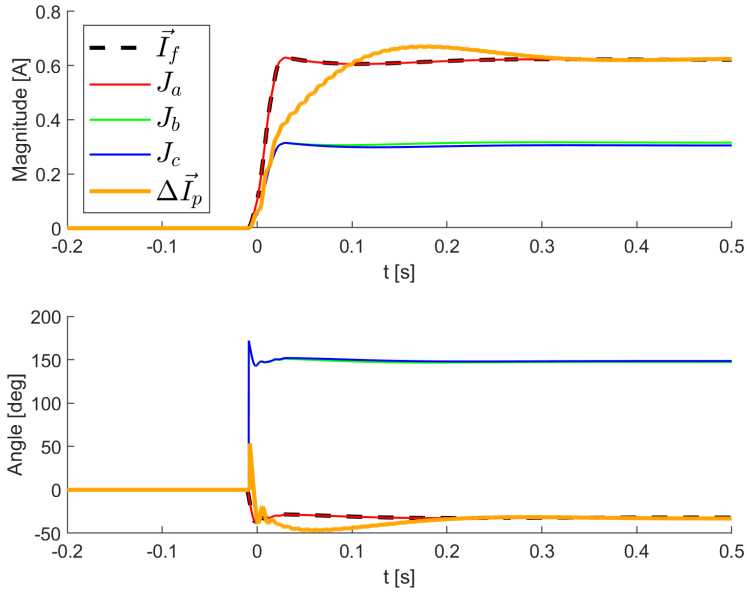

(b)

Fig. 4-29. (a) Test network and (b) resulting indicators based on wide-area measurements during a 20 kΩ fault

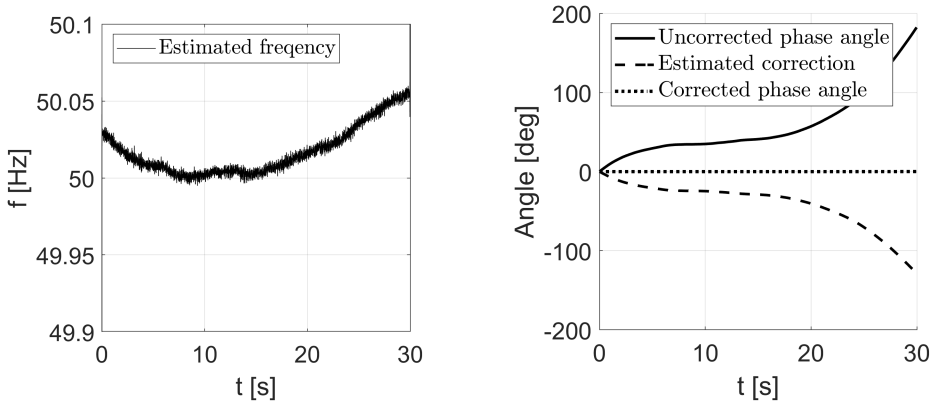

Fig. 4-30. (a) Estimated frequency and (b) resulting angles with (dotted) and without (solid) correction

almost always the case in physical networks, phasor estimation based on the assumption of a 50 Hz frequency will produce phasors with varying phase angles. The angles between all phasors are correct at any point in time, but when phasor increments are considered it represents a problem. The SDFT-algorithm [100] is used to counter this issue with good results in the laboratory tests, as illustrated in the example in Fig. 4-30.

The second issue not captured in the simulations in Paper V is the measurement quality. First of all, the measurement sensors need to be calibrated so that their magnitude and phase angle errors as function of their primary side signal can be accounted for. Constant measurement errors are less of an issue for the phase current indicators as the use of current increments to a large extent limits the negative impact from such errors. However, the sectionalizing indicator is highly sensitive to this due to the ASC parameters L_n and R_p being estimated from instantaneous current and voltage measurements. Even small measurement errors in the neutral current and voltage can then result in significant errors in the estimation of these parameters, so measurements must be calibrated.

Secondly, the current sensors used to measure the phase currents are found to have a big impact on the resulting measurements, and their adverse effects are identified as ultimately being the limiting factor for the

sensitivity of the method. When measuring a constant, healthy load current, the measured waveforms exhibit a varying magnitude, resulting in $\Delta\vec{I} \neq 0$. These variations in magnitude are determined as being induced by the sensors themselves as different sensors produce fluctuations with different magnitudes. For one of the sensors these fluctuations are observed to be dependent on the primary current, suggesting perhaps that interference from surrounding fields can be the source of the issue. However, a second type of sensor exhibit no such dependency of the primary current.

Fig. 4-31 shows the magnitudes and angles for the three phase current indicators and the fault current during two of the laboratory tests. The expected relationship between them, defined in (4.16), is observed: The magnitude of J_a is identical to $\vec{I}_f$ in magnitude and angle, while both J_b and J_c are 180 degrees out of phase with J_a with half the magnitude. This relationship only lasts for 100 ms (i.e., the length of T_{SW}), after which all the indicators have zero magnitude. The same relationship between the three indicators is observed again when the fault is disconnected, but with a 180 degree shift in angles.

These results also illustrate clearly how the fluctuating current magnitudes result in the indicators J_{a-c} never being exactly zero. Therefore, a magnitude criterion $|J_a| > \epsilon_J$ is introduced to avoid frequent false fault detection based on the fluctuations in healthy operation. Moreover, as the fault current is reduced when the fault resistance increases, the fault current at some point fails to stand out above this constant noise. This effect is observed by comparing Fig. 4-31a and Fig. 4-31b, where the ideal relationship between the indicators is seen during the 3 kΩ fault while being distorted during the 20 kΩ fault. At some point the indicators are no longer able to detect faults reliably, and this is identified as the limiting factor of the method. The exact absolute threshold where this occurs is difficult to determine as it depends on the sensor properties and the settings of the method, where the desired high sensitivity must be balanced against the need for selectivity. In the laboratory tests, with $\epsilon_J = 10$ mA, $K = 0.1$ and $\phi = 15°$, this occurs for R_f between 15 and 20 kΩ.

While the phase current indicators are limited to $R_f = 15$–20 kΩ, the sectionalizing indicator function as intended up to 50 kΩ. Fig. 4-32 and Fig. 4-33 show how the indicator $\Delta\vec{I}_p$ is able to estimate the fault current

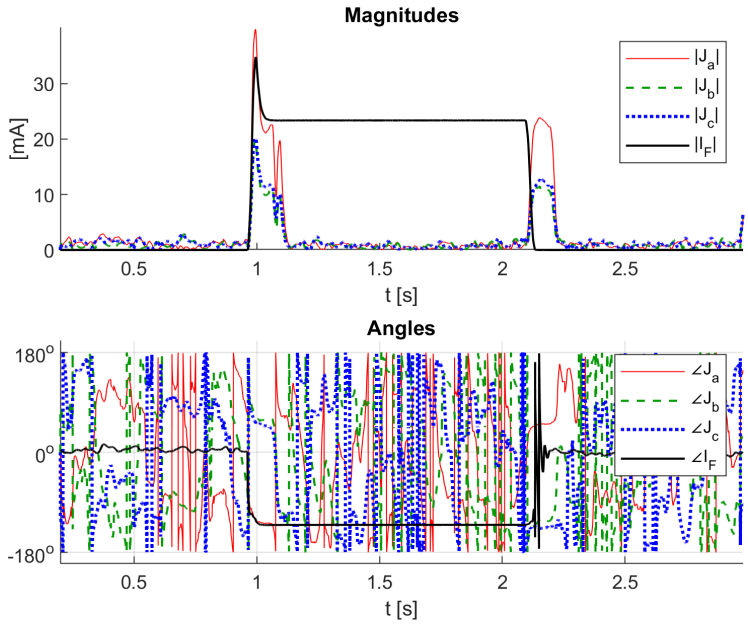

(a)

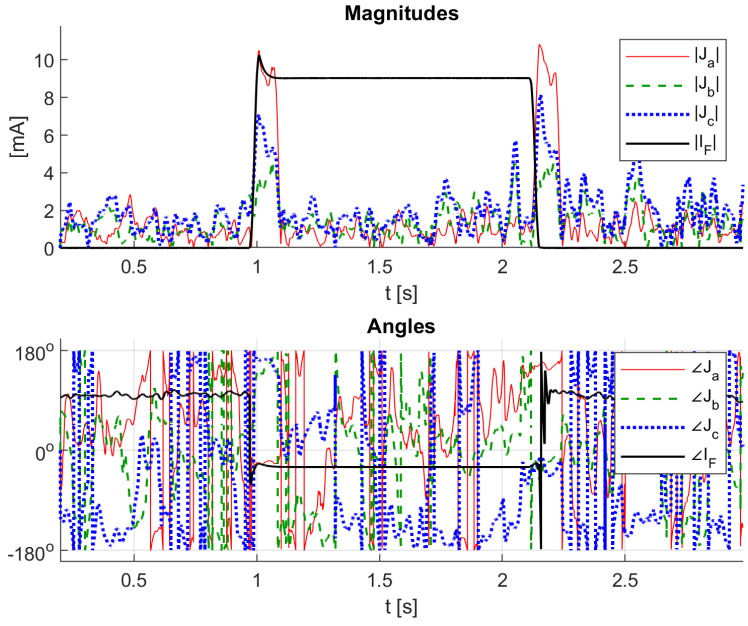

(b)

Fig. 4-31. Magnitudes and angles of the fault current and the phase current indicators J_{a-c} during (a) a 3 kΩ and (b) a 20 kΩ fault.

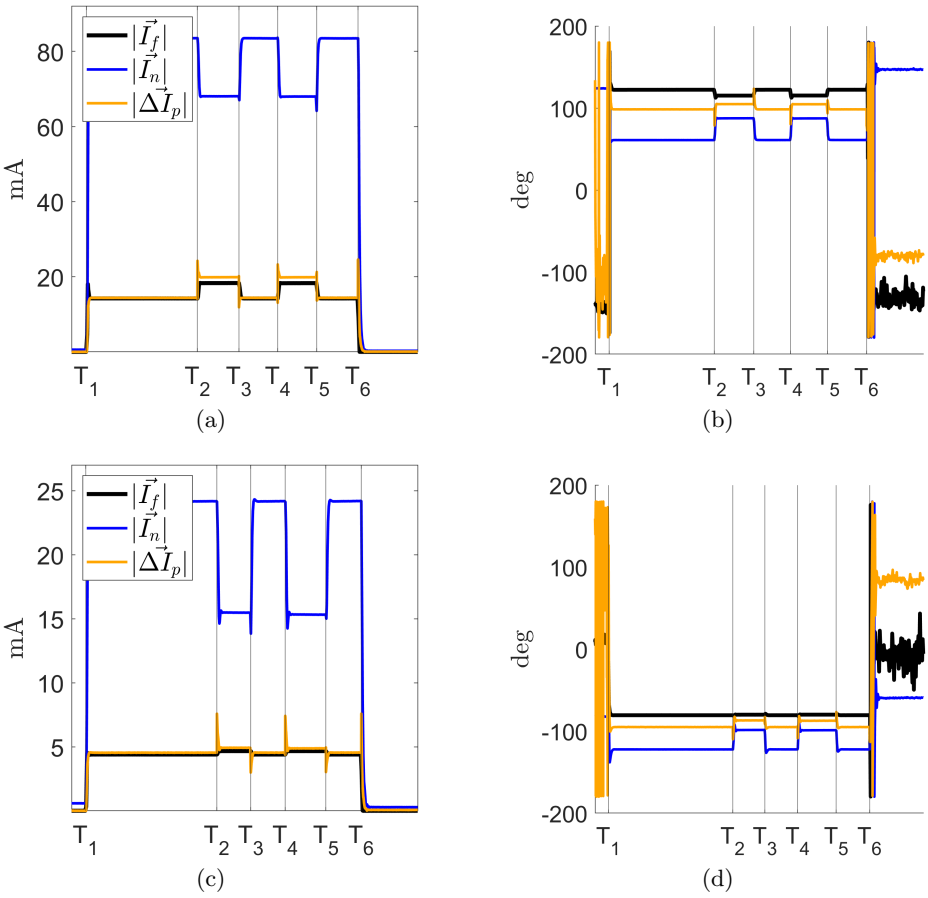

Fig. 4-32. Magnitudes and angles of the fault current, neutral current and sectionalizing indicator $\Delta\vec{I}_p$ during (a), (b) a 10 kΩ and (c), (d) a 50 kΩ fault clearing process in an over-compensated network.

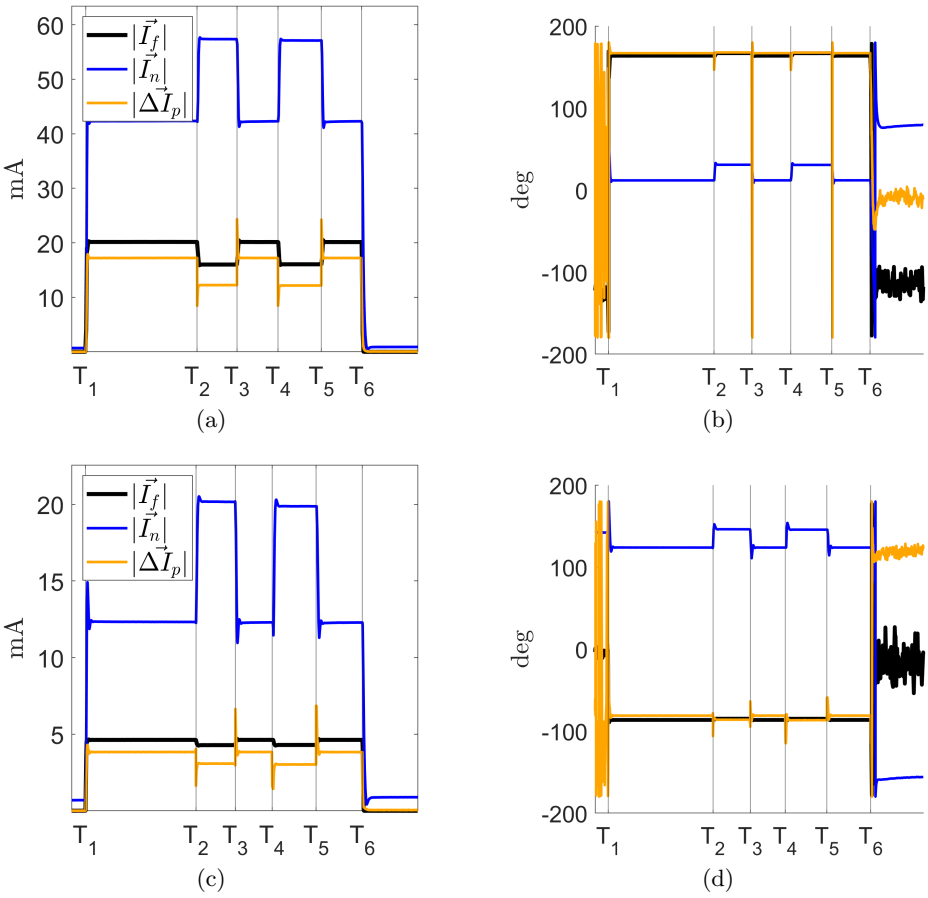

Fig. 4-33. Magnitudes and angles of the fault current, neutral current and sectionalizing indicator $\Delta\vec{I}_p$ during (a), (b) a 10 kΩ and (c), (d) a 50 kΩ fault clearing process in an under-compensated network.

during a process of switching in and out different parts of the network (the fault occurs at T_1, and times T_2, T_3, ... correspond to different switching times). The two figures also show that $\Delta\vec{I}_p$ matches the fault current magnitude better for the cases in the over-compensated network, such as the cases in Fig. 4-32 exemplify, while the angle appears to be better predicted in the under-compensated network. The explanation for this is likely that one or more of the measurements are not calibrated accurately enough, which, when coupled with the fact that the angle of $\vec{I}_p$ flips with respect to the current $\vec{I}_n$ when going from an over-compensated to an under-compensated network, could produce these results.

4.4.6 Discussion and future work

Together, Papers V and VI have presented a novel method for detecting, locating and clearing earth faults with very high fault impedances. The method uses a combination of phase currents and ASC-measurements to ensure selectivity. The main benefit of the proposed method is its ability to provide continuous fault indication via the sectionalizing indicator, a feature which is often overlooked in the scientific literature. The sectionalizing indicator is independent of any meshing in the network, making it applicable in any network topology. If the network has several ASCs, a wide-area approach must be used. The phase current indicators have been derived for and tested in a radial network, but with two-ended measurements they are applicable in a meshed network as well.

In this section, two important issues are addressed. First, the impact of conductance on the sectionalizing indicator is considered. When deriving the sectionalizing indicator, $\hat{G}$ was assumed to be negligible, which enabled $\Delta\vec{I}_p \approx \vec{I}_f$. This assumption introduces an error in the fault current estimation when $\hat{G} \neq 0$. Second, the scaling of the laboratory results is addressed. The proposed method has been verified in a low voltage, low current environment, but the validity of the results in real networks remains uncertain. The fault current approximations introduced earlier are used as a basis for a discussion on scaling and transferring the results to real distribution networks.

The effect of conductance on the sectionalizing indicator

When discussing the magnitude of $\hat{G}$, it is convenient to do so in terms of the shunt capacitance of the line. The variable $k_{\hat{G}} = \hat{G}/(\omega C_{tot})$ is defined and used in the following discussion and analysis.

Compared to the other line parameters the conductance is difficult to find typical values to use when modelling lines. In [81], G was measured on real insulators and calculated to be $1.5 \cdot 10^{-12}$–$3.7 \cdot 10^{-9}$ nS/km on a 138 kV line, depending on the insulator type and degree of pollution. These values correspond to $k_{\hat{G}}$ =0.0001–0.2%, assuming $C_0 = 7$ nF/km for that voltage level [87]. Temperature, weather and pollution impact the conductance of OH-lines, and the conductance is therefore both uncertain and variable in practice. For cables, the conductance stems from the resistive losses in the insulation, and it is determined by the cable geometry and the complex resistivity of the cable insulation [91]. According to [91, 101], $k_{\hat{G}}$ for a fluid-filled cable was measured to be approximately 0.2% in [102], while [91] states that the conductance is negligible for modern extruded cables. Some authors suggest higher values of $k_{\hat{G}}$ for use in modelling, such as $k_{\hat{G}} \approx$ 1–10% [40] and 2% [90]. In [90], the value is suggested as a rule of thumb for including all the resistive leakage currents in the network contributing to the fault current, both in the lines as well as in other components such as the ASC. Based on the aforementioned measured values of conductance for both line insulators and cables, values closer to 10% seem unrealistic for $k_{\hat{G}}$ of lines and cables. Rather, such values are more in line with the expected total resistive fault current in networks using a separate parallel resistor (typically rated 5–15 A in a 22 kV network [90]). However, support can clearly be found in the literature for a wide range of values for $k_{\hat{G}}$, so its impact on the sectionalizing indicator is investigated with this in mind.

According to (12) in Paper VI, repeated as (4.19) below, the error introduced in the fault current estimate by a non-zero $\hat{G}$ is $\hat{G}\Delta\vec{V}_n$. Using formulae for $\vec{V}_n$ in a healthy and faulty network, $\Delta\vec{V}_n$ can be computed as (4.20).

$$\Delta\vec{I}_p = \hat{G}\Delta\vec{V}_n + \vec{I}_f \tag{4.19}$$

$$\Delta\vec{V}_n = -\vec{E}_a \frac{1}{R_f} \frac{D - \hat{G} - \frac{1}{R_p} - \frac{1}{j\omega L_p}}{(\hat{G} + \frac{1}{R_p} + \frac{1}{j\omega L_p} + \frac{1}{R_f})(\hat{G} + \frac{1}{R_p} + \frac{1}{j\omega L_p})} \tag{4.20}$$

By combining (4.9), (4.19) and (4.20), the ratio $\Delta\vec{I}_p/\vec{I}_f$ can be calculated. Furthermore, by defining the factor $k_{Rp} = R_p/(\omega L_n)$, the ratio can be expressed as a function of the compensation degree k and the factors $k_{\hat{G}}$ and k_{Rp}. Equation (4.21) shows the resulting expression:

$$\frac{\Delta\vec{I}_p}{\vec{I}_f} = \frac{\frac{1}{R_p} + \frac{1}{j\omega L_p}}{\hat{G} + \frac{1}{R_p} + \frac{1}{j\omega L_p}} = \frac{\frac{k}{k_{R_p}} - j(k-1)}{k_{\hat{G}} + \frac{k}{k_{R_p}} - j(k-1)} \tag{4.21}$$

First, it is interesting to note that (4.21) does not depend on the fault resistance. This means that the fault current estimate will remain accurate as the fault resistance increases. Furthermore, inserting $\hat{G} = 0$ yields $\Delta\vec{I}_p = \vec{I}_f$, as expected. However, (4.21) does show that large values of $k_{\hat{G}}$ can reduce the accuracy of $\Delta\vec{I}_p \approx \vec{I}_f$ significantly. Fig. 4-34 shows the resulting magnitude and angle error for three different compensation degrees. The accuracy of the fault current estimate is reduced as the conductance is increased, and the compensation degree further impacts the accuracy. The value of k_{Rp} also impacts the results, with larger values leading to larger errors. The results in Fig. 4-34 can be verified qualitatively by inspection of Fig. 4-27, where each of the three parameters in (4.21) can be seen to impact the division of the current $I_f + I_D$ among the different shunt elements. The compensation degree k impacts the sign of the angle error because it determines whether L_p acts as an inductance or a capacitance.

For a vector comparison of $\Delta\vec{I}_p$ and J_{a-c}, large values of $k_{\hat{G}}$ must be accounted for. Equation (4.21) and Fig. 4-34 show that the effect of conductance is that $\Delta\vec{I}_p$ underestimates the fault current magnitude, while the angle error can be either positive or negative depending on the compensation degree. With reference to Fig. 4-28, the zone can be offset to account for the magnitude and angle error.

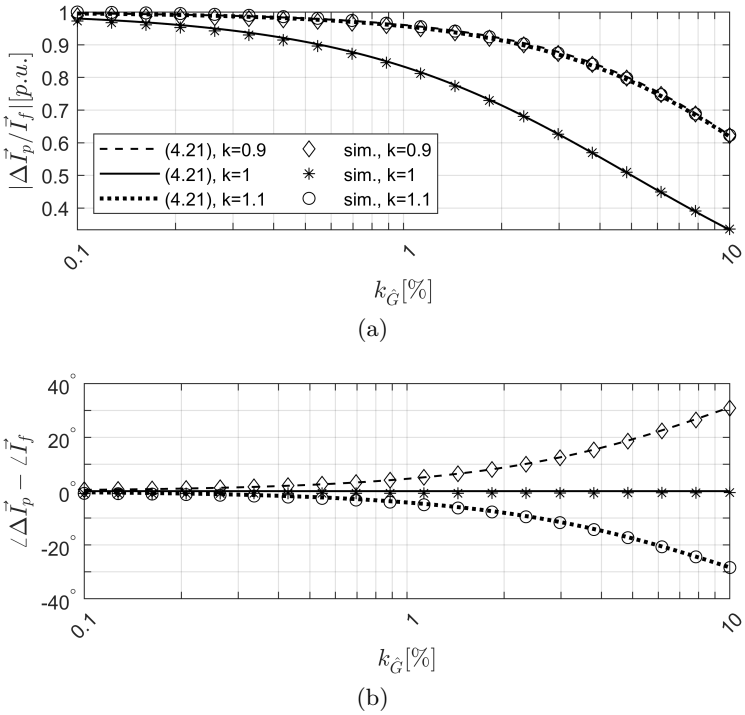

Fig. 4-34. (a) Magnitude and (b) phase angle accuracy of the sectionalizing indicator $\Delta\vec{I}_p$ as function of network conductance $k_{\hat{G}}$ and compensation degree k, calculated using (4.21) with $k_{Rp} = 20$ [17]. The markers show results from simulations of the network in Fig. 4-29a.

Scaling of the laboratory results

While the method would ideally have been tested in a real distribution network, a laboratory setup has been used instead to enable some degree of experimental validation of the method. This has provided some key insights into factors which are of importance in a physical implementation of the method, but it is limited in the sense that the scalability of the results is uncertain. While the laboratory results do show that the method performs as intended in the >10 kΩ-range, it is not apparent how these fault resistance values will transfer to a real network. Having identified earlier that the method works as long the magnitude of the fault current is sufficiently large compared to the naturally occurring non-zero magnitude of the phase current indicators J_{a-c}, the method will benefit from having a large fault current to detect. Equation (4.9) shows that there are multiple parameters affecting the magnitude of the fault current, and it is therefore not trivial to compare two different networks. However, (4.12) shows that at very high fault resistances, i.e., at the maximum detectable fault resistance, the fault current can be assumed proportional to the system voltage. Fig. 4-35 illustrates this for three imagined networks with different voltage levels. Therefore, the fault resistances in the 400 V lab will produce fault currents approximately 55 times higher in a 22 kV network (22/0.4=55). Alternatively, the fault current observed in the lab at one particular fault resistance will occur at a fault resistance 55 times higher in a 22 kV network.

With this approach to scaling the results, not considering any changes in measurement accuracy and noise, the 20 kΩ fault in the lab corresponds to a 1.1 MΩ fault in a 22 kV network. Such a high sensitivity does not appear realistic, and it leads to the second issue of scalability: the scaling of the measurement noise and indicator fluctuations. Given that detection of 1.1 MΩ fault resistances is not considered to be realistic, it is apparent that some increase in noise and measurement inaccuracy must take place when moving from the lab to a real network. If the phase current fluctuations scale by the same amount as the fault current, then the two effects cancel each other. In that case, the fault resistances in the lab correspond to the same fault resistances in a real network. The field test that was available for comparison in Paper VI suggests that this might be the case, but given how big impact different sensors can have on the results, the

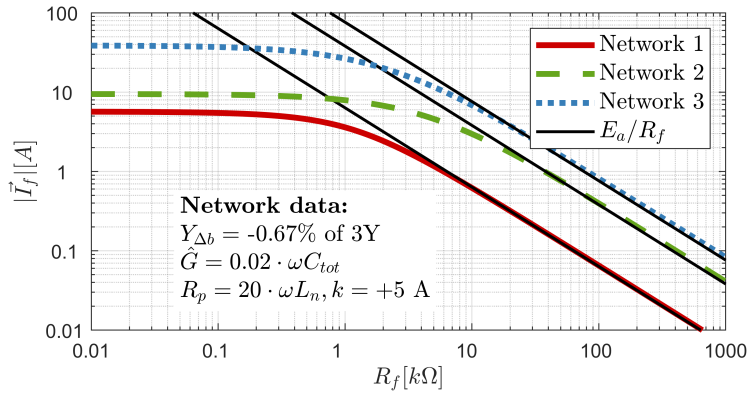

Fig. 4-35. Magnitude of $\vec{I}_f$ during fault in phase a in three networks with different line voltage and total capacitive charging current. Calculated using (4.9) and (4.12). Network 1 (11 kV, 30 A); Network 2 (66 kV, 100 A); Network 3 (132 kV, 500 A).

comparison between the laboratory measurements and a single field test is difficult to make. The two different sensors used in the laboratory yield vastly different sensitivity, demonstrating that the choice of sensors is critical. The field test referenced in Paper VI was conducted using class 5p20 protection cores, and better results could perhaps be achieved using dedicated sensors. While the measurement quality and the sensor properties have been identified as the likely limiting factor for the method, the exacts mechanism behind the observed measurement inaccuracies is not understood at this point. This also means that it is difficult to determine to what extent the sensor-induced inaccuracies discussed previously also scale in magnitude when applying the method in a physical network with higher current and voltage ratings. Therefore, as the theoretical concept behind the proposed method is verified both in simulations and experimentally, the most important future work is to study the impact of different current sensors and understand their impact on the method's sensitivity in a real network.

Chapter 5

Conclusion

This thesis presents research on earth faults in resonant grounded networks, with a special focus on fault location in networks with a non-radial topology. This research is divided in two almost independent research areas, each associated with a research objective. Each of these research areas are discussed in detail and summarized in subchapters 4.2–4.4, so this final chapter aims only to give a broader general summary of the main findings and conclusions in the thesis. The chapter also summarizes the most important limitations of the results and suggests further directions of research.

5.1 Main findings

The first research area covered in the thesis is the application of transient earth fault relays (TEFRs) in non-radial resonant grounded networks. One of the two associated research questions presented in chapter 1 asks how the directionality of the relays is determined in a non-radial network. The directionality of TEFRs is studied analytically using a simple closed-ring configuration in Paper I, where the charging transient and its appearance in the zero-sequence current measurements on the ring is examined. This analysis shows that for certain fault locations on the ring the charging transient will become too small to be measured as part of the zero-sequence current, and the relay will transition between seeing a fault as a forward or a reverse fault in these points. As a result, these fault locations are labeled

crossover points. This theoretical analysis is further expanded and confirmed experimentally using a laboratory setup in Paper II. However, the analytical approach to study the directionality of the relays is only possible to apply for the conventional relays based on the polarity principle. Two modern TEFRs are also considered, each having a more sophisticated operating principle which the theoretical analysis fails to capture. However, the general idea of a crossover point applies to any TEFR when part of a meshed network, and Paper I and II also present a qualitative analysis and comparison of all the different TEFRs under consideration.

The other research question related to the application of TEFRs in non-radial networks asks whether or not the TEFRs are equally applicable in radial and non-radial networks. From the results in Papers I and II, the answer to this question is that TEFRs are applicable in non-radial networks as well, but that their application is less straightforward and requires more careful consideration to ensure the desired coverage and selectivity. The lack of a clear forward/reverse direction coupled with the lack of a distance element makes the relay responses difficult to predict in advance, and it can lead to situations where the relay responses are either inconclusive or contradicting. Furthermore, in large meshed networks there are several parameters which can influence the responses of several relays in the network. These parameters are not necessarily intuitively linked to the responses of the relays, such as topology changes in the background network, making it important to perform planning and analysis of the relays in advance. Planning and analysis involves performing simulations and studying each relay location in advance to determine the optimal settings of the relays. This analysis must take into account the possible network configurations which may be utilized in normal operation. For relays which only support one setting this must cover all the network configurations, while modern relays which allow several settings to be stored in the relay can be tailored to different network configurations. The operating conditions for each relay in a meshed network can vary greatly, so each relay must be analysed and given individual settings. The planning and analysis should also verify that relays respond as intended to faults in different locations.

The main conclusion from this first research area is therefore that TEFRs are applicable in non-radial networks, but that they do require

planning and analysis in advance to ensure proper coverage and selectivity. A lack of such planning is identified as the most likely cause of issues with TEFRs experienced by network operators.

The second research area and its associated research objective are formulated more openly, aiming to develop new methods for more efficient fault location in non-radial networks. This research objective is realized by developing fault location methods aimed at two distinct applications, namely closed-ring distribution networks and high impedance faults.

The research in this thesis contributes to the development and analysis of three different methods for precise estimation of distance to fault in closed-ring distribution networks using current ratios. Two of these methods are based on fundamental frequency zero-sequence and negative sequence currents, respectively, while the third method utilizes the charging transient. After studying both permanent and transient faults in Papers III and IV, the method based on negative sequence currents is identified as the most promising alternative for further development and testing. Both this and the zero-sequence method locate permanent faults with high accuracy (within a few hundred metres), but the negative sequence method also manages to locate transient and restriking faults with almost the same accuracy. The zero-sequence method, however, is limited by the slower transients in the zero-sequence quantities, effectively limiting its application to more stable faults. The transient method is found to be too inaccurate in all the cases considered, primarily due to the presence of lateral branches and loads in the network, which makes the method ill-suited for application in distribution networks.

The thesis also presents a novel method aimed at high impedance earth faults. This method aims to provide both fault detection and fault location capabilities, as well as the ability to determine whether or not a fault is cleared successfully. The latter is achieved via an indicator which provides continuous fault indication, enabling the initial fault detection and fault location estimate to be further improved by the network operator through a sectionalizing process. A second indicator based on the phase currents is proposed as well, and together these two indicators provide sensitive and selective detection and fault location. The method is tested in a laboratory setup, and the results show that the method successfully detects and locates faults, although the phase current indicators are limited to

approximately 15–20 kΩ. The limiting factor is found to be the measurement accuracy of the phase currents, although the mechanism involved in this is not fully understood and represents the most important future work. The sectionalizing indicator functions without significant reduction in accuracy up to the highest available fault resistance, which is 50 kΩ. To predict the performance of the method in a real network, a scaling of the results is attempted by using a theoretical analysis of the earth fault current. If measurement errors and noise are neglected, the fault resistance can be scaled by the same factor as the system voltage. This approach predicts fault detection capabilities in the MΩ-range in real networks, but the magnification of measurement errors and noise is expected to reduce this in practice. Further study of current sensors is therefore required to determine the obtainable sensitivity of the method more precisely.

5.2 Recommended future work

- The analysis of the relays is verified with laboratory tests, and the next step is to apply the ideas from this thesis to the analysis of a larger benchmark network.
- The laboratory tests show that the quality of the current measurements ultimately limits the method for detection and location of high impedance faults. As a continuation of the laboratory tests, different current sensors and their impact on the method should be studied.
- Field tests should be used to further study the performance of all the proposed fault location methods. This is particularly relevant for the high impedance fault location method, for which the scaling of the laboratory tests is uncertain.

References

[1] IEEE, "IEEE guide for protective relay applications to distribution lines," *IEEE Std C37.230-2020 (Revision of IEEE Std C37.230-2007)*, pp. 1–106, 2021.

[2] X. Lin, J. Sun, I. Kursan, F. Zhao, Z. Li, X. Li, and D. Yang, "Zero-sequence compensated admittance based faulty feeder selection algorithm used for distribution network with neutral grounding through peterson-coil," *International Journal of Electrical Power & Energy Systems*, vol. 63, pp. 747–752, 2014.

[3] Y. Xue, X. Chen, H. Song, and B. Xu, "Resonance analysis and faulty feeder identification of high-impedance faults in a resonant grounding system," *IEEE Transactions on Power Delivery*, vol. 32, no. 3, pp. 1545–1555, 2017.

[4] A. Nikander and P. Järventausta, "Identification of high-impedance earth faults in neutral isolated or compensated MV networks," *IEEE Transactions on Power Delivery*, vol. 32, no. 3, pp. 1187–1195, 2017.

[5] A. Farughian, "Novel methods for earth fault passage indication in non-effectively grounded electricity distribution networks," Ph.D. dissertation, University of Vaasa, 2022.

[6] A. Wahlroos, J. Altonen, and J. Xavier, "Can compensated networks be an alternate solution to reduce the risk of ground faults causing forest fires?" in *2021 74th Conference for Protective Relay Engineers (CPRE)*, 2021, pp. 1–34.

[7] S. A. Bakken, "Stor risiko for mastebranner (in Norwegian)," *Xergi*, vol. 53, no. 1, 2013.

[8] K. Sjöberg, "Elsäkerhetsverkets föreskrifter och allmänna råd om hur starkströmsanläggningar ska vara utförda (in Swedish)," Elsäkerhetsverket, Tech. Rep. ELSÄK-FS 2022:1, 2022.

[9] Norwegian Directorate for Civil Protection (DSB), "Veiledning til forskrift om elektriske forsyningsanlegg (in Norwegian)," https://www.dsb.no/lover/elektriske-anlegg-og-elektrisk-utstyr/veiledning-til-forskrift/veiledning-til-forskrift-om-elektriske-forsyningsanlegg/, 2006, accessed: 22-04-2023.

[10] S. Hänninen and M. Lehtonen, "Characteristics of earth faults in electrical distribution networks with high impedance earthing," *Electr. Power Syst. Res.*, vol. 44, no. 3, pp. 155–161, 1998.

[11] K. Pandakov, "Improvements in protection of medium voltage resonant grounded networks with distributed sources," Ph.D. dissertation, Norwegian University of Science and Technology, 2018.

[12] M. Lehtonen, "Transient analysis for ground fault distance estimation in electrical distribution networks," Ph.D. dissertation, VTT Technical Reasearch Center of Finland, 1992.

[13] P. Imriš, "Transient based earth fault location in 110 kV subtransmission networks," Ph.D. dissertation, Helsinki University of Technology, 2006.

[14] M. R. Adzman, "Earth fault distance computation methods based on transients in power distribution systems," Ph.D. dissertation, Aalto University, 2014.

[15] M. Z. Habib, "Fault location in resonant earthed medium voltage distribution systems," Ph.D. dissertation, KTH Royal Institute of Technology, 2022.

[16] S. Hänninen, "Single phase earth faults in high impedance grounded networks: Characteristics, indication and location," Ph.D. dissertation, VTT Technical Research Centre of Finland, 2001.

[17] M. Loos, "Single phase to ground fault detection and location in compensated network," Ph.D. dissertation, Université Libre De Bruxelles, 2014.

[18] L. Döring, "Verfahren zur gerichteten erdschlusserkennung auf grundlage der transienten vorgänge nach erdschlusseintritt," Ph.D. dissertation, Technische Universität Darmstadt, 2021.

[19] T. Welfonder, "Localisation de défauts monophasés dans les résaux de distribution à neutre compensé," Ph.D. dissertation, Energie électrique. Institut National Polytechnique de Grenoble - INPG, 1998.

[20] A. Nikander, S. Repo, and P. Järventausta, "Utilizing the ring operation mode of medium voltage distribution feeders," in *Proc of 17th International Conference on Electricity Distribution*, 2003.

[21] M. Wadi, M. Baysal, and A. Shobole, "Comparison between open-ring and closed-ring grids reliability," in *2017 4th International Conference on Electrical and Electronic Engineering (ICEEE)*, 2017, pp. 290–294.

[22] IEEE, "IEEE trial-use guide for smart distribution applications," *IEEE Std 1854-2019*, pp. 1–65, 2019.

[23] J. D. Rios Penaloza, A. Borghetti, F. Napolitano, F. Tossani, and C. A. Nucci, "A new transient-based earth fault protection system for unearthed meshed distribution networks," *IEEE Transactions on Power Delivery*, vol. 36, no. 5, pp. 2585–2594, 2021.

[24] D. Wolter, M. Zdrallek, M. Stötzel, C. Schacherer, I. Mladenovic, and M. Biller, "Impact of meshed grid topologies on distribution grid planning and operation," in *24th International Conference & Exhibitionon Electricity Distribution (CIRED)*. IET, 2017, pp. 2338–2341.

[25] M. Wadi, M. Baysal, and A. Shobole, "Reliability and sensitivity analysis for closed-ring distribution power systems," *Electric Power Components and Systems*, vol. 49, no. 6-7, pp. 696–714, 2021.

[26] M. Biller and J. Jaeger, "Protection algorithms for closed-ring grids with distributed generation," *IEEE Transactions on Power Delivery*, vol. 37, no. 5, pp. 4042–4052, 2022.

[27] Z. Gajić, S. Aganović, R. Pajunen, and S. Zubić, "Universal earth-fault protection method for high impedance grounded power system," in *15th International Conference on Developments in Power System Protection (DPSP 2020)*, 2020, pp. 1–6.

[28] A. Petterteig, "Vurdering av vernløsninger i spolejorda regionalnett - lokalisering av stående jordfeil (in Norwegian)," SINTEF Energy Research, Trondheim, Norway, Tech. Rep., Nov. 1998.

[29] *UG03-3110 Manual: Typ RXPG 4 Transient jordströmsrelä (in Swedish)*, ABB Relays, Västerås, Sweden, 1990.

[30] *SIPROTEC 7SN600: Transient earth-fault relay: Instruction Manual*, Siemens AG (Version Oct. 2011), Nuremberg, Germany, 2011.

[31] D. Topolanek, M. Lehtonen, M. R. Adzman, and P. Toman, "Earth fault location based on evaluation of voltage sag at secondary side of medium voltage/low voltage transformers," *IET Generation, Transmission & Distribution*, vol. 9, no. 14, pp. 2069–2077, 2015.

[32] X. Wang, H. Zhang, F. Shi, Q. Wu, V. Terzija, W. Xie, and C. Fang, "Location of single phase to ground faults in distribution networks based on synchronous transients energy analysis," *IEEE Transactions on Smart Grid*, vol. 11, no. 1, pp. 774–785, 2020.

[33] K. J. Sagastabeitia, I. Zamora, A. J. Mazon, Z. Aginako, and G. Buigues, "Phase asymmetry: A new parameter for detecting single-phase earth faults in compensated MV networks," *IEEE Transactions on Power Delivery*, vol. 26, no. 4, pp. 2251–2258, 2011.

[34] K. Sagastabeitia, I. Zamora, A. Mazon, Z. Aginako, and G. Buigues, "Low-current fault detection in high impedance grounded distribution networks, using residual variations of asymmetries," *IET Generation, Transmission & Distribution*, vol. 6, no. 12, pp. 1252–1261, 2012.

[35] T. Schinerl, "A new sensitive detection algorithm for low and high impedance earth faults in compensated MV networks based on the admittance method," in *CIRED 2005-18th International Conference and Exhibition on Electricity Distribution*. IET, 2005, pp. 1–4.

[36] A. Wahlroos and J. Altonen, "Performance of novel neutral admittance criterion in MV-feeder earth-fault protection," in *CIRED 2009-20th International Conference and Exhibition on Electricity Distribution-Part 1*. IET, 2009, pp. 1–4.

[37] F. Ruz, A. Quijano, and E. Gómez, "DSTRP: a new algorithm for high impedance fault detection in compensated neutral grounded MV power systems," *European Transactions on Electrical Power*, vol. 13, no. 1, pp. 23–28, 2003.

[38] I. Zamora, A. J. Mazon, K. J. Sagastabeitia, and J. J. Zamora, "New method for detecting low current faults in electrical distribution systems," *IEEE Transactions on Power Delivery*, vol. 22, no. 4, pp. 2072–2079, 2007.

[39] T. Welfonder, V. Leitloff, R. Fenillet, and S. Vitet, "Location strategies and evaluation of detection algorithms for earth faults in compensated MV distribution systems," *IEEE Transactions on Power Delivery*, vol. 15, no. 4, pp. 1121–1128, 2000.

[40] A. Wahlroos, J. Altonen, and A. O. D. Automation-Finland, "Compensated networks and admittance based earth-fault protection," in *Kaunas University of Technology and Aalto University organized seminar on Methods and techniques for earth fault detection, indication and location, Espoo, Finland*, 2011.

[41] K. Pandakov, H. K. Høidalen, and J. I. Marvik, "Misoperation analysis of steady-state and transient methods on earth fault locating in compensated distribution networks," *Sustainable Energy, Grids and Networks*, vol. 15, pp. 34–42, 2018.

[42] D. Topolanek, M. Lehtonen, P. Toman, J. Orsagova, and J. Drapela, "An earth fault location method based on negative sequence voltage

changes at low voltage side of distribution transformers," *International Journal of Electrical Power & Energy Systems*, vol. 118, p. 105768, 2020.

[43] I. Diahovchenko, M. Kolcun, Z. Čonka, V. Savkiv, and R. Mykhailyshyn, "Progress and challenges in smart grids: Distributed generation, smart metering, energy storage and smart loads," *Iranian Journal of Science and Technology, Transactions of Electrical Engineering*, vol. 44, pp. 1319–1333, 2020.

[44] M. Kemal, R. Sanchez, R. Olsen, F. Iov, and H.-P. Schwefel, "On the trade-off between timeliness and accuracy for low voltage distribution system grid monitoring utilizing smart meter data," *International Journal of Electrical Power & Energy Systems*, vol. 121, 2020, Art. no. 106090.

[45] C. Raunig, L. Fickert, C. Obkircher, and G. Achleitner, "Mobile earth fault localization by tracing current injection," in *Proceedings of the 2010 Electric Power Quality and Supply Reliability Conference.* IEEE, 2010, pp. 243–246.

[46] G. Druml, C. Raunig, P. Schegner, and L. Fickert, "Fast selective earth fault localization using the new fast pulse detection method," in *22nd International Conference and Exhibition on Electricity Distribution (CIRED 2013).* IET, 2013, pp. 1–5.

[47] E. Burkhardt, L. Fickert, and F. Jenau, "The "short-term compensation change" to detect earth faults in compensated networks," in *2020 55th International Universities Power Engineering Conference (UPEC)*, 2020, pp. 1–5.

[48] E. Burkhardt, D. Hilbrich, N. Offermann, F. Jenau, and C. Rehtanz, "The "short-term isolated star point grounding" to detect earth faults in compensated networks – the concept," in *2020 55th International Universities Power Engineering Conference (UPEC)*, 2020, pp. 1–5.

[49] J. Altonen and A. Wahlroos, "Performance of modern fault passage indicator concept in compensated MV-networks," in *CIRED Workshop 2016*, 2016, pp. 1–4.

[50] K. Pandakov, H. K. Høidalen, and S. Trætteberg, "An additional criterion for faulty feeder selection during ground faults in compensated distribution networks," *IEEE Transactions on Power Delivery*, vol. 33, no. 6, pp. 2930–2937, 2018.

[51] K. Pandakov, H. K. Hoidalen, and J. I. Marvik, "Fast protection against islanding and unwanted tripping of distributed generation caused by ground faults," in *24th International Conference and Exhibition on Electricity Distribution: CIRED 2017-Proceedings*, 2017, Art. no. 0716.

[52] A. Farughian, L. Kumpulainen, and K. Kauhaniemi, "Review of methodologies for earth fault indication and location in compensated and unearthed MV distribution networks," *Electric Power Systems Research*, vol. 154, pp. 373–380, 2018.

[53] H. Borland, "Earth fault protection enablers for migration to high impedance neutral earthing ant medium voltage," in *16th International Conference on Developments in Power System Protection (DPSP 2022)*. IET, 2022, pp. 123–128.

[54] A. Wixon, P. Newman, and S. Injeti, "Optimising transient earth fault protection in peterson coil and ungrounded systems," in *16th International Conference on Developments in Power System Protection (DPSP 2022)*, vol. 2022, 2022, pp. 345–349.

[55] K. Venkataraman, B. Kirby, H. Ha, and P. Newman, "Transient earth fault detection on compensated earthed system," in *12th IET International Conference on Developments in Power System Protection (DPSP 2014)*, 2014, pp. 1–7.

[56] M. Loos, S. Werben, M. Kereit, and J.-C. Maun, "Fault direction method in compensated network using the zero sequence active energy signal," in *Eurocon 2013*, 2013, pp. 717–723.

[57] E. Burkhardt, D. Hilbrich, N. Offermann, F. Jenau, and C. Rehtanz, "A novel method for earth fault direction detection in compensated networks," in *2019 54th International Universities Power Engineering Conference (UPEC)*, 2019, pp. 1–6.

[58] G. Druml, P. Stachel, W. Leitner, O. Skrbinjek, U. Schmidt, and P. Schegner, "Results from the new method for measuring the earthfault-distance in compensated and isolated networks," in *16th International Conference on Developments in Power System Protection (DPSP 2022)*, vol. 2022, 2022, pp. 13–18.

[59] M. F. Abdel-Fattah and M. Lehtonen, "Transient-based protection as a solution for earth-fault detection in unearthed and compensated neutral medium voltage distribution networks," in *Proceedings of the 2010 Electric Power Quality and Supply Reliability Conference*, 2010, pp. 221–228.

[60] A. Wahlroos, J. Altonen, U. Uggla, and D. Wall, "Application of novel cumulative phasor sum measurement for earth-fault protection in compensated MV-networks," in *22nd International Conference and Exhibition on Electricity Distribution (CIRED 2013)*, 2013, pp. 1–4.

[61] A. Wahlroos and J. Altonen, "Application of novel multi-frequency neutral admittance method into earth-fault protection in compensated MV-networks," in *12th IET International Conference on Developments in Power System Protection (DPSP 2014)*, 2014, pp. 1–6.

[62] M. F. Abdel-Fattah and M. Lehtonen, "A transient fault detection technique with varying fault detection window of earth modes in unearthed MV systems," in *2008 Power Quality and Supply Reliability Conference*, 2008, pp. 181–186.

[63] ——, "A novel transient current-based differential algorithm for earth fault detection in medium voltage distribution networks," *Journal of Energy and Power Engineering*, vol. 6, no. 1, pp. 81–89, 2012.

[64] M. Abdel-Fattah and M. Lehtonen, "Transient algorithm based on earth capacitance estimation for earth-fault detection in medium-voltage networks," *IET Generation, Transmission & Distribution*, vol. 6, no. 2, pp. 161–166, 2012.

[65] G. Druml, A. Kugi, and O. Seifert, "A new directional transient relay for high ohmic faults," in *Proc of 17th International Conference on Electricity Distribution*, 2003.

[66] M. Loos, S. Werben, M. Kereit, and J.-C. Maun, "Detection of single phase earth fault in compensated network with C0 estimation," in *22nd International Conference and Exhibition on Electricity Distribution (CIRED 2013)*, 2013, pp. 1–4.

[67] S. Shi, A. Lei, X. He, S. Mirsaeidi, and X. Dong, "Travelling waves-based fault location scheme for feeders in power distribution network," *The Journal of Engineering*, vol. 2018, no. 15, pp. 1326–1329, 2018.

[68] N. I. Elkalashy, N. A. Sabiha, and M. Lehtonen, "Earth fault distance estimation using active traveling waves in energized-compensated MV networks," *IEEE Transactions on Power Delivery*, vol. 30, no. 2, pp. 836–843, 2015.

[69] C.-C. Zhou, Q. Shu, and X.-Y. Han, "A single-phase earth fault location scheme for distribution feeder on the basis of the difference of zero mode traveling waves," *International Transactions on Electrical Energy Systems*, vol. 27, no. 5, p. e2298, 2017.

[70] N. I. Elkalashy, H. K. Eldeeb, T. A. Kawady, N. G. Tarhuni, M. Lehtonen, A.-M. I. Taalab, and M. A. Elsadd, "Earth fault distance estimation using travelling waves provided with triacs-based reclosing in distribution networks," *IET Renewable Power Generation*, vol. 15, no. 1, pp. 43–57, 2021.

[71] G. Druml, G. Achleitner, W. Leitner, and L. Fickert, "New single-ended earthfault distance estimation for the 110-kV-and 20-kV-compensated network," *Elektrotech. Inftech.*, vol. 135, pp. 567–575, 2018.

[72] E. Bjerkan and T. Venseth, "Locating earth-faults in compensated distribution networks by means of fault indicators," in *International Conference on Power Systems Trasients*, vol. 21, 2005.

[73] A. Farughian, L. Kumpulainen, and K. Kauhaniemi, "Earth fault location using negative sequence currents," *Energies*, vol. 12, no. 19, 2019, Art. no. 3759.

[74] A. Silos-Sanchez, R. Villafafila-Robles, and P. Lloret-Gallego, "Novel fault location algorithm for meshed distribution networks with DERs," *Electric Power Systems Research*, vol. 181, 2020, Art. no. 106182.

[75] J. Altonen, A. Wahlroos, and A. O. D. Automation-Finland, "Advancements in fundamental frequency impedance based earth-fault location in unearthed distribution networks," in *19th International Conference, Electricity Distribution.–CIRED*, 2007, p. 1.

[76] J. Altonen and A. Wahlroos, "Novel algorithm for earth-fault location in compensated MV-networks," in *22nd International Conference and Exhibition on Electricity Distribution (CIRED 2013)*, 2013, pp. 1–4.

[77] M. Lehtonen, "Method for distance estimation of single-phase-to-ground faults in electrical distribution networks with an isolated or compensated neutral," *European Transactions on Electrical Power*, vol. 5, no. 3, pp. 193–198, 1995.

[78] G. Druml, P. Stachel, S. Gebhard, W. Leitner, O. Skrbinjek, G. Achleitner, U. Schmidt, and P. Schegner, "New method for measuring the earthfault-distance in compensated and isolated networks," in *CIRED 2021 - The 26th International Conference and Exhibition on Electricity Distribution*, vol. 2021, 2021, pp. 1416–1419.

[79] C. Claesson and L. Messing, "Fast and selective clearance of earth faults in high impedance earthed networks, with meshed structure," in *2004 Eighth IEE International Conference on Developments in Power System Protection*, vol. 2, 2004, pp. 465–468.

[80] S. Hänninen, M. Lehtonen, and U. Pulkkinen, "A probabilistic method for detection and location of very high resistive earth faults," *Electric Power Systems Research*, vol. 54, no. 3, pp. 199–206, 2000.

[81] A. Fernandes, W. Neves, E. Costa, and M. Cavalcanti, "Transmission line shunt conductance from measurements," *IEEE Transactions on Power Delivery*, vol. 19, no. 2, pp. 722–728, 2004.

[82] H. K. Høidalen, "Ground fault protection in grounded systems," [Lecture notes in course TET4215], 2020.

[83] R. Willheim and M. Waters, *Neutral grounding in high-voltage transmission.* New York: Elsevier, 1956.

[84] M. Abdel-Fattah, M. Lehtonen, R. Millar, and C. Kim, "The impact of the distribution network type and configuration on the transient behavior of the fault and neutral points during earth faults," in *The International Conference on Power Systems Transients (IPST2011)*, 2011.

[85] H. K. Høidalen, L. Prikler, and F. Peñaloza, *ATPDRAW version 7.3 for windows - users' manual*, 2021.

[86] "Matlab homepage." [Online]. Available: https://se.mathworks.com/products/matlab.html

[87] SINTEF Energi AS, "Planleggingsbok for kraftnett: Tekniske data," (in Norwegian), Trondheim, Norway, 2010.

[88] NEXANS, "Utility and power cables: Norwegian edition," https://www.nexans.no/en/support-toolspage/support/online-catalogues.html.

[89] J. D. Glover, S. M. S. Sarma, and T. J. Overbye, *Power System Analysis and Design.* Stamford, CT, USA: Cengage Learning, 2012, 5th ed.

[90] REN AS, "RENblad 7505: Retningslinjer for systemjording med spole for 12-24 kv nett (in Norwegian)," 2020, ver. 1.2.

[91] B. Gustavsen, J. Martinez, and D. Durbak, "Parameter determination for modeling system transients-part II: Insulated cables," *IEEE Transactions on Power Delivery*, vol. 20, no. 3, pp. 2045–2050, 2005.

[92] *Short-circuit currents in three-phase a.c. systems - Part 2: Data of electrical equipment for short-circuit current calculations*, IEC TR 60909-2:2008, 2008.

[93] SINTEF, "Smart grid laboratory," https://www.sintef.no/en/all-laboratories/smartgridlaboratory/, accessed Jun. 25, 2023.

[94] Hitachi Energy, "Average Power Transient Earth Fault Protection, APPTEF," in *Line differential protection RED670 Version 2.2 ANSI: Technical manual (Doc. ID: 1MRK 505 377-UUS)*. Västerås, Sweden: Hitachi Energy Sweden AB, 2022, pp. 679–695.

[95] Siemens, "Sensitive Ground-Fault Detection: Directional Transient Ground-Fault Stage," in *SIPROTEC 5: Generator Protection 7UM85 (Doc. ID. C53000-G5040-C027-9)*. Nuremberg, Germany: Siemens AG, 2021, pp. 959–967.

[96] J. Lorenc, J. Andruszkiewicz, B. Olejnik, B. Staszak, and P. Balcerek, "Earth fault detection and isolation system for MV network," in *2015 Modern Electric Power Systems (MEPS)*, 2015, pp. 1–7.

[97] J. Lorenc, A. Kwapisz, and K. Musierowicz, "Efficiency of admitance relays during faults with high fault resistance values in MV networks," in *2005 IEEE Russia Power Tech*, 2005, pp. 1–5.

[98] J. G. Balchen, T. Andresen, and B. A. Foss, *Reguleringsteknikk (in Norwegian)*. Trondheim: Institutt for teknisk kybernetikk, NTNU, 2016.

[99] Norwegian University of Science and Technology, "National smart grid laboratory," https://www.ntnu.edu/smartgrid, accessed Jun. 25, 2023.

[100] D. R. Gurusinghe, D. Ouellette, and A. D. Rajapakse, "Implementation of smart DFT-based PMU model in the real-time digital simulator," in *The International Conference on Power Systems Transients (IPST)*, 2017.

[101] T.-C. Yu, "Influences of frequency-dependent shunt admittances on underground cable systems," *IEEE Transactions on Power Delivery*, vol. 23, no. 4, pp. 2385–2391, 2008.

[102] O. Breien and I. Johansen, "Attenuation of travelling waves in single-phase high-voltage cables," in *Proceedings of the Institution of Electrical Engineers*, vol. 118, no. 6. IET, 1971, pp. 787–793.

Appendices

Appendix A

Papers

Paper I

T. Treider, B. Gustavsen and H. K. Høidalen, "Analysis of transient earth fault relays in meshed resonant grounded networks", *16th International Conference on Developments in Power System Protection (DPSP 2022)*, Hybrid Conference, Newcastle, UK, 2022, pp. 350-355.

ANALYSIS OF TRANSIENT EARTH FAULT RELAYS IN MESHED RESONANT GROUNDED NETWORKS

Thomas Treider[1*], Bjørn Gustavsen[1], Hans K Høidalen[1]

[1]Department of Electric Power Engineering, Norwegian University of Science and Technology, Trondheim, Norway
**thomas.treider@ntnu.no*

Keywords: TRANSIENT EARTH-FAULT RELAYS, COMPENSATED NETWORKS

Abstract

This paper discusses issues related to the application of transient earth fault relays in meshed resonance grounded networks. Although best suited for application in radial networks, the transient earth fault relays still have their use as earth fault detectors in meshed networks. In practice, most networks are equipped with a number of relays of different models from several manufacturers, and due to the gradual upgrade of relays in the network, system operators will still have to deal with a mixture of different relays in their network. This paper studies potential issues for transient earth fault relays in meshed networks through theoretical analysis of important transient protection principles, and simulations are used to confirm and illustrate important findings. The main issues observed are low residual current magnitude, polarity reversal and impact of distributed arc suppression coils. Handling of contradictory relay responses is discussed and mitigating measures for network operators are suggested.

1 Introduction

Earth faults in compensated networks is a challenging fault type for protection and location which is yet to be solved completely. Transient earth fault relays (TEFR) usually encompass a wide variety of relays all relying to some degree on a fixed relationship between the zero-sequence current and voltage measured at the network feeders in the first few milliseconds after a fault occurs [1]. Manufacturers continuously improve and update their products, and although significant improvements have been made by modern relays, legacy relays are still widely used. A system operator can in practice not be expected to replace all the earth fault relays in the network on a regular basis. Rather, it is common for relays to be replaced at the end of their expected economic lifetime, typically when a part of the network is replaced or when a new part is added. Relays are therefore utilized for several years before they are gradually replaced, resulting in a network with a mixture of different relay models, and thereby also different operating principles.

As transient earth fault relays are generally not considered by network operators to be reliable enough for use as protection in meshed networks, they are usually used as indicators, helping the network operator to locate the correct faulted section of the network which may then be disconnected. Knowing which relays to trust and which to discard in the case of contradictory responses is therefore highly relevant.

In this paper, challenges related to applying transient earth fault relays in meshed networks are presented and discussed. Important principles of transient relays are presented, and challenges are explained and further illustrated through simulations. The protection principles considered in this paper are implemented in various forms in several commercially available and widely used relays from several manufacturers.

The paper is organized as follows. Section 2 provides background on two common protection principles found in TEFRs, and on the use of TEFRs in meshed networks. Section 3 provides a detailed theoretical analysis of earth fault transients, and important characteristics of meshed networks are discussed. Challenges related to applying these in meshed networks are explained and illustrated in detail in section 4, and conclusions are provided in section 5.

2 Transient Earth Fault Relays

In this paper, the term TEFR is taken to include directional earth fault relays utilizing the transients associated with earth faults in compensated networks. This includes both fundamental component transients as well as higher frequency transients.

2.1 Transient Protection Principles

2.1.1 Polarity Principle: A fundamental approach to achieve directional earth fault indication is to consider the polarity of the current and voltage transients immediately following an earth fault inception [2,3]. Depending on the sign convention used, the polarity of the residual current transient and the residual voltage transient will be either identical or opposite depending on whether the fault is in the forward or reverse direction. This principle is easy to derive from a radial network structure with clearly defined forward and reverse directions, but it can in many cases work fine in meshed systems as well. This principle can be found in several relays by different manufacturers, although the specific implementation may vary with respect to signal processing, filtering and transient detection logic. Usually, a current pickup threshold is the main setting required if tripping is not desired, although some relays allow more detailed tuning of the logic used for detecting transients.

2.1.2 Transient Charging Energy: In order to make the polarity determination more secure, an alternative approach is to integrate measurements over time [4]. This avoids accidental misoperation due to fluctuations and unwanted frequencies in the measured quantities. It also improves the performance in cases where the initial transient magnitude is very low, cases that may be missed by relays based on the first peak only. One specific approach utilized by modern relays is the use of active zero sequence energy [5]. This approach is based on utilizing the charging process, in which active energy must be supplied by the faulty feeder and consumed by the healthy feeders. If this energy can be measured it should have opposite polarity on healthy and faulty feeders. This should also allow for directionality as the power flow must emanate from the fault point, even in a meshed network.

Although this principle should give a very sensitive ground fault detection compared to the polarity principle, it too is dependent on sufficient current and voltage magnitude to function. As integration is applied, determining the correct starting and stopping points becomes very important. The settings must also be sensitive enough to trip before the fault disappears naturally. However, too sensitive settings can cause unwanted trips due to imperfections in the filtering of operational zero sequence currents. The integration must also be stopped at some point, and if the logic fails to detect a fault the discharging process after a fault has disappeared can cause the measured energy to have the wrong polarity. Compared to the polarity principle, this approach requires a more sophisticated implementation in order to be reliable.

2.2 Implementation in Norway

The use of directional earth fault relays is demanded by Norwegian regulations [6]. These regulations apply to networks with a nominal voltage level >33 kV, and they will therefore in practice encompass the resonance grounded HV regional networks at 45 kV, 66 kV, 110 kV and 132 kV. These networks are intermediate levels between the 300 kV and 420 kV transmission system and the MV distribution systems, and their topologies differ from the radial topology found in distribution networks. The requirements for earth fault directionality apply to power lines (either overhead, cables or a mixture of the two) and they therefore in practice mandate that all lines must be equipped with a relay at both ends. The only realistic option to achieve directionality in these networks have been the use of TEFRs. However, as faults must be located within two hours [7], and as the relays are not considered reliable by operators, they are utilized as detectors rather than automatic protection. System operators can then gather input from all relays, display them graphically and use this as aid for locating the faulty section of the network.

3 Earth Fault Transients

3.1 The Charging Transient

Note that the equations in this section apply to the charging transient frequency only. Fundamental frequency components are discussed separately in section 3.2.

3.1.1 Origin of the Charging Transient: The charging transient is one of the earth fault transient components, and it stems from the charging of the healthy phase capacitances. In this process the charging current is commonly described as flowing from the faulted point along the faulted phase until it reaches the main transformer neutral. Here, it is divided in two equal parts and returning to ground via the healthy phase capacitances. In this path the transformer leakage inductance and the faulty phase series inductance make up to main inductance *L*, whereas the healthy phase capacitances to ground and to the faulted phase make up the main capacitance *C*. The charging current thus flows in some equivalent LC-circuit, resulting in the frequency given in (1). Different versions of this approximation are available in the literature [8,9], differing slightly in how the equivalent inductance and capacitance of the circuit are approximated. The frequency of this component is described as ranging from 100-2000 Hz [4].

$$f_{ch} \approx \frac{1}{2\pi\sqrt{LC}} \tag{1}$$

The direction of the transient in this model is a matter of convention – it is the direction in the faulty phase relative to the healthy phases which is of significance. The charging current measured in the faulty phase will be 180 degrees out of phase with the current measured in the two healthy phases. The resistance of the equivalent charging transient circuit is also of some importance, although not in determining the frequency. The resistance of the system, herein also the fault resistance, will primarily provide damping of the charging transient.

3.1.2 Measuring the Charging Transient: Although the charging transient is present with the largest magnitude in the faulted phase, the monitoring of three separate fault loops at every relay location in the network is impractical. Furthermore, in typical distribution networks the capacitance of each feeder is relatively much smaller than the total capacitance of the network. The fault current flowing towards the bus on the faulted feeder will therefore be much greater than the small current returning to ground through the healthy phases on the same feeder. Using the residual current ($3i_0$) for obtaining the charging transient is thus a practical solution which only requires a single measurement.

Fig. 1 illustrates the situation, where a simple radial network with a single transformer is considered. If the loads on the radials are sufficiently low, the load impedances will be large enough so that the entire charging transient current i_{ch} can be assumed to flow from the faulted point towards the transformer and returning to ground through the healthy phase capacitances. The charging frequency component of the residual current measured on the faulty feeder, in this case feeder 1, will be

$$3i_{0,1} = i_{ch}\left(\frac{C_1}{C_T} - 1\right) \tag{2}$$

whereas it on any healthy feeder *k* will be

$$3i_{0,k} = i_{ch}\left(\frac{C_k}{C_T}\right) \tag{3}$$

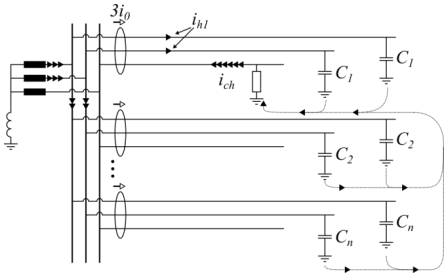

Fig. 1 Charging transient in a radial network

In (2) and (3), the capacitances C_k is the per phase capacitance to ground for each of the healthy phases on feeder k, and $C_T = C_1 + C_2 + \ldots + C_n$ is the total per phase capacitance to ground in each healthy phase of the n feeders in the network. The fraction C_k / C_T describes the portion of the charging transient returning in that particular feeder. Equation (2) shows that as the relative size of the faulty feeder compared to the background network increases – i.e., in terms of capacitance - the measured charging frequency component of the residual current is reduced. In the extreme case of a single feeder network, the charging frequency component of the residual current is zero. This will not be the case in a real network, and a residual current will therefore always be available for extracting the charging transient.

In a meshed network, the situation is different. Consider the same network as before, where feeders 1 and 2 have been connected in a ring. They are renamed line A and line B here for convenience, as the ring itself can be considered a feeder.

Consider a fault taking place somewhere on line A in Fig. 2. The charging transient will have two alternative paths along the faulted phase to the main transformer. The division of i_{ch} is based on the impedance of the faulted phase, and the ratio can be obtained by applying the current division principle. This ratio is defined as R, such that the current Ri_{ch} flows along line A, whereas $(1\text{-}R)i_{ch}$ flows along line B. The charging current reaches the transformer neutral where it is divided in two halves, assuming the two healthy phases to be identical. The current i_{hR} returns through both the healthy phases on the ring and is described by (4).

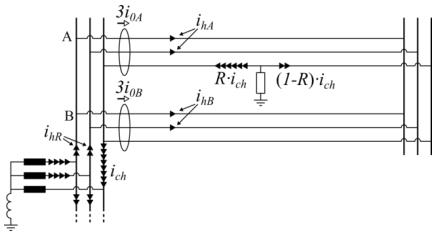

Fig. 2 Charging transient in a meshed network

$$i_{hR} = \frac{1}{2} i_{ch} \frac{C_R}{C_T} \tag{4}$$

In (4), C_R is the combined per phase capacitance to ground of lines A and B. Depending on the line parameters of the two lines in the ring this current will divide itself among line A and B. Let this be described by the factor m, such that the currents

$$\begin{aligned} i_{hA} &= m\, i_{hR} \\ i_{hB} &= (1-m) i_{hR} \end{aligned} \tag{5}$$

flows onto line A and line B, respectively. In the case of a homogeneous ring, the division of i_{hR} will be equal among the two lines (i.e., m=0.5). In practice, m will not be 0.5, but the important thing to consider is that it is fixed with respect to fault locations. The charging frequency component of the residual current measured on lines A and B can be written as

$$\begin{aligned} 3i_{0A} &= 2i_{hA} - Ri_{ch} \\ 3i_{0B} &= 2i_{hB} - (1-R) i_{ch} \end{aligned} \tag{6}$$

Combining (4), (5) and (6), (7) is obtained.

$$\begin{aligned} 3i_{0A} &= i_{ch} \left(m \frac{C_R}{C_T} - R \right) \\ 3i_{0B} &= i_{ch} \left((1-m) \frac{C_R}{C_T} - (1-R) \right) \end{aligned} \tag{7}$$

Equation (7) shows that the residual currents measured on lines A and B may become zero at certain fault locations, even in a network with several feeders. In the special case of a single ring network, for instance in the case of a two-feeder network operated as a single ring, both $3i_{0A}$ and $3i_{0B}$ can become zero for the same fault location.

The point where either $3i_{0A}$ or $3i_{0B}$ become zero depends on the relative size of the ring compared to the background network and will occur for $3i_{0A}$ when R = mC_R/C_T. Therefore, there will be fault locations on the ring for which either $3i_{0A}$ or $3i_{0B}$ will become difficult to measure. Furthermore, if the ring is relatively large, this point is moved closer to the middle of the ring, and it can thus be imagined that both currents will be difficult to measure at certain fault points.

Considering that the ratio R will vary between 0 and 1 for different fault locations, these points represent zero-crossings for which $3i_{0A}$ and $3i_{0B}$ will change polarity. For instance, if the current $3i_{0A}$ is considered, it will become zero at R = mC_R/C_T. If m is assumed 0.5 for simplicity, and the relative size of the ring mC_R/C_T = 0.2, then R = 0.1. This means that for such a network, the residual current measured on line A will have "wrong" polarity for faults on 10 % of the ring.

A solution to this issue could be to consider the phase currents as sources for extracting the charging transient. Although the residual current has the benefit of not being impacted by load currents, this concern is not relevant at the charging transient frequency anyway. This will however require monitoring each phase separately, and three times as many measurements compared to the conventional residual current solution.

3.2 Fundamental Frequency Transients

3.2.1 Origin of the Fundamental Frequency Transients: Although the charging transient is the typical transient utilized by conventional transient based relays, the fundamental

component can also be used. The charging transient energy is reduced for high impedance faults, and the fundamental component transients are used for added sensitivity.

The behaviour of the neutral voltage transient can be estimated by considering the resonant circuit comprised of the arc suppression coil (ASC), the system capacitance and the fault resistance [4]. Solving the resulting RLC-circuit shows that the neutral voltage will be on the form given in (8).

$$\begin{aligned} v_n(t) &= v_{n,ss}(t) + v_{n,tr}(t) \\ &= A\sin(\omega t + \varphi) + B\cos(\omega t + \varphi) + Ce^{-\tau_1 t} \\ &\quad + De^{-\tau_2 t} \end{aligned} \tag{8}$$

In (8), the subscripts "ss" and "tr" signify steady state and transient parts, respectively. The fundamental frequency zero sequence current transients on each feeder k become as given in (9), where the last term only appears on the faulty feeder.

$$3i_{0,k,tr}(t) = 3C_k \frac{\partial}{\partial t} v_{n,tr}(t) + v_{n,tr}(t) \frac{1}{R_f} \tag{9}$$

The characteristics of these transients are dependent on the parameters τ_1 and τ_2, which in turn are dependent on the fault resistance and the compensation degree of the system. For low impedance faults the oscillations become over-damped, and as the fault resistance increases the system becomes under-damped, leading to an oscillatory behaviour of the transient terms. The neutral voltage $v_n(t)$ and the transient terms $v_{n,tr}(t)$ are shown for these three cases in Fig. 3.

Measured residual currents and voltage can then be used to compute the zero-sequence power and energy. Reference [4] suggested for instance to monitor the parameter $e_0^a(t)$ defined in equation (10).

$$e_0^a(t) = \int_{t_0}^{t} p_0^a(\tau) d\tau \tag{10}$$

In (10), $p_0^a(t)$ is the instantaneous zero-sequence power averaged over one period of the fundamental frequency.

3.2.2 Measuring the Fundamental Frequency Transients: The fundamental frequency of the residual current is also susceptible to variations in magnitude for varying fault location, although any issues with zero magnitude are likely only theoretical. Furthermore, using the residual current to obtain transients is required to avoid unwanted impacts of load currents.

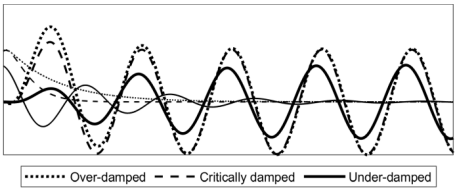

Fig. 3 Voltage $v_n(t)$ transient in over-, under- and critically damped cases. Thin lines show transient components $v_{n,tr}(t)$.

3.3 Properties of Meshed Networks

The classical distribution network is radial in structure. The transient based protection that is available have generally been designed based on principles deduced from radial networks. These same principles can in many situations be applied directly in a meshed system, although some key differences should be considered.

3.3.1 Circulating Zero-sequence Currents: Circulating zero sequence currents is a well-known issue for protection that have been described in some detail [10,11]. The source of these circulating currents is the coupling of the three sequence systems due to network asymmetry, which during loading induces currents in the zero-sequence system. As the load currents are fundamental frequency currents, so are the circulating zero sequence currents. Protection based on transient fundamental frequency zero sequence energy are susceptible to this effect, and the circulating currents must be accounted for. Reference [4] suggests using a sliding window approach where the zero sequence current is stored for 3 fundamental periods. This historical value is then subtracted from the instantaneous measurements, thus eliminating the circulating current from the measurements.

3.3.2: Distributed ASCs: The number of power transformers and ASCs in the network also introduces complications. In the previous section, for instance, the charging transient was explained and described as always flowing from the fault to the main transformer. Although load transformers are always present, the impedance of the loads does not permit any significant portion of the charging transient to pass. If a system is equipped with several power transformers, as may well be the case in large distribution networks and regional networks, the path of the charging transient is not apparent. The division of the charging transient current becomes challenging to predict, and the polarity of the measured residual current can change, as described in principle in the previous section. The fundamental component flowing between the fault and the ASC can also take several different paths as it divides itself among the ASCs in the network.

4 Challenges and Problems

A model as shown in Fig. 4 is implemented in ATPDraw to generate the results in this section. A feeder C can be connected in parallel via a remote end switch, and the compensation can be distributed between ASCs P1 and P2. See Table 1 for network data. Faults occur in phase *a.*

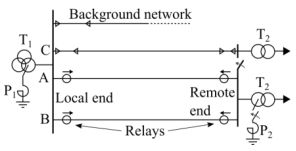

System voltage: 132 kV

	OH-line	Cable
Line A	41 km	-
Line B	26 km	-
Line C	30 km	4.5 km
Bck.gr	30 km	8 km

Fig. 4 Network model nr. 1

Table 1 Test Network Parameters

Simulation Data	
OH-line	Data per km: R=0.074 Ω, X=0.39 Ω, C=9.47 nF, R_0=0.401 Ω, X_0=0.87 Ω, C_0=7.055 nF, G_0=44.33 nS. Asymmetry: 2% and 4% are added to C_0 in phases *a* and *c*, respectively.
Cable	Data per km: R=0.037 Ω, X=0.17 Ω, C_0=0.2 µF. Asymmetry: 1.5% and 3% are added to C_0 in phases *b* and *c*, respectively.
Loads	3-phase 1 (low) or 10 (high) MVA constant impedance loads. Power factor 0.9.
Transformers	T_1: 250/250/80 MVA 400/132/12.5 kV Yyd1. T_2: 200 MVA 132/22 kV Yd11.
ASC	5% over-compensated. Parallel resistors Rp=50 k Ω represent losses in P1 and P2.
Other	Sample rate: 8 kHz. Software: ATPDraw version 7.2p11.

4.1 Sensitivity Issues

Section 3.1.2 showed that the charging transient component in the residual current can become zero at certain fault locations. The simulated currents were analysed using an FFT over a 200 ms window, and the magnitude $|I(\omega_{ch})|$ of the frequency ω_{ch} corresponding to the charging transient was plotted as function of fault location. Fig. 5 shows the results, where the distance on the x-axis is measured along the entire ring (lines A and B) starting from terminal A. Both 0 p.u. and 1 p.u. correspond to the local end busbar, and 0.61 p.u. is the remote end busbar. As can be seen from Fig. 4, the residual current measured at either terminal A or B becomes zero for faults inside the ring. The faulty phase current i_{ph} is included for comparison, which only becomes zero for faults at the main busbar.

4.2 Polarity and the Concept of Forward Faults

The points in Fig. 5 for which the residual current become zero also signify polarity changes of the charging transient, here referred to as crossover points. Fig. 6 shows the waveforms of faults at two locations before and after such a crossover point where the magnitude of the residual current is the same. However, the polarity of the current is now swapped. This phenomenon thus illustrates how and when the fault direction indication made by certain relays will change from forward to reverse, and it is an inherent property of meshed networks. It should be ensured that no line in a mesh becomes so much longer than the surrounding lines that this switchover can take place on the protected line itself.

4.3 Network Load and Distributed ASCs

Fig. 7 shows how network loading, impedance asymmetry and distributed ASCs can affect the zero-sequence energy. All three faults are in the same location on line B, and energy is computed for the remote end relay on line A. Measurements

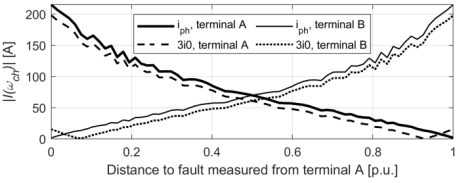

Fig. 5 FFT-magnitude $|I(\omega_{ch})|$ of charging transient component in $3i_0$ and faulty phase current i_{ph} measured at the local end of lines A and B, as function of fault location

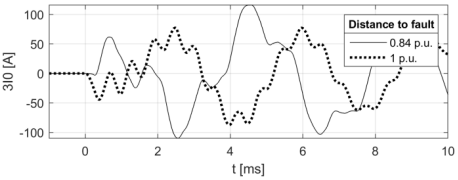

Fig. 6 Filtered $3i_0$ measured at local end of line A for faults located at 0.84p.u. and 1 p.u.

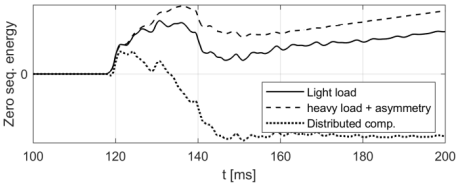

Fig. 7 Zero sequence energy for same fault location in light loading, heavy loading with series impedance asymmetry, and distributed compensation

are filtered to remove any offsets, and a sliding window approach with 100 ms window is being used to suppress any circulating currents. The solid line shows the energy computed with a low network load. The dashed line shows the energy obtained when adding an asymmetry of 2% to the phase *b* impedance and increasing the load. Despite filtering and suppression of any circulating currents, the energy is affected. The dotted line shows the third case in which the compensation is divided equally between P1 and P2. The active power flow towards these ASCs has a significant impact on the zero-sequence energy polarity in this case.

4.4 Network Re-configurations ad Universal Settings

Connecting Line C in parallel at the remote end bus was not found to have a considerable effect for the faults studied in network nr. 1. In a second network model as shown in Fig. 8, network re-configurations were found to be important. Three faults were applied on the line AB in varying distance from A, with and without the line BE connected. The residual currents seen by the relay in A facing B are shown in Fig. 9. The figure shows that faults close to A appear with minor differences, whereas faults close to B are now very difficult to measure.

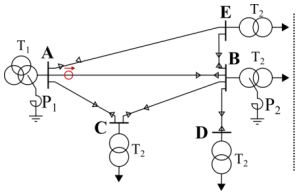

System voltage: 132 kV

	OH-line	Cable
Line AB	50 km	2 km
Line AC	30 km	2 km
Line AE	40 km	4 km
Line BC	40 km	2 km
Line BD	10 km	2 km
Line BE	4 km	9 km

Fig. 8 Network model nr. 2.

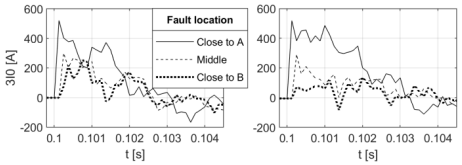

Fig. 9 Residual current $3i_0$ measured in A on line AB without (left) and with (right) line BE connected.

This particular case was tested on a commonly used TEFR in the laboratory. The relay in A would not see all faults on the line AB if the settings recommended by the relay manual were used – not even if both network configurations had been considered in advance. The fact that this issue was not reproduced in the network in Fig. 1 also suggests that it is challenging to predict how reconfiguring the network will affect the relays. Using simulations of different network configurations as aid in setting the individual relays would then be required.

5 Conclusion

This paper has explained, illustrated, and discussed some of the challenges related to applying transient earth fault relays in meshed networks. The main problem discussed in the paper is that of insufficient residual current magnitude for faults in specific locations in a loop. Faults occurring close to these locations may also pose problems as the polarity of the residual current changes, leading to unexpected fault direction indication. It is also shown that zero-sequence energy computations can be affected in some locations, and that properties of meshed networks such as distributed ASCs can have an impact on this energy. Correct thresholds for this protection principle are then very important for avoiding misoperation and erroneous fault direction indication.

Relays that are part of a mesh are inherently susceptible to lack of a meaningful forward/reverse direction, and contradictory responses from these are to be expected at times. This can be acceptable on healthy lines as long as both relays overseeing the line do not signal forward at the same time. It should be ensured that the two relays protecting a line will have sufficient sensitivity to detect all faults on the protected line in all network configurations, and that the polarity change in crossover points do not occur on the protected line itself.

It is concluded that the issues investigated here are inherent to meshed topologies, but they can be predicted in advance. Special considerations can then be made for problematic areas, for instance through different relay settings when supported by the IEDs. Adjusting the setting of relays at different locations based on probable network configurations could be considered to mitigate some of the problems discussed in this paper.

Future work will focus on testing relays in a laboratory setup.

5 Acknowledgements

The work was funded by the Norwegian Research Council project ProDig (295034/E20).

6 References

[1] Zhang, X., Xu, B., Pan, Z., et al: 'Study on single-phase earthed faulty feeder selection methods in non-solidly grounded systems'. 2008 Third International Conference on Electric Utility Deregulation and Restructuring and Power Technologies, 2008, pp. 1836-1840

[2] Siemens AG: 'Siprotec 7SN600 Transient earth-fault relay: Instruction Manual', Version Oct. 2011, (2011)

[3] ABB: 'Transient measuring direction relay and earth-fault protection: RXPG (1MRK 509 012-BEN Revision: B)', 2013

[4] Loos, M.: ' Single Phase to Ground Fault Detection and Location in Compensated Network'. PhD thesis, Université Libre de Bruxelles, 2014

[5] Siemens AG: 'Sensitive, digital transient ground fault function (brochure)', 2016

[6] 'Nasjonal veileder for funksjonskrav i kraftsystemet' (in Norwegian), https://www.statnett.no/globalassets/for-aktorer-i-kraftsystemet/systemansvaret/retningslinjer-fos/nvf-2021---nasjonal-veileder-for-funksjonskrav-i-kraftsystemet.pdf, accessed 1 September 2021

[7] 'Veiledning til forskrift om elektriske forsyningsanlegg' (in Norwegian), https://www.dsb.no/lover/elektriske-anlegg-og-elektrisk-utstyr/veiledning-til-forskrift/veiledning-til-forskrift-om-elektriske-forsyningsanlegg, accessed 1 September 2021

[8] Willheim, R., Waters, M.: 'Neutral grounding in high-voltage transmission' (Elsevier, 1956)

[9] Welfonder, T. 'Localisation de défauts monophasés dans les réseaux de distribution à neutre compensé.' PhD thesis, Institut National Polytechnique de Grenoble (INPG), 1998

[10] Loos, M., Werben, S., Maun, J. C.: 'Circulating currents in closed loop structure, a new problematic in distribution networks'. 2012 IEEE Power and Energy Society General Meeting, 2006, pp. 1–7

[11] Druml, G., Klein, R.-W., Seifert, O.: 'New adaptive algorithm for detecting low- and high ohmic faults in meshed networks'. CIRED 2009 - The 20th International Conference and Exhibition on Electricity Distribution, Prague, Czech Republic, June 2009, pp. 1–5

Paper II

T. Treider and H. K. Høidalen, "Polarity crossover regions of transient earth fault relays in non-radial resonant grounded networks," *Electric Power Systems Research*, vol. 223, 2023, Art. no. 109598.

[1] https://creativecommons.org/licenses/by/4.0/

Electric Power Systems Research 223 (2023) 109598

Contents lists available at ScienceDirect

Electric Power Systems Research

journal homepage: www.elsevier.com/locate/epsr

Polarity crossover regions of transient earth fault relays in non-radial resonant grounded networks☆,☆☆

Thomas Treider *, Hans Kristian Høidalen

Department of Electric Power Engineering, Norwegian University of Science and Technology, Trondheim, Norway

ARTICLE INFO

Keywords:
Earth fault protection
Transients
Resonant grounding
Meshed networks
Laboratory testing

ABSTRACT

Transient-based earth fault protection is widely used in all types of resonant grounded networks, and though the operating principles of the commonly available relays are usually derived from radial networks, manufacturers claim applicability in meshed networks as well. This paper utilizes a laboratory setup to study the directional indication of four transient earth fault relays in non-radial resonant grounded networks. Two of the relays considered are widely used analog single-purpose transient earth fault relays, whereas the other two relays represent two transient-based earth fault functions found in modern protective devices. The paper verifies the location of crossover points according to the presented theory, i.e. fault locations for which relays transition between seeing faults as forward and reverse faults, and demonstrates the viability of the proposed theoretical analysis of crossover points. However, presented analytical formulae only describe the two analog relays accurately, whereas the two modern relays have a more complex operating principle which requires further analysis to quantify properly. Finally, it is shown that relay misoperation which is not easily fixed by communication between relays can occur, and it is suggested that network operators conduct detailed relay coordination when applying transient earth fault relays instead of relying on standardized settings.

1. Introduction

Throughout Europe and Asia, MV and HV distribution systems are commonly resonant grounded. In this system earthing scheme, an inductor is placed between the transformer neutral and ground in one or several transformers in the network. These inductors are often referred to as Petersen coils, though Arc Suppression Coils (ASCs) is a more precise general term. During single phase faults, usually referred to as earth faults or ground faults in these systems, the capacitive part of the fault current is largely canceled out by the inductive current introduced by the ASCs in the system. As a result, with correctly tuned ASCs, the fault current can be brought to a minimum, leading to self-extinguishing arcing faults. This property leads to automatic clearing of many single phase faults, and due to the small fault current the permanent earth faults can be allowed to be present in the system for longer time periods and thus giving network operators time to move loads to other feeders and limit the number of affected customers. Resonant grounded networks thus have few interruptions and a high quality of supply, but the low fault current level also introduces significant challenges for protection systems. As the fault current can be in the same order of magnitude as the normal load currents, or even smaller, conventional over-current protection or distance protection cannot be applied.

In distribution systems, which have traditionally been radially operated, the earth fault protection system is often based on zero-sequence currents and voltage. As no reliable distance element has existed for earth faults in resonant grounded systems, the protection system is often limited to determining the faulty feeder using directional elements. Measuring the current and voltage, a directional element can be realized in a number of ways to identify the faulty feeder [1]. Some network operators utilize several measurement points along the feeder to narrow down the faulty section using fault passage indicators [2], but precise fault location is still a much more challenging exercise in these networks. Furthermore, to get reliable operation of the protection systems, a resistor is often required to be connected in parallel with the ASC to produce a significantly large watt-metric component for the protection systems to detect [3].

Quite a few different protection principles based on the relationship between voltage and currents in the zero-sequence system have been devised, but they are largely based on the assumption of a radial system for the directional element to work properly [4–8]. Some recent works

☆ The work was funded by the Norwegian Research Council project ProDig (295034/E20).
☆☆ Paper submitted to the International Conference on Power Systems Transients (IPST2023) in Thessaloniki, Greece, June 12–15, 2023.
* Corresponding author.
E-mail addresses: thomas.treider@ntnu.no (T. Treider), hans.hoidalen@ntnu.no (H.K. Høidalen).

https://doi.org/10.1016/j.epsr.2023.109598
Received 9 December 2022; Received in revised form 2 March 2023; Accepted 21 June 2023
Available online 1 July 2023

have presented novel algorithms and techniques which may be suited for meshed networks as well. The EDIST-method [9,10] introduces a transient-based distance element, remedying an important limitation often seen in transient-based protection which is the lack of any information pertaining to distance. In Refs. [11,12] a transient principle is proposed to serve as a directional element, and a communication system is used to implement a permissive overreach transfer trip scheme in order to ensure correct operation in a meshed network.

In the future, more distribution networks may be operated with some degree of meshing or ring-connection of feeders to increase the quality of supply and better integrate distributed generation [13]. Furthermore, the regional networks, the intermediate network level sitting between the distribution system and the transmission system, is often resonant grounded. These networks resemble transmission systems in terms of their topology, with larger meshes and often several power transformers and ASCs present in the system. In these networks the only option for directional earth fault indication has been what is broadly referred to as transient earth fault protection. Traditionally, this term has referred to a few analog relays based on a similar principle of operation utilizing the high frequency transients that occurs during earth faults [14,15]. In recent years modern protective relays have become equipped with more advanced functions based on these transients, such as [16,17], so the transient protection category is now more diverse.

Although many of the commonly used transient-based earth fault relays, hereafter referred to as Transient Earth Fault Relays (TEFRs), are said to be valid in non-radial networks [14–17], it is not well established whether or not they have some inherent limitations in such networks compared to radially operated networks. The availability of relay testing in the scientific literature is limited mainly to sparse results from tests conducted by relay manufacturers, and independent research papers studying their performance in detail is lacking. Furthermore, the TEFR-category is actually quite diverse, and it is not unlikely that previous generations of relays with a less reliable performance have been allowed to define a broad category of relays.

This paper therefore has two primary objectives. The first is to identify and investigate any inherent limitations for network operators to be aware of when applying TEFRs in non-radial networks. To do this, the paper focuses on studying the fault direction indication in non-radial networks and the transition between forward and reverse faults. Secondly, the paper aims to identify any variation in the responses of different TEFRs to determine how the various operating principles differ from each other. The paper will build on the theoretical analysis performed in [18] and investigate the performance of four different relays. These four relays are then tested in a laboratory setup with a variation of network configurations and parameters.

The rest of the paper is organized as follows. Section 2 briefly explains the theoretical foundation for the earth fault transients and discusses some potential issues related to sensitivity and polarity. Based on this theory, formulae are provided which predict the fault locations for which the relays will transition between forward and reverse fault indication. Section 3 describes the simulation models and the laboratory setup used to test the relays, whereas the results are discussed and analyzed in detail in Section 4. Section 5 discusses the impact of various parameters in the tests, and the validity and limitations of the laboratory tests are also discussed in detail. Finally, conclusions and recommendations for future work is provided in Section 6.

2. Earth fault transients in non-radial networks

A detailed presentation of important theoretical concepts was given in Ref. [18], but the key concepts required to discuss the results in this paper are repeated in this section. This section primarily deals with the earth fault transients in a non-radial system, and for more details on the charging transient and its behavior in radial networks interested readers are referred to [18] for further reading.

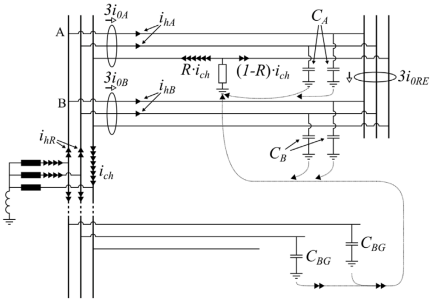

Fig. 1. Charging transient in a ring-operated network.

2.1. The charging transient

Note that the equations derived in this section apply at the charging transient frequency only.

During an earth fault in a network with isolated or compensated grounding, the phase-ground voltages of the two healthy phases increase. This charging process is associated with what is commonly referred to as the charging transient, which is described as a current flowing from the faulted point along the faulted phase until it reaches the main transformer neutral. Here, it is divided in two equal parts and returning to the fault point via the healthy phase capacitances. In this path the transformer leakage inductance and the faulty phase series inductance make up to main inductance L_{eq}, whereas the healthy phase capacitances to ground and to the faulted phase make up the main capacitance C_{eq}. The charging current thus flows in some equivalent LC-circuit with a natural frequency given by (1).

$$f = \frac{1}{2\pi\sqrt{L_{eq}C_{eq}}} \tag{1}$$

Different versions of this model are available in the literature, differing slightly from each other in how the equivalent inductance L_{eq} and capacitance C_{eq} of the circuit are approximated [9,19,20].

Consider a fault taking place somewhere on line A in Fig. 1. The charging transient i_{ch} flows along the faulted phase to the transformer neutral and returns to ground via the healthy phase capacitances. As the two lines A and B are connected to form a ring, the charging transient will have two alternative paths along the faulted phase to the main transformer. The division of i_{ch} is based on the impedance of the faulted phase, and the ratio can be obtained by applying the current division principle. This ratio is defined as R, such that the current $R \cdot i_{ch}$ flows towards the transformer neutral along line A, whereas $(1 - R) \cdot i_{ch}$ flows towards the transformer neutral along line B. The charging current reaches the transformer neutral where it is divided in two halves, assuming the two healthy phases to be identical. The current then returns to the faulted point via the capacitances of the healthy phases, as indicated in Fig. 1. In Fig. 1, the capacitances C_A and C_B are the per phase capacitances on line A and B, whereas C_{BG} is the total per phase capacitance of the background network, represented here as a single feeder.

Because $\frac{1}{2}i_{ch}$ returns to ground in each of the healthy phases in the network as a whole, the component that returns on the ring itself, denoted i_{hR} in Fig. 1, is given by (2).

$$i_{hR} = \frac{1}{2}i_{ch}\frac{C_R}{C_T} \tag{2}$$

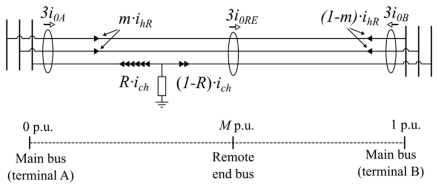

Fig. 2. Remote end bus measurement on a network ring.

In (2), $C_R = C_A + C_B$ is the total per phase capacitance of the ring, whereas $C_T = C_R + C_{BG}$ is the total per phase capacitance of the entire network. Eq. (2) shows that it is the amount of capacitance on the ring compared the background network which determines how much of i_{ch} returns on the ring itself. Depending on the parameters of the two feeders in the ring, the current i_{hR} will divide itself among lines A and B. Let this be described by the factor m, such that the currents

$$\begin{aligned} i_{hA} &= m \cdot i_{hR} \\ i_{hB} &= (1-m) \cdot i_{hR} \end{aligned} \tag{3}$$

flow onto line A and line B, respectively. In the case of a homogeneous ring, the division of i_{hR} will be equal among the two lines (i.e., $m = 0.5$). In any case, m is determined by the network topology and it is independent of the fault location.

The charging transient frequency component of the residual current measured on lines A and B can be written as

$$\begin{aligned} 3i_{0A} &= 2i_{hA} - R \cdot i_{ch} \\ 3i_{0B} &= 2i_{hB} - (1-R) \cdot i_{ch} \end{aligned} \tag{4}$$

Combining (2), (3) and (4), (5) is obtained.

$$\begin{aligned} 3i_{0A} &= i_{ch}\left(m\frac{C_R}{C_T} - R\right) \\ 3i_{0B} &= i_{ch}\left((1-m)\frac{C_R}{C_T} - (1-R)\right) \end{aligned} \tag{5}$$

Similarly, the measured current $3i_{0RE}$ at the remote end bus bar on the ring can also be derived. With the measurement polarity as shown in Fig. 1, this current is expressed as a function of the fault location as well as the location of the remote end bus itself on the ring. Fig. 2 illustrates this way of measuring the distance by drawing the ring AB as a straight feeder. Note how both ends of the figure correspond to the main bus. The per unit distance around the ring is measured along the ring in a clockwise direction starting on line A, and the distance to the remote end bus is denoted M. Then, a remote end bus would for instance be located at $M = 0.5$ p.u. in the case of two lines of the same length, or at $M = 0.67$ p.u. in the case of line A being twice as long as line B. It can then be shown that the current $3i_{0RE}$ is given by (6).

$$3i_{0RE} = i_{ch}\left(\frac{C_R}{C_T}(m-M) + 1 - R\right) \tag{6}$$

Eq. (5) and (6) describe the charging current measured at the three measurement locations shown in Fig. 1, and they apply for this particular topology. Note that the presence of loads on the ring, either at bus M or on branches connected to the feeders A and B, will not significantly impact these results as load transformers represent a much higher impedance path for the transient than the path indicated in Fig. 1.

2.2. Crossover points

Eq. (5) shows that the residual currents measured on lines A and B may become zero at certain fault locations, even in a network with several feeders. These fault locations are referred to as crossover points due to the fact that the polarity of the measured current transient will change from positive to negative in these points, and relays based on measuring this transient will therefore change their direction indication between forward and reverse as well. Furthermore, as the magnitude of the measured transient approaches zero, the relays may encounter problems in detecting the fault altogether when the fault is located close to this crossover point.

The point where either $3i_{0,A}$ or $3i_{0,B}$ becomes zero depends on the relative size of the ring compared to the background network and will occur for $3i_{0,A}$ when $R = m{\cdot}C_R/C_T$. Furthermore, if the ring is relatively large compared to the background network, this point is moved closer to the middle of the ring, and it can thus be imagined that both currents will be difficult to measure at certain fault points. In the special case of a single ring network ($C_R = C_T$), for instance in the case of a two-feeder network operated as a single ring, both $3i_{0,A}$ and $3i_{0,B}$ can become zero for the same fault location. The current measured at the remote end bus will also have its crossover point according to (6).

To be able to evaluate (5) and (6), the parameter m must be known. In the special case of a homogeneous ring, m is known to be exactly 0.5 due to the ring appearing identical seen from either main bus terminals of the ring. An analytical expression for the calculation of m has not been found, but it is understood to be governed by the distribution of capacitance around the ring. The formulae given in [19], used to describe a similar division of fundamental frequency zero-sequence currents, could serve as a starting point for deriving an analytical expression. In practice, however, the best way to locate the crossover points in a complex network would be to rely on simulations, seeing as analytical formulae quickly become difficult to derive when the network topology is changed from the one in Fig. 1. The purpose of deriving the formulae in this paper is to allow for a comparison between theory and practice using physical relays in a laboratory setup, which is presented in the next section.

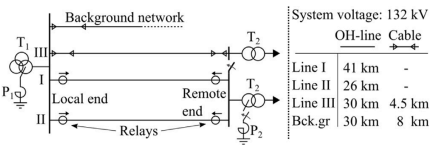

Fig. 3. Test network for investigating location of crossover points.

3. Laboratory testing

3.1. Test network modeling

The results presented in this paper are based on simulations generated from the test network shown in Fig. 3, modeled using ATPDraw. The network is a radial network where two of the feeders have been connected to form a ring. Note that the illustration in Fig. 3 is compact, and feeders I and II are assumed far enough apart to be uncoupled. A third feeder can be connected in parallel to the ring, and the compensation can be divided among two different ASCs. This topology is not based on a real network, but it is first and foremost intended to facilitate a comparison between the actual location of the crossover points and the theoretical locations predicted by (5) and (6). See Table 1 for detailed model data.

3.2. Relay settings

The four relays (manuals [14–17]) under investigation are for the sake of confidentiality referred to as relays A–D:

- Relay A: Analog earth fault relay. The simplest relay of the four considered, with pickup level for transient current and fundamental frequency voltage being the only required settings. The relay is based on detecting transients in the zero-sequence current and voltage and comparing their polarities to determine the direction to fault. The relay manual refers to the charging transient as basis for the operating principle, and the transient measurement circuits are centered at 200 Hz.
- Relay B: Analog earth fault relay with the same basic operating principle as Relay A, also citing the charging transient as basis for its operating principle. According to the manual, the transient measurement circuits filters out the fundamental frequency component, and the measurement circuits for the current transients filters out transients above 3 kHz as well. The pickup level for current transient at 1 kHz and for the fundamental frequency voltage can be set by the user. Additionally, relay B allows for more detailed settings than Relay A, such as filter frequency, length of time window for detection of current and voltage transients, as well as delays related to resetting and tripping.
- Relay C: Numerical IED with multiple earth fault functions, where only the transient earth fault function is being tested. This function is also based on the transient charging process that takes place during earth faults, but as opposed to relay A and B, this function also considers the fundamental frequency in addition to the higher frequency transients. According to the manual, this function is based on the energy in the zero-sequence system, citing that the charging process consists of a transfer of energy between the faulty feeder and the surrounding network. This zero-sequence energy is computed through integration and summation of phasors at several frequencies. The relay allows for setting of $3V_0$ and the integrated $3I_0$-current trigger levels, along with detailed settings of proprietary parameters. This relay also allows separate trigger levels for forward and reverse faults.
- Relay D: Numerical IED with multiple earth fault functions, where only the transient earth fault function is being tested. Similar to relay C, this function is based on the energy in the zero-sequence system, which is computed directly in the time domain. The relay manual for relay D contains less information on the signal processing and filtering, but it indicates that relay D also makes use of the fundamental frequency in addition to the higher frequencies, just as relay C does. The relay allows for setting of $3I_0$ and $3V_0$ trigger levels, along with detailed settings of proprietary parameters.

All the four relays require the same two measurements, $3I_0$ and $3V_0$. Relays A and B both refer directly to the charging transient discussed previously as basis for their operation. Relays C and D are based on zero-sequence energy, although they have different ways of implementing it. While the charging transient is part of this operating principle, relays C and D also incorporate more of the information contained in the transient period in their operation. The four relays thus represent two generations of relays utilizing two distinctly different operating principles. Whereas relays A and B are found in many Norwegian networks today, relays C and D are likely to be used increasingly in new substations.

Although the relays utilize similar operating principles, the implementation and configuration of each relay is unique. The only comparable setting is the pickup threshold for the fundamental frequency voltage $3V_0$, which is set to ensure fault detection for all the relays. The four relays all have a setting for the current threshold as well, although it has different interpretations for each relay. In the case of relays A and B, the current threshold has a recommended value based on network data and the CT-ratio used. This parameter is therefore set according to the recommendations in their respective manuals. All other proprietary settings are set according to the manuals unless otherwise specified. Relays C and D have current thresholds that are related to either the CT secondary current or as a percentage of some base value. Relay C limits the current threshold downwards to some percentage of base value, typically the CT primary value, while relay D allows setting the threshold to zero. However, the manual of relay D states that this threshold should perhaps be increased in meshed networks according to user experience.

Table 1
Test network data.

OH-lines	Phase conductors: radius 4.07 mm (inner) and 12.03 mm (outer), R_{DC} = 0.1115 ohm/km, 4.5 m spacing, plane geometry, tower height 11 m, 4.3 m sag. Ground conductors (x2): radius 1.45 mm, R_{DC} = 0.8 ohm/km, 4.5 m spacing, plane geometry, tower height 13 m, 4.3 m sag. Transposed lines, skin effect, JMarti-model. No coupling between feeder I and II. G_0 = 44.33 nS/km added manually.
Cables	Three single-phase cables in ground, depth 1 m, transposed. Core radii 8 mm (inner) and 17.35 mm (outer), sheath radii 32.15 mm (inner) and 33 mm (outer), cable radius 41 mm, semi.cond. layer w/ thickness 1 mm between core and sheath, conductor resistivity 2.651E−8 Ωm, relative permittivity of insulation 2.3. Modeled using JMarti. Asymmetry: 3.3 nF/km and 6.6 nF/km added to C_0 in phases b and c, respectively.
Transformers	T1: 250/250/80 MVA 400/132/12.5 kV Yyd1 T2: 50 MVA 132/22 kV Yd11
Loads	3-phase 10 MVA constant impedance loads. Power factor 0.9 lagging.
ASC	I_{nom} = 295 A (10% over-compensated). Parallel resistors Rp = 50 kΩ represent losses in P1 and P2.
CTs and VTs	$3I_0$ CTs 600/5A, $3V_0$ VTs 228/0.11 kV. Sampled at 10 kHz.
Fault	R_f = 100 Ω, inception angle approximately 40°.
Other	Software: ATPDraw version 7.2p11, simulation timestep Δt = 1 μs, ground resistivity 100 Ωm.

In either case, default pickup thresholds of relays C and D cannot be readily obtained from their manuals. Furthermore, the correct operation of all four relays is closely related to the quality of the measurements they receive. In reality, measurement noise will be present, and an appropriate CT-ratio must be used to give the relays optimal conditions. In this paper it is primarily the fault direction indication which is of interest to study, and the relays are therefore set to be very sensitive. Discussion of any observed issues pertaining to sensitivity of the relays will therefore be limited to a qualitative level.

3.3. Laboratory setup

Signals of $3I_0$ and $3V_0$ on Comtrade format are generated using ATPDraw's Comtrade block sampling at 10 kHz, where the fault records are obtained running sequential simulations with varying parameters. The Advanced TransPlay feature in Omicron CMC 356 is used to play the Comtrade files to the relays [21].

All the relays are capable of outputting binary signals to indicate both forward and reverse faults, and these signals are monitored to determine the location of the crossover points. The binary signals are synchronized in time with the signal played back by the relay tester with the setup shown in Fig. 4, and all binary signals are controlled to make sure that they coincide with the fault.

4. Results

4.1. Location of crossover points

Faults are applied in sequence at evenly distributed locations around the ring consisting of feeder I and feeder II in the network in Fig. 3 to investigate the location of the crossover points. Feeder III is assumed to be operated radially, and ASC P2 is disconnected. Based on the charging transient alone, the theoretical location of these points can be

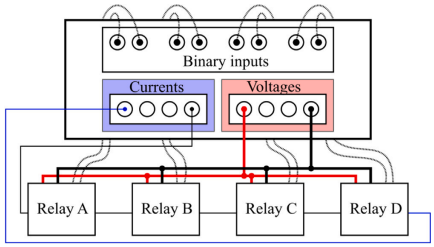

Fig. 4. Lab setup for testing multiple relays at once using the Omicron CMC 356 [21].

estimated using (5) and (6). The parameters M and m are determined as follows: M describes the per unit distance to the remote end bus as $M = 41\ \text{km}/67\ \text{km} = 0.612$, and $m = 0.5$ is assumed because the ring is homogeneous with only overhead lines. For the four relays on the ring, these theoretical locations are shown in Table 2 along with the observed crossover points for the four relays.

Using standard settings as recommended by the relay manufacturers, Relay A managed to detect the fault in all the fault locations. Relay D managed to detect all the faults as well, likely due to the fact that this relay both allows and recommends a very low current threshold. Relay C behaves differently as its sensitivity threshold is related to whatever current level is selected as its base value. The selection of this base value is up to the user, but with a sufficiently low value Relay C can also be made to be very sensitive. Relay B was the least sensitive, and its minimum allowable current threshold setting was used to determine its crossover point location. Furthermore, it was observed that the remote end relays had much poorer operating conditions than the local end relays did, requiring the output from the relay tester to be twice as high in order to determine the crossover point location. This demonstrates that a single setting for all the relays in the network, as suggested in the manuals of both relays A and B, is not advisable.

The results show that the relays have their crossover points close to the theoretical values, but that there is some variation. This may in part be due to differences in the operating principles, and partly due to the fact that faults close to the crossover point represent very challenging conditions for the relays. The precise locations of the crossover points were therefore difficult to determine accurately in the laboratory setup, as the observed locations of the crossover points shifted slightly in some instances (at most ± 4 km) when the tests were conducted with different relays settings and CT-ratios.

In addition to the results in Table 2, the impact of adding feeder III in parallel was investigated. This shifted the locations of the crossover points for all the relays, as would be expected from the theoretical discussions in Section 2.

Table 2
Theoretical and observed crossover points the test network.

Relay pos.	Local end		Remote end	
	Fd. I	Fd. II	Fd. I	Fd. II
	Crossover points - (km/*p.u.*) (measured from local end bus in clockwise direction around the ring)			
Theoretical crossover point	63.6/*0.95*	3.4/*0.05*	0.8/*0.01*	0.8/*0.01*
Relay A	58.5/*0.87*	8.5/*0.13*	1.5/*0.02*	1.5/*0.02*
Relay B	62.5/*0.93*	4.5/*0.07*	1.5/*0.02*	1.5/*0.02*
Relay C	65.5/*0.98*	1.5/*0.02*	0.5/*0.01*	0.5/*0.01*
Relay D	65.5/*0.98*	1.5/*0.02*	0.5/*0.01*	0.5/*0.01*

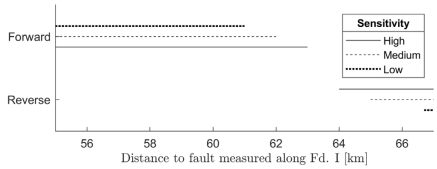

Fig. 5. The crossover point of relay A turns into a crossover region as the relay sensitivity is decreased.

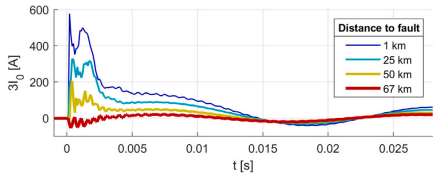

Fig. 6. The current $3I_0$ as measured on the local end of Fd. I for various fault locations.

4.2. Crossover regions

As discussed previously, two things occur in the crossover points: (1) the polarity of the charging transient changes, and (2) the magnitude of the charging transient goes to zero, as was shown in [18]. Although the transition from forward to reverse happens in the crossover point, the magnitude gradually decreases in the area around the crossover point. As a result, the relays may fail to detect faults in the region around the crossover point when less sensitive settings are used. Therefore, the crossover points would actually appear as crossover regions in reality. Fig. 5 illustrates this for Relay A, and similar results could be produced for the other relays as well. The relay was fed with currents of 30%, 25% and 15% magnitude to emulate a high, medium and low sensitivity setting. Note that because the relay was set less sensitive than its recommended settings. i.e., its pickup threshold was set higher than recommended, the crossover point in Fig. 5 is actually shifted slightly from the value in Table 2. The sensitivity of the relay and the approach used to locate the crossover point thus both impact the observed crossover point location, further illustrating that the exact crossover point location is difficult to determine. This was observed to a varying degree for all the four relays, with relay A showing the largest shift.

Fig. 5 illustrates how the crossover point turns into a crossover region as the sensitivity of the relay is decreased, and faults in this region are not detected by the relay. Fig. 6 shows the time domain signal obtained at the local end relay on feeder I. It illustrates that the initial transient is drastically reduced as the fault is moved farther away, and the polarity shift can also be observed to take place towards the other end of the ring corresponding to the 67 km curve. The magnitude of the fundamental frequency component is also visibly reduced for faults far away.

4.3. Impact of the fundamental frequency component

Dividing the compensation in the network evenly among ASC P1 and P2 further impacted relays C and D, whereas relays A and B were unaffected. Relays A and B only utilize frequencies above the fundamental frequency, for which the network appears ungrounded. Changing or moving the ASCs in the network will therefore not affect

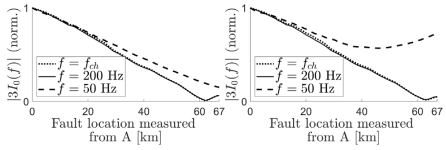

Fig. 7. Normalized magnitudes of the charging transient, 200 Hz and 50 Hz components in $3I_0$ during the first 20 ms of the fault, measured at local end Fd. I, in the case of one (a) or two (b) ASCs in the network.

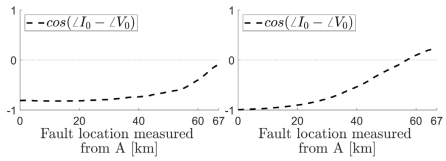

Fig. 8. 50 Hz zero-sequence power factor during the first 20 ms of the fault, measured at local end Fd. I, in the case of one (a) or two (b) ASCs in the network.

these relays. Relays C and D, however, both make use of the fundamental frequency, and their crossover points are therefore dependent on the location of the ASCs in the network. Fig. 7 shows how the magnitudes of the charging transient, the 200 Hz and 50 Hz component of $3I_0$ varies with fault location in these two scenarios, and it is clear that relays dependent on the 50 Hz component will be affected by adding the second ASC.

The addition of P2 not only affects the magnitude of the fundamental frequency component, but also the direction indication based on it. Relays C and D both rely the zero-sequence active energy as part of their operation, and Fig. 8 show that the fundamental frequency active power always indicates a forward fault ($cos(\phi_0) < 0$) in the case of a single ASC, while the addition of P2 changes this. Relays C and D do however not exhibit the exact same responses (the addition of P2 shifted the crossover points of relays C and D in opposite directions), demonstrating that they each have a distinct variation of the energy-based operating principle. The formulae presented in Section 2 only account for the behavior of the charging transient, and therefore do not accurately capture the behavior of relays C and D. This will require a separate study of the fundamental frequency component as well as the relays' weighting of the different frequencies, which is outside the scope of this paper.

4.4. Challenges for protection

Assuming that the relays could be set as sensitive in reality as they were during this test, the data in Table 2 show that misoperation could occur. Fig. 9 illustrates the situation: The remote end relay on feeder II see faults on the first 0.5–1.5 km of feeder I as forward faults, whereas the remote end relay on feeder I see them as reverse faults. As a result, no pair of relays on the ring can determine the fault to be between them. Instead, a network operator would have two options in this case: (1) increase the pickup threshold of the relays and only rely on the local end relays to determine the fault location, or (2) divide feeder I in two shorter segments equipped with another pair of relays.

Because the different relays are affected differently by the presence of ASCs, a network with a mixture of different relays could result in another more critical type of misoperation. Consider the situation in

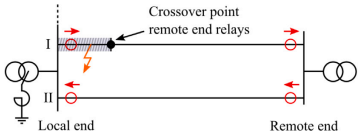

Fig. 9. The shaded region shows fault locations with inconclusive relay responses.

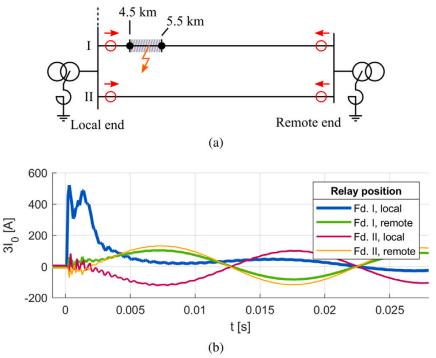

Fig. 10. Faults in the shaded region in (a) appear as a forward fault on both lines. Current magnitudes in (b) clearly indicate a fault on Fd. I (actual fault location is 5 km from the local end on Fd. I).

Fig. 10(a), where the compensation is divided evenly among P1 and P2. Assume that the relays in the local end substation are of type B, whereas the remote end substation is equipped with type D relays. Table 3 shows the location of the crossover points in this configuration. Because the crossover point of the remote end relay on feeder II is located farther out on feeder I than the crossover point of the local end relay on feeder II, all four relays see faults in the shaded region as forward faults. The local-end relay on feeder II must in this case have its pickup threshold increased to avoid this situation.

The actual magnitude of the transients will depend on several factors such as inception angle and fault resistance, and therefore it is difficult to relate the magnitude to any particular fault location. However, if the magnitudes of the currents measured by each relay had been available for comparison in the previous example, the fault could easily have been determined to be on feeder I. The maximum recorded value of $3I_0$ in the local end relay on feeder I is much higher than at the other three relays, as shown in Fig. 10(b), indicating that the fault could not possibly be located on feeder II.

5. Discussion

Testing relays based on simulations is a challenge, as replicating both the earth fault transients as well as the fundamental frequency components accurately is difficult.

Firstly, the relay tester must reproduce the waveforms accurately, which may be difficult for very fast transients. Furthermore, the Omicron is limited to playing back 10 kHz, although this should be more than any of the relays require.

Secondly, the use of the frequency dependent line model does not perfectly replicate both the fundamental frequency (50 Hz) and the fault transients (0.2–2 kHz). This is however only of concern for relays

Table 3
Observed crossover points for relay B and D when ASC P2 is connected.

Relay pos.	Local end		Remote end	
	Fd. I	Fd. II	Fd. I	Fd. II
Crossover points - (km/*p.u.*) (measured from local end bus in clockwise direction around the ring)				
Relay B	62.5/*0.93*	4.5/*0.07*		
Relay D			64.5/*0.97*	5.5/*0.08*

C and D, for which the impact of the fundamental component is only discussed on a qualitative level. Furthermore, the effect of CT and VT accuracy and noise is not implemented in these tests, and the very sensitive relay settings required in these tests may not be realistic to implement in reality to avoid false alarms during other network events. It may also be the case that the set sensitivity of the relays should be deliberately reduced to avoid the simultaneous operation of too many relays in the network and to reduce the risk of misoperation due to poor conditions near the crossover points.

Finally, it is noted that the topology of the test network is intentionally simple to enable derivation of the analytical formulae which could be compared against laboratory tests. In reality, such a ring-network would likely have many lateral branches which complicates the process of estimating the location of the crossover points. The fact that crossover points would exist in any type of non-radial network is obvious, and in complex networks their location may be more efficiently determined through simulations.

6. Conclusion

Transient earth fault relays (TEFRs) are frequently applied to non-radial resonant grounded networks, but they are susceptible to issues related to both sensitivity and polarity. This paper has presented and verified a theoretical approach for estimating the location of crossover points for relays based on the charging transient, i.e. fault locations in which a relay will change its direction indication between forward and reverse, and tested four different commercially available TEFRs in a laboratory setup. The important conclusions and scientific contributions are as follows:

- Crossover points were found in the predicted locations, and b polarity swap and sensitivity issues were observed there, showing that the theoretical approach for understanding crossover points is correct. This approach can therefore be used to understand relay behavior in other networks as well, although simulations likely are more efficient in the case of complex topologies.
- The location of the crossover points for the modern relays based on zero-sequence energy are also influenced by the fundamental frequency component, which in turn is affected by network topology and the placement of arc suppression coils in the network. This is not accounted for in the analytical formulae presented in this paper, and future work should focus on extending the theory to encompass this.
- Because the location of the crossover points depend on the network topology, and as different relay locations can have significantly different operating conditions with respect to expected current magnitudes, static and system-wide settings for all relays in the network, as suggested in some relay manuals, is not advisable. Rather, each relay location should be analyzed separately, and this analysis should take into account all the possible network topologies to ensure the desired behavior during faults.
- All the TEFRs must deal with the lack of a clear forward/reverse orientation in a loop, and due to the lack of a distance element in TEFRs, the evaluation of relay responses with respect to this issue becomes difficult. Ring-operation of distribution networks is particularly challenging to protect with TEFRs when one or more relays have their crossover points on the protected line itself. Knowledge of the likely crossover regions and comparison of the current magnitudes of relays in the system could however be used to aid the network operator when assessing the relay responses.

CRediT authorship contribution statement

Thomas Treider: Conceptualization, Methodology, Software, Formal analysis, Investigation, Data curation, Writing – original draft, Writing – review & editing, Visualization. **Hans Kristian Høidalen:** Methodology, Software, Writing – review & editing.

Declaration of competing interest

The authors declare that they have no known competing financial interests or personal relationships that could have appeared to influence the work reported in this paper.

Data availability

The authors do not have permission to share data.

Acknowledgment

The authors would like to thank the ProDig partners for providing relays for testing.

References

[1] X. Zhang, B. Xu, Z. Pan, P. Wei, Study on single-phase earthed faulty feeder selection methods in non-solidly grounded systems, in: 2008 3rd Int. Conf. Elect. Utility Deregulation and Restructuring and Power Techn., 2008, pp. 1836–1840.
[2] E. Bjerkan, Efficient fault management using remote fault indicators, in: CIRED 2009 - the 20th Int. Conf. Exhib. Electricity Distribution - Part 1, 2009, pp. 1–4.
[3] A. Wahlroos, J. Altonen, Performance of novel neutral admittance criterion in MV-feeder earth-fault protection, in: CIRED 2009 - 20th Int. Conf. Exhib. Electricity Distribution - Part 1, 2009, pp. 1–4.
[4] T. Henriksen, Faulty feeder identification in high impedance grounded network using charge–voltage relationship, Electr. Power Syst. Res. 81 (9) (2011) 1832–1839.
[5] M. Loos, S. Werben, M. Kereit, J.-C. Maun, Detection of single phase earth fault in compensated network with C0 estimation, in: CIRED 2013 - 22nd Int. Conf. Exhib. Electricity Distribution, 2013, pp. 1–4.
[6] K. Pandakov, H.K. Høidalen, S. Trætteberg, An additional criterion for faulty feeder selection during ground faults in compensated distribution networks, IEEE Trans. Power Deliv. 33 (6) (2018) 2930–2937.
[7] J. Rios Penaloza, A. Borghetti, F. Napolitano, F. Tossani, C. Nucci, Performance analysis of a transient-based earth fault protection system for unearthed and compensated radial distribution networks, Electr. Power Syst. Res. 197 (2021) 107306.
[8] M. Abdel-Fattah, M. Lehtonen, Transient algorithm based on earth capacitance estimation for earth-fault detection in medium-voltage networks, IET Gener., Transmiss. Distrib. 6 (2) (2012) 161–166.
[9] G. Druml, P. Stachel, S. Gebhard, W. Leitner, O. Skrbinjek, G. Achleitner, U. Schmidt, P. Schegner, New method for measuring the earthfault-distance in compensated and isolated networks, in: CIRED 2021 - the 26th Int. Conf. Exhib. Electricity Distribution, 2021, pp. 1416–1419.
[10] G. Druml, P. Stachel, W. Leitner, O. Skrbinjek, U. Schmidt, P. Schegner, Results from the new method for measuring the earthfault-distance in compensated and isolated networks, in: 16th Int. Conf. Develops. Power Syst. Protection, DPSP 2022, 2022, pp. 13–18.
[11] J.D. Rios Penaloza, A. Borghetti, F. Napolitano, F. Tossani, C.A. Nucci, Performance analysis of a communication-supported earth fault protection system of medium voltage loop and meshed networks, in: 2018 IEEE Int. Conf. Environ. and Elect. Eng. and 2018 IEEE Ind. and Commercial Power Sys. Europe (EEEIC / I&CPS Europe), 2018, pp. 1–6.
[12] J.D. Rios Penaloza, A. Borghetti, F. Napolitano, F. Tossani, C.A. Nucci, A new transient-based earth fault protection system for unearthed meshed distribution networks, IEEE Trans. Power Deliv. 36 (5) (2021) 2585–2594.
[13] T.A. Zerihun, T. Treider, H. Taxt, L.B. Nordevall, T.S. Haugan, Two novel current-based methods for locating earth faults in unearthed ring operating MV networks, Electr. Power Syst. Res. 213 (2022) 108774.
[14] Siemens AG, 7SN600 Transient Earth-Fault Relay: Instruction Manual, Oct. 2011, Nuremberg, Germany, 2011.

[15] ABB Relays AB, Type RXPG 4 Transient Ground-Fault Relay, B03-3110E, Västerås, Sweden, 1989.
[16] Hitachi Energy Sweden AB, "Average Power Transient Earth Fault Protection, APPTEF," in Relion 670 Series: Line differential protection RED670, Version 2.2 ANSI Technical Manual, Västerås, Sweden, 2022.
[17] Siemens AG, "Directional Transient Ground-Fault Stage," in SIPROTEC 5, Generator Protection, Manual C53000-G5040-C027-9, 04.2021, Nuremberg, Germany, 2021.
[18] T. Treider, B. Gustavsen, H.K. Høidalen, Analysis of transient earth fault protection in meshed resonant grounded networks, in: 16th Int. Conf. Develops. Power Syst. Protection (DPSP 2022), 2022, pp. 1–6.
[19] R. Willheim, R. Waters, Neutral Grounding in High-Voltage Transmission, Elsevier, New York, NY, USA, 1956, pp. 198–200.
[20] T. Welfonder, Localisation de défauts monophasés dans les réseaux de distribution à neutre compensé (Ph.D. thesis), Grenoble INPG, 1998.
[21] Omicron, CMC 356 : User Manual, Omicron electronics GmbH.

Paper III

T. A. Zerihun, T. Treider, H. Taxt, L. B. Nordevall and T. S. Haugan, "Two novel current-based methods for locating earth faults in unearthed ring operating MV networks," *Electric Power Systems Research*, vol. 213, 2022, Art. no. 108774.

As this author is listed as a co-author of Paper III, the following description — agreed upon by all the authors of the paper — is given to clarify the relevant contributions. This author contributed to paper III by:

- Developing and writing the theory required to derive and explain the two fault location methods. This author provided existing theory for analysis of earth faults, and developed this to describe the division of negative and zero sequence currents on two ring-connected feeders.
- Developed the analytical method for estimating the parameters m_A and m_B using network data.
- Developing one of the experimental techniques for estimating the parameters m_A and m_B (using a fault at the beginning of either feeder).
- Contributing in adapting the main fault location principle to be viable for earth faults in isolated and compensated networks. This author showed that the two new methods, based on the zero and negative sequence currents, respectively, required evaluating the impedance ratios of their respective sequence system in order to function.
- Creating a simulation model in ATPDraw which included the necessary parameters to test the developed methods, such as phase admittance asymmetry, load asymmetry and phase coupling.
- Generating the results included in the paper in Matlab
- Contributing in interpreting and analysing the results
- Contributing in writing and approving the final version of the paper

[2]https://creativecommons.org/licenses/by/4.0/

Electric Power Systems Research 213 (2022) 108774

Contents lists available at ScienceDirect

Electric Power Systems Research

journal homepage: www.elsevier.com/locate/epsr

Two novel current-based methods for locating earth faults in unearthed ring operating MV networks

Tesfaye Amare Zerihun [a,*], Thomas Treider [b], Henning Taxt [a], Lars B. Nordevall [c], Thomas S. Haugan [b]

[a] SINTEF Energy Research, Trondheim, Norway
[b] Norwegian University of Science and Technology - NTNU, Trondheim, Norway
[c] Elvia AS, Oslo, Norway

ARTICLE INFO

Keywords:
Earth fault location
Closed-ring MV network
Distribution network
Impedance method
Negative sequence currents
Zero sequence currents

ABSTRACT

Automated fault location plays a key role in improving the reliability of modern power grids—it helps to reduce the power outage time and the number of affected customers. Earth faults in isolated systems are among the fault types that are difficult to detect and locate with a reasonable accuracy, and there has therefore not been a well-established method for detecting and locating such faults in isolated systems. This paper presents two novel current-based methods for locating earth faults in unearthed closed-ring MV networks. The methods are based on the utilisation of sequence components of standard current and voltage measurement at a primary substation and they do not require new devices or measurements in the field. Both methods are tested with a simulation of a network based on data provided by a Norwegian network operator and their prediction performances were investigated considering different scenarios on fault resistance, load asymmetry and measurement errors. Both methods performed well and showed good accuracy. The simulation results are promising and strengthens the prospect of further testing of the methods in real networks and adoption of the methods for a real-world implementation.

1. Introduction

In modern power systems, self-healing and automation of the grid is increasingly applied to distribution grid with the objective of performing automated fault location, isolation and service restoration. These new applications aim to significantly improve the reliability of the grid as less time will be needed to locate and resolve the faults in the grid.

Fault indication and location are key functionalities in the self-healing and automation of the grid. There are many well established methods for locating most short circuit faults (symmetrical or unsymmetrical faults). However, among these fault types, there has not been a commonly accepted, reliable and efficient method for single phase to earth fault location in ungrounded or compensated networks. Locating single phase earth faults is crucial as it is the most common fault type in the distribution network, representing 50 to 90 % of faults in Nordic countries [1].

1.1. Related work

Several fault location methods for single phase earth faults have been proposed and studied. The methods often consider a radial operation of the grid and they can be broadly divided into centralised and decentralised methods. Centralised methods are mainly based on measurements at a primary substations while distributed approaches use measurements along feeders and a communication infrastructure for collection, coordination and management of these measurements.

Some of the most commonly used centralised approaches are the impedance based methods which are based on measuring the apparent impedance seen from either end of a feeder when a fault occurs. Some works such as [2–6] presented an impedance based fault location methods for distribution grids. The works in [5,6] presented an impedance method for ungrounded distribution networks utilising current and voltage measurements at a primary substation. Where as, the method in [5], in addition to the voltage and current measurements of MV primary substations, considered dynamic load models to achieve higher accuracy. The work in [7] presented earth fault location methods that

* Corresponding author.
E-mail addresses: tesfaye.zerihun@sintef.no (T.A. Zerihun), thomas.treider@ntnu.no (T. Treider), henning.taxt@sintef.no (H. Taxt), lars.nordevall@elvia.no (L.B. Nordevall), thomas.haugan@ntnu.no (T.S. Haugan).

https://doi.org/10.1016/j.epsr.2022.108774
Received 27 January 2022; Received in revised form 18 July 2022; Accepted 29 August 2022
Available online 15 September 2022

mainly utilise zero sequence voltage and current measurements on feeders rearranged to ring structure after the occurrence of a fault. It then calculates the distance to the earth fault from the phase to earth admittance and distribution of the components of the zero sequence current. The method apply, however, to radially operated networks. The main challenge with the impedance based approaches is that the fault current in isolated and compensated networks is often very small to allow a satisfactory fault location accuracy.

Another method is the travelling-wave-based method such as in [8–11] which, theoretically, can give accurate fault location. In this method, by measuring the transient voltage and current waves and their reflection and arrival times at either end of the line, the distance to the fault point can be determined. However, due to the availability of numerous branches and laterals in distribution network, the reflection captured at the substation (beginning of the feeder) may come from other sources in the network (noises and disturbances) and not necessarily only from the fault point [12]. Travelling wave based methods are often complex and incur high implementation cost as they often require high sampling rate and sophisticated measurement equipment. This makes it challenging to apply these methods in real distribution networks.

Recently, there has been also the use of artificial intelligence based methods such as [13–19] which use historical data and develop learning algorithms that can determine fault locations. The work in [18] presented a fault location method for unearthed distribution network using Support Vector Machine (SVM) and wavelet technique, however the method assumes a radial operation and requires closing a switch to form a ring after the occurrence of a fault. Other works such as in [17,20] presented a hybrid method combining Discrete Wavelet Transform (DWT) and artificial neural network (ANN) which only use line currents available from substations. Although these type of methods attracted some attention for some time as they often give fairly accurate performance in simulation studies, the research into this direction seems to be declining, and it is difficult to find evidence of real-life implementations [12].

Decentralised fault location methods are realised by the recent modernisation and automation of the grid with the introduction of intelligent electronic devices (IEDs), smart meters, fault passage indicators (FPI), etc. equipping secondary substations with monitoring and communication capability. The utilisation of these components with a communication infrastructure enabled the distributed fault location. The fault location is carried out either locally by the IEDs or by higher level controllers receiving measurements from the IEDs/ICT devices.

Distributed fault location methods in [21,22] used the measurements from smart meters, though it only works for faults with low fault resistance. Fault passage indicators, supported by advanced sensor and communication technology are used for locating earth faults in [23,24]. A list of FPIs that has been used in real implementations and field tests are presented in [25]. The major drawbacks in using FPI based methods is the dependence on the communication infrastructure and the fact that they are only capable of identifying the faulted section between two FPIs.

Some works such as [26,27] used state estimation based methods where sufficient data is provided to the fault location using recorded data from a set of measurement points such as AMI, SCADA, or PMUs that have been used in distribution grids recently. Other works in [28–31] presented methods to locate earth faults which are solely based on low voltage measurements from secondary substations of the distribution grid. A similar approach called 'Vdip' is presented in [32], but in addition to the voltage monitors at LV side of the distribution grid, the method uses current measurement at the primary MV substation.

Other works such as [33,34] presented decentralised methods that are based solely on current measurements. These methods specifically look into the changes in symmetrical components of currents during fault, assuming that the negative sequence current from the feeding substation up to the fault location is relatively higher compared to the negative sequence current after the fault point.

Recent works such as [35–38] presented decentralised methods to locate faults in meshed distribution networks with distributed energy resources (DERs) using information provided by distributed controllers, Intelligent Electronic Devices (IEDs) and IoT devices such as Directional Fault Passage Indicators (DFPI). In [39], an earth fault location method utilising synchronous measurement from PMUs is proposed for an active distribution grid with DERs. The authors in [37,38], presented a multi agent system based fault location methods for distribution systems in the presence of DERs.

Overall, the distributed fault location methods using sensors, IEDs, FPIs, and IoT devices are becoming increasingly common and they are especially promising for next generation distribution networks with ring or meshed operation and high penetration of DERs. However, compared with other approaches such as the impedance based method, their implementation is often costly.

1.2. Aim and contribution

A reliable and efficient fault location method has to be simple, accurate, cost effective, and shall be applicable in different types of network topologies and configurations. Unlike most short circuit faults which are relatively easy to detect and locate, locating earth faults in unearthed systems is challenging. The various fault location methods presented above had their own strengths and drawbacks. The impedance based methods being the most simple and cost effective but highly dependant on estimation of the system parameters while the distributed method with IEDs and FPIs utilise simple measurements along feeders but with a relatively complex implementation requiring field devices and advanced communication capabilities.

This paper aims to propose a simple and cost effective earth fault location method for isolated systems utilising the readily available measurements at MV primary substations. Considering the architectural changes in a futuristic distribution networks, the method exploits the possibilities arising from a ring operation of MV networks. Closed ring operation is seldom used in medium voltage networks in Norway so far. Historically the network is built as pure radials or as open ring network. Radials and open ring network are easy to monitor and the protective scheme is simple and straight forward. However, to improve the overall reliability in the network, ring networks are getting more and more common. Closed ring operation adds some complexity and may increase vulnerability, but there are also benefits like lower losses and possibly improved fault localisation. The paper presents two methods which are mainly based on sequence components of current measurements and neutral voltage measurements at a substation. Overall, the aim is to develop a method that can:

- locate earth faults with error margin of a few hundred meters.
- deal with different load situations (balanced/unbalanced)
- deal with various fault resistances
- be less costly and easy to implement (with simple logic using current and neutral voltage measurements at a substation)

This paper is limited to fault location of single phase to ground faults considering unearthed MV distribution networks only.

1.3. Organisation of the paper

The paper is organised as follows. Section 2 gives a brief theoretical background on the methods used for locating single phase to ground faults using sequence components. Section 3 presents the proposed methods. In Section 4, a brief description of the system considered for illustration of the performance of the methods is presented. Section 5 presents and discusses the results obtained from the case study investigation. Lastly, conclusive remarks and future works are summarised in Section 6.

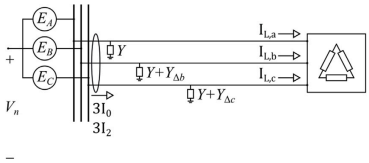

Fig. 1. Healthy feeder.

2. Theory

2.1. Sequence currents in a ring topology

2.1.1. Healthy state

The equations describing the flow of currents on a single feeder is used as the basis for developing a similar set of equations describing the currents on two ring-connected feeders. Consider the feeder in Fig. 1, with phase-ground admittances Y, $Y + Y_{\Delta b}$ and $Y + Y_{\Delta c}$ in phases a, b and c, respectively. The feeder supplies a load with load currents $\vec{I}_{L,a}$, $\vec{I}_{L,b}$ and $\vec{I}_{L,c}$. The phase currents flowing onto the feeder can be derived from Fig. 1 and are given by (1).

$$\begin{aligned}\vec{I}_a &= (\vec{V}_n + \vec{E}_a)Y + \vec{I}_{L,a}\\ \vec{I}_b &= (\vec{V}_n + \vec{E}_b)(Y + Y_{\Delta b}) + \vec{I}_{L,b}\\ \vec{I}_c &= (\vec{V}_n + \vec{E}_c)(Y + Y_{\Delta c}) + \vec{I}_{L,c}\end{aligned} \tag{1}$$

Transforming the phase currents into symmetrical components [40], the zero and negative sequence currents on the feeder are given by (2),

$$\begin{aligned}3\vec{I}_0 &= \vec{V}_n\hat{Y} + \vec{E}_a\hat{Y}\\ 3\vec{I}_2 &= \vec{V}_n\hat{Y} + \vec{E}_a\tilde{Y} + \vec{I}_L\end{aligned} \tag{2}$$

where

$$\begin{aligned}\tilde{Y} &= 3Y + Y_{\Delta b} + Y_{\Delta c}\\ \hat{Y} &= h^2Y_{\Delta b} + hY_{\Delta c}\\ \bar{Y} &= hY_{\Delta b} + h^2Y_{\Delta c}\\ \vec{I}_L &= \vec{I}_{L,a} + h^2\vec{I}_{L,b} + h\vec{I}_{L,c}\end{aligned}$$

have been introduced for more compact notation. The voltage $\vec{E}_a$ is the phase-neutral voltage at the transformer terminal of phase a, $\vec{V}_n$ is the neutral-ground voltage, and $h = e^{j120^\circ}$.

Next, consider instead two feeders, feeders A and B. The phase-ground admittances of feeder A are Y_A, $Y_A + Y_{\Delta b,A}$ and $Y_A + Y_{\Delta c,A}$ as illustrated in Fig. 2. Similarly for feeder B, the phase-ground admittances of the three phases are Y_B, $Y_B + Y_{\Delta b,B}$ and $Y_B + Y_{\Delta c,B}$. If the two feeders are radially operated, the zero and negative sequence currents on each feeder can be described by inserting the admittances and load currents of each feeder into (2). If the two feeders are connected to form a ring, however, the sequence currents measured on the terminals of the two feeders are not straight forward to compute. To overcome this problem, the two ring-connected feeders are treated as a single, equivalent feeder by defining $Y = Y_A + Y_B$, $Y_{\Delta b} = Y_{\Delta b,A} + Y_{\Delta b,B}$ and $Y_{\Delta c} = Y_{\Delta c,A} + Y_{\Delta c,B}$ to maintain the notation used in (1) and (2), and the sum of sequence currents on the two feeders are obtained by (2), here re-written as (3).

$$\begin{aligned}3\vec{I}_{0,A} + 3\vec{I}_{0,B} &= \vec{V}_n\tilde{Y} + \vec{E}_a\hat{Y}\\ 3\vec{I}_{2,A} + 3\vec{I}_{2,B} &= \vec{V}_n\hat{Y} + \vec{E}_a\tilde{Y} + \vec{I}_L\end{aligned} \tag{3}$$

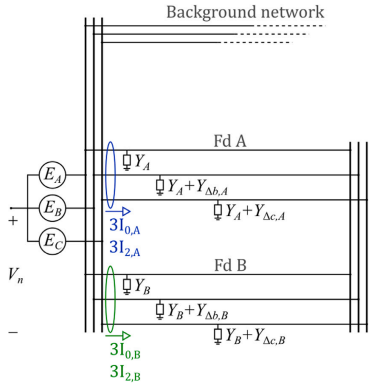

Fig. 2. Ring operating MV distribution network.

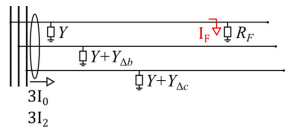

Fig. 3. Earth fault in phase a on a single feeder.

The approach suggested in this paper is to express the sequence currents measured on feeder A and B when connected in a ring as fractions of the sum of sequence currents flowing onto the ring, as described by (4).

$$\begin{aligned}3\vec{I}_{0,A} &= \vec{V}_n\tilde{Y}\cdot m_A + \vec{E}_a\hat{Y}\cdot n_A + \vec{I}_{0,ring}\\ 3\vec{I}_{0,B} &= \vec{V}_n\tilde{Y}\cdot m_B + \vec{E}_a\hat{Y}\cdot n_B - \vec{I}_{0,ring}\\ 3\vec{I}_{2,A} &= \vec{V}_n\hat{Y}\cdot q_A + \vec{E}_a\tilde{Y}\cdot s_A + \vec{I}_L\cdot t_A + \vec{I}_{2,ring}\\ 3\vec{I}_{2,B} &= \vec{V}_n\hat{Y}\cdot q_B + \vec{E}_a\tilde{Y}\cdot s_B + \vec{I}_L\cdot t_B - \vec{I}_{2,ring}\end{aligned} \tag{4}$$

In (4), all the factors m_A, m_B, n_A, ... $\in [0, 1]$, and $m_A + m_B = n_A + n_B = q_A + q_B = s_A + s_B = t_A + t_B = 1$. These factors are used to describe the general case where each component in the sequence currents may be distributed differently among the two feeders, as will be the case when the feeders' admittances and impedances are not evenly distributed around the ring. The currents $\vec{I}_{0,ring}$ and $\vec{I}_{2,ring}$ are included to account for any circulating sequence currents which may arise from asymmetry in the network [41,42]. These currents will be opposite in polarity on the two feeders, and hence they are not observed when considering the sum of currents on the two feeders.

2.1.2. Sequence currents during fault

A ground fault is assumed to occur in phase a somewhere on the feeder in Fig. 3. Eq. (2) is modified to account for the fault current, and (5) is obtained.

$$\begin{aligned}3\vec{I}_0 &= \vec{V}_n\tilde{Y} + \vec{E}_a\hat{Y} + \vec{I}_F\\ 3\vec{I}_2 &= \vec{V}_n\hat{Y} + \vec{E}_a\tilde{Y} + \vec{I}_L + \vec{I}_F\end{aligned} \tag{5}$$

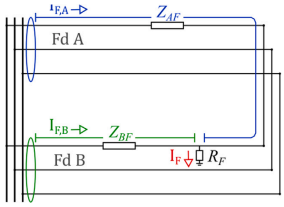

Fig. 4. The impedances Z_{AF} and Z_{BF}.

Using the same approach to describe the currents measured on each feeder in the ring as previously, (4) is rewritten as (6).

$$\begin{aligned}
3\vec{I}_{0,A} &= \vec{V}_n\hat{Y}\cdot m_A + \vec{E}_a\hat{Y}\cdot n_A + \vec{I}_{0,ring} + \vec{I}_{F,A}\\
3\vec{I}_{0,B} &= \vec{V}_n\hat{Y}\cdot m_B + \vec{E}_a\hat{Y}\cdot n_B - \vec{I}_{0,ring} + \vec{I}_{F,B}\\
3\vec{I}_{2,A} &= \vec{V}_n\hat{Y}\cdot q_A + \vec{E}_a\hat{Y}\cdot s_A + \vec{I}_L\cdot t_A + \vec{I}_{2,ring} + \vec{I}_{F,A}\\
3\vec{I}_{2,B} &= \vec{V}_n\hat{Y}\cdot q_B + \vec{E}_a\hat{Y}\cdot s_B + \vec{I}_L\cdot t_B - \vec{I}_{2,ring} + \vec{I}_{F,B}
\end{aligned} \tag{6}$$

The currents $\vec{I}_{F,A}$ and $\vec{I}_{F,B}$ are the fault current components measured on feeder A and B, respectively.

3. Proposed method

3.1. Estimating the impedance ratio

The per phase series impedances measured along feeders A and B to the fault point are labelled Z_{AF} and Z_{BF}, respectively, as illustrated in Fig. 4. Current division suggests that the ratio of these impedance are the inverse of the ratio of the fault current components $\vec{I}_{F,A}$ and $\vec{I}_{F,B}$, as expressed in (7).

$$\frac{Z_{BF}}{Z_{AF}} = \frac{\vec{I}_{F,A}}{\vec{I}_{F,B}} \tag{7}$$

If the components $\vec{I}_{F,A}$ and $\vec{I}_{F,B}$ can be obtained from measurements, and the impedances of the two lines are known in advance, the distance to fault can easily be estimated. To obtain $\vec{I}_{F,A}$ and $\vec{I}_{F,B}$, the change in zero and negative sequence currents before and after fault inception are utilised as described by (8).

$$\begin{aligned}
\Delta 3\vec{I}_{0,A} &= \Delta\vec{V}_n\hat{Y}\cdot m_A + \vec{I}_{F,A}\\
\Delta 3\vec{I}_{0,B} &= \Delta\vec{V}_n\hat{Y}\cdot m_B + \vec{I}_{F,B}\\
\Delta 3\vec{I}_{2,A} &= \Delta\vec{V}_n\hat{Y}\cdot q_A + \vec{I}_{F,A}\\
\Delta 3\vec{I}_{2,B} &= \Delta\vec{V}_n\hat{Y}\cdot q_B + \vec{I}_{F,B}
\end{aligned} \tag{8}$$

The Δ-notation introduced in (8) is used to described the change in a current or voltage phasor compared to its value at some pre-fault time t_{pre}. The value of this change at any time t is then $\Delta\vec{I}(t) = \vec{I}(t) - \vec{I}(t_{pre})$.

From (8) the ratio of the fault current components can be found by using either of the two sequence currents. In terms of change in zero sequence current and change in neutral voltage, this ratio is given by (9).

$$\frac{\vec{I}_{F,A}}{\vec{I}_{F,B}} = \frac{\Delta 3\vec{I}_{0,A} - \Delta\vec{V}_n\hat{Y}\cdot m_A}{\Delta 3\vec{I}_{0,B} - \Delta\vec{V}_n\hat{Y}\cdot m_B} \tag{9}$$

Similarly, if the term $\Delta\vec{V}_n\hat{Y}$ is assumed negligible, then the same ratio can be obtained by (10).

$$\frac{\vec{I}_{F,A}}{\vec{I}_{F,B}} = \frac{\Delta\vec{I}_{2,A}}{\Delta\vec{I}_{2,B}} \tag{10}$$

Because $\hat{Y} \ll \bar{Y}$ in any real network, omitting $\Delta\vec{V}_n\hat{Y}$ in (10) is assumed to be a valid simplification. The term $\Delta\vec{V}_n\hat{Y}$ can however not be omitted from (9). It is shown in Section 5 that the contribution from the term $\Delta\vec{V}_n\hat{Y}$ is quite small in the test network considered in this paper, where the theoretical value of this component is approximately $0.9A$. For comparison, the term $\Delta\vec{V}_n\bar{Y}$ has a theoretical value of $168A$ in the same network.

Both of the above approaches for estimating the ratio of the fault current components can then be combined with (7). However, a note on the correct impedances should be considered first. So far, the mutual coupling between the phases has been neglected. When the mutual coupling is assumed to be zero, no difference exists between the per phase series reactance, positive sequence reactance or zero sequence reactance of the line. However, as the mutual coupling will be present in any real network, along with an earth return affecting the zero sequence currents, the fault current component ratio as expressed by (9) and (10) will not equal the ratio of the per phase series impedances. Instead, when combining (7) with either (9) or (10), the corresponding sequence impedance must be applied. Eqs. (11) and (12) illustrate this, where the subscripts "0" and "2" have been added to signify zero sequence and negative (and positive) sequence impedances, respectively.

$$\frac{|Z_{0,BF}|}{|Z_{0,AF}|} = \frac{|\Delta 3\vec{I}_{0,A} - \Delta\vec{V}_n\hat{Y}\cdot m_A|}{|\Delta 3\vec{I}_{0,B} - \Delta\vec{V}_n\hat{Y}\cdot m_B|} \tag{11}$$

$$\frac{|Z_{2,BF}|}{|Z_{2,AF}|} = \frac{|\Delta\vec{I}_{2,A}|}{|\Delta\vec{I}_{2,B}|} \tag{12}$$

In the following discussion, (11) is defined as the zero sequence method, and (12) as the negative sequence method.

3.2. Estimating m_A and m_B

As the term $\Delta\vec{V}_n\hat{Y}$ is significant, values for m_A, m_B and $\hat{Y}$ must be available in order for the zero sequence method to be applied. The factors m_A and m_B represent the division of the part of the zero sequence current which is driven by the neutral voltage, and they depend on the topology and line parameters of the ring-connected feeders and their laterals. In this paper, three methods for determining m_A and m_B are considered.

3.2.1. From line parameters

The ring is divided into n zero-sequence PI-equivalents, chosen so that the magnitude of the zero-sequence series impedance for each PI-section is the same, i.e. $|z_1| = |z_2| = |z_3| = \cdots = |z_n|$. The total capacitance of PI-section k is labelled C_k. Next, the parallel capacitances of adjacent PI-equivalents are summed, and $n+1$ capacitances $\tilde{C}_0 - \tilde{C}_n$ are defined in (13).

$$\tilde{C}_i = \begin{cases} \frac{C_i}{2} & x = 0, n \\ \frac{\tilde{C}_{i-1}+C_i}{2} & x = 1, 2, \ldots, n-1 \end{cases} \tag{13}$$

By assuming that all these capacitances experience the same voltage, V_0, and by applying the principle of current division, the expressions below for m_A and m_B can be derived:

$$m_A = \frac{\sum_{i=0}^{n}\tilde{C}_i\frac{n-i}{n}}{\sum_{i=0}^{n}\tilde{C}_i} \tag{14}$$

$$m_B = \frac{\sum_{i=0}^{n}\tilde{C}_i\frac{i}{n}}{\sum_{i=0}^{n}\tilde{C}_i} \tag{15}$$

Laterals on the feeders are simply accounted for by summing their entire zero-sequence capacitance to the corresponding $\tilde{C}_i$.

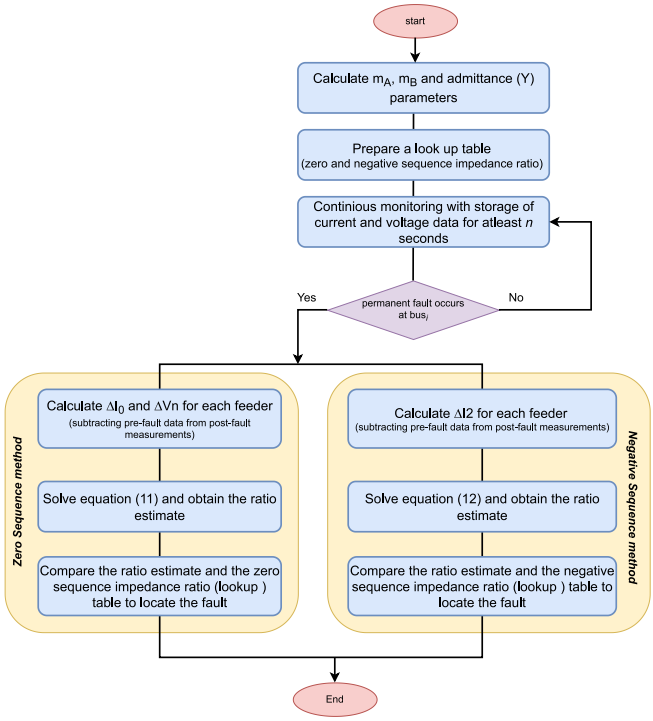

Fig. 5. The proposed earth fault location method.

3.2.2. Ratio of zero sequence currents

This approach is based on cases, either from fault records or earth fault tests, where an earth fault occurred either in the background network or at the substation. In such cases the fault current will not flow through the feeders forming the ring and the change in zero sequence current in these feeders will be due to the change in neutral voltage. Looking at (8), $\vec{I}_{F,A}$ and $\vec{I}_{F,B}$ will both be zero and hence the fraction of zero sequence current flowing through each feeders due to $\Delta\vec{V}_n$ can be obtained as described by (16).

$$\frac{\Delta\vec{I}_{0,A}}{\Delta\vec{I}_{0,B}} = \frac{m_A}{1-m_A} \tag{16}$$

By recognising that the factors m_A and m_B are real numbers, (16) can be further developed to produce (17).

$$m_A = \frac{|\,\Delta\vec{I}_{0,A}\,|}{|\,\Delta\vec{I}_{0,A}\,| + |\,\Delta\vec{I}_{0,B}\,|} \tag{17}$$

3.2.3. Ratio of zero sequence current and voltage

This approach considers a fault somewhere in the background network, at the main busbar, or at the beginning of one of the two feeders. For faults in the background network or at the main busbar $\vec{I}_{F,A}$ and $\vec{I}_{F,B}$ will be zero as established previously. If a fault occurs at the beginning of one of the feeders, the fault current component on the other feeder will be zero. Assume for instance that the fault occurred on the beginning of feeder B. If the neutral voltage is available in the fault records, the factor m_A can be obtained as described by (18).

$$m_A = \frac{|\Delta 3\vec{I}_{0,A}|}{|\Delta\vec{V}_n\bar{Y}|} \tag{18}$$

If the admittance $\bar{Y}$ is not known, or if it cannot be determined with sufficient accuracy, earth fault tests can be performed to obtain it along with m_A and m_B. By applying faults consecutively at the beginning of each feeder, the factors $\bar{Y}\cdot m_A$ and $\bar{Y}\cdot m_B$ can be obtained directly.

The flowchart of the proposed algorithm is shown in Fig. 5. Overall, the method requires to define system level parameters (such as m_A, m_B, $\bar{Y}$) beforehand and to store the pre-fault current and voltage measurements at the primary substation. When a fault occurs, Eqs. (11) and (12) are used to estimate ratio of fault currents in the two feeders forming the ring. The ratio estimate is then compared with the ideal impedance ratio and interpolation will be used to locate the earth fault.

4. System description and modelling

The test case network used for the evaluating the methods is based on an existing 22 kV distribution network. Network data have been provided by Norwegian network operator Elvia, and some changes have

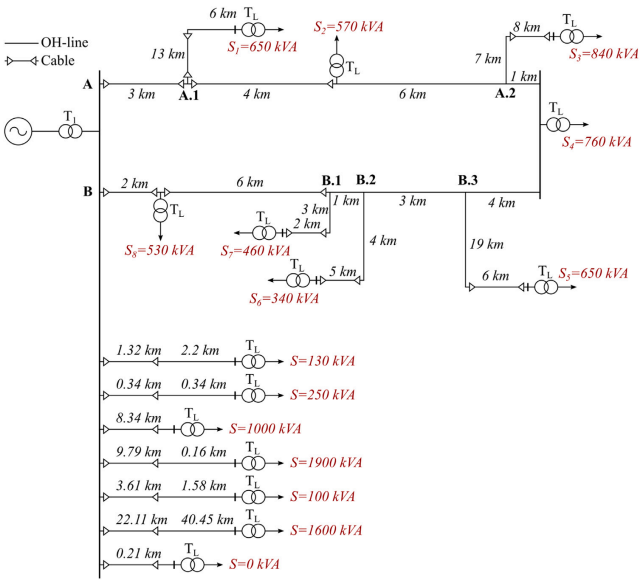

Fig. 6. Topology of ring-connected feeders A and B.

been made to the topology both to obtain the desired properties and to be able to disclose the model used.

The network consists of a single main transformer with isolated neutral supplying nine feeders connected at a main bus bar. The supplying grid is modelled as an ideal 132 kV voltage source with a source impedance modelled according IEC 60909 [43] to produce the desired short circuit capacity in the network. The short circuit power is expected to be in the range of 130–450 MVA, and the results are obtained using a 250 MVA source unless otherwise specified.

Feeders A and B have been connected to form a ring, and all faults are applied to these feeders. Fig. 6 shows the details of the ring connected feeders. Feeder A and B are modelled in greater detail, with five laterals included (A.1, A.2, B.1, B.2 and B.3), and with loads distributed around the ring. Furthermore, feeders A and B are modelled as series connected PI-segments of length 1 km to better represent the distributed nature of the line parameters. All the loads in the network are constant impedance loads with power factor 0.9 connected via load transformers. As a simplification, the other seven feeders C-I are modelled without laterals and with loads concentrated at the feeder ends. Complete network data can be found in Table 1.

Table 1
Test network and model parameters.

Network data	
OH-line	3-phase PI-section: 50 Hz, R=0.077 Ω/km, X=0.34 Ω/km, C=10.806 nF/km, R_0 = 0.413 Ω/km, X_0 = 1.134 Ω/km, C_0=5.976 nF/km, G_0=37.55 nS/km. Asymmetry: 2% and 3% are added to C_0 in phases *a* and *b*, respectively.
Cable	3-phase PI-section: 50 Hz, R=0.125 Ω/km, X=0.11 Ω/km, C = C_0=0.28 μF/km. Asymmetry: 1% and 2% are added to C_0 in phases *a* and *c*, respectively.
Main transformer	100 MVA 132/22 kV Dy1 transformer. X=6%, R=0.25%. Modelled using the Hybrid transformer model in ATPDraw with typical values for inductance and resistance, no capacitance or core effects included.
Load transformers	2 MVA 22/0.4 kV Dy1 transformer grounded on the LV-side. X=5%, R=0.78%. Modelled using the Hybrid transformer model in ATPDraw with typical values for inductance and resistance, no capacitance or core effects included.
Loads	Grounded Y-connected constant impedance loads.
Simulation and data processing	
Sample rate: 2 kHz. Matlab-designed equiripple FIR high-pass filter: f_{pass} = 45 Hz, passband ripple = 0.1 dB. Software: ATPDraw version 7.2p11.	

5. Simulation result and analysis

The methods are tested for earth faults at 30 different fault locations evenly spaced around the ring, i.e. every km. The distance to fault is measured from the beginning of feeder A for all cases. The parameters m_A and m_B are set to m_A = 0.5486 and m_B = 0.4514, obtained by applying a fault at the main bus bar and using (17). For comparison, the estimation of m_A and m_B from line parameters yielded m_A = 0.5489 and m_B = 0.4511.

The final estimates produced by each method are obtained as the average estimates between 250 ms and 270 ms after fault inception to allow for steady state conditions, whereas the pre-fault values are obtained 150 ms before fault inception.

5.1. Fault resistance and load asymmetry

Both the fault resistance and the load symmetry is varied. The load symmetry is varied by changing the load impedance in the individual

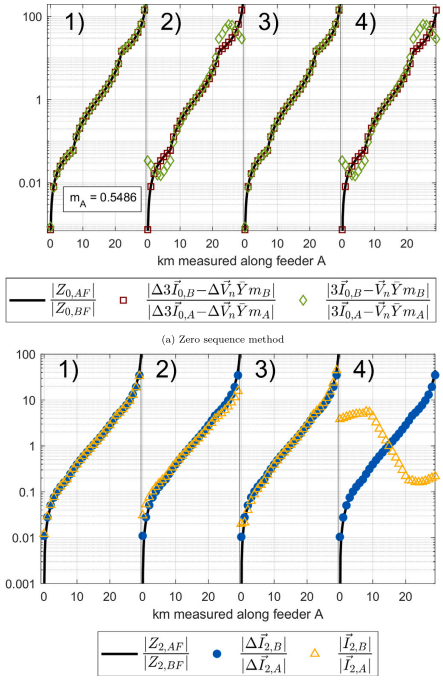

Fig. 7. Results for scenarios 1–4. Simplified versions not considering pre-fault values are included for reference.

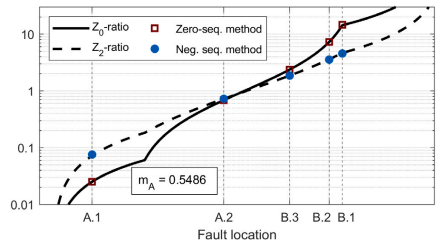

Fig. 8. Zero sequence method and negative sequence method results when faults occur on laterals.

phases of the load supplied by the ring, whereas the other loads in the system remain balanced. During asymmetrical loading, the load impedance of phases *a*, *b*, and *c* are Z_L, $1.1{\cdot}Z_L$ and $0.9{\cdot}Z_L$, respectively, where Z_L is the per phase impedance corresponding to the nominal loads S1-S8 in Fig. 6. The following four scenarios are then considered:

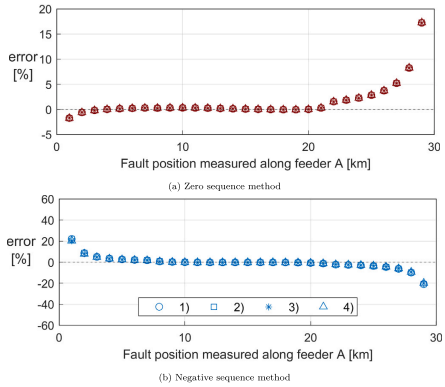

Fig. 9. Percentage errors for both methods in scenario 1–4.

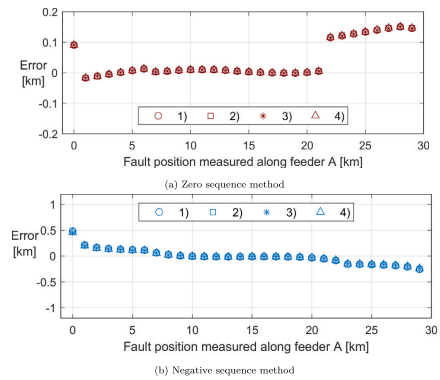

Fig. 10. Distance estimate errors for both methods in scenario 1–4.

1. $R_f = 1\ \Omega$, symmetrical load
2. $R_f = 1\ \text{k}\Omega$, symmetrical load
3. $R_f = 1\ \Omega$, asymmetrical load
4. $R_f = 1\ \text{k}\Omega$, asymmetrical load

The results are shown in Fig. 7. The results show that both methods are resilient against load asymmetry and fault resistance. Fig. 7(a) shows that applying the zero sequence method without considering pre-fault values can provide reasonable accuracy for low impedance faults, whereas the accuracy is drastically reduced for large fault resistances. The zero sequence method is however unaffected by the load asymmetry, even when pre-fault values are not considered. Fig. 7(b) illustrates that the application of negative sequence currents directly without subtracting their pre-fault values, as done in [44], is only a viable option for low impedance faults. Unbalanced loads also have a negative impact on this particular method, especially in conjunction with a large fault resistance.

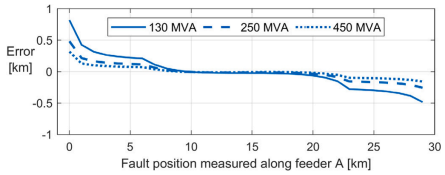

Fig. 11. Distance estimate errors for negative sequence method for different source impedances.

To investigate the effect of faults on laterals, faults are applied to each of the five laterals in turn. The faults are applied at the intersection of the cable and OH-lines on the laterals, and the results are shown in Fig. 8. Both methods see these faults as if they occurred at the connection point between the lateral and the ring itself. No variation was observed across scenarios 1–4 in these fault cases.

Fig. 9 shows the percentage prediction error for the two methods in the four scenarios considered above, where positive errors correspond overestimating the impedance ratio. Fig. 10 shows the errors in absolute distance. It can be seen that when mapped to this view, the seemingly large errors towards the line ends are less pronounced. As the slope of the impedance ratio is quite steep towards the ends, an error in the estimate ratio translates to a relatively small error in distance estimate compared to faults in the middle of the ring. This presentation also shows the discontinuities in the graph more clearly, which occur due to the different impedances of the cable sections and the OH-lines.

Figs. 9 and 10 suggest that the methods are complementary, and that their simultaneous application may yield better results. In the scenarios shown in the figures this would be the case, but as shown later in the paper, the two methods will not be complementary in the presence of measurement errors and other imperfections. Therefore, an average of the two methods is not guaranteed to give any real improvements.

The figures confirm that the zero sequence method and the negative sequence method have pretty similar performance in all the four scenarios. Both methods show good accuracy for faults in the middle of the line, whereas the accuracy tapers off towards the outer ends of the ring. For the negative sequence method this is in part assumed to be caused by the terms $\Delta\vec{V}_n\hat{Y}\cdot q_A$ and $\Delta\vec{V}_n\hat{Y}\cdot q_B$ in (8), which were assumed negligible when deriving (12). As the fault is moved closer to either end of the ring, for instance at the beginning of feeder A, the fault current component on feeder B should in theory approach 0. The terms $\Delta\vec{V}_n\hat{Y}\cdot q_A$ and $\Delta\vec{V}_n\hat{Y}\cdot q_B$ are then no longer negligible. For instance, assuming that $\Delta\vec{V}_n \approx \frac{22}{\sqrt{(3)}}kV$, the term $\Delta\vec{V}_n\hat{Y}$ should be approximately $0.9A$, which is close to the observed value of $\Delta\vec{I}_{2.B} = 1.2A$ when the fault occurs close to terminal A. A similar argument can be made to explain why the zero sequence method shows poorer accuracy near the two ends of the ring, although this method is sensitive to a variety of parameters as will be discussed in later sections of this paper.

The main source of error for the negative sequence method is however the source impedance of the network. If this is assumed to be very large, the negative sequence method becomes less accurate. Fig. 11 illustrates to impact of the source impedance as the short circuit capacity is varied between 130 MVA and 450 MVA. When the short circuit capacity increases and the source impedance decreases, the estimation error is reduced. However, even with a stiff grid the error does not reach zero, suggesting that the factors discussed above are of some importance. The zero sequence method is not affected by this parameter.

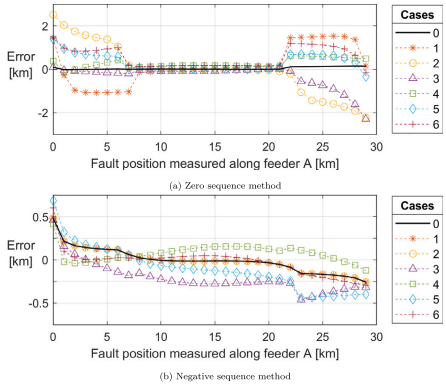

Fig. 12. Distance estimate errors for both methods considering current measurement errors.

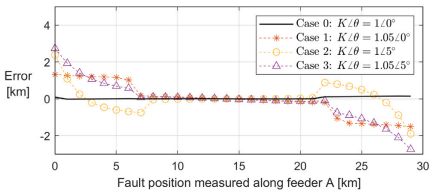

Fig. 13. Zero sequence method distance estimate error for various neutral voltage measurement errors.

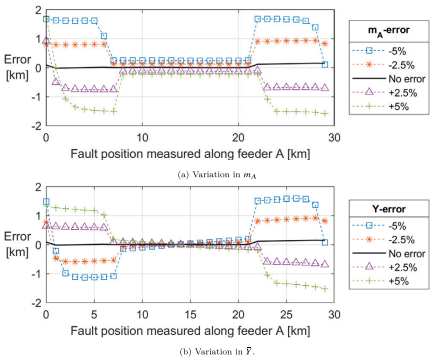

Fig. 14. Zero sequence method distance estimate error for inaccurate values of m_A and $\bar{Y}$.

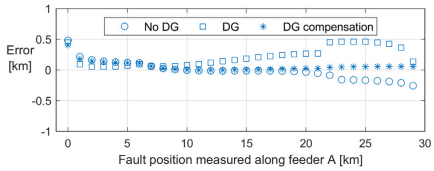

Fig. 15. Impact of DG on the negative sequence method.

Table 2
Phase current measurement errors.

Case	$K\angle\theta$					
	Feeder B			Feeder A		
	Ph. a	Ph. b	Ph. c	Ph. a	Ph. b	Ph. c
0	$1\angle 0°$	$1\angle 0°$	$1\angle 0°$	$1\angle 0°$	$1\angle 0°$	$1\angle 0°$
1	$1.05\angle 0°$	$1.05\angle 0°$	$1.05\angle 0°$	$1.05\angle 0°$	$1.05\angle 0°$	$1.05\angle 0°$
2	$1\angle 5°$	$1\angle 5°$	$1\angle 5°$	$1\angle 5°$	$1\angle 5°$	$1\angle 5°$
3	$1\angle 0°$	$1\angle 0°$	$1\angle 0°$	$1.05\angle 5°$	$1.05\angle 5°$	$1.05\angle 5°$
4	$1.5\angle 0°$	$1.02\angle 0°$	$0.96\angle 0°$	$1.01\angle 0°$	$1.03\angle 0°$	$0.99\angle 0°$
5	$1\angle 5°$	$1\angle 2°$	$1\angle 1°$	$1\angle -5°$	$1\angle -4°$	$1\angle 2°$
6	$1.05\angle 5°$	$1.02\angle 2°$	$0.96\angle 1°$	$1.01\angle -5°$	$1.03\angle -4°$	$0.99\angle 2°$

Overall, the simulation analysis showed that the negative sequence method can locate earth faults with a ±250-meter margin for most fault locations around the ring, and in the worst case, there is a ±500-meter error margin for fault locations close to the end of the lines. The negative sequence method is unaffected by variations in fault resistance and load symmetry. The short circuit capacity of the network does however impact the results. The zero sequence method can locate earth faults within a ±150-meter margin for most fault locations, and is not affected by fault resistance, load symmetry or the short circuit capacity of the network.

5.2. Measurement errors

The performance of the two methods were investigated against measurement inaccuracies. To emulate measurement errors, the measured phasors are multiplied by some disturbance $K\angle\theta$.

5.2.1. Phase currents

Measurement errors are applied to each of the six phase currents measured on feeders A and B, as described by Table 2. Scenario (1) is considered, and the distance error for both methods with the various combinations of measurement errors applied are showed in Figs. 12(a) and 12(b).

The results show that symmetrical measurement errors, i.e. the same measurement error in all the six current transformers (CTs), have no visible effect on the negative sequence results, whereas the zero sequence method is affected. This is as expected when inspecting (12), in which symmetrical measurement errors applied to the negative sequence measurements will cancel. Eq. (11) shows that this is not the case for the zero sequence method, as the nominator and denominator will not be equally affected.

The unsymmetrical measurement errors will as expected have a negative effect on both methods, although it is less apparent how a particular set of measurement errors will affect the accuracy at various fault locations. It is noted that symmetrical measurement errors within each set of measurements at terminal A and B, here represented by case 3, still gives a considerable negative effect on the results.

The measurement errors also accentuates the effect of the different line segments. Faults occurring in the overhead line consistently produces lower distance estimate errors in the case of the zero sequence methods, whereas the negative sequence method generally becomes less accurate for faults in the overhead line. However, the magnitude of the errors are significantly larger for the zero sequence method, whereas the negative sequence method accuracy is mostly kept within $\pm 500m$.

In a realistic implementation the zero sequence method could however utilise zero sequence current transformers to measure the zero sequence current directly, and thus achieve higher measurement accuracy than the phase current measurements.

5.2.2. Neutral voltage

Measurement errors are applied to the neutral voltage measurements in the same way as was done for the phase currents, and both the cases and the results are shown in Fig. 13. Compared to the effect of phase current measurement errors, the measurement error in neutral voltage gives a similar reduction in precision for the zero sequence method, with a reduced precision towards the ends of the ring. The negative sequence method is obviously not impacted by this measurement.

5.3. Other sensitivity analysis

The zero sequence method requires values for the ring admittance to ground $\bar{Y}$, as well as m_A and m_B. These values are varied within ±5% of their correct values, and the resulting errors are shown in Fig. 14. Note that the parameter $\bar{Y}$ also includes the admittance to ground of the laterals connected to feeders A and B, not just the admittances of A and B.

Both variation in m-values and $\bar{Y}$ result in a significant degradation of the zero sequence method results. Variation in m_A has a greater impact on the results than variation in $\bar{Y}$, as is expected when considering (11). As $m_B = 1 - m_A$, variation in m_A is necessarily accompanied by variation in m_B, which gives a larger impact than simply varying $\bar{Y}$.

Eq. (11) also has the interesting property of becoming independent of $\bar{Y}$ at the fault location corresponding to

$$\frac{Z_{0,BF}}{Z_{0,AF}} = \frac{m_A}{m_B}$$

This effect is observed at approximately 13 km, where the zero sequence method produce the same result regardless of $\bar{Y}$.

The methods have also been tested in a compensated network, as well as a network without any background network, both of which yielded good results. A reduction in accuracy was however observed, particularly for the compensated network, suggesting that the fault current level will have an impact on the methods.

The behaviour of the two methods during two phase and three phase short circuit faults was investigated briefly. The negative sequence method works for two-phase short circuits as well as some three-phase faults, though it appears dependent on the short circuit capacity of the network. The zero sequence method is only valid for single phase faults.

During testing of the methods it was observed that the zero sequence method was much more sensitive to large fault resistances when unfiltered measurements were used. This occurred due to the slow exponential decay which is observed in the neutral voltage and the fault current for high impedance faults. Although this effect was also observed for the negative sequence method, the effect on the distance estimates was much less pronounced. Including a high-pass filter therefore becomes critical when applying the zero sequence method.

Lastly, the presence of DG in the network was investigated briefly. A source rated at approximately 1 MVA was added to the network in parallel with load S_2, and scenario (1) from earlier was evaluated with and without the presence of this DG. As expected, the presence of the generator had a minor impact on the negative sequence method as shown in Fig. 15. If the negative sequence current is measured at the DG location, the effect of the DG can however be eliminated. The negative sequence current measured at the DG will be observable in the measurements at feeders A and B, and the magnitude of this current

in these two locations can simply be estimated using current division between the DG location and the main bus. The DG current can then be eliminated from the measurements on feeders A and B, and the result of compensating for the effect of the DG in this way is also shown in Fig. 15. Using such an approach will however turn the method into a wide-area method with added complexity, and given the small impact of the DG on the results this may not be necessary. Finally, as the DG is separated from the network via a load transformer, the zero sequence method is not impacted by DG in the network.

6. Conclusion

This paper has presented two novel methods for locating earth faults in a MV distribution network. The two methods are based on utilising the ratio of change in zero and negative sequence current during fault on ring-connected feeders, though one of the methods also requires zero sequence voltage measurements. Compared to previous work, the paper have made the following contributions: (1) improved accuracy of earth fault location compared to methods not considering pre-fault measurement; (2) provided equations describing sequence currents in a ring network, particularly the division of zero sequence currents among two ring-connected feeders. The paper also provides experimental approaches for determining this division of zero sequence currents.

The two methods developed in this paper show good accuracy in fault location. The negative sequence method yielded maximum distance estimate errors in the range of 0.3–1 km in the test network, depending measurement errors and on the assumed source impedance of the supplying network. The zero sequence method yielded errors less than 200 m in the ideal cases, but the estimation error increased when measurement errors were applied. Fault resistance and unbalanced loads have little effect on either of the methods, whereas inaccurate current and voltage measurements represent the largest sources of error. The negative sequence method appears to be robust against most sources of error. The measurement of negative sequence currents may however not be readily available in most distribution networks, and the method is affected by the source impedance of the supplying network. The zero sequence method is likely easier to implement due to the availability of measurements, but it is relatively less robust due to its dependency on several uncertain parameters.

The size of the background network have been found to have little effect on the method, although this has not been tested extensively. The methods have also been verified in a resonance grounded system where it yielded promising results, though further testing is required in order to describe the performance properly in such networks.

Future work will mainly focus on further testing of the methods on a laboratory setup and later on a real power grid network.

CRediT authorship contribution statement

Tesfaye Amare Zerihun: Conceptualization, Methodology, Software, Validation, Formal Analysis,Visualisation, Investigation, Writing – original draft, Writing – review & editing. **Thomas Treider:** Conceptualization, Methodology, Software, Validation , Formal Analysis,Visualisation, Investigation, Writing – original draft, Writing – review & editing. **Henning Taxt:** Conceptualization, Methodology, Writing – review & editing, Supervision. **Lars B. Nordevall:** Conceptualization, Writing – review & editing, Supervision. **Thomas S. Haugan:** Methodology, Software, Writing – review & editing.

Declaration of competing interest

The authors declare that they have no known competing financial interests or personal relationships that could have appeared to influence the work reported in this paper.

Acknowledgements

This paper has been funded by the CINELDI - Centre for intelligent electricity distribution, an 8 year Research Centre under the Research Council of Norway's FME-scheme (Centre for Environment-friendly Energy Research, 257626/E20), and the Norwegian Research Council project ProDig (295034/E20). The authors gratefully acknowledge the financial support from the Research Council of Norway and the CINELDI and ProDig partners.

References

[1] S. Hänninen, et al., Single Phase Earth Faults in High Impedance Grounded Networks: Characteristics, Indication and Location, VTT Technical Research Centre of Finland, 2001.
[2] F. Aboshady, D. Thomas, M. Sumner, A new single end wideband impedance based fault location scheme for distribution systems, Electr. Power Syst. Res. 173 (2019) 263–270.
[3] R. Dashti, J. Sadeh, Accuracy improvement of impedance-based fault location method for power distribution network using distributed-parameter line model, Int. Trans. Electr. Energy Syst. 24 (3) (2014) 318–334.
[4] R. Dashti, J. Sadeh, Applying dynamic load estimation and distributed-parameter line model to enhance the accuracy of impedance-based fault-location methods for power distribution networks, Electr. Power Compon. Syst. 41 (14) (2013) 1334–1362.
[5] A.D. Filomena, M. Resener, R.H. Salim, A.S. Bretas, Fault location for underground distribution feeders: An extended impedance-based formulation with capacitive current compensation, Int. J. Electr. Power Energy Syst. 31 (9) (2009) 489–496, http://dx.doi.org/10.1016/j.ijepes.2009.03.026, URL https://www.sciencedirect.com/science/article/pii/S0142061509000544, Power Systems Computation Conference (PSCC) 2008.
[6] Y. Liao, Generalized fault-location methods for overhead electric distribution systems, IEEE Trans. Power Deliv. 26 (1) (2011) 53–64, http://dx.doi.org/10.1109/TPWRD.2010.2057454.
[7] A. Nikander, P. Jarventausta, Methods for earth fault identification and distance estimation in a compensated medium voltage distribution network, in: Proceedings of EMPD '98. 1998 International Conference on Energy Management and Power Delivery, Vol. 2, Cat. No.98EX137, 1998, pp. 595–600 vol.2, http://dx.doi.org/10.1109/EMPD.1998.702754.
[8] M.A. Aftab, S.S. Hussain, I. Ali, T.S. Ustun, Dynamic protection of power systems with high penetration of renewables: A review of the traveling wave based fault location techniques, Int. J. Electr. Power Energy Syst. 114 (2020) 105410, http://dx.doi.org/10.1016/j.ijepes.2019.105410, URL https://www.sciencedirect.com/science/article/pii/S0142061518331594.
[9] C.Y. Evrenosoglu, A. Abur, Fault location in distribution systems with distributed generation, in: Proc. Power Systems Computation Conference, 2005.
[10] D. Coggins, D.W. Thomas, B.R. Hayes-Gill, Y. Zhu, An fpga based travelling-wave fault location system, in: 2007 International Conference on Field-Programmable Technology, IEEE, 2007, pp. 277–280.
[11] H. Liu, X. Zeng, Y. Wang, F. Peng, Research on travelling wave transmission characteristics in distribution network, in: 2012 China International Conference on Electricity Distribution, IEEE, 2012, pp. 1–5.
[12] A. Farughian, L. Kumpulainen, K. Kauhaniemi, Review of methodologies for earth fault indication and location in compensated and unearthed MV distribution networks, Electr. Power Syst. Res. 154 (2018) 373–380.
[13] R. Dashti, M. Tahavori, M. Daisy, H.R. Shaker, A new matching algorithm for fault section estimation in power distribution networks, in: 2018 International Symposium on Advanced Electrical and Communication Technologies, ISAECT, IEEE, 2018, pp. 1–4.
[14] E. Gord, R. Dashti, M. Najafi, H.R. Shaker, Real fault section estimation in electrical distribution networks based on the fault frequency component analysis, Energies 12 (6) (2019) 1145.
[15] J. Mora-Florez, V. Barrera-Nunez, G. Carrillo-Caicedo, Fault location in power distribution systems using a learning algorithm for multivariable data analysis, IEEE Trans. Power Deliv. 22 (3) (2007) 1715–1721, http://dx.doi.org/10.1109/TPWRD.2006.883021.
[16] F. Chunju, K. Li, W. Chan, Y. Weiyong, Z. Zhaoning, Application of wavelet fuzzy neural network in locating single line to ground fault (SLG) in distribution lines, Int. J. Electr. Power Energy Syst. 29 (6) (2007) 497–503, http://dx.doi.org/10.1016/j.ijepes.2006.11.009, URL https://www.sciencedirect.com/science/article/pii/S0142061506002092.
[17] M. Pourahmadi-Nakhli, A.A. Safavi, Path characteristic frequency-based fault locating in radial distribution systems using wavelets and neural networks, IEEE Trans. Power Deliv. 26 (2) (2010) 772–781.
[18] X. Deng, R. Yuan, Z. Xiao, T. Li, K.L.L. Wang, Fault location in loop distribution network using SVM technology, Int. J. Electr. Power Energy Syst. 65 (2015) 254–261, http://dx.doi.org/10.1016/j.ijepes.2014.10.010, URL https://www.sciencedirect.com/science/article/pii/S0142061514006139.

[19] G. Liang, P. Liyuan, L. Ruihuan, Z. Fen, W. Xin, Fault location in distribution network with distributed generation based on neural network, in: 2014 China International Conference on Electricity Distribution, CICED, IEEE, 2014, pp. 209–212.

[20] A.C. Adewole, R. Tzoneva, S. Behardien, Distribution network fault section identification and fault location using wavelet entropy and neural networks, Appl. Soft Comput. 46 (2016) 296–306.

[21] K. Jia, Z. Ren, T. Bi, Q. Yang, Ground fault location using the low-voltage-side recorded data in distribution systems, IEEE Trans. Ind. Appl. 51 (6) (2015) 4994–5001, http://dx.doi.org/10.1109/TIA.2015.2425358.

[22] F.C.L. Trindade, W. Freitas, J.C.M. Vieira, Fault location in distribution systems based on smart feeder meters, IEEE Trans. Power Deliv. 29 (1) (2014) 251–260, http://dx.doi.org/10.1109/TPWRD.2013.2272057.

[23] J. Altonen, A. Wahlroos, Performance of modern fault passage indicator concept in compensated MV-networks, in: CIRED Workshop 2016, IET, 2016, pp. 1–4.

[24] J.-H. Teng, W.-H. Huang, S.-W. Luan, Automatic and fast faulted line-section location method for distribution systems based on fault indicators, IEEE Trans. Power Syst. 29 (4) (2014) 1653–1662.

[25] R. Calone, A. Cerretti, A. Fatica, Evolution of the fault locator on MV distribution networks: From simple stand alone device, to a sophisticated strategic component of the smart grid control system, in: Proc. 21st Int. Conf. Exhib. Electr. Distrib., CIRED, 2011.

[26] M. Pignati, L. Zanni, P. Romano, R. Cherkaoui, M. Paolone, Fault detection and faulted line identification in active distribution networks using synchrophasors-based real-time state estimation, IEEE Trans. Power Deliv. 32 (1) (2016) 381–392.

[27] S. Jamali, A. Bahmanyar, E. Bompard, Fault location method for distribution networks using smart meters, Measurement 102 (2017) 150–157, http://dx.doi.org/10.1016/j.measurement.2017.02.008, URL https://www.sciencedirect.com/science/article/pii/S0263224117301033.

[28] D. Topolanek, P. Toman, V. Jurak, M. Jurík, J. Jiricka, J. Drápela, Evaluation of the New Method Vdip for an Earth Fault Location, AIM, 2019.

[29] L.J. Awalin, H. Mokhlis, A.H.A. Halim, Improved fault location on distribution network based on multiple measurements of voltage sags pattern, in: 2012 IEEE International Conference on Power and Energy, PECon, 2012, pp. 767–772, http://dx.doi.org/10.1109/PECon.2012.6450319.

[30] M.A. Elsadd, N.I. Elkalashy, T.A. Kawady, A.-M.I. Taalab, M. Lehtonen, Incorporating earth fault location in management-control scheme for distribution networks, IET Gener. Transm. Distrib. 10 (10) (2016) 2389–2398.

[31] P. Bountouris, H. Guo, D. Tzelepis, I. Abdulhadi, F. Coffele, C. Booth, MV faulted section location in distribution systems based on unsynchronized LV measurements, Int. J. Electr. Power Energy Syst. 119 (2020) 105882.

[32] D. Topolanek, M. Lehtonen, P. Toman, J. Orsagova, J. Drapela, An earth fault location method based on negative sequence voltage changes at low voltage side of distribution transformers, Int. J. Electr. Power Energy Syst. 118 (2020) 105768.

[33] A. Farughian, L. Kumpulainen, K. Kauhaniemi, Earth fault location using negative sequence currents, Energies 12 (19) (2019) 3759.

[34] M. Lehtonen, O. Siirto, M.F. Abdel-Fattah, Simple fault path indication techniques for earth faults, in: 2014 Electric Power Quality and Supply Reliability Conference, PQ, IEEE, 2014, pp. 371–378.

[35] A. Silos-Sanchez, R. Villafafila-Robles, P. Lloret-Gallego, Novel fault location algorithm for meshed distribution networks with DERs, Electr. Power Syst. Res. 181 (2020) 106182.

[36] K. Sun, Q. Chen, P. Zhao, Automatic faulted feeder section location and isolation method for power distribution systems considering the change of topology, Energies 10 (8) (2017) 1081.

[37] A. Mohamed, B. Younes, T. Lamhamdi, H. El Moussaoui, H. El Markhi, Fault location and isolation technique in smart distribution systems with distributed generation, in: 2020 1st International Conference on Innovative Research in Applied Science, Engineering and Technology, IRASET, IEEE, 2020, pp. 1–5.

[38] M.A. Ataei, M. Gitizadeh, M. Lehtonen, R. Razavi-Far, Multi-agent based protection scheme using current-only directional overcurrent relays for looped/meshed distribution systems, IET Gener. Transm. Distrib. 16 (8) (2022) 1567–1581.

[39] T. Zhang, H. Yu, P. Zeng, L. Sun, C. Song, J. Liu, Single phase fault diagnosis and location in active distribution network using synchronized voltage measurement, Int. J. Electr. Power Energy Syst. 117 (2020) 105572, http://dx.doi.org/10.1016/j.ijepes.2019.105572, URL https://www.sciencedirect.com/science/article/pii/S0142061519314887.

[40] H. Saadat, Power System Analysis, third ed., PSA Publishing, S.l., 2010.

[41] M. Loos, S. Werben, J.C. Maun, Circulating currents in closed loop structure, a new problematic in distribution networks, in: 2012 IEEE Power and Energy Society General Meeting, 2012, pp. 1–7, http://dx.doi.org/10.1109/PESGM.2012.6344889.

[42] A. Kalyuzhny, G. Kushnir, Analysis of current unbalance in transmission systems with short lines, IEEE Trans. Power Deliv. 22 (2) (2007) 1040–1048, http://dx.doi.org/10.1109/TPWRD.2006.883011.

[43] Short-circuit currents in three-phase A.C. systems - Part 0: Calculation of currents, 2016.

[44] M. Biller, J. Jaeger, Novel distance protection algorithm based on current comparison for closed-ring structures with distributed generation, in: 15th International Conference on Developments in Power System Protection, DPSP 2020, 2020, pp. 1–6, http://dx.doi.org/10.1049/cp.2020.0043.

Paper IV

T. Treider and H. K. Høidalen, "Estimating distance to transient and restriking earth faults in high-impedance grounded, ring-operated distribution networks using current ratios," *Electric Power Systems Research*, vol. 224, 2023, Art. no. 109765.

[3]https://creativecommons.org/licenses/by/4.0/

Electric Power Systems Research 224 (2023) 109765

Contents lists available at ScienceDirect

Electric Power Systems Research

journal homepage: www.elsevier.com/locate/epsr

Estimating distance to transient and restriking earth faults in high-impedance grounded, ring-operated distribution networks using current ratios ☆

Thomas Treider *, Hans Kristian Høidalen

Department of Electric Energy, Norwegian University of Science and Technology, Trondheim, Norway

ARTICLE INFO

Keywords:
Closed-ring networks
Earth faults
Fault location
Intermittent faults
Restriking faults

ABSTRACT

Earth faults occur frequently in distribution networks, and in resonant grounded networks they are challenging to locate precisely due to their naturally low fault current. Transient and restriking faults are more challenging still due to the short time available for the fault location logic, as well as the absence of steady-state conditions. This paper investigates the performance of three fault location methods utilizing the ratios of various current components in a network operated in a closed-ring configuration. A frequency dependent model of a distribution network is used to simulate transient and restriking faults, and both isolated grounding and resonance grounding are considered. The results show that fault location based on negative-sequence currents is able to locate transient faults, and its accuracy of a few hundred metres is comparable to what has been observed during permanent faults. A zero-sequence method is observed to be less accurate, particularly in resonant grounded networks. A transient method is also proposed, and while it is fast, it is ultimately limited by the presence of loads and branches in the network. It is concluded that the negative sequence method is best suited for transient and restriking faults.

1. Introduction

Earth faults are the most common fault type in distribution networks, and 50%–80% of faults in the Nordic countries are of this type [1]. Because the earth fault current is naturally low in small isolated networks, or made low in resonant grounded networks, earth faults have always represented a challenge for the protection and fault location systems in these networks. Due to the unique properties of isolated and resonant grounded networks, earth faults require an entirely different analysis than what can be applied in solid grounded networks. Protection principles such as distance protection and overcurrent protection are not suited due to the low fault current levels, and the fault location process is usually limited to the identification of the faulted feeder or section based on directional earth faults relays or fault passage indicators (FPIs). Furthermore, transient and restriking or intermittent faults represent one sub-category of earth faults which are notoriously challenging to locate. These faults are very common in distribution networks, particularly in resonant grounded cable networks [2], and they can often be the start of a more serious fault if not disconnected [3].

A variety of different approaches for detection and location of earth faults can be found in the scientific literature. Usually, the methods assume a radial networks and are often limited to locating the faulty feeder or section of the network. The use of the charge-voltage relationship of different feeders is proposed in [4,5], while estimation of the feeder capacitances is used to find the faulty feeder in [6,7]. Other directional transient principles exist which are supposed to be applicable in non-radial network as well, such as methods based on transient zero sequence energy [8,9]. In [10], a novel protection principle based on the charging transient is proposed specifically for meshed systems, where the angle between the zero sequence current and voltage is used as a directional element. By using a communication scheme and multiple relays the faulty line in a mesh can be determined, but the protection scheme requires relays on both ends of the line. The aforementioned methods are only able to determine the correct feeder or line, not the exact fault location. The authors of [11] present a comprehensive overview of the state-of-the-art for location of earth faults in distribution networks with isolated and compensated grounding schemes, demonstrating that accurate fault location in these networks is lacking. The available options are fewer still when considering transient and intermittent faults, in which case methods requiring steady-state conditions cannot be used. Refs. [12,13] are two examples of recently developed methods for detection and selective protection of intermittent faults in isolated and compensated

☆ The work was funded by the Norwegian Research Council project ProDig (295034/E20).

* Corresponding author.
E-mail addresses: thomas.treider@ntnu.no (T. Treider), hans.hoidalen@ntnu.no (H.K. Høidalen).

https://doi.org/10.1016/j.epsr.2023.109765
Received 4 April 2023; Received in revised form 27 July 2023; Accepted 9 August 2023
Available online 19 August 2023

Nomenclature

$i_{a,A}(t)$	Time domain current in phase a on feeder A
$i_{a,B}(t)$	Time domain current in phase a on feeder B
$i_{a,sum}(t)$	Sum of $i_{a,A}$ and $i_{a,B}$
$I_{a,A}(f)$	Frequency domain transform of $i_{a,A}$
$I_{a,B}(f)$	Frequency domain transform of $i_{a,B}$
$I_{a,sum}(f)$	Frequency domain transform of $i_{a,sum}$
f_{ch}	The frequency of the charging transient component
$\tilde{I}_{a,A}$	$I_{a,A}$ evaluated at the charging transient frequency, i.e. $\tilde{I}_{a,A} = I_{a,A}(f_{ch})$
$\tilde{I}_{a,A}$	$I_{a,B}$ evaluated at the charging transient frequency, i.e. $\tilde{I}_{a,B} = I_{a,B}(f_{ch})$
$\tilde{I}_{a,A}$	$I_{a,sum}$ evaluated at the charging transient frequency, i.e. $\tilde{I}_{a,sum} = I_{a,sum}(f_{ch})$
ASC	Arc suppression coil
DG	Distributed generation
FPI	Fault passage indicator
TW	Travelling wave

networks, but accurate fault location capabilities are missing. Refs. [14–16] are examples of efforts into the development of a transient distance element which may be sufficiently fast for location of intermittent faults, but the presented results are sparse and their performance during intermittent faults is not demonstrated. Methods based on travelling waves (TW) are in theory very accurate and fast [17], but they are challenging to apply in distribution networks due to multiple reflection points, and research into this field is ongoing and not solved [11]. The authors of [11] highlight FPIs as a promising alternative for earth fault location and further develops this in [2], but the fault location accuracy is inherently limited by the spacing of the FPIs. While intermittent transient fault detection and selective protection is a standard feature in modern protective devices, accurate location of intermittent faults requires more research [11].

A closed-ring topology can be an alternative to the conventional radial topology commonly used in distribution networks [18]. Distribution networks are often built with the option of closed-ring operation to add flexibility during fault clearing events and network re-configurations. While a permanent transition to a closed-ring operation of the network will require an adjustment of the protection systems, it can be beneficial due to more balanced load and voltage profiles [19,20], it can save costs by reducing the need for grid expansion [20] and by reducing losses [21], and it has been shown to increase the network reliability [22]. A closed-ring operation of parts of the network can also be beneficial by facilitating new fault location solutions [18]. In [18], two fault location methods were proposed utilizing a novel current ratio principle which takes advantage of a closed-ring topology. These methods were based on the negative sequence currents and zero-sequence currents measured on the two ring-connected feeders, respectively, and their performance was evaluated for permanent earth faults. While the methods showed very good results in the case of permanent faults (faults located within a few hundred metres in most cases), their performance during transient and restriking faults has not been studied. In this paper, a more accurate frequency dependent line model is implemented so that this can be investigated. Furthermore, it is hypothesized that a specific earth fault transient can be used to implement the same basic fault location principle. Thus, a novel transient principle is proposed and investigated as well.

The rest of the paper is organized as follows. In Section 2 the two methods from [18] are summarized, the new transient version is derived, and their implementation is discussed in detail. Sections 3 and 4 presents the modelling and results from simulations using ATPDraw. The results are discussed and summarized in Section 5 before a conclusion is given in Section 6.

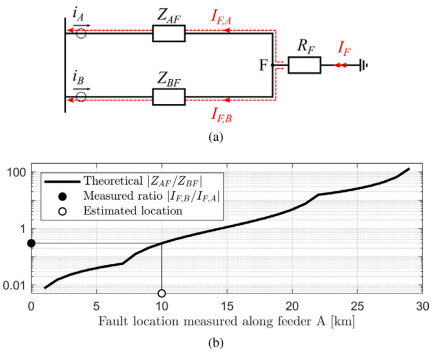

Fig. 1. (a) Division of the charging transient component in the faulty phase, and (b) converting an observed current ratio to a distance estimate on a 30 km long ring.

2. Fault location based on current ratios

In [18], two fault location methods based on current ratios were proposed, using either negative sequence or zero-sequence quantities. Generally, the current ratio principle can be explained by considering Fig. 1(a). The fault current $\vec{I}_F$ is divided in two components which are contained in the currents measured on the beginning of each of the two ring-connected feeders. By extracting these fault current components, their ratio can be used to estimate the ratio of the impedances between the fault and the measurements:

$$\frac{Z_{AF}}{Z_{BF}} = \frac{\vec{I}_{F,B}}{\vec{I}_{F,A}} \tag{1}$$

With knowledge of the impedance of the lines, the impedance ratio can be converted to a distance estimate. Fig. 1(b) illustrates this in the case of a ring with total length 30 km.

2.1. Using the negative sequence currents

The ratio of the negative sequence currents can be used to estimate the ratio of the negative sequence impedances, as shown in (2). The pre-fault values of the currents are removed by using the current increments $\Delta\vec{I}_{2,A}$ and $\Delta\vec{I}_{2,B}$, making the method robust against both large fault resistance and asymmetric loads in the network.

$$\frac{Z_{2,AF}}{Z_{2,BF}} = \frac{\Delta\vec{I}_{2,B}}{\Delta\vec{I}_{2,A}} \tag{2}$$

2.2. Using the zero-sequence currents

Using the same approach as for the negative sequence currents, the zero-sequence currents can be utilized as well. However, two modifications must be made. First, the zero-sequence impedance must be used instead of the negative sequence impedance. Secondly, the capacitive components in the zero-sequence currents are not canceled when using incremental values of the currents, and therefore they must be subtracted in some other way. It is shown in [18] that this can be

done using the neutral voltage $\vec{V}_n$, assuming that the total three-phase admittance of the two feeders and their branches $\bar{Y}$ is known. This gives the following equation for estimating the impedance ratio:

$$\frac{Z_{0,AF}}{Z_{0,BF}} = \frac{\Delta 3\vec{I}_{0,B} - \Delta\vec{V}_n m_B \bar{Y}}{\Delta 3\vec{I}_{0,A} - \Delta\vec{V}_n m_A \bar{Y}} \tag{3}$$

The factors m_A and m_B describe the division of the capacitive parts of the zero-sequence currents on the two feeders, and an analytical approach for their calculation is given in Appendix A.

2.3. Using the charging transient

The charging transient is a specific earth fault transient which is well known and described in the literature [14–16,23–26]. In a radial network, this transient flows from the fault in to the main transformer along the faulty phase. In a ring network, the same principle of current division will apply, meaning that this component can also be used to implement the current ratio principle.

Using the same approach as in [24], the charging transient behaviour in a ring-operated network can be derived. For simplicity, two unloaded feeders without any laterals connected to form a ring, as shown in Fig. 2(a), is assumed. The network is shown as ungrounded, but the same circuit is valid for a resonant grounded network as well when considering frequencies above the fundamental frequency [27]. It is further assumed that the charging current is divided along these two paths according to the principle of current division, and that the resistance in the circuit can be neglected so that $Z \approx \omega L$. The sum of currents in these two paths then meets a parallel connection of the inductances in the two paths, L_{eq}:

$$L_{eq} = \frac{L_{AF} L_{BF}}{L_{AF} + L_{BF}} \tag{4}$$

The network in Fig. 2(a) can be represented by the LC-circuit in Fig. 2(b). By using L_{eq} to represent the ring, the charging frequency can be estimated by (5).

$$f_{ch} = \frac{1}{2\pi\sqrt{(1.5L_T + L_{eq})(2C_g + 2C_p)}} \tag{5}$$

Because the value of L_{eq} varies with the fault location, so does f_{ch}. Eq. (5) shows that the minimum frequency occurs approximately on the middle of the ring, where L_{eq} reaches its maximum value, while the maximum frequency occurs for faults at the main bus, for which $L_{eq} = 0$.

When a fault occurs somewhere on two ring-connected feeders, the division of the charging transient among feeders A and B depends on the ratio of the impedances faced in the two paths. Assume that the fault occurs in phase k. Let $\tilde{I}_{k.A}$ and $\tilde{I}_{k.B}$ be the charging transient components of the phase currents $i_{k.A}$ and $i_{k.B}$ measured on feeders A and B, respectively. $Z_{k.AF}$ and $Z_{k.BF}$ are the self-impedances of the faulty phase in the two paths, evaluated at the charging frequency f_{ch}. With these modifications, the current ratio in principle can be implemented as described by (6).

$$\frac{Z_{k.AF}}{Z_{k.BF}} = \frac{\tilde{I}_{k.B}}{\tilde{I}_{k.A}} \tag{6}$$

2.4. Implementation

The methods considered in this paper are only providing fault location, and it is assumed that an external fault detection stage has determined the time of the fault inception t_0, as well as the faulty phase.

The methods based on the negative and zero-sequence currents are described in [18], and their implementation is summarized by the flowchart in Fig. 3. The only setting to vary is the time t_x, measured from the time of fault inception, at which the fault location estimate for the two fundamental frequency methods should be extracted. This was not considered in detail in [18] because permanent faults allowed

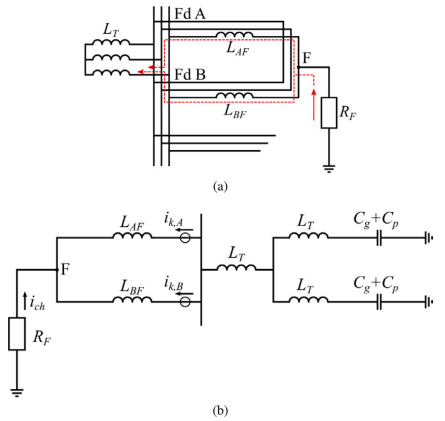

Fig. 2. Example of (a) two ring-connected feeders A, and B and (b) the equivalent LC-network for charging frequency estimation.

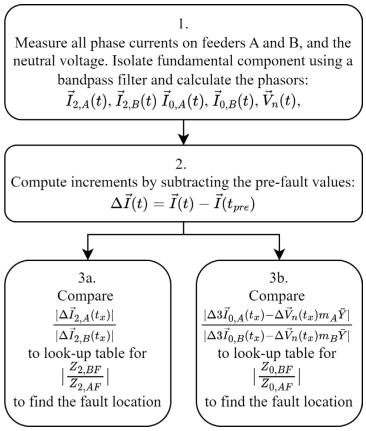

Fig. 3. Flowchart for the two methods in [18].

waiting for steady-state conditions. For transient faults however, the fault location estimate must be extracted in a few milliseconds after the fault. This parameter will be illustrated and discussed in more detail in Section 4.

The transient method requires more steps before a distance estimate is obtained. The entire process is summarized in Fig. 4, and the estimation of the charging transient frequency and the frequency dependent impedances is described in more detail in the following subsections.

2.4.1. Estimating the charging transient frequency

Consider a fault occurring in phase a. In order to estimate the frequency of the charging transient, the sum $i_{a,sum} = i_{a,A} + i_{a,B}$ is used.

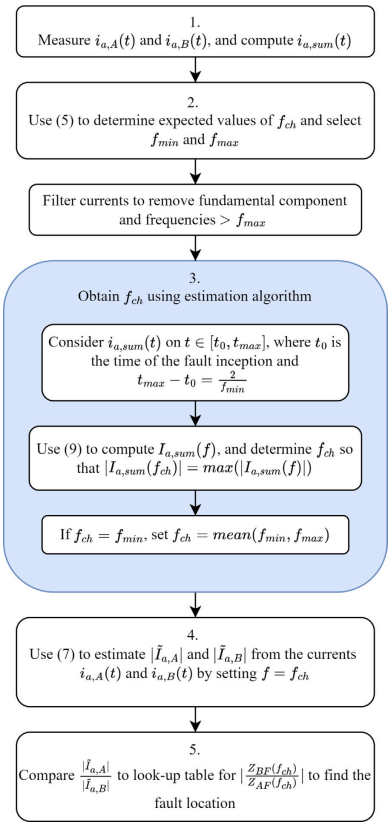

Fig. 4. Flowchart showing fault location in phase a using the charging transient.

The sum of the currents is used to ensure that the charging transient component $\tilde{I}$ is present with a sufficient magnitude no matter where on the ring the fault is located, as either $\tilde{I}_{a,A}$ or $\tilde{I}_{a,B}$ will approach zero when the fault is located close to the main bus.

Before being transformed into the frequency domain, $i(t) = i_{sum,a}(t)$ is filtered to remove the fundamental frequency component as well as disturbing high frequency content. The time domain signal is transformed into the frequency domain using (7). Eq. (7) is applied on the frequency range $F = [f_{min}, f_{max}]$, which is selected by estimating the expected frequency range of the charging transient using (5) with the maximum and minimum values of L_{eq}.

$$I(f) = \sum_{t=t_0}^{t_{max}} i(t) \cdot e^{-j2\pi ft} \tag{7}$$

In (7), the current $i(t) = i_{sum,a}(t)$, $t \in [t_0, t_{max}]$. The frequency of the charging transient depends on the fault location and is not known in advance, and the length of the DFT-window, i.e. $T_{DFT} = t_{max} - t_0$, must therefore be long enough to accurately reproduce the lowest likely value of the charging transient frequency f_{min}. Therefore, the DFT-window is set to cover two periods of this frequency, i.e. $T_{DFT} = 2/f_{min}$. Fig. 5 illustrates the signal acquisition in the time domain.

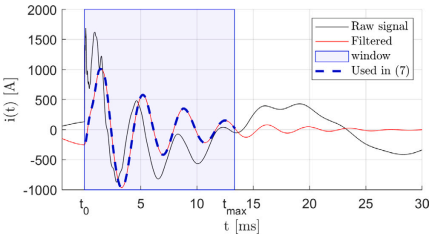

Fig. 5. Obtaining the current $i(t) = i_{sum,a}(t)$ used in (7) to estimate f_{ch}.

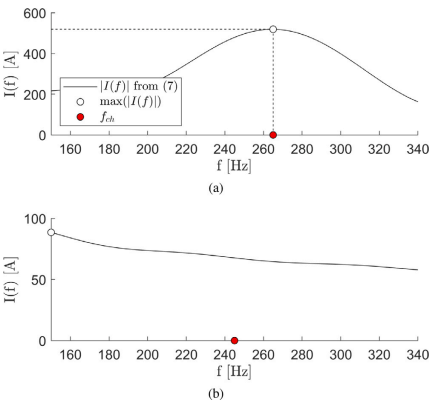

Fig. 6. Frequency spectrum and estimated charging frequency for (a) 1 Ω and (b) 15 Ω fault resistance.

The frequency corresponding to the maximum magnitude of $I(f)$ is chosen as an estimate of f_{ch}, as shown in Fig. 6(a). The fundamental frequency is not perfectly filtered out in practice, and when the fault impedance causes the charging transient magnitude to be reduced, the peak value of $|I(f)|$ will not correspond to the charging transient frequency. When this occurs, the maximum value of $|I(f)|$ will be found at f_{min}. To account for this, the above algorithm discards the estimate of f_{ch} when it corresponds to f_{min}. Instead, the mean value of the frequency range considered is used to estimate f_{ch}. Fig. 6(b) illustrates how the transient becomes too small during a 15 Ω fault to be located with this approach. In this case, the mean frequency is used.

2.4.2. Estimating the frequency dependent impedance

In order to compare the measured ratio of the currents to the correct impedance ratio, the impedances at the correct frequency must be considered. Typically, it is the 50 Hz impedance $Z_{50\ \mathrm{Hz}}$ of the line which is known to the network operator. Estimating the frequency dependent impedance as $Z(\omega) \approx R_{50\ \mathrm{Hz}} + j\omega L_{50\ \mathrm{Hz}}$ is not accurate, and the frequency dependent values $R(\omega)$ and $L(\omega)$ should instead be estimated analytically. For overhead lines, (2.11), (2.12) and (2.27) or

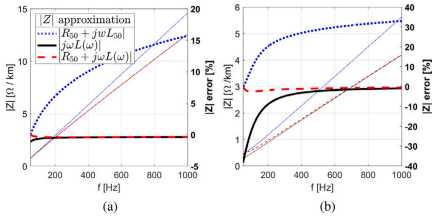

Fig. 7. Different approximations of the self impedance $|Z(\Omega)|$ for an (a) OH-line and (b) a cable, and their percentage errors (thick curves on right y-axis).

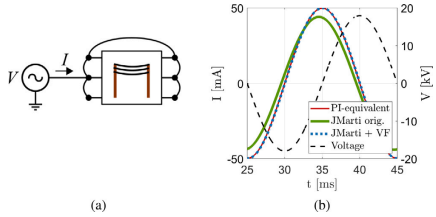

Fig. 8. (a) Simulation model for determining capacitive current to ground in a 1 km line segment, and (b) simulated currents with three different line models.

(3.23d) in [28] can be used to estimate the self impedance. For cables, Ref. [29] gives a detailed description of how to estimate the impedance. Fig. 7 shows that estimating $|Z(\omega)|$ using frequency independent parameters gives significant errors. In the case of the OH-line in Fig. 7(a), reasonable accuracy can be obtained using only the line inductance, whereas the cable in Fig. 7(b) with its higher R/X-ratio requires the inclusion of the resistance to avoid large errors at low frequencies. Fig. 7 also confirms that there is very little to gain from accounting for the frequency dependency of R given that $\omega L(\omega)$ dominates at higher frequencies.

3. Modelling

3.1. Line model for studying earth fault transients

To study both the fundamental frequency component as well as the charging transient, it is of interest to use a line model which accurately represents the line from 50 Hz and up to the charging transient frequency (approximately 300 Hz in the test network in this paper). Conventional travelling wave models work poorly at low frequencies, particularly when it comes to representing the capacitance of the lines. PI-equivalents can be accurate at 50 Hz, but they are in turn inaccurate at higher frequencies. However, some models can provide frequency dependent line parameters and at the same time represent the capacitance with sufficient accuracy in the frequency range of interest [30–32]. The model in [30] combines JMarti and vector fitting (VF) and is implemented in ATPDraw version 7.4. Compared to the regular JMarti model, it has the benefit of being accurate in lower frequency ranges. Fig. 8 shows how the regular JMarti model in ATPDraw fails to reproduce the correct capacitance at 50 Hz, whereas the model in [30] closely matches the PI-equivalent. Fig. 9 shows that the line model also impacts the earth fault transients of interest. A network with 5 × 20 km OH-lines was modelled using the three different line models discussed previously. It can be seen that the PI-equivalent has too little damping, and the constant parameters result in the charging frequency being too low (here ≈ 650 Hz). The two JMarti models have similar responses, but over a few periods it is apparent that both their magnitudes and frequencies are different. Based on Figs. 8 and 9, the JMarti model in [30] is preferred.

3.2. Test network

The test network used to verify the proposed fault location method is the network shown in Fig. 10, which is based on data from a Norwegian network operator, and the topology corresponds to the test network used in [18]. The network can be operated either with a resonant grounded or isolated grounding scheme, and the DG-units are disconnected unless otherwise stated. According to (5), the charging

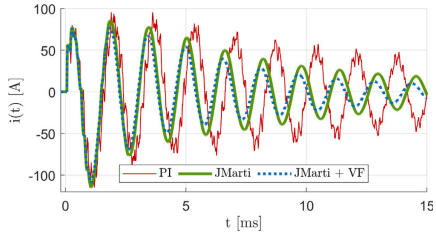

Fig. 9. Earth fault transient with different line models.

transient frequency is expected to vary between 187 Hz and 284 Hz for different fault locations on the ring. Adding a 20% security margin, the frequency range $F = [150\ \text{Hz}, 340\ \text{Hz}]$ is considered when applying (7). Note that the source impedance of the supplying network, transformed to the 22 kV-side of the transformer, has been included in L_T when applying (5).

The model in [30] is used to represent the OH-lines and cables in the network. The positive and zero-sequence line parameters at 50 Hz are found through measurements (i.e., using ATPDraw's Line Check feature [33]), and the self impedance $Z_{50\ \text{Hz}}$ is derived from these values. With Line Check available, it could be used to estimate $L(\omega)$ directly, but in this case $L(\omega)$ is estimated from $L_{50\ \text{Hz}}$ using the analytical formulae referenced in 2.4.2. The frequency dependent impedance is then approximated as $Z(\omega) = R_{50\ \text{Hz}} + j\omega L(\omega)$.

3.3. Modelling faults

The permanent faults are modelled by connecting a resistance between the faulty phase and ground using a time-controlled switch, while the transient and-striking faults are modelled using a voltage dependent switch. This switch connects the faulty phase to ground via the fault resistance when the voltage over the switch exceeds the flashover voltage V_{flash} of the switch, and it opens when the fault current drops below a set threshold I_{mar}. This results in the duration of each fault and the time between restrikes varying depending on the flashover voltage, the fault resistance and the grounding scheme.

4. Results

A variety of fault scenarios are used to test the three methods. The validity of the new transient method is first investigated separately using permanent faults, after which all three methods are tested for transient and restriking faults. See Appendix B for complete data and settings.

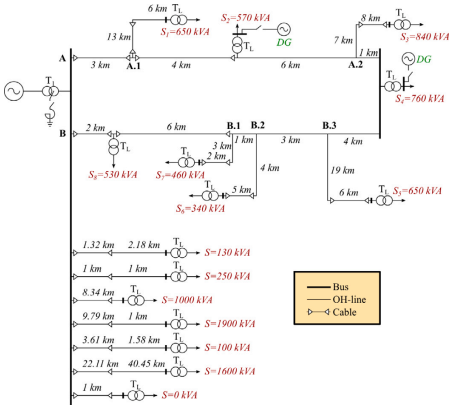

Fig. 10. Single line diagram of simulated network.

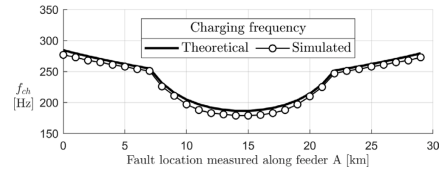

Fig. 11. Theoretical frequency predicted by (5), and observed frequency in the base case network.

4.1. Accuracy of the charging transient ratio

First, the novel transient method is investigated with a set of permanent 1Ω faults applied in phase a in sequence at various fault locations around the ring. Fig. 11 shows the observed charging transient frequency for different fault locations on the ring. The figure also shows the theoretical values predicted by (5), illustrating that the LC-circuit in Fig. 2(b) is a reasonable approximation for the purpose of estimating the frequency. Note that the frequency dependency of the line inductance was accounted for when computing the theoretical frequency in Fig. 11, but very little change (< 2.7%) was observed when using its 50 Hz-value.

Fig. 12(a) shows that the transient method successfully estimates the impedance ratio, but the presence of loads and lateral branches on the ring reduces the accuracy. It can be seen that connecting the loads directly on the ring by removing lateral in between (labelled "Loads, no laterals" in Fig. 12) improves the accuracy, showing that it is the laterals themselves as well as the load which disturb the results. The exact mechanism involved has not been investigated in detail, but simulations have shown that each lateral contributes with an induced transient current at the charging frequency proportional to the amount of capacitance on that particular lateral. The loads themselves have the biggest impact on the results, however, and the effect of loads is to provide the transient with another path then the one assumed in Fig. 2(a). This creates significant errors close to the edges of the ring due to the fact that either $\tilde{I}_{a.A}$ or $\tilde{I}_{a.B}$ should approach zero as the fault moves towards the main bus, making the ratio between them susceptible to even small errors in the estimation of the magnitudes.

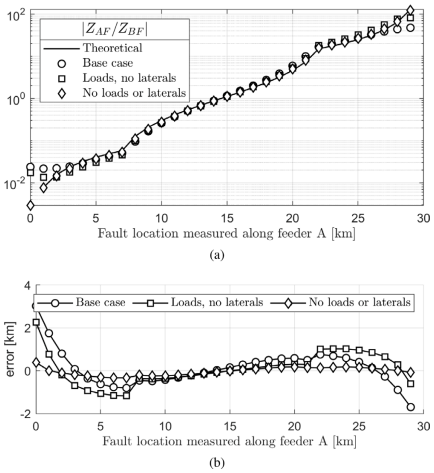

Fig. 12. (a) Estimated $|Z_{AF}/Z_{BF}|$-ratio and (b) corresponding distance estimate errors for the transient method.

4.2. Speed of the fundamental frequency methods

Fig. 13 shows how the impedance ratio estimates vary with time during a permanent fault. The negative sequence method reaches its final value much faster than the zero-sequence methods does, allowing a lower value of t_x. The zero-sequence estimate is very sensitive to even small differences in the current and voltage transients, resulting in very large variations in the estimate before steady state is reached. The negative sequence current has an equally long transient period, but because both $\Delta\tilde{I}_{2.A}$ and $\Delta\tilde{I}_{2.B}$ display a similar transient dynamic, the ratio between them stabilizes much earlier than the zero-sequence method does.

Fig. 14 illustrates how different settings of t_x impacts the accuracy of the negative sequence method during transient faults, and similar results apply for the zero-sequence method as well. The highest value of t_x gives good accuracy in Fig. 14(a), where the restrikes are regular and frequent. In Fig. 14(b), the situation is reversed. There, the network is resonant grounded, leading to longer intervals between restrikes. This occurs due to the much slower build-up of the phase voltage between strikes in the resonant grounded network [34], which is illustrated clearly in the example in Fig. 15. For the remainder of the paper, t_x = 5 ms is used.

4.3. Restriking faults distance estimates

Figs. 16–19 show how the fault resistance impacts the three methods during transient faults in both an isolated and a resonant grounded network. The negative sequence method works best and is not significantly affected by the fault resistance, grounding scheme or flashover voltage. The transient method works best for low-ohmic faults and low flashover voltages, but it is still the less accurate then the negative sequence method. The zero-sequence method varies greatly, where the main issue is seen to be the grounding scheme. It works reasonably well in the isolated network (although less accurate than the negative

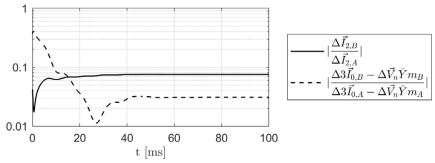

Fig. 13. The two ratios during a permanent 1 Ω fault occurring at $t = 0$ at point A.1 in Fig. 10 with the network operating with an isolated neutral point.

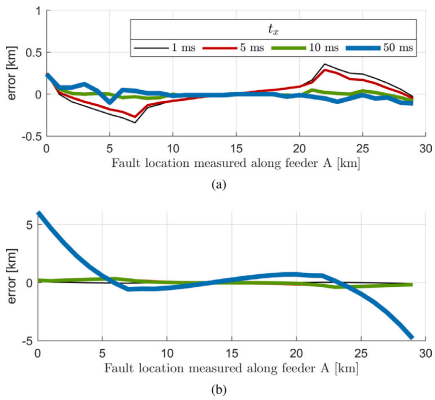

Fig. 14. The impact of t_x on the negative sequence method's fault distance estimate for restriking faults in (a) an isolated network and (b) a resonant grounded network. V_{flash} = 16 kV.

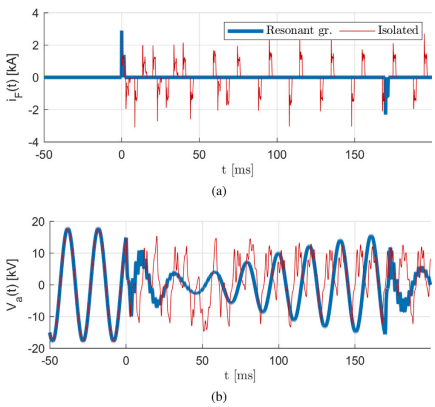

Fig. 15. Comparison of (a) fault current and (b) main bus faulty phase voltage during restriking fault at location A.1 in Fig. 10. V_{flash} = 16 kV.

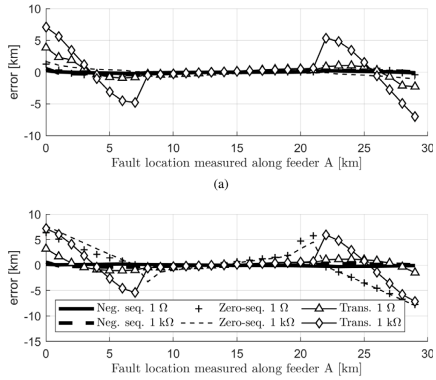

Fig. 16. Faults with flashover voltage 1.8 kV and 1 Ω or 1 kΩ in (a) isolated network and (b) resonant grounded network.

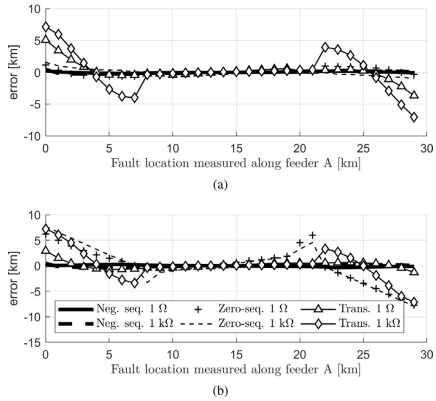

Fig. 17. Faults with flashover voltage 4.5 kV and 1 Ω or 1 kΩ in (a) isolated network and (b) resonant grounded network.

sequence method), but it is severely reduced in the resonant grounded network. For the cases in Figs. 16–19, the mean and maximum absolute errors were {0.13 km; 0.64 km} for the negative sequence method, {1.52 km; 10.35 km} for the zero-sequence method, and {1.38 km; 7.26 km} for the transient method.

4.4. Impact of harmonics and measurement noise

Next, permanent faults in the isolated network is considered, with t_x = 5 ms. Fig. 20 shows the results of 500 randomly selected combinations of DC-components, fifth and seventh harmonics added to the two current measurements, and noise added to the neutral voltage. The DC-component has a value between ±5% of the pre-fault load current, whereas the two harmonics have magnitudes between 0%–5% and phase angles between 0°–360°. In addition, random noise have

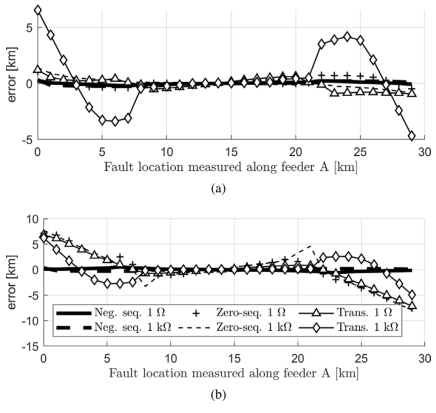

Fig. 18. Faults with flashover voltage 9 kV and 1 Ω or 1 kΩ in (a) isolated network and (b) resonant grounded network.

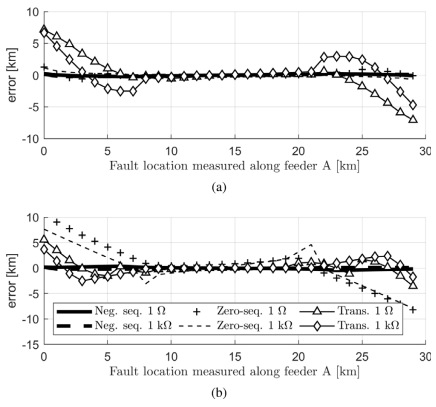

Fig. 19. Faults with flashover voltage 16 kV and 1 Ω or 1 kΩ in (a) isolated network and (b) resonant grounded network.

been added to each sample, with a magnitude between 0 and 5% of the actual magnitude at that sample. The blue areas in Fig. 20 show the envelope of all the resulting estimate errors for the three methods, along with the errors without harmonics or noise added (labelled "Base case"). It can be seen that the impact of noise and harmonics is negligible on the fundamental frequency methods, while the distance estimate changes by up to a few hundred metres in the case of the transient method.

5. Discussion

The results have shown that despite being based on fundamental frequency components and derived from a steady-state analysis, the

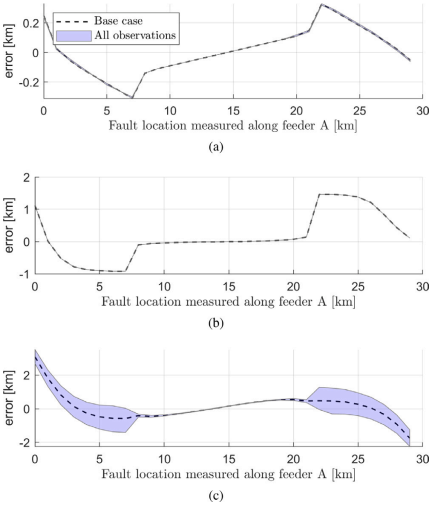

Fig. 20. Impact of harmonics and noise on (a) the negative sequence method, (b) the zero-sequence method and (c) the transient method.

methods based on the negative and zero-sequence currents can be applied to transient and restriking faults as well.

While the negative sequence method performs very well in both grounding schemes, the zero-sequence method is less accurate in the resonant grounded network. Though not included in the paper, similar results was observed for permanent faults. A possible explanation for this is that the fault current is much lower in the resonant grounded network compared to an isolated network of the same size. The capacitive parts of $\Delta 3\vec{I}_0$, i.e. $\Delta\vec{V}_n\hat{Y}$, is increased relative to the fault current, making the method more susceptible to small errors in the estimation and removal of this component. $\Delta\vec{I}_2$, however, consists mainly of the fault current, and faults in the resonant grounded network therefore resemble high impedance faults in the isolated network, for which this method is known to be robust [18].

It was also hypothesized at the beginning of this paper that the charging transient could be used to implement a similar current ratio principle. While the results demonstrate that this is correct, this transient method is not feasible in practice. To give sufficient accuracy comparable to that of the two fundamental frequency methods, the ring must be without loads and branches. Furthermore, as it is based on the measurement of transients, it is limited to low-ohmic faults.

From [18] it is known that the negative sequence method is affected by DG units in the network as well, where the accuracy was observed to be reduced by 700 metres at most, while the zero-sequence method is not impacted by DG-units. It was also observed in the simulations performed in this paper that the presence of DG units in the network reduced the accuracy of the transient method by a few hundred metres for faults in the middle of the ring and up to 2 km for faults close to the main bus. The effect of DGs on the transient method is comparable to that of loads and branches as the DG units provide the transient with an alternative path, and more DG units therefore further increase this effect.

5.1. Alternative methods for fault location

As determined by the authors of [11], few methods for accurate location of transient and restriking faults exists. TW-based methods appear be both difficult and costly to apply in distribution networks, and conventional earth fault relays cannot determine the exact fault location. For impedance-based methods, the method in [14,16] seems to be a likely alternative to the methods presented in this paper. However, results from transient faults are lacking, and it is likely to face many of the same challenges as the transient method proposed in this paper as they both utilize the same transient component. Without a more detailed description of its correct implementation available, a quantitative comparison cannot be made in this paper. Ref. [2] also proposes FPIs. The benefit is that faults can be located on the lateral branches as well, a property which the current ratio method lacks, but the drawback is the high number of FPIs needed to obtain an accurate fault location. Using the current ratio methods in conjunction with FPIs on the lateral branches can therefore be a good solution.

6. Conclusion

This paper has investigated the performance of three different methods for location of transient and restriking earth faults based on current ratios in closed-ring distribution networks. Two of the methods are based on fundamental frequency negative sequence currents and zero-sequence currents, while a novel transient principle has been proposed.

Using a frequency dependent line model in ATPDraw, the analysis has shown that:

- The negative sequence method works best in all the cases considered, with a mean distance estimate error of 0.13 km during transient and restriking faults.
- The zero-sequence method can be an option in an isolated network, but not in a compensated network.
- The transient principle proposed can only compete with the negative sequence method when the ring-connected feeders have no loads or laterals connected to them, making it less suited for a distribution network.
- The transient method is affected by harmonics close to the charging transient frequency as these harmonics cannot be filtered out, although the reduction in accuracy was observed to be a few hundred metres at most. The other two methods are not impacted by harmonics in the currents as these can be filtered out without affecting the fundamental component.

The main advantage of the current ratio methods compared to other solutions is that only readily available measurements in a single substation are required, making them easy and cost-efficient to implement in existing networks without the need for communication networks. The main drawback with these methods is that faults on lateral branches connected to the ring appear at the connection points, requiring other solutions for precise fault location on the branch itself.

CRediT authorship contribution statement

Thomas Treider: Conceptualization, Methodology, Software, Formal analysis, Investigation, Writing – original draft, Writing – review & editing, Visualization, Project administration. **Hans Kristian Høidalen:** Software, Writing – original draft, Writing – review & editing, Supervision, Funding acquisition.

Declaration of competing interest

The authors declare that they have no known competing financial interests or personal relationships that could have appeared to influence the work reported in this paper.

Data availability

No data was used for the research described in the article.

Acknowledgement

The authors appreciate discussions with and advice from B. Gustavsen at SINTEF Energy Research.

Appendix A. Estimating the parameters m_A and m_B

Table B.1
Test network and model parameters.

Network data	
OH-lines	Conductor geometry: radius 11.87 mm, DC resistance 0.1115 Ω/km, height tower/mid 7 m/6 m. Plane geometry, 2 m between conductors. Ground wire geometry: radius 3.84 mm, DC resistance 0.8 Ω/km, height tower/mid 5 m/4 m, vertical position 1 m. Ground resistivity 100 Ωm. Lines are transposed and skin effect is included.
Cable	Core radii 0 mm (inner) and 9.1 mm (outer), sheath radii 14.75 mm (inner) and 17.25 mm (outer), cable radius 18.95 mm. Conductor resistivity 2.65E−8 Ωm, Relative permittivity of insulation 2.3. Triangular configuration with snaking at 1 m depth. Ground resistivity 100 Ωm.
Main transformer	100 MVA 132/22 kV Dy1 transformer. X = 6%, R = 0.25%. Modelled using the Hybrid transformer model in ATPDraw with typical values for inductance and resistance, no capacitance or core effects included.
Load transformers	2 MVA 22/0.4 kV Dy1 transformer grounded on the LV-side. X = 5%, R = 0.78%. Modelled using the Hybrid transformer model in ATPDraw with typical values for inductance and resistance, no capacitance or core effects included.
Loads	Grounded Y-connected constant impedance loads with power factor 0.9.
Source	Line voltage 132 kV, source impedance $3.47 + j34.67\Omega$ corresponding to 500 MVA according to [35].
DG units	$S = 0.85$ MVA, $V_{line} = 400$ V, $X = 0.15$ p.u. [36].
Arc suppression coil	5 A over-compensated. Resistor $R_p = 20 \cdot X_n$ added in parallel to emulate losses.
Faults	Permanent faults in phase a with inception angle approximately 60°. Restriking faults are modelled using a voltage dependent switch in ATPDraw with $T - de = 1$ ms (minimum time the switch remains closed) and $I_{mar} = 1$ A (switch opens when $I_f < I_{mar}$).
Simulation, signal processing and filters	
Software: ATPDraw version 7.4. Filters: 3rd order Butterworth low-pass filter with 500 Hz cut-off frequency before sampling in ATPDraw. Sample rate: 8 kHz. High-pass filter for transient method: 5th order Butterworth with 100 Hz cut-off frequency. Band-pass filter for 50-Hz methods: Matlab-designed equiripple with Fstop1 = 0 Hz, Fpass1 = 40 Hz, Fpass2 = 100 Hz, Fstop2 = 150 Hz, Astop1 = Astop2 = 60 dB, Apass = 0.1 dB.	

Table B.2
Positive and zero sequence line parameters obtained using ATPDraw's line check feature.

	OH-line	Cable
Z^+	0.1077+j0.356 Ω/km	0.152+j0.0997 Ω/km
Z_0	0.4587+j1.1604 Ω/km	0.2072+j0.0535 Ω/km
C^+	10.492 nF/km	263.98 nF/km
C_0	5.8376 nF/km	261.5 nF/km

This theory is from [18]: The ring is divided into n zero-sequence PI-equivalents, chosen so that the magnitude of the zero-sequence series impedance for each PI-section is the same, i.e. $|z_1| = |z_2| = |z_3| = \cdots = |z_n|$. The total capacitance of PI-section k is labelled C_k. Next, the parallel capacitances of adjacent PI-equivalents are summed, and $n+1$ capacitances $\tilde{C}_0 - \tilde{C}_n$ are defined in (A.1).

$$\tilde{C}_i = \frac{1}{2}\begin{cases} C_{i+1} & i = 0 \\ C_i & i = n \\ C_i + C_{i+1} & i = 1, 2, \ldots, n-1 \end{cases} \tag{A.1}$$

By assuming that all these capacitances experience the same voltage, V_0, and by applying the principle of current division, the expressions below for m_A and m_B can be derived:

$$m_A = \frac{\sum_{i=0}^{n} \tilde{C}_i \frac{n-i}{n}}{\sum_{i=0}^{n} \tilde{C}_i} \tag{A.2}$$

$$m_B = \frac{\sum_{i=0}^{n} \tilde{C}_i \frac{i}{n}}{\sum_{i=0}^{n} \tilde{C}_i} \tag{A.3}$$

The accuracy of m_A and m_B increases as $n \to \infty$. Laterals on the feeders are accounted for by summing their entire zero-sequence capacitance to the corresponding $\tilde{C}_i$.

Appendix B. Network data

The network in Fig. 10 is implemented in ATPDraw with the data given in the figure and in Table B.1. The lines and cables are modelled using the version of JMarti given in [30], where the model is fitted from 1–10^7 Hz. The positive and zero sequence line parameters obtained using Line Check is given Table B.2, and they are used to compute the self impedance.

References

[1] S. Hänninen, M. Lehtonen, Characteristics of earth faults in electrical distribution networks with high impedance earthing, Electr. Power Syst. Res. 44 (3) (1998) 155–161.

[2] A. Farughian, L. Kumpulainen, K. Kauhaniemi, P. Hovila, Intermittent earth fault passage indication in compensated distribution networks, IEEE Access 9 (2021) 45356–45366.

[3] A. Wahlroos, J. Altonen, J. Xavier, Can compensated networks be an alternate solution to reduce the risk of ground faults causing forest fires? in: 2021 74th Conference for Protective Relay Engineers, CPRE, College Station, TX, USA, 2021, pp. 1–34.

[4] G. Druml, R. Klein, O. Seifert, New adaptive algorithm for detecting low- and high ohmic faults in meshed network, in: 20th International Conference on Electricity Distribution, Prague, 2009, pp. 1–6.

[5] T. Henriksen, Faulty feeder identification in high impedance grounded network using charge-voltage relationship, Electr. Power Syst. Res. 81 (9) (2011) 1832–1839.

[6] M. Loos, S. Werben, M. Kereit, J.-C. Maun, Detection of single phase earth fault in compensated network with C0 estimation, in: 22nd International Conference and Exhibition on Electricity Distribution, CIRED 2013, 2013, pp. 1–4.

[7] M.F. Abdel-Fattah, M. Lehtonen, Transient algorithm based on earth capacitance estimation for earth-fault detection in medium-voltage networks, IET Gener. Transm. Distrib. 6 (2) (2012) 161–166.

[8] M. Loos, S. Werben, M. Kereit, J.-C. Maun, Fault direction method in compensated network using the zero sequence active energy signal, in: Eurocon 2013, 2013, pp. 717–723.

[9] Z. Gajić, S. Aganović, R. Pajunen, S. Zubić, Universal earth-fault protection method for high impedance grounded power system, in: 15th Int. Conf. Developments in Power System Protection, DPSP 2020, 2020, pp. 1–6.

[10] J.D.R. Penaloza, A. Borghetti, F. Napolitano, F. Tossani, C.A. Nucci, A new transient-based earth fault protection system for unearthed meshed distribution networks, IEEE Trans. Power Deliv. 36 (5) (2021) 2585–2594.

[11] A. Farughian, L. Kumpulainen, K. Kauhaniemi, Review of methodologies for earth fault indication and location in compensated and unearthed MV distribution networks, Electr. Power Syst. Res. 154 (2018) 373–380.

[12] P. Liu, C. Huang, Detecting single-phase-to-ground fault event and identifying faulty feeder in neutral ineffectively grounded distribution system, IEEE Trans. Power Deliv. 33 (5) (2018) 2265–2273.

[13] M. Lukowicz, W. Rebizant, M. Kereit, New approach to intermittent earth fault detection with admittance criteria, Int. J. Electr. Power Energy Syst. 123 (2020) 106271.

[14] G. Druml, New method for measuring the earthfault-distance in compensated and isolated networks, in: CIRED 2021-26th Int. Conf. Exhib. Electricity Dist, 2021, pp. 1–4.

[15] W. Zhang, X. Xiao, Y. Wang, T. Zheng, H. Zhao, H. Wang, Charging-transient based SLG fault location in neutral-unearthed distribution system, in: 2011 Asia-Pacific Power and Energy Engineering Conference, 2011, pp. 1–4.

[16] G. Druml, Results from the new method for measuring the earthfault-distance in compensated and isolated networks, in: 16th Int. Conf. Developments in Power System Protection, DPSP 2022, 2022, pp. 1–4.

[17] C. Galvez, A. Abur, Fault location in meshed and active power distribution networks, in: 2021 IEEE Madrid PowerTech, 2021, pp. 1–6.

[18] T.A. Zerihun, T. Treider, H. Taxt, L.B. Nordevall, T.S. Haugan, Two novel current-based methods for locating earth faults in unearthed ring operating MV networks, Electr. Power Syst. Res. 213 (2022) 108774.

[19] M. Biller, J. Jaeger, Protection algorithms for closed-ring grids with distributed generation, IEEE Trans. Power Deliv. 37 (5) (2022) 4042–4052.

[20] D. Wolter, M. Zdrallek, M. Stötzel, C. Schacherer, I. Mladenovic, M. Biller, Impact of meshed grid topologies on distribution grid planning and operation, in: CIRED 2017-24th Int. Conf. Exhib. Electricity Dist, 2017, pp. 2338–2341.

[21] M. Wadi, M. Baysal, A. Shobole, Comparison between open-ring and closed-ring grids reliability, in: 2017 4th Int. Conf. on Electrical and Electronic Engineering, ICEEE, Ankara, Turkey, 2017, pp. 290–294.

[22] M. Wadi, M. Baysal, A. Shobole, Reliability and sensitivity analysis for closed-ring distribution power systems, Electr. Power Compon. Syst. 49 (6–7) (2021) 696–714.

[23] R. Willheim, R. Waters, Transient phenomena associated with ground faults in three-phase systems, in: Neutral Grounding in High-Voltage Transmission, Elsevier, New York, NY, USA, 1956, pp. 198–200, ch. 3.

[24] T. Welfonder, Localisation de défauts monophasés dans les réseaux de distribution à neutre compensé (Ph.D. dissertation), Energie électrique, Institut National Polytechnique de Grenoble INPG, Grenoble, 1998.

[25] M. Lehtonen, Transient Analysis for Ground Fault Distance Estimation in Electrical Distribution Networks (Ph.D. dissertation), Technical Research Centre of Finland, Espoo, 1992.

[26] M. Loos, Single Phase to Ground Fault Detection and Location in Compensated Network (Ph.D. dissertation), Université Libre De Bruxelles, Brussels, 2014.

[27] M.F. Abdel-Fattah, M. Lehtonen, R.J. Millar, C.J. Kim, The impact of the distribution network type and configuration on the transient behavior of the fault and neutral points during earth faults, in: Int. Conf. on Power Systems Transients, Vol. 21, IPST2011, pp. 1–8.

[28] J.A. Martinez-Velasco (Ed.), Power System Transients: Parameter Determination, Taylor & Francis Group, Boca Raton, FL, USA, 2010.

[29] T. Noda, Numerical techniques for accurate evaluation of overhead line and underground cable constants, IEEJ Trans. Electr. Electron. Eng. 3 (5) (2008) 549–559.

[30] E.S. Bañuelos-Cabral, J.A. Gutiérrez-Robles, J.L. García-Sánchez, J. Sotelo-Castañón, V.A. Galván-Sánchez, Accuracy enhancement of the JMarti model by using real poles through vector fitting, Elect. Eng. 101 (2019) 635–646.

[31] B. Gustavsen, A. Semlyen, Admittance-based modeling of transmission lines by a folded line equivalent, IEEE Trans. Power Deliv. 24 (1) (2009) 231–239.

[32] J.S.L. Colqui, L.C. Timaná, P.T. Caballero, S. Kurokawa, J.P. Filho, A modified implementation of the Folded Line Equivalent transmission line model in the Alternative Transient Program, Electr. Power Syst. Res. 211 (2022) 108185.

[33] H.K. Høidalen, L. Prikler, F. Peñaloza, ATPDRAW version 7.3 for windows - users' manual, 2021.

[34] A. Nikander, E. Lakervi, J. Suontausta, Applications of transient phenomena during earth-faults in electricity distribution networks, in: Proceedings 1995 International Conference on Energy Management and Power Delivery, Vol. 1, EMPD '95, Singapore, 1995, pp. 234–239.

[35] Short-circuit currents in three-phase a.c. systems - Part 0: Calculation of currents, 2016, IEC 60909-0:2016.

[36] K. Pandakov, Improvements in Protection of Medium Voltage Resonant Grounded Networks with Distributed Sources (Ph.D. dissertation), Department of electric power engineering, Norwegian University of Science and Technology, Trondheim, Norway, 2018.

Paper V

T. Treider, B. Gustavsen and H. K. Høidalen, "Steady-state, iterative method for locating and clearing permanent high impedance earth faults in compensated networks", *16th International Conference on Developments in Power System Protection (DPSP 2022)*, Hybrid Conference, Newcastle, UK, 2022, pp. 327-332.

STEADY-STATE, ITERATIVE METHOD FOR LOCATING AND CLEARING PERMANENT HIGH IMPEDANCE EARTH FAULTS IN COMPENSATED NETWORKS

Thomas Treider[1]*, Bjørn Gustavsen[1], Hans K Høidalen[1]

[1]Department of Electric Power Engineering, Norwegian University of Science and Technology, Trondheim, Norway
**thomas.treider@ntnu.no*

Keywords: HIGH IMPEDANCE EARTH-FAULT, FAULT LOCATION, RESONANCE GROUNDING

Abstract

This paper presents a method for locating permanent high impedance earth faults in compensated networks. The method locates the faulty feeder and provides aid to the operator when clearing the fault by determining whether the fault was cleared successfully, allowing precise determination of the faulty section on the feeder in question through manual sectionalizing. The method does not require any added equipment or advanced control of the arc suppression coil, but basic network data is required. The feasibility of the method is verified through simulations and illustrated through an example showing the successful clearing of a 20 kΩ earth fault. The attainable sensitivity of the method is discussed, and it is shown that the accuracy of the initial fault resistance estimate is limited mainly by the accuracy of the current and voltage measurements. The upper fault resistance limit of the fault clearing assessment is further affected by the accuracy of the system data, as well as the change in shunt admittance asymmetry of the network after sectionalizing. Further research will focus on practical implementation and testing of the method.

1 Introduction

In compensated networks the transformer neutral is grounded through an arc suppression coil (ASC). The purpose of the ASC is to minimize the earth fault current, leading to self-extinction of arcing faults. The low fault current makes permanent faults very challenging to locate. High impedance earth faults can be caused by trees, sagging conductors or insulator failure, and they may cause significant damage if left undiscovered. HIFs also pose a serious safety issue for people and animals who may inadvertently come into contact with a live part of the network.

In Norway, network operators are required to detect and clear ground faults up to 3kΩ within 10 seconds in distribution systems, whereas a two-hour limit is set for regional networks [1]. In Sweden, earth faults below 3kΩ are required to be cleared by protection systems [2]. Faults above 3 kΩ are still important to locate, and it is usually a challenging and time-consuming task for network operators. It is achieved by reconfiguring the network and disconnecting lines until the fault appears to be cleared, although the reconfiguration itself makes this fault clearing assessment difficult. Even if a faulty feeder could be determined, locating the faulty section is challenging with this approach.

Several methods have been developed for the faulty feeder selection in compensated networks. Methods based on recognizing capacitive feeders [3,4] and current-based methods [5,6] have been proposed, and methods based on zero sequence energy are found in commercially available relays [7,8]. These methods are however focused on the faulty feeder selection, and assessment of the fault clearing success is not considered. Advanced methods based on changes in residual currents and voltages during faults generally give highly accurate results [9-13], but the sectionalizing renders the comparison with the pre-fault reference values invalid. Therefore, there is a need for a method which can assess the fault clearing success and provide a continuous fault indication until the faulty section has been found.

This paper proposes a method for locating the faulty feeder in a radial distribution network, as well as determining the faulty section through iterative manual sectionalizing. Fault detection capabilities, estimation of the system compensation degree, method implementation and practical considerations are discussed. The paper is organized as follows. The theoretical foundation of the proposed method is given in section 2. Section 3 outlines the steps of the method and its implementation, while the method is illustrated, tested, and discussed in detail in section 4 and 5. Finally, section 6 provides conclusions and thoughts on future work.

2 Theory

1.1 Neutral Current Splitting

Consider a network compensated by an ASC tuned to some degree k, so that its value L_n is given by

$$L_n k = L_{res} \tag{1}$$

The inductance L_{res} corresponds to the resonance condition, i.e. the coil inductance which compensates for the total shunt capacitance of the network C_{tot} as described by (2).

$$\frac{1}{j\omega L_{res}} + j\omega C_{tot} = 0 \tag{2}$$

The coil L_n is replaced, in theory, by two coils in parallel, L_{res} and L_p, such that L_n=L_{res}||L_p. This is illustrated in Fig. 1(a). The coil L_p is related to the actual value of the coil L_n through the compensation degree k as described by (3).

$$L_p = \frac{k}{k-1} L_n \tag{3}$$

The benefit of introducing this notation is the more compact form of the equations derived in this paper as the total capacitance to ground in the system is cancelled by L_{res}, as described in (2).

1.2 Neutral Voltage

In the network in Fig. 1(b) the total phase-ground admittances for the three phases are as given in (4),

$$\begin{aligned} Y_a &= Y = G + j\omega C \\ Y_b &= Y + Y_{\Delta b} = G + G_{\Delta b} + j\omega(C + C_{\Delta b}) \\ Y_c &= Y + Y_{\Delta c} = G + G_{\Delta c} + j\omega(C + C_{\Delta c}) \end{aligned} \tag{4}$$

where C and G are the total capacitance and conductance in phase a, respectively, and $C_{\Delta b}$, $C_{\Delta c}$, $G_{\Delta b}$ and $G_{\Delta c}$ describe the deviation of capacitance and conductance in phases b and c with respect to phase a. The neutral voltage can be expressed as

$$\boldsymbol{V}_n = -\boldsymbol{E}_a \frac{D}{G_t + \frac{1}{R_p} + \frac{1}{j\omega L_p}} \tag{5}$$

where $\boldsymbol{E}_a$ is the phase-neutral voltage of the reference phase, in this case phase a, and

$$\begin{aligned} D &= h^2 Y_{\Delta b} + h Y_{\Delta c} \\ G_t &= 3G + G_{\Delta b} + G_{\Delta c} \end{aligned} \tag{6}$$

In (6), the operator $h = e^{j120°}$. The resistor R_p represents the coil losses and any additional parallel resistor. When a fault occurs in phase a, the neutral voltage becomes instead as given in (7).

$$\boldsymbol{V}_n = -\boldsymbol{E}_a \frac{D + \frac{1}{R_f}}{G_t + \frac{1}{R_p} + \frac{1}{j\omega L_p} + \frac{1}{R_f}} \tag{7}$$

2.2 Estimating the Fault Current from Measurements

The fault current can be estimated using either the neutral point measurements or feeder phase quantities.

2.2.1 Using Neutral Quantities: Assume that the compensation degree k of the network is known. Then, the current $\boldsymbol{I}_p$ flowing through R_p and L_p as illustrated in Fig.1 can be computed based on the measured neutral current $\boldsymbol{I}_n$ and voltage $\boldsymbol{V}_n$ as shown in (8).

$$\boldsymbol{I}_p = \boldsymbol{I}_n + \frac{\boldsymbol{V}_n}{j\omega L_{res}} \tag{8}$$

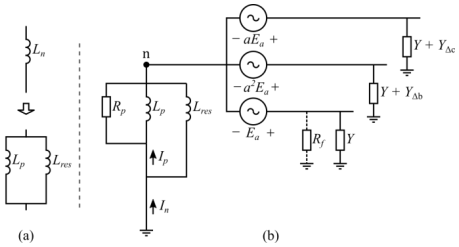

Fig. 1 (a) Neutral point impedance splitting, (b) Network model

It can be shown that $\boldsymbol{I}_p$ will, during healthy (pre) and faulty conditions, satisfy (9).

$$\begin{aligned} \boldsymbol{I}_{p,pre} &= G_t \boldsymbol{V}_{n,pre} + D\boldsymbol{E}_{a,pre} \\ \boldsymbol{I}_{p,fault} &= \left(G_t + \frac{1}{R_f}\right)\boldsymbol{V}_{n,fault} + \left(D + \frac{1}{R_f}\right)\boldsymbol{E}_{a,fault} \end{aligned} \tag{9}$$

By assuming that the voltage $\boldsymbol{E}_a$ remains unchanged during the fault, (10) is obtained.

$$\Delta\boldsymbol{I}_p = \boldsymbol{I}_{p,fault} - \boldsymbol{I}_{p,pre} = G_t \Delta\boldsymbol{V}_n + \boldsymbol{I}_f \approx \boldsymbol{I}_f \tag{10}$$

The term $G_t\Delta\boldsymbol{V}_n$ is assumed to be small due to the low value of G_t. Therefore, the fault current can be approximated as $\Delta\boldsymbol{I}_p$.

2.2.2 Using Phase Currents

When a fault occurs in the network, the phase currents will change on all feeders. Assuming that the load current remains unchanged in all three phases, and that the change observed in each phase current due to the neutral voltage is approximately identical, i.e. assuming $Y_{\Delta b} \approx Y_{\Delta c} \approx 0$, then (11) describes the changes in phase currents on the faulty feeder x. The admittance Y_x is the per phase admittance of feeder x, and $\boldsymbol{I}_{a,x}$ is the current in phase a on feeder x.

$$\begin{aligned} \Delta\boldsymbol{I}_{a,x} &= \Delta\boldsymbol{V}_n Y_x + \boldsymbol{I}_f \\ \Delta\boldsymbol{I}_{b,x} &= \Delta\boldsymbol{V}_n Y_x \\ \Delta\boldsymbol{I}_{c,x} &= \Delta\boldsymbol{V}_n Y_x \end{aligned} \tag{11}$$

The faulty feeder and phase may then be found by monitoring indicators $\boldsymbol{J}$ in phases a, b and c on each feeder m:

$$\begin{aligned} \boldsymbol{J}_{m,a} &= \Delta\boldsymbol{I}_{a,m} - \frac{1}{2}\left(\Delta\boldsymbol{I}_{b,m} + \Delta\boldsymbol{I}_{c,m}\right) \\ \boldsymbol{J}_{m,b} &= \Delta\boldsymbol{I}_{b,m} - \frac{1}{2}\left(\Delta\boldsymbol{I}_{a,m} + \Delta\boldsymbol{I}_{c,m}\right) \\ \boldsymbol{J}_{m,c} &= \Delta\boldsymbol{I}_{c,m} - \frac{1}{2}\left(\Delta\boldsymbol{I}_{a,m} + \Delta\boldsymbol{I}_{b,m}\right) \end{aligned} \tag{12}$$

On a healthy feeder, all these indicators will be approximately zero during fault. On the faulty feeder, the indicator in the faulty phase will correspond to the fault current $\boldsymbol{I}_f$, while the indicators in the healthy phases will be approximately $-0.5\boldsymbol{I}_f$. The indicators should therefore be able to distinguish between earth faults and other fault types, where such a pattern is not observed.

2.3 Estimating the Compensation Degree

If the compensation degree is not known, (10) cannot be applied to estimate the fault current. The compensation degree can however be estimated by combining (10) and (12). A value of k is selected so that the fault current estimated by (10) equals the fault current estimated by (12). For a fault in phase r on feeder m, this corresponds to solving (13), where $\boldsymbol{J}_{m,r}$ is the indicator in (12) which corresponds to phase r on feeder m.

$$k = \frac{\Delta \boldsymbol{V}_n}{j\omega L_n(\boldsymbol{J}_{m,r} - \Delta \boldsymbol{I}_n)} \tag{13}$$

2.4 Estimating Fault Resistance

Once the fault current and compensation degree are estimated, the fault resistance can be estimated using (14).

$$R_f \approx -\frac{\Delta \boldsymbol{V}_n}{\Delta \boldsymbol{I}_p}\left(\frac{1}{R_p} + \frac{1}{j\omega L_p} - D\right)\frac{1}{D} - \frac{1}{D} \tag{14}$$

Here, the asymmetry D can be obtained by solving (5) using pre-fault measurements. This value of D can then be stored and assumed unchanged as long as the network topology remains the same.

3 Iterative Fault Location and Clearing

This section presents and explains the different steps in the proposed method. In section 3.5 the implementation of the method is summarized with detailed description of the steps and the relation between them.

3.1 Initial Fault Detection

The compensation degree k is considered a somewhat uncertain parameter. It may be available from the ASC controller, or it may be considered inaccurate or altogether unavailable. It is therefore beneficial to discuss the two possible situations in some detail.

If the compensation degree is available, (10) and (12) may be used for fault detection purposes. For instance, if the indicators suggest a possible 5 A fault current, and the current $\Delta \boldsymbol{I}_p$ takes a similar value, it can be assumed that an earth fault is present in the system.

If the compensation degree is not available with sufficient accuracy, it may be estimated using (13). However, it has not been properly investigated whether or not (12) is sufficient as a fault detection stage on its own. A single-phase load event could in theory give the appearance of an earth fault if only the indicators are monitored, although this is not a likely scenario. If (12) is not sufficient to reliably detect and determine earth faults, then some external fault detection logic is required.

3.2 Faulty Feeder Selection

The availability of k is primarily a concern for a possible fault detection stage. In either case, whether k is known in advance or estimated during fault, the first step of the algorithm is the estimation of the fault current using (10) and (12). This first step then becomes an all-in-one operation in which the fault current is estimated, the faulty feeder is found via the indicators, and k is optionally estimated.

3.3 Sectionalizing and Searching

At this point the faulty phase and feeder have been found. However, it may be beneficial to obtain a more precise estimate for where the fault is located on the feeder. Although an accurate fault detection can be achieved, methods which are based on mapping all the system parameters in advance will face the same challenge once sectionalizing begins. As the network topology changes, so does the system capacitance, asymmetry, and compensation degree. In order to be able to estimate the fault current accurately during sectionalizing as well, it is suggested to estimate the new compensation degree in the network. This is done based on an estimate of the amount of capacitance being switched out during the searching process. If a feeder representing 10 % of the system capacitance is disconnected, the compensation degree k can be updated accordingly. This information may come from capacitance measurements performed in advance or from standardized line parameter tables. Estimating the change in network asymmetry D is however not as easy, and very large changes in this parameter represent some uncertainty as shown in the following paragraphs.

Let the subscript "pre" refer to the state before the fault occurred. The subscript "post" refers to the state after a part of the network has been disconnected in an attempt to clear the fault. The current $\boldsymbol{I}_p$ can in these two states be expressed as

$$\begin{aligned} \boldsymbol{I}_{p,pre} &= G_{t,pre}\Delta \boldsymbol{V}_{pre} + D_{pre}\boldsymbol{E}_{a,pre} \\ \boldsymbol{I}_{p,post}^{healthy} &= G_{t,post}\Delta \boldsymbol{V}_{n,post} + D_{post}\boldsymbol{E}_{a,post} \\ \boldsymbol{I}_{p,post}^{faulty} &= G_{t,post}\Delta \boldsymbol{V}_{n,post} + D_{post}\boldsymbol{E}_{a,post} + \boldsymbol{I}_{f,post} \end{aligned} \tag{15}$$

The superscripts "healthy" and "faulty" here refer to the two possible states of the network after the switching operation. Either the fault was cleared successfully, in which case no fault current is present, or, if the fault was not successfully cleared a fault current will be present. This fault current will not have the same value as the fault current observed before the switching, hence the added subscript "post".

The current $\boldsymbol{I}_p$ can still be computed using (8), keeping in mind that a new compensation degree k_{post} must be utilized after the switching. When computing $\Delta \boldsymbol{I}_p = \boldsymbol{I}_{p,post} - \boldsymbol{I}_{p,pre}$, the result depends on whether the fault was cleared or not as described by (16).

$$\begin{aligned} \Delta \boldsymbol{I}_p^{healthy} &= \boldsymbol{E}_a \Delta D \\ \Delta \boldsymbol{I}_p^{faulty} &= \boldsymbol{E}_a \Delta D + \boldsymbol{I}_{f,post} \end{aligned} \tag{16}$$

The interpretation of (16) is so that if the fault is not cleared, the new fault current will be contained in $\Delta \boldsymbol{I}_p$. If the fault was cleared, $\Delta \boldsymbol{I}_p$ would not contain any fault current. However, due to the term $\boldsymbol{E}_a \Delta D$, which cannot be compensated for without knowing how the asymmetry D has changed, $\Delta \boldsymbol{I}_p$ would still not return to zero as it was before the fault originally occurred.

3.4 Assessing the Fault Clearing

The current $\Delta \boldsymbol{I}_p$ have been established as the key parameter to monitor due to some very beneficial properties. First, regardless of the availability of k, $\Delta \boldsymbol{I}_p$ can be continuously monitored as long as some initial value of k is provided. In healthy pre-fault conditions, $\Delta \boldsymbol{I}_p$ will remain close to zero anyway. If k is accurately estimated throughout the sectionalizing, $\Delta \boldsymbol{I}_p$ will continue to remain high as long as the fault is present. If the faulted section is successfully disconnected, $\Delta \boldsymbol{I}_p$ will drop down to a small residual value described by (16). Although, as explained earlier, the change in the asymmetry D will impact this residual value. So, if the magnitude of the fault current was similar to that of the residual value of $\Delta \boldsymbol{I}_p$, this fault clearing assessment will not be possible.

The fault resistance may however be a more intuitive parameter to monitor. Equation (14) also incorporates the change in neutral voltage in addition to $\Delta \boldsymbol{I}_p$, and R_f is suggested used as the monitored parameter throughout this process. As $\Delta \boldsymbol{I}_p$ is zero in healthy operation, R_f should in theory be infinitely large. When the fault is cleared, R_f should then return to a very large value, though not as large it was pre-fault due to the residual value of $\Delta \boldsymbol{I}_p$.

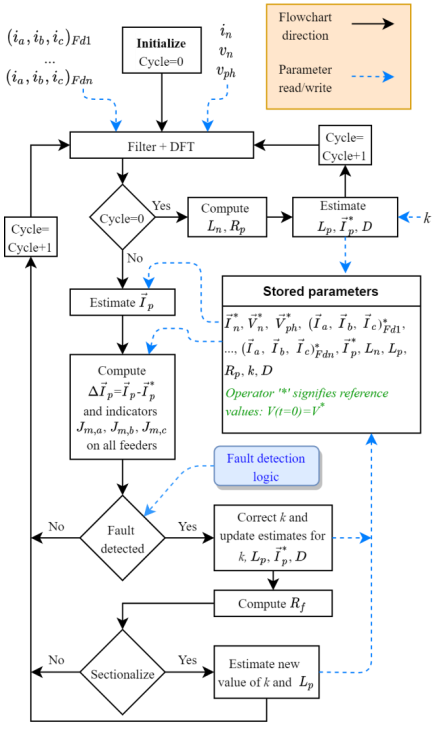

Fig. 2 Flowchart describing the method.

3.5 Algorithm Implementation

A flowchart for the method is shown in Fig. 2. Measurements of neutral current and voltage, phase-neutral voltages and phase currents on all n feeders are used as inputs to a lowpass filter which extracts the 50 Hz components. A DFT computes the corresponding phasors. In this diagram the DFT is assumed to output phasors once per cycle, but it can also be implemented as outputting phasors once per sample, always considering measurements from the past cycle (20 ms). In the first iteration, the parameters L_n and R_p are computed, an estimated value of k is inputted, and the parameters L_p, D and $\boldsymbol{I}^*_p$ are all estimated. Here, the asterisk operator is used to label pre-fault reference values obtained during the first iteration at $t = 0$, for instance $\boldsymbol{V}_n(t=0) = \boldsymbol{V}^*_n$. The changes in currents and voltages are then computed with respect to these references, for instance $\Delta \boldsymbol{V}_n(t) = \boldsymbol{V}_n(t) - \boldsymbol{V}^*_n$. All parameters and pre-fault reference values are stored until they are updated or replaced later on, or until the algorithm is restarted.

The method is initialized manually at a time when the network is assumed to be healthy. The computation of $\Delta \boldsymbol{I}_p$ and the indicators in (12) is done continuously. Although fault detection is not considered in detail in this paper, the fault detection stage is placed after the computation of $\Delta \boldsymbol{I}_p$ and the indicators as these may serve as the basis for a fault detection stage.

4 Test Case Network

The test network used is a 22 kV distribution network with 5 identical radials as depicted in Fig. 3. Each radial consists of 15 km OH-line and two 500 m cable segments located at each end modelled as PI-lines. Asymmetry is added to each phase individually by adjusting the capacitance to ground. The compensation degree of the network is approximately $k = 1.05$. Two circuit breakers are located on feeder 1; one at the main bus and another 10.5 km out on the feeder. See Table I for complete system data.

5 Results and Discussion

5.1 Case Study: Earth Fault Clearing Sequence

A permanent fault is simulated by adding a constant resistance to ground on feeder 1 at a distance 6.5 km from the main bus, i.e. between the two circuit breakers. The method is initialized assuming that the compensation degree of the network is $k = 1.1$. At the time T0 a fault occurs in phase a. Fig. 4 shows that the fault current estimate $\Delta \boldsymbol{I}_p$ is much too large due to the erroneous compensation degree assumed when initializing the algorithm. The connection of a parallel resistor R_e at T1 improves the situation somewhat. The indicator $\boldsymbol{J}_{1,a}$ on the faulty feeder closely matches the correct value of the fault current and is used to estimate k using (13). This is done before the parallel resistor is connected, but in this example the new value of k is applied at T2 to illustrate the effect of these two steps more clearly. At T3 the outer circuit breaker on feeder 1

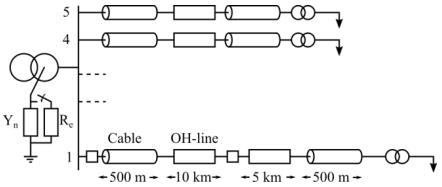

Fig. 3 Test case network

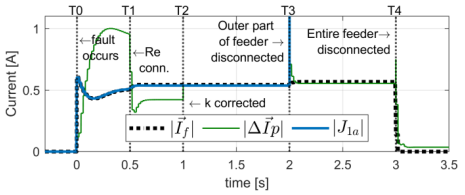

Fig. 4 Fault current $\boldsymbol{I}_f$, $\Delta\boldsymbol{I}_p$ and indicator $\boldsymbol{J}_{1a}$.

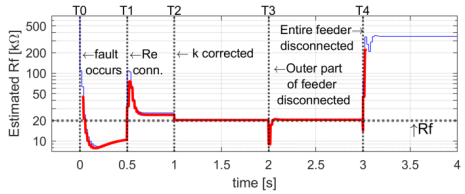

Fig. 5 Real part (red, thick line) and absolute value (blue, thin line) of estimated fault resistance.

is opened in an attempt to clear the fault. Because loads were disconnected at T3, $\boldsymbol{J}_{1,a}$ can no longer accurately estimate the fault current. Based on the amount of capacitance disconnected the new compensation degree is estimated and used for continuous computation of $\Delta\boldsymbol{I}_p$. As explained by (16), $\Delta\boldsymbol{I}_p$ still contains the fault current, but with an added disturbance from $\boldsymbol{E}_a\Delta\boldsymbol{D}$. The fault current estimate is therefore less accurate than it was before the switching of the network. At T4 the inner circuit breaker disconnects feeder 1 in its entirety, and the fault is cleared. $\Delta\boldsymbol{I}_p$ drops to a value close to zero, indicating that no fault current is present.

Fig. 5 shows how the fault resistance estimate varies throughout this sequence of events. At the time T0 it drops down to approximately 10 kΩ. The connection of the parallel resistor improves the estimate. At T2 the compensation degree is corrected, and the fault resistance estimate correctly settles at 20 kΩ. This is also achieved in the case where no parallel resistor is used. At T3 the outer part of feeder 1 is disconnected, but the fault resistance estimate remains correctly at approximately 20 kΩ. At T4 the entire feeder is disconnected, and the fault resistance estimates jumps up to 350 kΩ. As discussed previously, this finite value of R_f is due to the non-zero value of $\Delta\boldsymbol{I}_p$. The asymmetry of the network is now unknown, and it cannot be compensated for. However, because the actual fault current was much larger than this residual value of $\Delta\boldsymbol{I}_p$, the fault clearing is easily confirmed.

Table 1 Test Network Parameters

Simulation Data	
OH-line	3-phase PI-section: 50 Hz, R=0.076 Ω/km, X=0.322 Ω/km, C=11.416 nF/km, R_0=0.223 Ω/km, X_0=1.507 Ω/km, C_0=5.222 nF/km, G_0=32.81 nS/km. Asymmetry: 5% and 2% are added to C_0 in phases *b* and *c*, respectively.
Cable	3-phase PI-section: 50 Hz, R=0.125 Ω/km, X=0.11 Ω/km, C_0=0.28 µF/km. Asymmetry: 4% and 3% are added to C_0 in phases *a* and *b*, respectively.
Loads	3-phase 2 MVA loads connected via Δ-Δ load transformers. Power factor 0.9.
Main Transformer	25 MVA 66/22 kV Dy11, 3-leg stacked transformer. X=5.9%, R=0.35%. Modelled using the Hybrid transformer model in ATPDraw with no capacitance or core effects included.
Neutral point impedance	R_p=50 kΩ (coil losses), L_n=1.76 H. ASC tuning *k*=1.05. Parallel resistor R_c=2543 Ω.
Other	Sample rate: 4 kHz. Software: ATPDraw version 7.2p11.

5.2 *Reliability and Practical Considerations*

Load changes does not have an impact on the method. A single-phase load event could in theory trigger the indicators, but $\Delta\boldsymbol{I}_p$ is not affected. Variation in load asymmetry was investigated and found to have negligible effect on the accuracy. Measurement accuracy is a potential issue, especially in the case of asymmetric measurement errors. Errors within ± 5% and ± 5° yielded a resistance estimate error of 13 % in the case considered earlier. Measurement errors may be particularly critical when faults occur on lightly loaded feeders, though this requires further investigation and testing. Unsystematic measurement errors, due to for instance noise, will perhaps limit the method's sensitivity further.

Network changes are also easily managed. The current $\Delta\boldsymbol{I}_p$ can have a similar response to that of an earth fault during network reconfigurations due to the change in compensation degree, but this will however coincide with a registered breaker action. The indicators will also not be triggered for three-phase events, making it easy to discard such events. Permanent changes made to the network configuration or operating point requires re-initialization of the method. The method is also valid during under-compensated operation of the network. However, the fault clearing stage becomes unreliable as the disconnection of feeders may cause the network to come into resonance, giving a very low fault current. It then becomes difficult to distinguish between a successful and an unsuccessful fault clearing.

A parallel resistor is not required, but it provides damping as illustrated in Fig. 6. This in turn causes the fault current and fault resistance estimates to settle quicker, which is desirable.

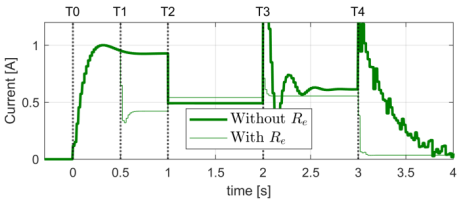

Fig. 6 Estimate of $\Delta \boldsymbol{I}_p$ with and without R_e connected at T1.

6 Conclusion

In this paper a method for locating and clearing high impedance earth faults in compensated distribution networks has been proposed. Though it can be used for precise estimation of the fault resistance, its main benefit is the ability to give reliable assessment of whether or not a fault clearing attempt is successful. The method is further strengthened by its ability to obtain estimates for several of the required parameters, and its ability to distinguish earth faults from other network events. It does however require information pertaining to the network topology. The method shows promising results based on the simulations performed in this paper. Although measurement inaccuracy reduces the precision of the fault resistance estimate somewhat it can still be a reliable tool for location and confirmation for fault clearing for high impedance faults. The paper has also shown that the obtained sensitivity will vary based not only on non-ideal conditions such as measurement inaccuracy, but also on system parameters such as the shunt admittance asymmetry of the network.

Future work will focus on testing the method using fault records obtained from a real network, and on investigating the impact of current transformer accuracy on the feasibility of detecting very small current changes. Developing criteria and correct thresholds for confirmation of fault clearing is also of great importance for obtaining maximum sensitivity. Extending the method to work beyond radially operated networks will also be studied.

7 Acknowledgements

The work was funded by the Norwegian Research Council project ProDig (295034/E20).

8 References

[1] 'Veiledning til forskrift om elektriske forsyningsanlegg,' (in Norwegian), https://www.dsb.no/lover/elektriske-anlegg-og-elektrisk-utstyr/veiledning-til-forskrift/veiledning-til-forskrift-om-elektriske-forsyningsanlegg, accessed 21 October 2021

[2] 'Elsäkerhetsverkets föreskrifter ochallmänna råd om hur elektriska starkströmsanläggningar ska vara utförda (ELSÄK-FS 2008:1)' (in Swedish), https://www.elsakerhetsverket.se/globalassets/foreskrifter/elsak-fs-2008-1-konsoliderad, accessed 21 October 2021

[3] Druml, G., Kugi, A., Seifert, O.: 'A new directional transient relay for high ohmic earth faults'. CIRED 2003 - 17th International Conference and Exhibition on Electricity Distribution, Barcelona, Spain, May 2003, pp. 1-6

[4] Abdel-Fattah, M.F., Lehtonen, M.: 'Transient algorithm based on earth capacitance estimation for earth-fault detection in medium-voltage networks', IET Gener. Transm. Distrib., 2012, 6, (2), pp. 161-166

[5] Habib, M. Z., Abdel-Fattah, M. F., Taylor, N.: 'A current-based solution for earth-fault location in resonant-earthed medium-voltage distribution systems'. 15th International Conference on Developments in Power System Protection (DPSP 2020), Liverpool, UK, March 2020, pp. 1-6

[6] Berggren, J., Hammarson, L.: 'Novel method for selective detection of earth faults in high impedance grounded distribution networks'. CIRED 2005 - 18th International Conference and Exhibition on Electricity Distribution, Turin, Italy, June 2005, pp. 1-4

[7] Loos, M., Werben, S., Kereit, M., et al.: 'Fault direction method in compensated network using the zero sequence active energy signal'. EuroCon 2013, Zagreb, Croatia, July 2013, pp. 717-723

[8] Gajić, Z., Aganović, S., Pajunen, R., et al.: 'Universal earth-fault protection method for high impedance grounded power system'. 15th International Conference on Developments in Power System Protection (DPSP 2020), Liverpool, UK, March 2020, pp. 1-6

[9] Schinerl, T.: 'A new sensitive detection algorithm for low and high impedance earth faults in compensated MV networks based on the admittance method'. CIRED 2005 - 18th International Conference and Exhibition on Electricity Distribution', Turin, Italy, June 2005, pp. 1-4

[10] Nikander, A., Järventausta, P.: 'Identification of high-impedance earth faults in neutral isolated or compensated MV networks', IEEE Trans. Power Deliv., 2017, 32, (3), pp. 1187-1195

[11] Welfonder, T., Leitloff, V., Feuillet, R., et al.: 'Location strategies and evaluation of detection algorithms for earth faults in compensated MV distribution systems', IEEE Trans. Power Deliv., 2000, 15, (4), pp. 1121-1128

[12] Hänninen, S., Lehtonen, M.: 'Method for detection and location of very high resistive earth faults', ETEP, 1999, 9, (5), pp. 285-291

[13] Sagastabeitia, K. J., Zamora, I., Mazón, A. J., et al.: 'Low-current fault detection in high impedance grounded distribution networks, using residual variations of asymmetries', IET Gener. Transm. Distrib., 2012, 6, (12), pp. 1252-1261

Paper VI

T. Treider and H. K. Høidalen, "Implementation and laboratory verification of method utilizing phase and neutral quantities for detection and location of low-current earth faults in resonant grounded networks", *IET Generation, Transmission & Distribution*, vol. 17, no. 24, pp. 5446-5457, 2023.

Implementation and Laboratory Verification of Method Utilizing Phase and Neutral Quantities for Detection and Location of Low-Current Earth Faults in Resonant Grounded Networks

Thomas Treider, Hans Kristian Høidalen

***Abstract*—Earth faults is a challenging fault type to locate in resonant grounded networks due to their naturally low fault current, and the problem increases with an increased fault impedance. This paper describes the detailed implementation and laboratory testing of a method for detection, location and clearing of earth faults with very small fault currents. The method consists of two indicators used in the fault detection stage, where their simultaneous operation ensures selective fault detection and faulty feeder selection. One of these indicators also enables continuous fault indication throughout a sectionalizing process. The laboratory tests demonstrate that both indicators function as intended, and it is the current sensors which ultimately limit the attainable sensitivity. Faults up to 15 kΩ were detected successfully in the laboratory network based on phase current measurements, while the sectionalizing indicator showed much higher sensitivity and functioned as intended in a 50 kΩ fault. Measurements from one field test in a 22 kV network corroborate the laboratory results and demonstrate the expected earth fault indicator response.**

***Index Terms*—Compensated networks, Fault detection, Fault location, High-impedance earth fault, Sectionalizing.**

I. Introduction

EARTH faults in resonant grounded systems represent a particularly challenging case for protection systems due to their very low fault currents. As a result, conventional protection systems such as over-current and distance protection can not be used. Large fault impedances also create problems for transient based earth fault protection due to the absence of earth fault transients with sufficient magnitude. The terms "high impedance" and "low current" are relative terms, given different meaning by different authors in the scientific literature. While for example Norwegian regulations require detection of faults up to 3 kΩ [1], faults up to hundreds of kΩ's are not uncommon [2], [3]. High impedance faults may evolve into more serious faults over time, so it is of interest to be able to detect them as early as possible. Therefore, this paper is concerned with faults above 3 kΩ.

Specialized earth fault location schemes have been proposed extensively in the literature. The magnitude of the neutral voltage is the standard fault detecting approach in the case of low impedance faults, but this is not reliable in the case of very high fault impedances [3]. The neutral voltage increment can be used instead to provide sensitive detection [3], while the slow transient build-up of the fault current is used in [4]. The method presented in [5] uses the deviation of the neutral voltage and current from their known healthy values to estimate an equivalent fault resistance, and a sufficiently low resistance estimate signifies a fault. Methods based on the admittance-principle are also common, monitoring the ratio of the zero-sequence voltage and current to obtain detection and directionality [6].

Fault location may be implemented as a separate stage or integrated with the fault detection stage. If not integrated with the fault detection, it can then be either passive or active. Active methods can for instance involve injection of a superimposed signal that can be traced in the network [7], [8], or a short-time de-tuning of the arc suppression coil (ASC) [5], [9], [10]. The drawbacks of such methods are the added complexity and the need for external equipment or integration with the ASC controller. Reference [11] describes a mobile solution based on injection of non-fundamental frequency currents. This is however meant for ground personnel and represents a much slower, manual localization process. Decentralized or wide-area methods using either fault passage indicators (FPIs) [6] or feeder terminal units (FTUs) [12] have also been proposed, requiring more units and infrastructure to provide sufficient coverage.

Several passive methods for earth fault location can also be found in the literature. In [13] it is proposed to monitor the zero-sequence energy on each feeder, where the sign of the energy will indicate forward/reverse fault. The authors of [14] report that this principle becomes less reliable for very high fault impedances combined with network asymmetry, and [15] further illustrates the problem with asymmetry. In [16], very sensitive detection is achieved based on a charge similarity approach. However, the method assumed and was verified with a perfectly symmetrical network in which no zero-sequence currents flow in healthy operation. Real networks can have considerable asymmetry [17] in which the high impedance fault may be difficult to separate from the natural asymmetry, and it may even temporarily reduce the asymmetry [3]. Reference [18] proposes a complex method where the faults are detected based on neutral voltage displacement, the faulty phase is identified based on the phase voltage variations, and a transient principle is applied to locate the faulty feeder. Again, the asymmetry of the network is mentioned as a limitation, and the method requires several relay units in the network for

The work was funded by the Norwegian Research Council project ProDig (295034/E20).

faulty section determination.

To deal with the problem of measurement errors and network asymmetry, current and voltage increments are often used [3], [19]–[21]. This enables more sensitive detection as the healthy state asymmetry contribution can be canceled out. These methods generally report very sensitivity, i.e. in the 10-200 kΩ range.

Except for reference [5], it is only the task of fault detection and an initial faulty feeder indication which is emphasized in the literature, whereas the ability to provide continuous fault indication throughout a sectionalizing process is neglected. In [5] the fault indication is achieved using a short-time de-tuning of the ASC to map the parameters of the healthy system, but it is not apparent how reliable this is during sectionalizing. Fault indication during a sectionalizing process is an important feature to consider as 1) the initial faulty feeder indication may be inconclusive or wrong, and 2) it may be of interest to determine the faulted section more precisely, not just the faulted feeder. High impedance faults are not time critical, and it is preferable to isolate the faulty part of the network systematically while affecting a limited number of customers. During this process fault indication based on the increments of the feeder currents will be inaccurate, and the neutral voltage magnitude, which can serve this purpose during low-impedance faults, is not reliable when the fault impedance is very high due to its much lower displacement during fault and its possibly equally large displacement during sectionalizing.

This paper contributes with the following: Firstly, the detailed implementation of a novel method for detection and location of earth faults with very low fault currents in compensated networks. The method is based on two independent fault current estimates which together provide sensitive and selective fault detection. One of these estimates is based on the phase currents on each feeder, while the other makes use of the ASC current, voltage and compensation degree. The method also enables continuous monitoring of the fault's presence in the network during sectionalizing, and it can therefore aid operators when clearing the fault. Secondly, this paper presents laboratory tests to validate the proposed method, and to investigate factors limiting the sensitivity. A physical 400 V laboratory network model is used for this purpose, which enables real-life complicating factors such as measurement sensor accuracy and off-nominal network frequency to be included in the tests. The paper also discusses the applicability of such laboratory tests as substitutes for field tests.

The rest of the paper is organized as follows: Section II describes the theoretical foundation for the method, and this is used to derive the proposed fault detection and location method which is presented in Section III. Section IV describes the laboratory test setup, and the results from these tests are presented in Section V. The applicability of the results is discussed along with the challenge of transferring the laboratory results to a real network in section VI, and conclusions are given in Section VII.

II. Modelling Earth Faults

The theoretical foundation for the method discussed in this paper has previously been published in shorter format in reference [22], but it is included here for the sake of readability and further development.

A. Neutral coil split

Consider a network compensated by an ASC tuned to some degree $k > 0$, so that its value L_n is given by (1).

$$L_n = \frac{1}{k} \cdot L_{res} \tag{1}$$

The inductance L_{res} corresponds to the resonance condition, i.e. the coil inductance which compensates for the total shunt capacitance of the network C_{tot} as described by (2).

$$\frac{1}{j\omega L_{res}} + j\omega C_{tot} = 0 \tag{2}$$

The coil L_n is replaced, in theory, by two coils in parallel, L_{res} and L_p, such that $L_n = L_{res}||L_p$. This is illustrated in Fig. 1(a). The coil L_p is related to the actual value of the physical coil L_n through the compensation degree k as described by (3).

$$L_p = \frac{k}{k-1} \cdot L_n \tag{3}$$

The benefit of introducing this notation is the more compact form of the equations derived in this paper as the total capacitance to ground in the system is cancelled by L_{res}, as described in (2).

B. Neutral voltage

In the network in Fig. 1b the total phase-ground admittances for the three phases are as given in (4),

$$\begin{aligned} Y_a &= Y = G + j\omega C \\ Y_b &= Y + Y_{\Delta b} = G + G_{\Delta b} + j\omega(C + C_{\Delta b}) \\ Y_c &= Y + Y_{\Delta c} = G + G_{\Delta c} + j\omega(C + C_{\Delta c}) \end{aligned} \tag{4}$$

where C and G are the total phase-ground capacitance and conductance in phase a, respectively, and $C_{\Delta b}, C_{\Delta c}, G_{\Delta b}$ and $G_{\Delta c}$ describe the deviation of capacitance and conductance in phases b and c with respect to phase a that stems from the natural asymmetry in the network. The neutral voltage in the healthy network can be expressed as

$$\vec{V}_n = -\vec{E}_a \frac{D}{\hat{G} + \frac{1}{R_p} + \frac{1}{j\omega L_p}} \tag{5}$$

where $\vec{E}_a$ is the phase-neutral voltage of the reference phase, in this case phase a, and

$$\begin{aligned} D &= h^2 Y_{\Delta b} + h Y_{\Delta c} \\ \hat{G} &= 3G + G_{\Delta b} + G_{\Delta c} \end{aligned} \tag{6}$$

In (6), the operator $h = e^{j120^\circ}$. The resistor R_p represents the coil losses as well as any external resistor which may be permanently connected. When a fault occurs in phase a, the neutral voltage becomes instead as given in (7).

$$\vec{V}_n = -\vec{E}_a \frac{D + \frac{1}{R_f}}{\hat{G} + \frac{1}{R_f} + \frac{1}{R_p} + \frac{1}{j\omega L_p}} \tag{7}$$

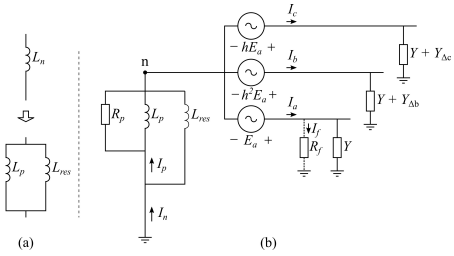

Fig. 1. (a) Neutral point impedance coil split and (b) network model.

C. Fault current

Assuming a fault taking place in phase a, the fault current according to Fig. 1 is

$$\vec{I}_f = \frac{\vec{V}_n + \vec{E}_a}{R_f} \tag{8}$$

A more useful expression for the fault current in the system can be derived by combining (7) and (8):

$$\vec{I}_f = \vec{E}_a \frac{1}{R_f} \left(\frac{\hat{G} + \frac{1}{j\omega L_p} + \frac{1}{R_p} - D}{\hat{G} + \frac{1}{j\omega L_p} + \frac{1}{R_p} + \frac{1}{R_f}}\right) \tag{9}$$

Fig. 2 shows the magnitude of the fault current as a function of fault resistance for a selected set of network parameters, both from simulations in ATP and by using (9).

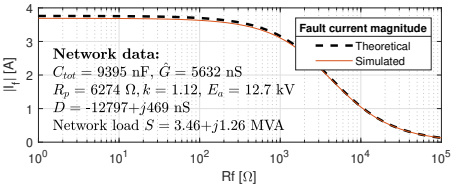

Fig. 2. Fault current magnitude estimated using (9) and simulations in ATP

III. Method for Fault Detection and Location

A. Estimating the fault current during fault

The fault detection and location method described in this paper relies on two separate approaches for estimating the earth fault current, and the theoretical foundation for both these approaches is explained in the following two subsections of the paper.

1) Using the neutral current: Assume that the compensation degree k of the network is known. Then, the current $\vec{I}_p$ flowing through R_p and L_p as illustrated in Fig. 1 can be computed based on the measured neutral current $\vec{I}_n$ and voltage $\vec{V}_n$ as shown in (10).

$$\vec{I}_p = \vec{I}_n + \frac{\vec{V}_n}{j\omega L_{res}} \tag{10}$$

It can be shown that $\vec{I}_p$ will, during healthy (pre) and faulty (fault) conditions, satisfy (11).

$$\begin{aligned} \vec{I}_{p,pre} &= \hat{G}\vec{V}_{n,pre} + D\vec{E}_a \\ \vec{I}_{p,fault} &= (\hat{G} + \frac{1}{R_f})\vec{V}_{n,fault} + (D + \frac{1}{R_f})\vec{E}_a \end{aligned} \tag{11}$$

By assuming that the voltage $\vec{E}_a$ remains unchanged during the fault, as is reasonable considering small fault currents, and recognizing that the asymmetry factor D is constant as long as the network topology does not change, (12) is obtained. The term $\hat{G}\Delta\vec{V}_n$ is assumed negligible, and thus the fault current can be approximated as $\Delta\vec{I}_p$.

$$\Delta\vec{I}_p = \vec{I}_{p,fault} - \vec{I}_{p,pre} = \hat{G}\Delta\vec{V}_n + \vec{I}_f \approx \vec{I}_f \tag{12}$$

Equation (12) can also be derived considering Fig. 3, which is derived from Fig. 1 using Thevenin-Norton transformations. It shows that the current flowing in L_p and R_p in the healthy state is caused by the asymmetry of the system, and if the conductance is assumed negligible, then the current $\vec{I}_{p,pre} = \vec{I}_D = \vec{E}_a D$. When the fault occurs, the switch is closed and the fault current is found as $\vec{I}_f = \vec{I}_p - I_D = \Delta\vec{I}_p$, which is the same result as in (12).

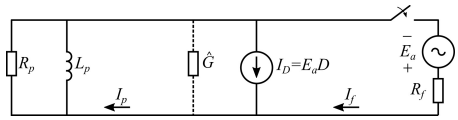

Fig. 3. Equivalent circuit for healthy and faulty network considering the asymmetry as a current source

2) Using phase currents: The currents flowing onto the feeders are assumed to consist of a load current, a capacitive current to ground, a capacitive current to the two others phases, as well as an induced current caused by the mutual inductance between the phases. Equation (13) shows these components for the healthy state current in phase a.

$$\vec{I}_a = (\vec{V}_n + \vec{E}_a)Y + \vec{V}_{ab}j\omega C_{ab} + \vec{V}_{ac}j\omega C_{ac} + \vec{I}_{ind.} + \vec{I}_{load} \tag{13}$$

When a fault occurs in the network in Fig. 1, the phase currents will change. By assuming that 1) line voltages remain constant during fault, 2) the loads remain unchanged due to the constant line voltages, and 3) that the change in phase current magnitude is so small that the induced currents can be assumed constant, then (14) describes the changes in phase currents during a fault in phase a.

$$\begin{aligned} \Delta\vec{I}_a &= \Delta\vec{V}_n Y + \vec{I}_f \\ \Delta\vec{I}_b &= \Delta\vec{V}_n (Y + Y_{\Delta b}) \\ \Delta\vec{I}_c &= \Delta\vec{V}_n (Y + Y_{\Delta c}) \end{aligned} \tag{14}$$

These current increments can be combined to produce three earth-fault indicators, named J_a, J_b and J_c, as described

by (15).

$$\begin{aligned} J_a &= \Delta\vec{I}_a - \frac{1}{2}(\Delta\vec{I}_b + \Delta\vec{I}_c) \\ J_b &= \Delta\vec{I}_b - \frac{1}{2}(\Delta\vec{I}_a + \Delta\vec{I}_c) \\ J_c &= \Delta\vec{I}_c - \frac{1}{2}(\Delta\vec{I}_a + \Delta\vec{I}_b) \end{aligned} \tag{15}$$

By inserting (14) in (15), and by assuming that $Y_{\Delta b} = Y_{\Delta c} \approx 0$, it is seen that the three earth-fault indicators remain at approximately zero during healthy operation. For an earth-fault in phase a, the three earth-fault indicators on the faulty feeder takes on the values in (16), whereas they remain zero on the healthy feeders.

$$J_{a,fault} = \vec{I}_f, \qquad J_{b,fault} = J_{c,fault} = -\frac{1}{2}\vec{I}_f \tag{16}$$

As mentioned earlier, the asymmetries $Y_{\Delta b}$ and $Y_{\Delta c}$ can not be assumed to be zero in real networks. Generally, the transition from (15) to (16) becomes less accurate as $Y_{\Delta b}$ and $Y_{\Delta c}$ increase. Equation (17) shows the values of the indicators J_{a-c} during fault when the asymmetries are included:

$$\begin{aligned} J_{a,fault} &= \vec{I}_f - \Delta\vec{V}_n\frac{1}{2}(Y_{\Delta b} + Y_{\Delta c}) \\ J_{b,fault} &= -\frac{1}{2}\vec{I}_f + \Delta\vec{V}_n(Y_{\Delta b} - \frac{1}{2}Y_{\Delta c}) \\ J_{c,fault} &= -\frac{1}{2}\vec{I}_f + \Delta\vec{V}_n(-\frac{1}{2}Y_{\Delta b} + Y_{\Delta c}) \end{aligned} \tag{17}$$

The errors introduced by the asymmetry are only a few percent of the magnitude of the fault current even in the case of very unsymmetrical networks ($D \approx 5\%$ of $3Y$ [17]), and this can be shown to be independent of the fault resistance. As a result, (16) is a valid simplification of (17).

B. Criterion for fault detection

To detect earth faults in the network, it is proposed to monitor the three indicators in (15) on each feeder. During an earth fault they are expected to have a fixed relationship between them as indicated by (16):

1) The magnitude of the faulty phase indicator is approximately twice as large as the magnitudes of the indicators in the two healthy phases.
2) The phase angles of the healthy phase indicators are equal and approximately 180 degrees out of phase with the faulty phase indicator.

For all other fault types, this relationship will not be observed. Asymmetric load changes could in theory result in a similar response from the indicators, but the current $\Delta\vec{I}_p$ is unaffected by load changes and can be used to give an extra criterion for secure detection of earth faults. If the compensation degree of the network is known with reasonable accuracy, the value obtained for $\Delta\vec{I}_p$ should be comparable with the faulty phase indicator, both in magnitude and angle. A similar approach was suggested in [5], although by utilizing zero sequence currents increments on every feeder. The difference is that the zero sequence currents are less suited to provide information on faulted phase, and directionality can not be obtained without comparing the current increments on all the feeders. The phase current indicators in (15) can perform the required computations without input from the other feeders.

C. Searching for and clearing faults

As the load in the network can not be assumed constant over long periods, the indicators in (15) are not reliable for prolonged fault indication. Once a permanent fault has been detected in the network, the continued monitoring of the fault is done through $\Delta\vec{I}_p$. The pre-fault value $\vec{I}_{p,pre}$ is then no longer updated but instead kept at its last value before the fault was detected. This way $\Delta\vec{I}_p$ remains high as long as the fault is present in the network, whereas it returns to zero if the fault is cleared.

Once the sectionalizing process begins, the ASC is assumed to be kept constant. If a section of the network is disconnected during this process, the compensation degree k increases due to the reduced network capacitance. This increases the value of L_{res}, and the computation of the current $\vec{I}_p$ using (10) must then be done with an updated value of L_{res}. Keeping the current $\vec{I}_{p,pre}$ as an estimate of the current $\vec{I}_D$ in the network is a simplification because the sectionalizing process may alter the asymmetry parameter D, and as a result, the current $\Delta\vec{I}_p$ will most likely not return exactly to zero when the fault is cleared. If the fault current was in the same order of magnitude as this residual value the success of the fault clearing is not possible to determine.

D. Logic implementation and settings

The computation of the current increments is implemented using a sliding window. The current phasors are updated every sample, and the increment of current $\vec{I}$ at sample j is then computed as

$$\Delta\vec{I}_{[j]} = \vec{I}_{[j]} - \vec{I}_{[j-T_{SW}\cdot f_s]} \tag{18}$$

where T_{SW} is the length of the sliding window in seconds and f_s the sampling frequency in Hz. Based on (16), a fault in phase a can be signaled when the criteria in (19) are met.

$$\begin{aligned} |\angle J_b - \angle J_a| &\in [180^\circ - \phi, 180^\circ + \phi] \\ |\angle J_c - \angle J_a| &\in [180^\circ - \phi, 180^\circ + \phi] \\ \frac{|J_b|}{|J_a|} &\in [0.5 - K, 0.5 + K] \\ \frac{|J_c|}{|J_a|} &\in [0.5 - K, 0.5 + K] \end{aligned} \tag{19}$$

The criteria in (19) are visualized in Fig. 4, where a fault in phase a is considered. The parameters K and ϕ are margins added to allow for some deviation from the ideal vector relationship in (16). A fault is detected when both the vectors J_b/J_a and J_c/J_a come into the shaded area. Similar zones are implemented for the fault indication in phases b and c as well, and they are mutually exclusive.

The criteria in (19) are derived from the expected relationship between the vectors J_{a-c}, and in simulations these are sufficient. However, in a physical implementation the indicators are never truly zero. Small fluctuations due to noise

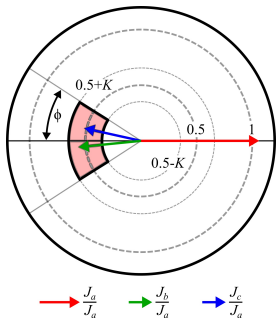

Fig. 4. Indicator relationship during fault in phase a, with the red field representing "trip zone" for a fault in phase a according to (19)

and cross-talk from surrounding conductors can cause the criteria in (19) to be met accidentally and quite frequently unless a magnitude threshold is considered. The criterion in (20) is added to account for this.

$$|\vec{J_a}| > \epsilon_J \tag{20}$$

Adding the magnitude threshold is necessary for secure operation of the indicators, but it does necessarily reduce the sensitivity of the fault detection. Determining the value of this threshold is also a challenge as it must be set higher than the aforementioned noise in healthy operation, and this will require study on the network in question. A final criterion is as mentioned previously to consider the neutral current component $\Delta\vec{I_p}$ as well, discarding all trips from the indicators that do not coincide with a similar response in this current. This way, the neutral current criterion provides added security against false fault detection. The parameter $\Delta\vec{I_p}$ is computed in the same way as the phase current increments, as shown in (18), but with a longer sliding window length T_{SWp} to account for the slower current dynamics in the coil.

A vector comparison between $\Delta\vec{I_p}$ and the faulty phase indicator could be made as well, but this assumes knowledge of the compensation degree k. If k is considered to be uncertain, a simple magnitude criterion like the one in (21) could be used to monitor $\Delta\vec{I_p}$.

$$|\Delta\vec{I_p}| > \epsilon_p \tag{21}$$

If k is known, (21) is extended to (22) to include a vector comparison such as the one used for the phase current indicators, where K_p and ϕ_p are margins similar to K and ϕ in (19). Both J_a and $\Delta\vec{I_p}$ should be identical during fault according to (12) and (16), and the detection logic in (22) can be used in addition to (21). Fig. 5 illustrates this vector comparison.

$$\begin{aligned} \frac{|\Delta\vec{I_p}|}{|J_a|} &\in [1-K_p, 1+K_p] \\ |\angle\Delta\vec{I_p} - \angle\vec{J_a}| &< \phi_p \end{aligned} \tag{22}$$

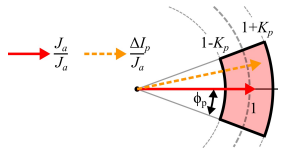

Fig. 5. Indicator relationship during fault in phase a, with the red field representing "trip zone" for a fault in phase a according to (22)

Correct values for the settings in (19)-(22) will primarily be affected by the quality of the measurements, and selecting the correct settings to balance the need for precision and avoiding misoperation is the major challenge. Generally, the sliding window length T_{SW} should be long enough to capture the transients during earth faults, but not so long that the load current can not be assumed constant on the interval, making the transition from (13) to (14) incorrect. The window T_{SWp} should be long enough to allow for the current to increase in the coil, but limiting this window length is not critical as the neutral current is relatively constant. Once a fault has been detected, the computation of $\Delta\vec{I_p}$ using the sliding window is stopped. Assuming that a fault was detected at time t_f, $\Delta\vec{I_p}(t)$ is computed as $\Delta\vec{I_p}(t) = \Delta\vec{I_p}(t) - \Delta\vec{I_p}(t_f - T_{SWp})$ going forward. This way, continuous fault indication is obtained for the sectionalizing process. The phase current indicators can not assist in the sectionalizing process because 1) the load currents can not be assumed constant over many seconds, and 2) the sectionalizing process will necessarily change the phase currents and render (14) invalid. However, their continued calculation using sliding windows is still of interest as the relationship between the indicators that signal a fault is also observed if a fault disappears on its own.

The flowchart in Fig. 6 details the fault detection and localization process described above.

IV. Test Setup and Measurement Processing

A. Norwegian National Smart Grid Laboratory

The laboratory verification is conducted in the distribution network model implemented in the National Smart Grid Laboratory, which is a joint NTNU-SINTEF facility intended for testing of various smart grid technologies [23], [24].

1) Distribution network model: The laboratory contains a 400 V distribution network model which is constructed using physical resistors, inductances and capacitors to emulate a real distribution network. Fig. 7 shows the network topology, where two feeders with three PI-sections each can be operated radially or as a ring-network. The Pi-equivalents can be tuned to represent a 22 kV system with two radials with up to 24 km of overhead lines each, and the network has a voltage scaling of 22:0.4 and current scaling of 50:3 [25]. The network is supplied through a Δ/Y 400 V transformer which is grounded through an inductor for the tests considered in this paper.

2) Network configuration: Both feeders represent 24 km of FeAl 240 mm^2 conductors. The laboratory network has a total of $3C_g$=2.4 µF capacitance to ground, resulting in an uncompensated earth fault current of approximately 175 mA.

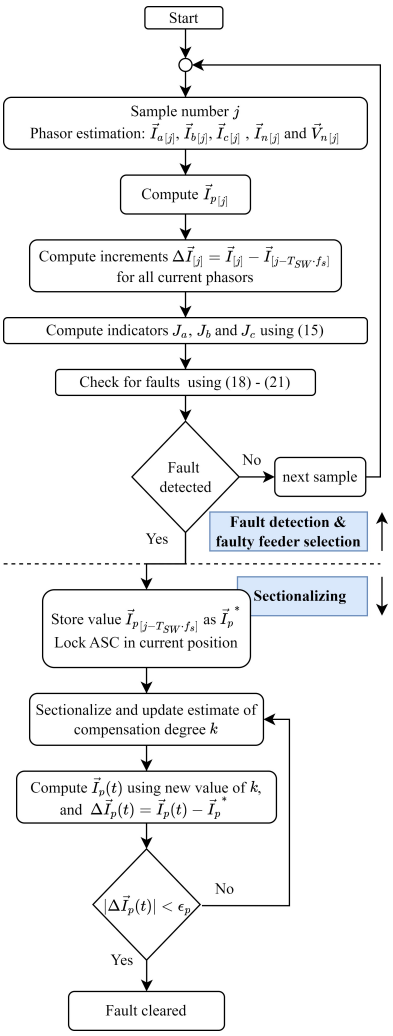

Fig. 6. Flowchart for fault detection process.

A variable inductor is placed in the transformer neutral to make the network resonant grounded. As the ASC is not perfectly linear, its impedance will vary with the voltage across it. This impedance is therefore estimated continuously by measuring the current and voltage of the ASC. Two resistor banks are used to provide loads up to 9 A and 3 A at the end

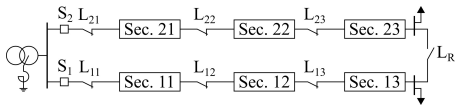

Fig. 7. Test network single line diagram

of feeder 1 and 2, respectively. According to the laboratory documentation, this corresponds to loads in the range 50–150 A [25]. Finally, a variable resistor is connected between phase and ground through a controllable switch to emulate a high impedance fault. Fig. 8 shows the magnitude of the fault current as function of the fault resistance obtained through measurements in the lab with the chosen ASC setting. The complete setup of the lab and the equipment used is given in Table I and Fig. 9, and an overview of the complete laboratory can be found in [25].

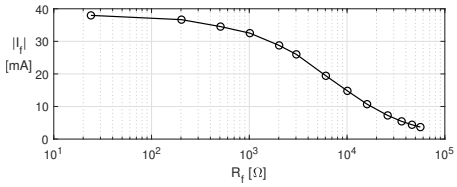

Fig. 8. Measured fault current magnitude as function of fault resistance for the selected ASC setting.

TABLE I
LABORATORY EQUIPMENT

Current sensors	CT_{ph} (default): Fluke i200s, set to 0.1V/A $CT_{ph,2}$: LEM HAS 50-s, 50/5A CT_f and CT_N: Gossen Metrawatt WZ 12-C, 1mV/mA. Both I_f and I_n are measured on a 50-turn coil in order to better suit the measurement range of the probes used.
Voltage sensors	VT_{line}: Tektronix P5200, ratio 1V/500V VT_N: Tektronix P5200A, ratio 1V/50V
ASC	Leybold three-phase inductor, model nr. 732 42.
Other	Sampling frequency 4 kHz.

B. Processing of measurements

1) Phasor estimation: The fault detection method is based on current and voltage phasors. Most phasor estimation techniques assume a 50 Hz signal, and off-nominal frequencies result in a gradual drift of the phase angle over time. For many applications this is not an issue as the relationship between the phasors at any point in time is correct, but because the method presented in this paper relies on phasor increments, i.e. changes over time, the phasor estimation must account for the drift in phase angle that can occur when the system frequency deviates from its nominal value.

The SDFT algorithm [26] is used for this purpose. It is based on a conventional recursive DFT-based phasor estimation,

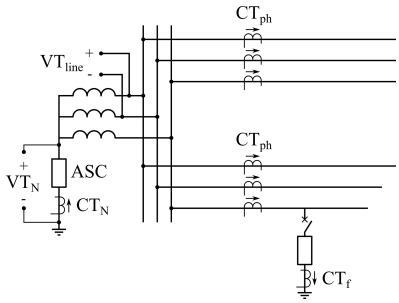

Fig. 9. Laboratory setup with equipment as given in Table I

along with a frequency estimation stage. The frequency of the signal in each window is estimated based on the previous three consecutive phasor outputs using equations (10), (12) and (13) in [26]. By estimating the frequency of the signal at each sample, the expected drift in phase angle can be estimated. The resulting phasors can then be rotated back to their correct values, thus producing phasors with constant phase angles.

In order to produce a stable and accurate frequency estimate, a constant sinusoidal signal must be used. The line voltage is proposed to be used for this purpose as it remains constant during earth faults. The estimated phase angle drift based on this voltage measurement is then used to correct all the other phasor estimates. A 100 Hz low-pass filter is applied to the line voltage measurements to give a better phasor estimation, whereas all other measurements are unfiltered.

Fig. 10 shows the estimated frequency and resulting phasor angle before and after this method has been used. The uncorrected phasor angle which assumes a constant 50 Hz frequency can be seen to drift considerably.

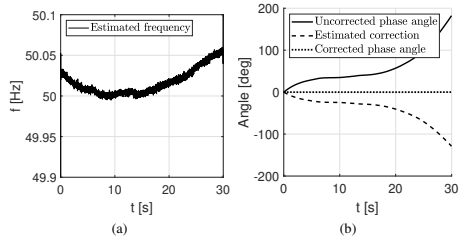

Fig. 10. From measurement of the line voltage in the laboratory: a) estimated frequency and b) resulting phase angle with (dotted) and without (solid) correction of the phase angle drift.

V. Laboratory Test Results and Analysis

A. Phase current indicators

To illustrate the desired response of the phase current indicators in (15), the faulty feeder indicators during a 5 kΩ fault is showed in Fig. 11. It can be seen that the expected relationship between the three indicators is observed, both in terms of phase angles and magnitudes. Furthermore, the indicators relate to the fault current as predicted by (16). The fault detection response for phase a with settings ϵ_J=10 mA, T_{SW}=100 ms, K=0.1 and ϕ=15° is also shown on the right y-axis, illustrating that the fault detection logic is triggered both when the fault occurs as well as when it disappears. The indicators on the healthy feeder did not increase during the fault.

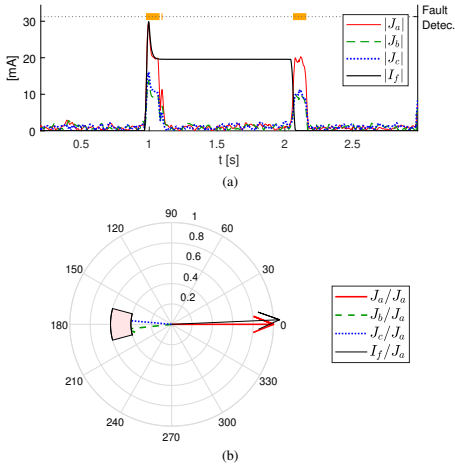

Fig. 11. a) Fault current and indicator magnitudes on the faulty feeder during a 5 kΩ fault, and b) corresponding normalized vectors obtained at time t=1.02 s. The fault is applied at t=1 s and disconnected at t=2.1 s.

By inspection of Fig. 11a, it can be seen that the phase current indicator magnitudes are not truly zero in healthy operation. These small fluctuations give rise to the need for the threshold ϵ_J to avoid frequent false detections in healthy operation, and this effectively limits the maximum sensitivity of the fault detection. Fig. 12 shows the indicator magnitudes during a 20 kΩ fault, where the magnitude of the fault current and indicators no longer are detectable with the ϵ_J=10 mA setting. Furthermore, the magnitude of the fluctuations are now more significant compared to the fault current magnitude, distorting the ideal expected relationship between the three vectors as predicted by (16). Lowering the sensitivity threshold ϵ_J is thus not necessarily going to guarantee detection of very small fault currents, and it also increases the probability of false detections. The indicators detected faults successfully up to 15 kΩ using $\epsilon_J = 10$ mA.

To investigate the magnitude of the fluctuations, a constant load current was measured in the lab using two different sensors, i.e. CT_{ph} and $CT_{ph,2}$ in Table I. The resulting magnitude of the indicator J_a, computed with T_{SW}=100 ms, is shown in Fig. 13. The different curves correspond to different nominal values of the load current, and the results illustrate clearly that

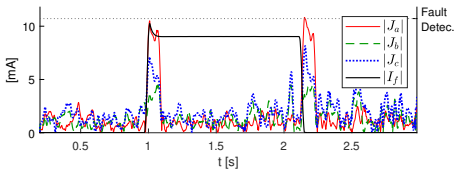

Fig. 12. Indicator magnitudes during a 20 kΩ fault. The fault is applied at t=1 s and disconnected at t=2.2 s.

the two sensors have different properties. In the case of $CT_{ph,2}$ sensor, the magnitudes are relatively large compared to CT_{ph}, but they are also independent of the magnitude of the primary current. CT_{ph} generally gives smaller fluctuations in J_a, but it is in turn dependent on the primary side current. Table II shows the number of false detections over the same period using CT_{ph}, as function of the load level and the sensitivity ϵ_J. To avoid false detection in this case the sensitivity must either 1) be limited to $\epsilon_J = 10$ mA, or 2) adapted in real-time based on the present value of the load current, which would allow more sensitive settings during low-load conditions. To identify the exact mechanism involved in determining the magnitude of these fluctuation requires further studies, but the importance of sensor quality is clearly seen.

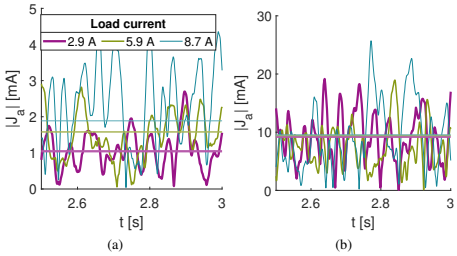

Fig. 13. Magnitude of indicator J_a when measuring a constant load current with (a) the Fluke sensor or (b) the LEM sensor. Horizontal lines show average values over 30 seconds.

TABLE II
NUMBER OF FALSE DETECTIONS DURING 30 SECONDS AS FUNCTION OF LOAD CURRENT $\vec{I}_L$, WITH $\phi = 15°$, $K = 0.1$, $T_{SW} = 0.1s$

$\vec{I}_L$ [A]	ϵ_J = 4 mA	ϵ_J = 6 mA	ϵ_J = 8 mA	ϵ_J = 10 mA
2.9	2	0	0	0
5.9	22	1	1	0
8.7	35	3	0	0

B. Sectionalizing

In order to verify the sectionalizing principle, a series of breaker operations is performed. By monitoring $\Delta\vec{I}_p$ throughout this process, the faulty section can be determined as explained in section III-C. Fig. 14 illustrates how $\Delta\vec{I}_p$ is estimated throughout the sectionalizing sequence when clearing a fault, compared to both the fault current and the neutral current. The fault resistance was 20 kΩ. See Fig. 7 for breaker locations:

- At $t = T_1$, the fault is applied between section 11 and L_{12}.
- At $t = T_2$, L_{13} is opened. Section 13 is now disconnected from the network, but the fault is still present. Disconnecting section 13 increased the compensation degree and decreased the neutral voltage. As a result, the neutral current decreased as well, but the fault current increased slightly. $\Delta\vec{I}_p$ correctly captures this behavior.
- At $t = T_3$, L_R is closed to bring section 13 back in, but now fed from feeder 2. The network now regains its original compensation degree.
- From $t = T_4$–T_5, section 12 is also disconnected from feeder 1 and connected to feeder 2.
- At $t = T_6$, the faulty section, section 11, is correctly disconnected by opening breaker L_{11}. $\Delta\vec{I}_p$ goes to zero, confirming that the fault is cleared.

The entire process from T_1 to T_6 took 11 seconds. Note that this breaker sequence is only intended to demonstrate the behavior of $\Delta\vec{I}_p$ during temporary disconnection of both healthy and faulty sections of the network. In a real network with a different feeder layout and breaker arrangement, the optimal breaker sequence may be different. The optimization of this sectionalizing process is not considered in this paper.

In addition to the case shown in Fig. 14, the sectionalizing indicator was verified for faults in the range 10-50 kΩ. There were no signs of reduced accuracy for increased fault resistances, but fault resistances above 50 kΩ were not available at the time of testing. The indicator also functioned as intended in both an over-compensated and under-compensated network.

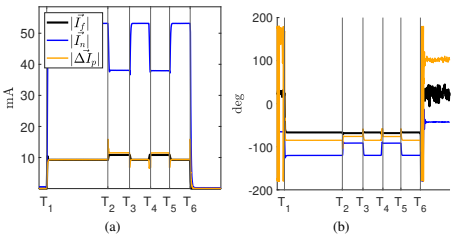

Fig. 14. Magnitude (a) and angle (b) of fault current, neutral current and $\Delta\vec{I}_p$ during sectionalizing process for a 20 kΩ fault.

The network in the lab is very symmetrical, meaning that $\vec{V}_n$ and $\vec{I}_n$ are both very small in normal operation. This makes it quite easy to determine the presence of the fault based on either $\vec{V}_n$ or $\vec{I}_n$ as well, but in a network with a larger healthy state $\vec{V}_n$ and $\vec{I}_n$, this would not be possible. $\Delta\vec{I}_p$ could then provide a much more sensitive fault indication, because the change in compensation degree is accounted for. Furthermore, $\Delta\vec{I}_p$ will also match the faulty phase indicator J_a, enabling a

more trustworthy and selective fault detection. The test shown in Fig. 14 illustrates that $\Delta\vec{I}_p$ is a good approximation of the fault current, and it enables continuous monitoring of much higher fault resistances than $|V_n|$ can.

VI. Laboratory vs. real networks

The results in section V have verified the feasibility of the proposed method both for detecting and locating faults, and a few key factors have been identified and discussed in detail. It remains a challenge, however, to determine to what extent these laboratory tests can be used to predict the behavior in a real network.

A. Scaling up the laboratory quantities

The first issue is the scaling of the laboratory model, and how the normal phase current indicator fluctuations (noise) are related to the load currents and the earth fault current. The results so far have shown that the phase current indicators are ultimately limited by the magnitudes of these fluctuations, as the fault current eventually fails to stand out above them when the fault resistance increases. The question then becomes how the currents and fault resistances should be scaled.

To analyse the sensitivity of the method, the system currents can be scaled based on the fault current's relationship with the network voltage. By analysing (9), it can be found that the fault current, for a given fault resistance, is proportional to the system voltage when the fault resistance is high enough. Exactly how high R_f needs to be for this approximation to be valid is best illustrated with a figure. Consider a hypothetical 22 kV network with a 50 A charging current $I_{ch} = \omega C_{tot} V_{LL}/\sqrt{3}$. The fault current magnitude is computed using (9) and two approximations of (9) valid at low and high fault resistances, respectively, as shown in Fig. 15. The breaking point of the curve, marked by the vertical line, is found where $R_f^* = 1/(\omega C_{tot}(1-k))$. This limit is approximately 10 kΩ in the lab, and it is lower in larger networks where C_{tot} is higher. Below this limit, the fault current is determined by multiple parameters such as $\hat{G}$, R_p, k and D, while the approximation $|\vec{I}_f| \approx |\vec{E}_a|/R_f$ is valid beyond R_f^*. The latter is therefore valid when discussing the upper limit of the method's sensitivity.

The above approximation implies that a fault resistance in the 400 V laboratory network is equivalent to a fault resistance 55 times higher in a 22 kV network (22/0.4 = 55). Alternatively, the fault current is increased 55 times when considering the same fault resistance in a 400 V and a 22 kV network. The laboratory load currents, which are in the range 2.9 – 8.7 A, will then correspond to 160 – 480 A in a 22 kV network. Similarly, the 175 mA capacitive charging current in the laboratory network will correspond to a 10 A current. 10 A is a too low value for a realistic resonant grounded network (a more realistic value would be in the range of 50 A and higher), but this will only impact $|\vec{I}_f|$ up to the threshold R_f^*. The unusually small charging current is therefore not affecting the fault current magnitude for high fault resistances, i.e., at the maximum detectable fault resistance.

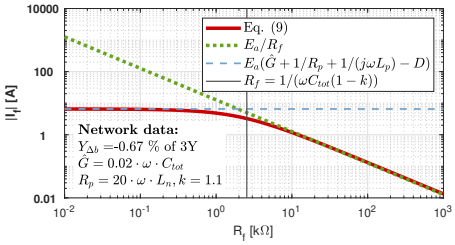

Fig. 15. $|\vec{I}_f|$ computed using (9) and two approximations for low and high values of R_f, in a 22 kV network with a 50 A charging current

It is the method's maximum detectable fault resistance which is of primary interest to be able to scale so that it can be compared to other methods. The method proposed in this paper relies on detecting the fault current, and if the method's sensitivity is absolute — i.e., it has some constant downward threshold for a detectable fault current — then the previous analysis have demonstrated that the laboratory results can be scaled directly based on the network voltage. This implies that a 20 kΩ fault resistance in the lab is equivalent to a 1.1 MΩ in the 22 kV network, which is not realistic. It is instead more reasonable to expect that the lowest detectable fault current will increase when moving from the 400 V laboratory to a 22 kV network, due to for instance increased measurement noise. The results so far have shown that the phase current fluctuations are the limiting factor, so the results in a real network will depend on how they scale. If their increase cancels out the effect of a larger fault current, then the maximum detectable fault resistance in the real network will be the same as in the laboratory. This remains uncertain until sensors and their properties can be studied in the field, as will be discussed next.

B. Current sensor properties

The second challenge encountered when analysing these results is comparing the properties of the current sensors used in the laboratory to those of CTs in real networks. Fig. 13 showed that two different sensors radically impacted the feasibility of the fault detection method. One of the sensors was impacted by the current magnitude, suggesting that the interference from surrounding conductors impacted its measurements. The other sensor, however, while being unaffected by the current magnitude, generally gave much higher measurement noise. Whether this is due to the measurement principle, current rating or something else entirely is not known. Whatever the reason, the results have shown that the indicators J_{a-c} will have a non-zero value in healthy operation, and a sufficiently large fault current is required to stand out above this noise.

Fig. 16 shows the phase current indicator magnitudes on the faulty feeder measured during two 20 kΩ earth fault tests, where one set of measurements comes from the laboratory tests conducted in this paper, and the other from a field test conducted by Norwegian network operator Glitre Energi Nett

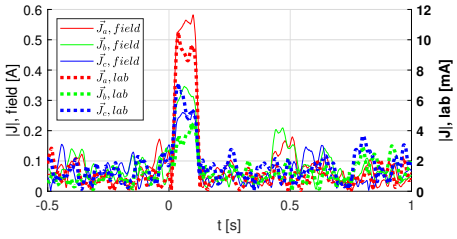

Fig. 16. Earth fault indicator magnitudes during a field test and laboratory test (right y-axis). R_f=20 kΩ in both cases, with pre-fault phase currents approximately 3 A and 20 A in the lab and the real network, respectively.

in their 22 kV network. The 22 kV network was operated with a 55 A ASC, which corresponded to a compensation degree of 10% over-compensation. Note that the indicators estimate a 10 mA and 0.55 A fault current in the two networks, fitting well with the analysis in section VI-A where a scaling factor of 55 was predicted. In the lab test the phase currents were 2.9 A, whereas they were 20 A in the field tests. Although the ratio between the fault current and the load currents is higher in the field tests, so is the ratio between the fluctuations and the load currents. In other words, the ratio between the fault current and the fluctuations is almost identical in the two recordings, making the fault detection equally challenging.

This finally raises the question about whether different sensors in the 22 kV network could have given better results and lower fluctuations. The field tests were conducted using class 5p20 protection cores, which are likely less accurate than the laboratory measurements. The field tests were not conducted with the purpose of verifying the method presented in this paper, and using metering cores or a different sensor type in a different location could have yielded different results. A detailed overview of the measurement chain used in the field tests is unfortunately not available, and their comparison with the lab tests is therefore done cautiously. The simple example in Fig. 16 corroborates the lab results and demonstrates that the phase current indicators function as intended, but dedicated field tests are required to study the current sensors and the measurement quality in a real network, which currently is the limiting factor for the proposed method.

C. Comparison with other methods

There are comparable methods found in the literature which are able to detect and locate faults for very high fault resistances, and which have been verified experimentally. These methods are all based on incremental values and on manipulating the same basic set of equations as in section II, but using zero-sequence currents. In [27], a probabilistic method is presented which functioned up to 220 kΩ, and the method in [3] can detect faults in the range 100–200 kΩ. The method in [28] functioned successfully up to 180 kΩ, but does require closed-ring operation of the network. Two methods functioning up to 100 kΩ are presented in [20], along with a fault location method aimed at narrowing down the faulted section. It is however dependent on detailed network data and may not always give a conclusive fault location estimate. The method in [19] functioned up to 160 kΩ, and the authors mention potential challenges with normal system operation triggering responses in the zero-sequence parameters similar to those observed during faults.

The sectionalizing indicator showed no considerable loss of accuracy up to the maximum available 50 kΩ fault resistance, indicating that its limit is well above 50 kΩ. The phase current indicators functioned up to 15–20 kΩ, but, as discussed earlier, the exact mechanism involved in determining this threshold is not fully understood. The scaling of the fault resistances in the lab is as discussed earlier a challenge; with ideal measurements the results can in theory be scaled up to any network by the same factor as the system voltage increase, but this implies sensitivity in the MΩ-range for the proposed method and does not seem realistic. The evaluation of the fault resistances and their scaling can not be done separately from the analysis of the current sensors and their properties, and this does require field tests with applicable sensors.

Regarding the sectionalizing indicator, no comparable method for during-fault sectionalizing has been found in the literature.

VII. Conclusion

This paper has presented a detailed description of the implementation and laboratory verification of a novel earth fault detection and location method. The method shows promising results in the laboratory tests, and one field test from a 22 kV network corroborate this. The main contributions of these results are as follows:

1) The new method makes each feeder capable of determining a forward fault using only local phase current measurements without need for input from other feeders or using voltage as a polarizing quantity.
2) A sectionalizing indicator is presented and verified, which can be used to provide continuous fault indication in a network during the sectionalizing process. The indicator is based on the neutral current in the network and is not limited to radial networks.

The results also show that phase currents can be used for low-current earth faults, a domain which traditionally has been handled exclusively with zero-sequence currents.

In addition to the mentioned contributions, the paper has also identified limitations, both of the method itself and the applicability of the tests, as well as further work required before the method can be implemented. The measurement quality is currently identified as the main limitation of the method, and 50 Hz noise found to be dependent on the current sensors and the magnitude of the load currents limits the sensitivity. This phenomenon is dependent on the sensors used, and understanding and quantifying this represents the most important future work as it relates directly to the attainable sensitivity and reliable pickup levels for the fault detection. Dedicated field tests are required to study the impact of different current sensors and CT cores on the method further.

ACKNOWLEDGMENT

The authors would like to thank S. E. Norum and B. Almås at the Department of Electric Energy at NTNU for their contributions during the laboratory testing, and Glitre Energi Nett for sharing measurements and data from field tests.

REFERENCES

[1] Norwegian Directorate for Civil Protection (DSB). "Veiledning til forskrift om elektriske forsyningsanlegg (In Norwegian)." dsb.no. https://www.dsb.no/lover/elektriske-anlegg-og-elektrisk-utstyr/veiledning-til-forskrift/veiledning-til-forskrift-om-elektriske-forsyningsanlegg/ (accessed Jun. 25, 2023)

[2] S. Hänninen and M. Lehtonen, "Characteristics of earth faults in electrical distribution networks with high impedance earthing," *Electr. Power Syst. Res.*, vol. 44, no. 3, pp. 155-161, 1998.

[3] A. Nikander and P. Järventausta, "Identification of High-Impedance Earth Faults in Neutral Isolated or Compensated MV Networks," *IEEE Transactions on Power Delivery*, vol. 32, no. 3, pp. 1187-1195, June 2017, doi: 10.1109/TPWRD.2014.2346831.

[4] X. Wang, X. Wei, J. Gao, G. Song, M. Kheshti and L. Guo, "High-Impedance Fault Detection Method Based on Stochastic Resonance For a Distribution Network With Strong Background Noise," *IEEE Transactions on Power Delivery*, vol. 37, no. 2, pp. 1004-1016, April 2022, doi: 10.1109/TPWRD.2021.3075472.

[5] T. Schinerl, "A new sensitive detection algorithm for low and high impedance earth faults in compensated MV networks based on the admittance method," *CIRED 2005 - 18th International Conference and Exhibition on Electricity Distribution*, 2005, pp. 1-4, doi: 10.1049/cp:20051166.

[6] J. Altonen, A. Wahlroos and S. Vähäkuopus, "Application of multi-frequency admittance-based fault passage indication in practical compensated medium-voltage network," *CIRED-Open Access Proceedings Journal*, vol. 2017, no. 1, pp. 947-951, October 2017, doi: 10.1049/oap-cired.2017.0967.

[7] G. Druml,C. Raunig, P. Schegner and L. Fickert, "Fast selective earth fault localization using the new fast pulse detection method," in *22nd International Conference and Exhibition on Electricity Distribution (CIRED 2013)*, 2013, pp. 1-5.

[8] A. Farughian, L. Kumpulainen and K. Kauhaniemi, "Review of methodologies for earth fault indication and location in compensated and unearthed MV distribution networks," *Electr. Power Syst. Res.*, Vol. 154, 2018, pp. 373-380.

[9] P. Wang, B. Chen, H. Zhou, T. Cuihua and B. Sun, "Fault Location in Resonant Grounded Network by Adaptive Control of Neutral-to-Earth Complex Impedance," *IEEE Transactions on Power Delivery*, vol. 33, no. 2, pp. 689-698, April 2018, doi: 10.1109/TPWRD.2017.2716955.

[10] E. Burkhardt, L. Fickert and F. Jenau, "The "Short-term Compensation Change" to Detect Earth Faults in Compensated Networks," *2020 55th International Universities Power Engineering Conference (UPEC)*, 2020, pp. 1-5, doi: 10.1109/UPEC49904.2020.9209841.

[11] C. Raunig, L. Fickert, C. Obkircher and G. Achleitner, "Mobile earth fault localization by tracing current injection," *Proceedings of the 2010 Electric Power Quality and Supply Reliability Conference*, 2010, pp. 243-246, doi: 10.1109/PQ.2010.5549991.

[12] J. Li, Y. Liu, C. Li, D. Zeng, H. Li and G. Wang, "An FTU-Based Method for Locating Single-Phase High-Impedance Faults Using Transient Zero-Sequence Admittance in Resonant Grounding Systems," *IEEE Transactions on Power Delivery*, vol. 37, no. 2, pp. 913-922, April 2022, doi: 10.1109/TPWRD.2021.3074217.

[13] M. Loos, S. Werben, M. Kereit and J. Maun, "Fault direction method in compensated network using the zero sequence active energy signal," *Eurocon 2013*, 2013, pp. 717-723, doi: 10.1109/EUROCON.2013.6625062.

[14] H. Ji, Y. Yang, H. Lian and S. Cong, "Effect on Earth Fault Detection Based on Energy Function Caused by Imbalance of Three-Phase Earth Capacitance in Resonant Grounded System," *2006 International Conference on Power System Technology*, 2006, pp. 1-5, doi: 10.1109/ICPST.2006.321670.

[15] K. Pandakov, H. K. Høidalen and J. I. Marvik, "Misoperation analysis of steady-state and transient methods on earth fault locating in compensated distribution networks," *Sustainable Energy, Grids and Networks*, 15, pp. 34-42, 2018. https://doi.org/10.1016/j.segan.2017.12.001.

[16] S. K. Pirmani, Md. A. Mahmud, S. N. Islam and M. T. Arif, "A modified charge similarity approach for detecting high impedance earth faults in resonant grounded power distribution networks," *Electr. Power Syst. Res.*, vol. 220, 109264, 2023.

[17] K. Pandakov, "Improvements in protection of medium voltage resonant grounded networks with distributed sources," Ph.D. dissertation, Dept. Electric Power Eng., NTNU, Trondheim, Norway, 2018.

[18] M. A. Barik, A. Gargoom, M. A. Mahmud, M. E. Haque, H. Al-Khalidi and A. M. Than Oo, "A Decentralized Fault Detection Technique for Detecting Single Phase to Ground Faults in Power Distribution Systems With Resonant Grounding," *IEEE Transactions on Power Delivery*, vol. 33, no. 5, pp. 2462-2473, Oct. 2018, doi: 10.1109/TPWRD.2018.2799181.

[19] S. Hänninen and M. Lehtonen, "Method for Detection and Location of Very High Resistive Earth Faults", *ETEP*, vol. 9, no. 5, pp. 285-291, September/October 1999.

[20] T. Welfonder, V. Leitloff, R. Fenillet and S. Vitet, "Location strategies and evaluation of detection algorithms for earth faults in compensated MV distribution systems," *IEEE Transactions on Power Delivery*, vol. 15, no. 4, pp. 1121-1128, Oct. 2000, doi: 10.1109/61.891492.

[21] K. J. Sagastabeitia, I. Zamora, A. J. Mazónm Z. Agiako and G. Buigues, "Low-current fault detection in high impedance grounded distribution networks, using residual variations of asymmetries", *IET Gener. Transm. Distrib.*, vol. 6, no. 12, pp. 1252-1261, 2012.

[22] T. Treider, B. Gustavsen and H. K. Høidalen, "Steady-state, iterative method for locating and clearing permanent high impedance earth faults in compensated networks," in *16th international conference on developments in power system protection 2022 (DPSP 2022)*, Newcastle, U. K., 2022, pp. 1-6.

[23] Norwegian University of Science and Technology. "National Smart Grid Laboratory." NTNU.edu. https://www.ntnu.edu/smartgrid (accessed Jun. 25, 2023).

[24] SINTEF. "Smart Grid Laboratory." Sintef.no. https://www.sintef.no/en/all-laboratories/smartgridlaboratory/ (accessed Jun. 25, 2023).

[25] A. Petterteig, "Distribution Network Laboratory Model: Consisting of a HV/MV substation model, a synchronous generator DG model and a flexible line equivalent.," SINTEF Energy Research, Trondheim, Norway, Rep. TR A7122, 2011.

[26] D. R. Gurusinghe, D. Ouellette, and A. D. Rajapakse,"Implementation of smart DFT-based PMU model in the real-rime digital simulator," in *International Conference on Power Systems Transients (IPST2017)*, pp. 1-6, 2017.

[27] S. Hänninen, M. Lehtonen, and U. Pulkkinen, "A probabilistic method for detection and location of very high resistive earth faults," *Electr. Power Syst. Res.*, vol. 54, no. 3, pp. 1999-206, 2000.

[28] A. Nikander, S. Repo and P. Järventausta, "Utilizing the ring operation mode of medium voltage distribution feeders," in *17th International Conference and Exhibition on Electricity Distribution (CIRED 2003)*, 2003, pp. 1-6.

Appendix B

Zero-sequence current division on ring-connected feeders

Consider two feeders A and B, connected to form a closed-ring configuration. Equation (B.1), written with the notation from Paper III, describes the zero sequence currents flowing onto each of them:

$$\begin{aligned} 3\vec{I}_{0A} &= m_A \vec{V}_n \bar{Y} + n_A \vec{E}_a \hat{Y} \\ 3\vec{I}_{0B} &= m_B \vec{V}_n \bar{Y} + n_B \vec{E}_a \hat{Y} \end{aligned} \tag{B.1}$$

Here, $m_B = 1 - m_A$ and $n_B = 1 - n_A$. During fault, the terms $\vec{V}_n Y_{A+B} \cdot m_A$ and $\vec{V}_n Y_{A+B} \cdot m_B$ are the dominant components of the zero-sequence currents. Therefore, m_A and m_B must be found to be able to remove their contributions to the zero-sequence current an isolate the fault current component.

Consider Fig. B-1a, where two feeders are connected to form a ring. The ring is divided into n zero-sequence PI-equivalents as shown in Fig. B-1b, chosen so that the magnitude of the zero-sequence series impedance for each PI-section is the same, i.e. $|z_1| = |z_2| = |z_3| = ... = |z_n|$.

Next, the parallel capacitances of adjacent PI-equivalents are summed, and $n + 1$ capacitances $\tilde{C}_0 - \tilde{C}_n$ are defined in (B.2).

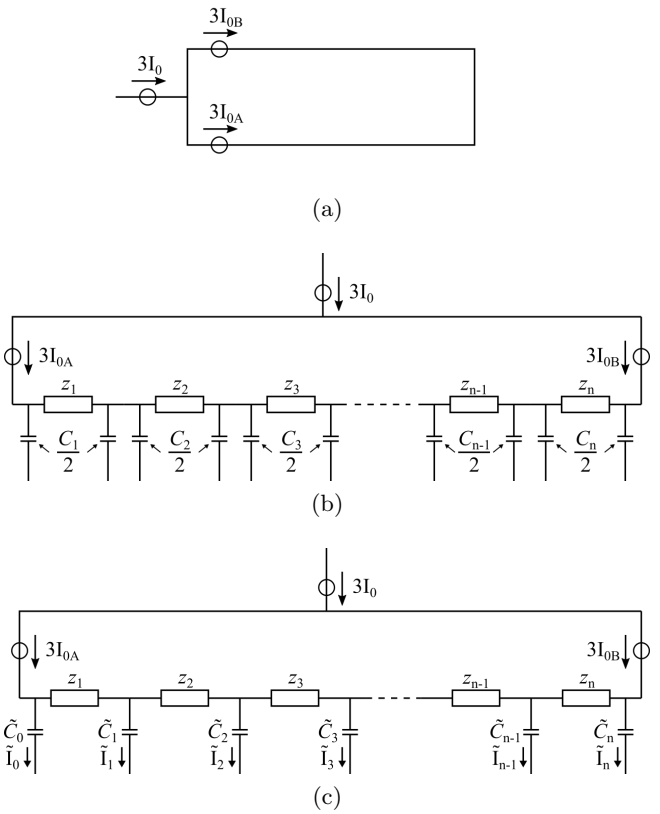

Fig. B-1. Ring-connected feeders divided in n PI-equivalents to calculate the division of $3I_0$ on each feeder

$$\tilde{C}_i = \frac{1}{2}\begin{cases} C_{i+1} & i = 0 \\ C_i & i = n \\ C_i + C_{i+1} & i = 1, 2, ..., n-1 \end{cases} \tag{B.2}$$

Fig. B-1c shows the resulting network with capacitances $\tilde{C}_0 - \tilde{C}_n$.

The currents $\tilde{I}_0 - \tilde{I}_n$ flowing in $\tilde{C}_0 - \tilde{C}_n$ can be approximated by assuming that the voltage over each of them is V_0. This assumption is based on the fact that most of the zero sequence voltage drop occurs over the capacitances compared to the series impedance. The current through each

of these capacitances can thus be approximated as

$$\tilde{I}_i = j\omega\tilde{C}_i V_0 \tag{B.3}$$

The sum of these currents must equal the current $3I_0$ flowing onto the ring. Using current division, the currents measured on feeder A and B are obtained in (B.4).

$$\begin{aligned} 3I_{0A} &= \tilde{I}_0 + \tilde{I}_1\frac{n-1}{n} + \tilde{I}_2\frac{n-2}{n} + ... + \tilde{I}_{n-1}\frac{1}{n} + \tilde{I}_n\frac{0}{n} \\ 3I_{0B} &= \tilde{I}_0\frac{0}{n} + \tilde{I}_1\frac{1}{n} + \tilde{I}_2\frac{2}{n} + ... + \tilde{I}_{n-1}\frac{n-1}{n} + \tilde{I}_n \end{aligned} \tag{B.4}$$

Equation (B.4) can be written more compact as in (B.5).

$$\begin{aligned} 3I_{0A} &= \sum_{i=0}^{n} \tilde{I}_i\frac{n-i}{n} \\ 3I_{0B} &= \sum_{i=0}^{n} \tilde{I}_i\frac{i}{n} \end{aligned} \tag{B.5}$$

Inserting (B.3) into (B.5):

$$\begin{aligned} 3I_{0A} &= j\omega V_0 \sum_{i=0}^{n} \tilde{C}_i\frac{n-i}{n} \\ 3I_{0B} &= j\omega V_0 \sum_{i=0}^{n} \tilde{C}_i\frac{i}{n} \end{aligned} \tag{B.6}$$

Because the zero-sequence network assumes symmetrical impedances and admittances in the three phases, n_A and n_B in (B.1) are zero in this analysis. The ratio of m_A and m_B is then found as:

$$\frac{m_A}{m_B} = \frac{\sum_{i=0}^{n} \tilde{C}_i\frac{n-i}{n}}{\sum_{i=0}^{n} \tilde{C}_i\frac{i}{n}} \tag{B.7}$$

Recognizing that $m_B = 1 - m_A$, m_A is found as

$$m_A = \frac{\sum_{i=0}^{n} \tilde{C}_i\frac{n-i}{n}}{\sum_{i=0}^{n} \tilde{C}_i} \tag{B.8}$$

The correct solution is found as $n \to \infty$, so the value of n is selected to give the desired accuracy. To account for laterals, the entire zero-sequence capacitance of the lateral is added to the capacitance $\tilde{C}_i$ in the corresponding location.

See below for an example of a Matlab-script computing the values of m_A and m_B for the network in Paper III.

Calculating m_A and m_B in Paper III

The following Matlab-script shows how m_A and m_B can be calculated with the analytical approach. Network data correspond to Paper III.

```
%Select the size of the series impedance in each segment. Smaller
%values gives more accurate results as n approaches infinity.
z=0.00001;

%The network has eight unique segments A-H counting from the
%start of feeder A.
L_segA=3;
L_segB=4;
L_segC=6;
L_segD=5;
L_segE=3;
L_segF=1;
L_segG=6;
L_segH=2;

%zero sequence line parameters for overhead (oh) and cables
z_cable=0.125+1j*0.11;
c0_cable=280*1e-9;
z_oh=0.413+1j*1.134;
c0_oh=6.1*1e-9;

%segment impedances
Z_segA=z_cable*L_segA;
Z_segB=z_cable*L_segB;
Z_segC=z_oh*L_segC;
Z_segD=z_oh*L_segD;
Z_segE=z_oh*L_segE;
Z_segF=z_oh*L_segF;
Z_segG=z_cable*L_segG;
```

```
Z_segH=z_cable*L_segH;

%segment capacitances
C_segA=c0_cable*L_segA;
C_segB=c0_cable*L_segB;
C_segC=c0_oh*L_segC;
C_segD=c0_oh*L_segD;
C_segE=c0_oh*L_segE;
C_segF=c0_oh*L_segF;
C_segG=c0_cable*L_segG;
C_segH=c0_cable*L_segH;



%Computing the number of PI-equivalents per segment, based on the
%selected value of z. Rounding to give integer.
A=round(abs(Z_segA)/z);
B=round(abs(Z_segB)/z);
C=round(abs(Z_segC)/z);
D=round(abs(Z_segD)/z);
E=round(abs(Z_segE)/z);
F=round(abs(Z_segF)/z);
G=round(abs(Z_segG)/z);
H=round(abs(Z_segH)/z);

%Total number of segments on the ring
n=A+B+C+D+E+F+G+H;

%compute all regular capacitances Cs for each of the n segments
%on the ring
Cs=zeros(1,n);
for segment=1:n
    if (segment<=A)
        Cs(segment)=C_segA/A;
    elseif (segment>A && segment <=A+B)
        Cs(segment)=C_segB/B;
    elseif (segment>A+B && segment <=A+B+C)
        Cs(segment)=C_segC/C;
    elseif (segment>A+B+C && segment <=A+B+C+D)
        Cs(segment)=C_segD/D;
    elseif (segment>A+B+C+D && segment <=A+B+C+D+E)
        Cs(segment)=C_segE/E;
    elseif (segment>A+B+C+D+E && segment <=A+B+C+D+E+F)
        Cs(segment)=C_segF/F;
    elseif (segment>A+B+C+D+E+F && segment <=A+B+C+D+E+F+G)
```

```
        Cs(segment)=C_segG/G;
    else
        Cs(segment)=C_segH/H;
    end
end

%compute all derived Cs, C_tilde.

CCs=zeros(1,n+1);

for current=1:n+1
    if (current==1)
        CCs(current)=Cs(current)/2;
    elseif (current>1 && current <n+1)
        CCs(current)=(Cs(current-1)+Cs(current))/2;
    else
        CCs(current)=Cs(current-1)/2;
    end
end

%add laterals between segments manually by summing the
%capacitance of the lateral to the corresponding element in CCs.

%Lateral AB is between A and B, corresponds to element A+1 in
%CCs. We have laterals between segments A and B, C and D,
%D and E, E and F, F and G.
C_latAB=13*c0_cable+6*c0_oh;
C_latCD=8*c0_cable+7*c0_oh;
C_latDE=6*c0_cable+19*c0_oh;
C_latEF=5*c0_cable+4*c0_oh;
C_latFG=2*c0_cable+3*c0_oh;

%adding the entire capacitance of each lateral to the correct
%location on the ring:
CCs(A+1)=CCs(A+1)+C_latAB;
CCs(A+B+C+1)=CCs(A+B+C+1)+C_latCD;
CCs(A+B+C+D+1)=CCs(A+B+C+D+1)+C_latDE;
CCs(A+B+C+D+E+1)=CCs(A+B+C+D+E+1)+C_latEF;
CCs(A+B+C+D+E+F+1)=CCs(A+B+C+D+E+F+1)+C_latFG;


%Computing the sums required for compting mA and mB
sumA=0;
sumB=0;
```

```
for i=1:n+1
    sumA=sumA+CCs(i)*(n-i-1)/n;
    sumB=sumB+CCs(i)*(i-1)/n;
end

R=sumA/sumB;
R2=sumB/sumA;
fprintf('Resulting values:\n')
mA=R/(1+R);
mB=R2/(1+R2);

%mA can also be calculated directly as: %
%mA=sumA/(C_segA + C_segB + C_segC + C_segD + C_segE + C_segF
%+ C_segG + C_segH + C_latAB + C_latCD + C_latDE +C_latEF +
%C_latFG
%or simply
%mA=sumA/sum(CCs)

fprintf('%s%.4f%s%.4f%s\n','*** mA = ',mA,', mB= ',mB,' ***')
fprintf('\n')
```

ISBN 978-82-326-7718-4 (printed ver.)
ISBN 978-82-326-7717-7 (electronic ver.)
ISSN 1503-8181 (printed ver.)
ISSN 2703-8084 (online ver.)

NTNU

Norwegian University of
Science and Technology